Characterization and modelling of pervious concrete.

DOCTORAL THESIS

Doctoral Thesis by:

Ricardo Pieralisi

Directed by:

Sergio H. P. Cavalaro

Antonio Aguado de Cea

Barcelona, March 2016

Universitat Politècnica de Catalunya

Departament d´Enginyeria de la Construcció

UNIVERSITAT POLITÈCNICA DE CATALUNYA
BARCELONATECH
Escola de Doctorat

Acta de calificación de tesis doctoral	Curso académico:

Nombre y apellidos: Ricardo Pieralisi

Programa de doctorado: Ingeniaría de la Construcción

Unidad estructural responsable del programa: Departamento de Ingeniaría de la Construcción

Resolución del Tribunal

Reunido el Tribunal designado a tal efecto, el doctorando / la doctoranda expone el tema de la su tesis doctoral titulada Characterization and modelling of pervious concrete

_____.

Acabada la lectura y después de dar respuesta a las cuestiones formuladas por los miembros titulares del tribunal, éste otorga la calificación:

☐ NO APTO ☐ APROBADO ☐ NOTABLE ☐ SOBRESALIENTE

(Nombre, apellidos y firma) Presidente/a	(Nombre, apellidos y firma) Secretario/a	
(Nombre, apellidos y firma) Vocal	(Nombre, apellidos y firma) Vocal	(Nombre, apellidos y firma) Vocal

_____, _____ de _____ de _____

El resultado del escrutinio de los votos emitidos por los miembros titulares del tribunal, efectuado por la Escuela de Doctorado, a instancia de la Comisión de Doctorado de la UPC, otorga la MENCIÓN CUM LAUDE:

☐ SÍ ☐ NO

(Nombre, apellidos y firma) Presidente de la Comisión Permanente de la Escuela de Doctorado	(Nombre, apellidos y firma) Secretario de la Comisión Permanente de la Escuela de Doctorado

Barcelona a _____ de _____ de _____

"You see, I went on with this research just the way it led me. That is the only way I ever heard of true research going. I asked a question, devised some method of obtaining an answer, and got a fresh question. Was this possible or that possible? You cannot imagine what this means to an investigator, what an intellectual passion grows upon him! You cannot imagine the strange, colourless delight of these intellectual desires!"

Doctor Moreau (from the book "The Island of Doctor Moreau" H.G. Wells)

ACKNOWLEDGEMENTS

Once Isaac Newton states, "*If I have seen further it is by standing on the shoulders of Giants*". I would like to thank the giants that help me expand the limits of my horizon Sergio and Antonio. For both of them I would like to thank the opportunity of working with an excellent team, and for believe that I was strong enough to success and grow on the doctoral journey. Sergio, thank you for the very productive talks that we had during these years. Be sure that each one of the thought exchanges was special and I will carry them with me. Antonio, thank you for guiding me and instigating me to always do my best in each task.

The development of this thesis would not have been possible without the financial support of the Educational Ministry of Spain for the FPU Scholarship (AP2012-4188). I would like to thank the companies CPV and BASF for the dedication to several research projects (especially HoPo) throughout the years.

I thank Montse Santos, Mercè, Carme and Carmeta who have always been very attentive. Also, I thank the technicians of the laboratory, especially to Camilo and Robert for the attention and the help during the experimental programs.

I would like to thank the friends that I met during these years in Barcelona: Ahmed, Albert, Amin, Ana, André, Andressa, Carlos, Cécile, Cristián, Cristina, Daniela, Diego, Eduardo, Francesc, Gustavo, Helen, Jenny, Jordi, Jorge, Julia, Juliana, Karmele, Liao, Liliana, Martha, Mylene, Nacho, Natalia, Pau, Razmik, Ricard, Ruben, Sandra, Talita, Tai and Yohei. In special, I would like to thank Fran, Isaac, Luis Segura (Nico Perez, the zookeeper), Luis and Renan.

I would like to express my deepest gratitude and love to Lu for her patience and understand for the years that we shared during my PhD, special the moments that I was on the verge of madness (with my thesis) and you rescued me. You helped me grow and mature. Also, we had countless amazing experiences during the last two years!

I would like to thank my family (Wilson, Luzia, Osvaldo, Cida, Nelci, Sergio, Nelí, Dilene, Marcos, Sergio Henrique, Maria Fernanda, Ana Elisa, Guilherme, Luis Gustavo, Luisa, Keila, Claudia and Frida) for the love and support that you all gave me during my life.

Finally, I want to express all the love that I have to the four most important people in my life. Nelson and Denise (my parents), thank you for all the love and affection that you have brought me up. If today I am who I am, you can be sure that you are the major responsible. Júnior and Rodrigo (my brothers), thank you for grown up with me and taught me many things about life, you were and always will be my first and most important friends.

SUMMARY

Pervious concrete is a special material with high permeability usually obtained by reducing the amount of fine aggregates in the composition of concrete. The increase in permeability generally implies a reduction in the mechanical performance. The properties of pervious concrete not only depend on its composition but also on the construction methods. The compaction process has a direct influence on the values of permeability and mechanical properties achieved. In fact, depending on the level of compaction applied, the same composition might give a highly pervious or even an almost impervious concrete. The interest of the scientific and technical community about pervious concrete has increased significantly since the 90's. Nowadays the most common applications are found in the field of pavements, in which the material contributes to mitigate problems such as flooding and runoff water that affect densely populated areas. For that reason and due to the smaller consumption of materials and resources, pervious concrete is perceived as an environmental friendly alternative.

Despite the technological advances on this field, the definition of the most adequate composition and compaction process to comply with the requirements of each application is normally based on trial and error or previous experiences. The lack of composition design methods in the literature may be attributed to the high complexity of the factors that intervene in the final performance of pervious concrete, which may hardly be generalized for all practical situations. In this context, the objective of this PhD thesis is to achieve a deeper understanding about pervious concrete and promote a new composition design philosophy based on advanced numerical simulations to minimize the need of experimental tests.

This work covers the main aspects of production and performance of pervious concrete, from the fresh to the hardened state. The first subject refers to the compaction process in the fresh state. An Evolutionary Lattice Model (ELM) is developed for simplified 2D simulations. As a more realistic alternative, new constitutive laws are developed and implemented in Discrete Element Models (DEM) for 3D simulations. To validate these models, experimental programs that emulate a controlled compaction were performed. The results confirm the representativeness of the models developed.

The second subject focuses on the permeability of concrete in the hardened state. The meso-structure derived from 3D simulations of the compaction process in the previous subject are evaluated in terms of their permeability. Computational Fluid Dynamics (CFD) models are used to simulate the water flow through the material. An experimental program is conducted with a constant head permeameter and different types of pervious concrete. The results obtained are used to validate the numerical models, confirming that it is possible to reproduce the real permeability results based on combined

numerical simulations of the compaction process and of the water flow within the material.

The third subject is centred on the mechanical properties of pervious concrete in the hardened state. A new constitutive law is developed and implemented in DEM to simulate the interaction between the connected particles that form the material. The meso-structure obtained as a result of the compaction simulations are used to assess numerically the expected mechanical properties of the pervious concrete. An experimental program is conducted to evaluate the compressive and indirect tensile strength of pervious concrete with different compositions and subjected to several degrees of compaction. The numerical results estimated with this constitutive law together with the meso-structure show good agreement with the experimental results.

The studies conducted in this work confirm that it is also possible to predict the performance expected in reality. Consequently, the numerical tools might be used to accelerate the process of defining the concrete composition and the production process for each application.

RESUMEN

El hormigón poroso es un material especial de alta permeabilidad que se obtiene generalmente mediante la reducción de la cantidad de áridos finos en la composición del hormigón. El aumento de la permeabilidad suele implicar una reducción del comportamiento mecánico. Las propiedades del hormigón poroso no sólo dependen de su composición, sino también de los métodos de construcción. El proceso de compactación tiene una influencia directa en los valores de la permeabilidad y propiedades mecánicas obtenidos. De hecho, dependiendo del nivel de compactación aplicada, la misma composición podría resultar en un hormigón altamente permeable o incluso casi impermeable. El interés de la comunidad científica y técnica sobre el hormigón poroso ha aumentado significativamente desde la década de los 90. En la actualidad las aplicaciones más comunes se encuentran en el campo de los pavimentos, en el que el material contribuye a reducir problemas tales como las inundaciones que afecta a las zonas densamente pobladas. Por esta razón y debido al menor consumo de materiales y recursos, el hormigón poroso es percibido como una alternativa ecológica.

A pesar de los avances tecnológicos en esta temática, la definición de la composición y del proceso constructivo y de compactación más adecuados para cumplir con los requerimientos de cada aplicación se basa normalmente en prueba y error o experiencias previas. La falta de métodos de diseño en la literatura se puede atribuir a la alta complejidad de los factores que intervienen en el comportamiento final del hormigón poroso, que difícilmente pueden generalizarse para todas las situaciones prácticas. En tal contexto, el objetivo de esta tesis doctoral es lograr una comprensión más clara sobre el hormigón poroso y promover una nueva filosofía de dosificación basada en simulaciones numéricas avanzadas para reducir la necesidad de pruebas experimentales.

Este trabajo abarca los principales aspectos de la producción y del comportamiento del hormigón poroso, desde el estado fresco hasta el estado endurecido. El primer tema se refiere al proceso de compactación en el estado fresco. El Evolutionary Lattice Model (ELM) ha sido desarrollado para simulaciones 2D simplificadas. Como una alternativa más realista, nuevas leyes constitutivas han sido desarrollados e implementados en Discrete Element Method (DEM) para las simulaciones 3D. Con el fin de validar estos modelos, se llevaron a cabo campañas experimentales que emulan una compactación controlada. Los resultados confirman la representatividad de los modelos desarrollados.

El segundo tema se centra en la permeabilidad del hormigón en el estado endurecido. Las meso-estructuras derivadas de las simulaciones 3D del proceso de compactación en el tema anterior han sido utilizadas para evaluar numéricamente la permeabilidad. Modelos de Computational Fluid Dynamics (CFD) han sido empleados para simular el flujo de agua a través del material. Asimismo se llevó a cabo una campaña

experimental con un permeámetro de carga constante y diferentes tipos de hormigones porosos. Los resultados obtenidos en dicha campaña han servido para validar los modelos numéricos, confirmando que es factible reproducir los resultados reales de permeabilidad basado en simulaciones numéricas combinando el proceso de compactación y el flujo de agua dentro del material.

El tercer tema se centra en las propiedades mecánicas del hormigón poroso en el estado endurecido. Una nueva ley constitutiva ha sido desarrollada e implementada en DEM para simular la interacción entre las partículas que forman el material. Las meso-estructuras derivadas de las simulaciones 3D del proceso de compactación en el tema anterior han sido usadas para evaluar numéricamente las propiedades mecánicas esperadas del hormigón poroso. Además, se llevó a cabo una campaña experimental para evaluar la resistencia a compresión y a tracción indirecta de hormigones porosos con diferentes composiciones y sometido a varios grados de compactación. Los resultados numéricos estimados con esta ley constitutiva en la meso-estructura muestran una buena concordancia con los resultados experimentales.

Los estudios realizados en este trabajo confirman que es posible predecir el desempeño esperado de los hormigones porosos en la realidad. Consecuentemente, las herramientas numéricas pueden ser utilizadas para acelerar el proceso de definición de la composición del hormigón y el proceso de producción adecuado para cada aplicación.

TABLE OF CONTENTS

LIST OF FIGURES

LIST OF TABLES

1. INTRODUCTION

1.1. PROLOGUE

The rapid growth of the world population and the socioeconomic development of the past decades conducted to a significant expansion of the urbanization. Consequently, the urbanization conducted to land development. Land development is characterized by the modification of the landscape, which increases the impervious surface area (ISA). Fig. 1.1 presents the global spatial distribution and density of constructed ISA in the years 2000-2001. The density of ISA for each grid cell is shown as a percentage of the total area. Examples of ISA include roads, parking lots, building, driveways, sidewalks and other manmade surfaces [1]. Fig. 1.2 shows a global map with the centers of the major floods reported during the years of 1985 and 2010 [2].

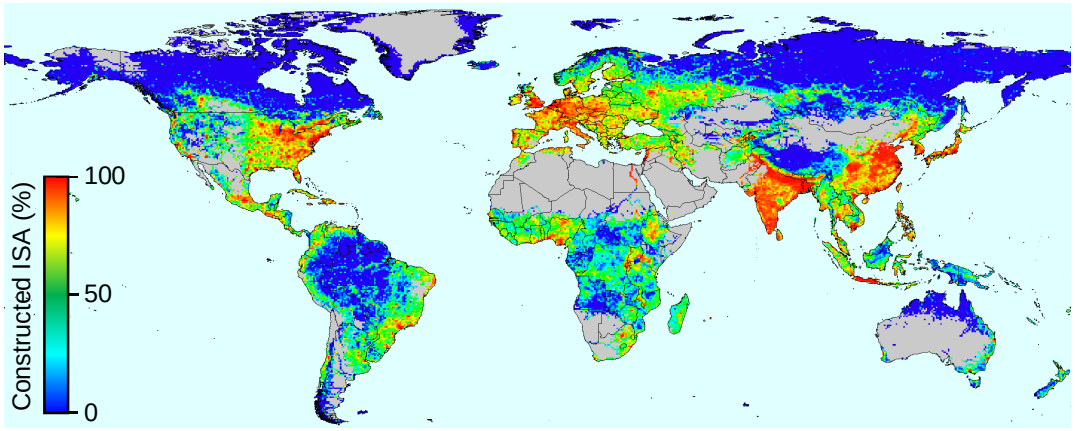

Figure 1.1 – Constructed Impervious Surface Areas (ISA), adapted from [1].

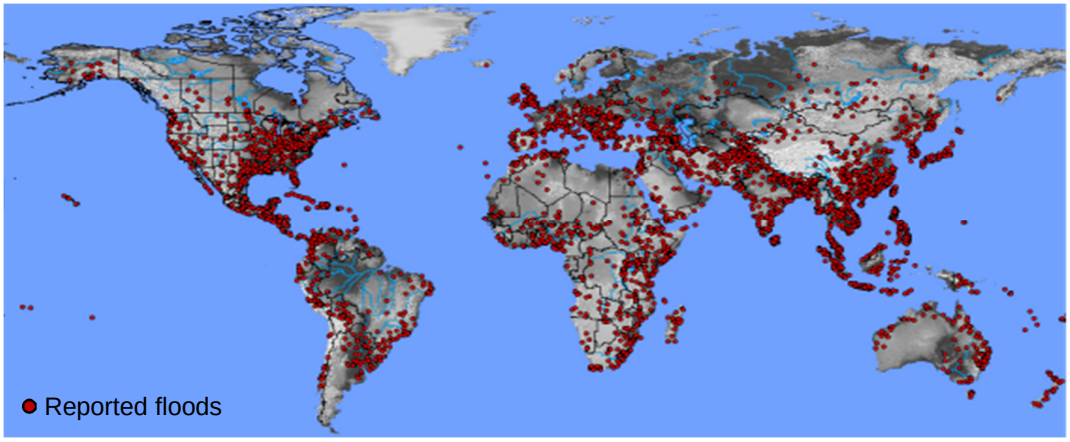

Figure 1.2 – Major global flood reported from 1985 to 2010, adapted from [2].

It is observed that the majority of the reported flood occurred where the constructed ISA is more intensive. Hence, during rainstorms, the constructed ISA carries storm water to drains instead of allowing the water to infiltrate the soil. Among other problems, this causes lowering of the groundwater recharge, runoff water and flooding since the amount of water that remains on the surface is greater on constructed ISA than natural areas.

Within this context, solutions to prevent storm water from generate urban flooding were sought. One of the most functional solution is to change the impervious pavements to permeable ones. In this sense, the pervious concrete is used as permeable pavement and satisfy the need for storm water management. Pervious concrete is obtained with narrowly graded coarse aggregate that is covered with a thin layer of cement paste [3]. This configuration produces a concrete with interconnected porosity in the other of 20 % of its volume. It is commonly produced to water from rainfall to pass through the body of the concrete

Therefore, the pervious concrete became interesting for both scientific and technical community. In this sense, Fig. 1.3 presents the number of published papers obtained with the pages of ScienceDirect and SpringerLink (with the search words: “pervious concrete”, “permeable concrete” and “porous concrete”) from 1985 to 2015. It is observed that the researches about this thematic starts to increase since the 95’s. However, the productions are more related to experimental experiences with different compositions. Practically no advances were observed regarding an improvement of the composition design methodology for pervious concrete apart of trial and error experiments in laboratory. Also, just a few researchers focused on the numerical development for simulation of the characteristics of pervious concrete

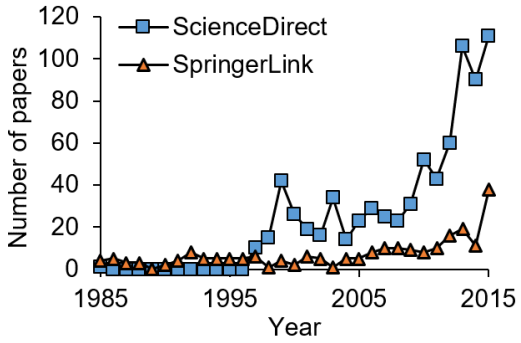

Figure 1.3 – Number of papers published along the years.

1.2. OBJECTIVES

1.2.1. General Objective

The general objective of this thesis is to propose a paradigm shift about 'how the pervious concrete is designed'. Nowadays, an extensive experimental program is necessary to design a pervious concrete with specific characteristics. However, this Doctoral Thesis aims to propose a design process of pervious concrete based on numerical simulations. With this improvement, less experimental work is required, which reduces the costs related to the design process.

In order to experiment this paradigm shift, the development of a numerical tool capable to predict the different characteristics of the pervious concrete is necessary. This numerical tool should allow to generate a geometrical model of the pervious with a representative spatial disposal of the aggregates. The geometrical model needs to consider the grading curve of the aggregates, the amount and rheological properties of the cement paste. Once the geometrical model is obtained, simulations to predict the hydrological and mechanical behavior of the pervious concrete should be performed.

1.2.2. Specific Objectives

In order to achieve the general objective several specific objectives are set. Tab. 1.1 shows the specific objectives for each subject treated in the thesis.

Table 1.1 – Specific objectives.

Subject	Specific Objectives
Fresh State behavior	• identify the factors that influence the behavior of the pervious concrete in fresh state; • propose a constitutive law to simulation the interaction between two aggregates connected by fresh cement paste; • calibrate and validate the proposed constitutive law with experimental results obtained during the development of this Doctoral Thesis; • generate geometrical models considering the mix design of the pervious concrete and the applied degree of compaction.
Hydrological behavior	• determine the factors that influence the permeability coefficient of the pervious concrete; • propose an analytical model to evaluate the permeability coefficient of the pervious concrete, considering its composition; • validate the geometrical model generation with the comparison between experimental and numerical permeability results.
Mechanical behavior	• establish the factors that influence the compressive and tensile strength of the pervious concrete; • propose an analytical model to evaluate the compressive and tensile behavior of the pervious concrete, considering its composition; • propose a constitutive law to simulate the interaction between two aggregates bonded by cement paste; • calibrate and validate the proposed constitutive law; • compare the fracture behavior observed in the numerical models with the ones obtained experimentally.

1.3. METHODOLOGY

In order to achieve the proposed general and specific objectives, the thesis is divided in four parts as shown in Fig. 1.4. Part I describes the motivations of the thesis and it is composed by the Chapter 1 and Chapter 2. Chapter 1 is the introduction, where the background, the objectives, scope and research strategy are presented.

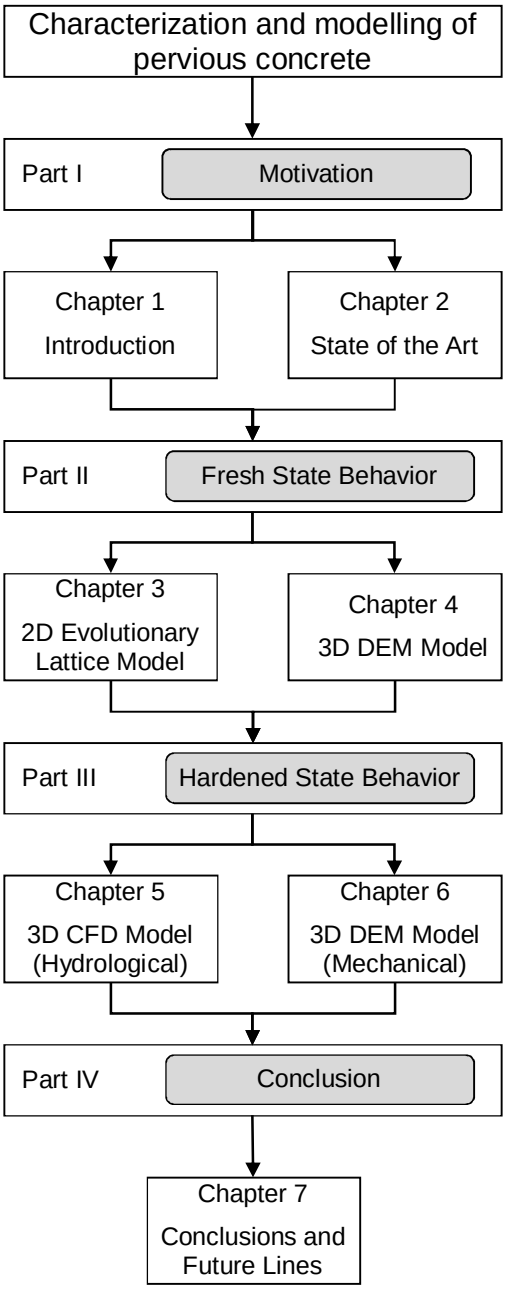

Figure 1.4 – Outline of the Thesis.

Chapter 2 is the state of the art, which covered the literature review of the pervious concrete production and properties. This includes the background of the models used to simulate the visco-elastic interactions of concretes and other materials. Furthermore, the models used to simulate the hydrological and mechanical behavior are also discussed.

Part II of the Thesis convers the fresh state behavior of the pervious concrete, as presented in Fig. 1.5. This subject is subdivided into two chapters (3 and 4). In Chapter 3 a 2D simplified framework, based on Lattice Model theory, to simulate the compaction process of pervious concrete in fresh state is presented and validate for low compaction levels. A more realistic model is presented in Chapter 4. In the latter, a constitutive law developed to simulate the interaction between aggregates connected by cement paste in fresh state is discussed and implemented in Discrete Element Method (DEM). In the sequence, the constitutive law is calibrated and validated with experimental results, also presented in this chapter. Finally, the results of both methods are compared.

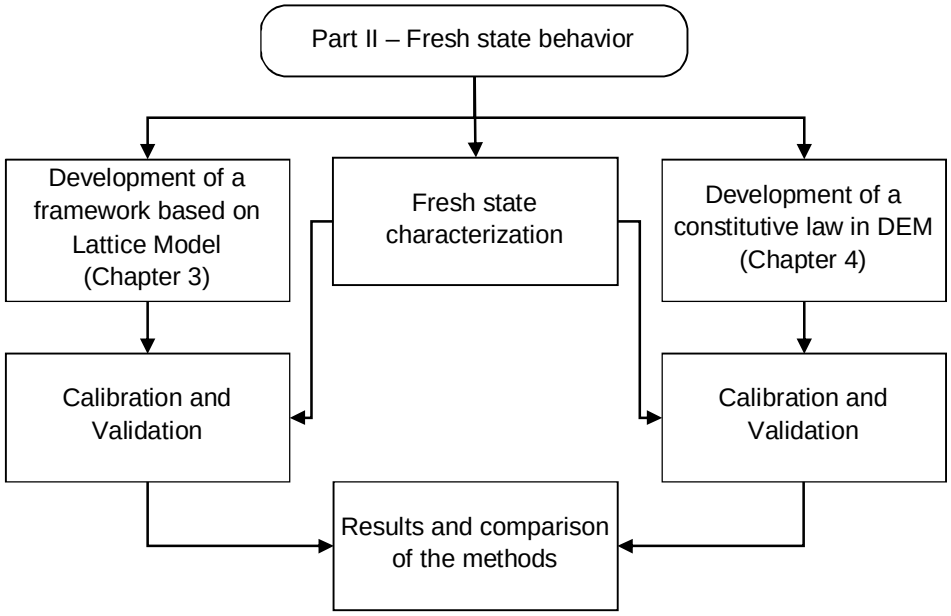

Figure 1.5 – Outline of Part II of the Thesis.

Once the spatial disposal of the aggregates resulting from the compaction process is determined, Part III focuses on the behavior of the hardened state of the pervious concrete, as depicted in Fig. 1.6. Chapter 5 deals with the hydrological behavior, centered on the permeability coefficient. In this chapter is presented an experimental campaign to characterize the permeability of different specimens of pervious concrete. Then, the experimental results is compared with the permeability obtained using CFD models.

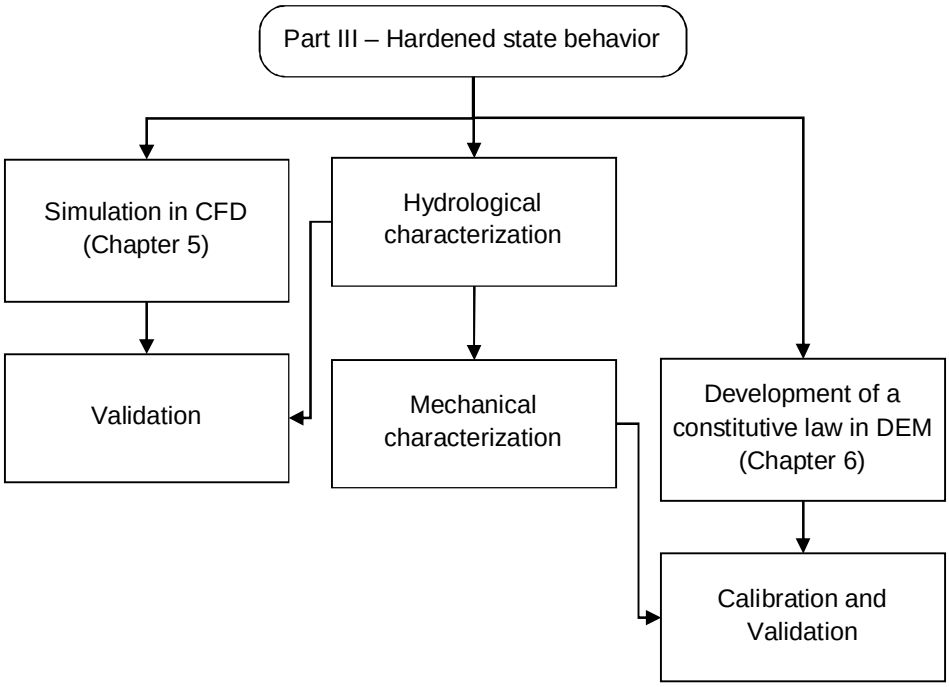

Figure 1.6 – Outline of Part III of the Thesis.

In Chapter 6, the mechanical properties of the pervious concrete is studied, identifying the compressive and tensile strengths and the fracture behavior when the specimens are subjected to uniaxial and diametric compressive loads. A constitutive law to simulate the interaction between two aggregates bonded by cement paste is proposed using DEM. The constitutive law is calibrated and validated considering the experimental results.

Finally, the conclusions of each of the subject addressed in this Thesis and the future lines of research are presented and discussed.

An important point to be presented before the continuity of the Thesis is the organization of the experimental work. In accordance with the previous paragraphs, several experimental campaigns are included in different parts of the work. In order to optimize the production of amount of specimens necessary to the realization of all the experimental campaigns, it took place once at the begging. This production process was described in the Chapters 3 and 4. The specimens tested in the experimental campaigns detailed in Chapters 5 and 6 were produced with the same process. However, just the specific tests according to the topic discussed (permeability – Chapter 5 – and mechanical properties – Chapter 6) are described. The organization of the experimental work is depicted in Fig. 1.7.

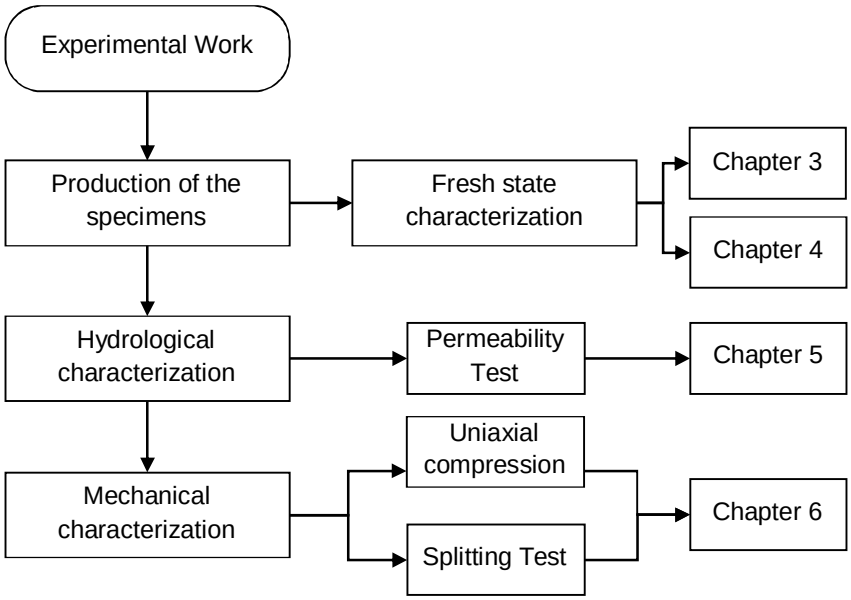

Figure 1.7 – Organization of the Experimental Work.

2. STATE OF THE ART

2.1. INTRODUCTION

The pavements are one of the basics structures for the transport system. They have an important role in social, environmental and economic development of the human life. Different pavement technologies were used along the years in the construction of roads. The oldest register of paved roads belonged to the city of Ur in the Middle East in about 4000 B.C.. This roads were constructed with stone-paved. Millenniums after the first road, the Romans revolutionized the concept of the construction of roads and built approximately 80.000 km of roads [4].

The pavement technologies evolved throughout the years. Nowadays, the asphalt and concrete are the predominant materials used in road construction. The composition that uses asphalt as binder material is characterized as flexible pavement. On the contrary, the rigid pavement uses Portland cement as binder in the composition of the concrete. Moreover, both technologies are subdivided into two other categories: impervious and pervious. The impervious pavement is the most used type of pavement. However, it is an environmental concern due the impediment it cases in the rainwater infiltration and natural groundwater recharge. On the contrary, the environmental effects of the pervious pavement is qualitatively different. It allows rainwater to percolate and infiltrate the surface areas. In other words, it is an environmental friendly pavement. In this context, pervious pavements presents a great number of applications. Wherein the pervious concrete is used in large scale.

Therefore, a revision of the bibliography concerning the topics presented in Chapter 1 was performed. As result of this study a state of the art of the pervious concrete in fresh and hardened state is presented. Moreover, the numerical models to predict the properties of the pervious concrete in the fresh and hardened are presented.

2.2. PERVIOUS CONCRETE

Pervious concrete (also known as porous concrete, permeable concrete and enhanced porosity concrete) is a special type of concrete with an opened macro-porosity that allows water to drain through the material. The traditional philosophy [3] used to achieve a pervious concrete is to reduce the amount of fines provided by the sand and to use cement paste contents just enough to create a connection between coarse aggregates. This leads to a material with interconnected porosity (20 to 35 %).

2.2.1. Materials

Pervious concrete uses the same materials as conventional concrete: cement, aggregates and water. According to ACI 522 [3], Portland cement is employed as main binder component. Additionally, supplementary cementitious materials (silica fume [5-8], fly-ash [5;9-11], rice husk [12], latex polymer [13-14] and tie rubber [15]) are used to increase the pervious concrete durability and properties [16].

The aggregate grading used in pervious concrete are typically either single-sized coarse aggregate or grading between 9.5 to 19 mm. Fine aggregate content is limited in pervious concrete mixtures, since it tends to compromise the connectedness of the pore system. The addition of fine aggregate increases mechanical strengths and density. On the other hand, the porosity and permeability decreases when fine aggregate are added [3].

The water quality for pervious concrete is governed by the same requirements as those for conventional concrete. Further discussion of water quality is found in ACI 301 [17].

2.2.2. Properties and Test Methods.

Porosity

The total porosity is one of the most important parameters, which determines the properties of pervious concrete. The total porosity inside the pervious concrete is divided in three types: pores of the mortar, air voids and pores of the structure, as presented in Fig. 2.1. The pores of the mortar are formed during the hydration process of the cement. They are subdivide into the capillary pores and gel pores. The former is the space not filled by solid products of hydration. The gel pores are inside the calcium silicate hydrate gel (C-S-H).

The air voids are subdivide into entrained and entrapped air voids. The entrained air voids are small spherical voids enfolded by the mixer. The entrapped air voids are voids that are larger than the entrained voids but have internal surfaces that indicate they were formed by air bubbles.

The pores of the structure are formed by the lack of cement paste. Equally, they are highly dependent on several factors: grading of the aggregates, aggregate / cement paste ratio (A/P) and compaction degree. The pores of the structure may be isolated or connected of each other.

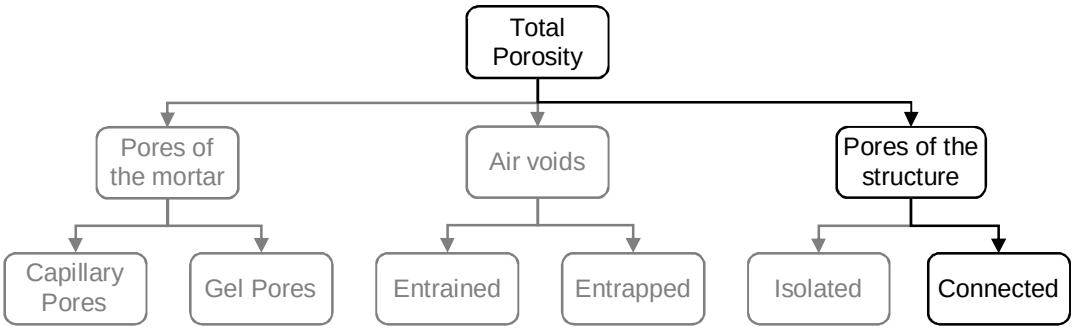

Figure 2.1 – Types of pores in pervious concrete.

The ASTM C1688/C1688-14a [18] proposed a method to calculate the porosity of the fresh pervious concrete by the density of fresh material. The porosity of fresh pervious concrete 'P_f' is calculated by Eq. 2.1. In this equation, ρ_t represents the theoretical density and ρ_f represents the density of the fresh pervious concrete determined with ASTM C1688/C1688-14a [18].

$$P_f = \frac{\rho_t - \rho_f}{\rho_t} \cdot 100 \tag{2.1}$$

The ASTM C1754/C1754M-12 [19] provides a procedure for determining the density and porosity of hardened pervious concrete specimens. The porosity 'P' of a specimen is estimated using Eq. 2.2. In this equation, W_1 represents the dry weight, W_2 is the hydrostatic weight, $\emptyset_s$ is the diameter of the specimen, L_s represents the height of the specimen and ρ_w is the density of the water at 25ºC.

$$P = \left[1 - \frac{4 \cdot (W_1 - W_2)}{\rho_w \cdot \pi \cdot \emptyset_s^2 \cdot L_s}\right] \cdot 100 \tag{2.2}$$

Two additional methods that determine porosity of hardened pervious concrete were reported in the literature. Researchers [20-22] employed an image analysis

procedure. This procedure is advantageous in ascertaining the variation in porosity with depth of a pervious concrete. Other authors [12;14;23] used the ASTM D7063/D7063M-11[24]. This standard is used to determine the effective porosity of bituminous specimens. Tab. 2.1 presents main methods used in studies with the porosity ranges determined by authors.

Table 2.1 – Methods and values ranges for porosity present in the literature.

Test Method	Reference	Porosity (%)
ASTM C1754 [18]	Hesami *et al.* [11]	10 - 30
	Ibrahim *et al.* [25]	30 - 40
	Gaedicke *et al.* [26]	15 - 35
ASTM C1688 [19]	Tho-in *et al.* [27]	28 - 35
ASTM D7063 [24]	Shu *et al.* [14]	5 - 30
	Huang *et al.* [11]	20 - 30
	Martin *et al.* [23]	10 - 40
Water required to fill a pervious concrete specimen enclosed in a latex sleeve	Lian *et al.* [8]	5 - 20
	Neithalath *et al.* [28]	19 - 22
3-DX-ray CT image acquisition	Coleri *et al.* [29]	22 - 35
Computed tomography using	Ozbek *et al.* [30]	18 - 25

Permeability

According to ACI 522 [3], permeability is one of the most important features of pervious concrete. It is a property that describes how easily water can pass through the interconnected porosity of the pervious concrete. Therefore, permeability is an indirect way to determine qualitatively how connects pores are.

The principle of the method used to estimate the permeability is to measure the amount of water that pass through the specimen in a certain time interval. In the literature, two types of methods are commonly used to measure the permeability of pervious concrete: falling head permeameter and constant head permeameter. The concept of the equipment used for both methods are the same, as depicted in Fig. 2.2a. The equipment is composed by 3 parts: top tube, water proof layers and bottom tube. The top tube is placed above the specimen. It is used to control the initial and final water level. The water proof layers are placed around the specimen to reduce the water flow along the side of the specimen during the test. Finally, the bottom tube is positioned bellow the specimen with an outlet to control the water flow. The difference of the methods is related to the test procedure.

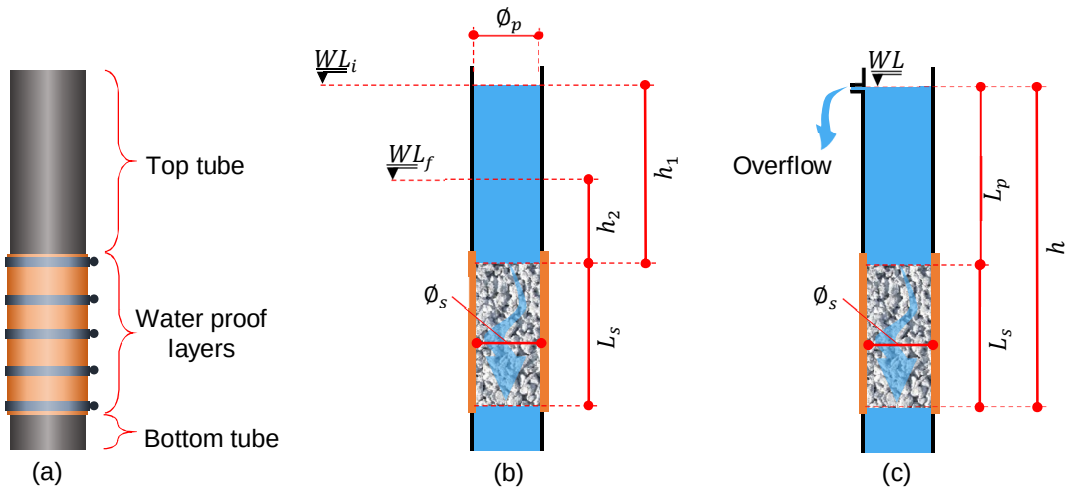

Figure 2.2 – Permeameter scheme (a) and cross section schema of the falling (b) and constant (c) head permeameters.

Fig. 2.2b presents the cross section scheme of the falling head permeameter. This equipment was used by [12;31-35] and reported in ACI 522 [3]. Test using the falling head permeameter is performed with the following procedure:

- First, the end of the bottom tube is closed;
- Next, the apparatus is filled with water until reach the initial water level (WL_i) and the bottom tube is opened;
- Finally, the time required for water to reach the final water level (WL_f) is measured (Δt).

The permeability 'K' is estimated using Eq. 2.3. In this equation, $\emptyset_p$ is the internal diameter of the tube, h_1 is the distance from the top of the specimen to the initial water level (WL_i) and h_2 is the distance from the top of the specimen to the final water level (WL_f)

$$K = \frac{\emptyset_p^2 \cdot L_s}{\emptyset_s^2 \cdot \Delta t} \cdot ln\left(\frac{h_1}{h_2}\right) \quad (2.3)$$

On the other hand, Fig. 2.2c presents the cross section scheme of the constant head permeameter. This equipment was used by [27;36-39]. Test using the constant head permeameter is performed with the following procedure:

- First, the end of the bottom tube was closed;
- Next, the volume of water necessary to fill the bottom tube and the pore spaces of the specimen is measured (q_1);

- Then, the apparatus was filled with water until reaching the water level (WL) and the bottom tube is opened;
- Finally, the volume of water that passed through the specimen in an interval of time determined is measured (q_2).

The permeability 'K' is estimated using Eq. 2.4. In this equation, q is the difference between both measured volumes of water ($q_2 - q_1$), h is the distance from the top of the specimen to the water level (WL) and t is time interval.

$$K = \frac{4 \cdot q \cdot L_s}{\pi \cdot \emptyset_s^2 \cdot h \cdot t} \tag{2.4}$$

In literature [12;27;31-39], the permeability of pervious concrete is related to its porosity. Fig. 2.3 shows a compilation of porosity–permeability relationships from a few reported studies, where is compared the values obtained by the falling head permeameter [12;31-35] and the constant head permeameter [27;36-39]. The data expressed with triangles represent the values reported by tests with the falling head permeameter. The data expressed with squares represent the values reported by tests done with the constant head permeameter. The increase of the porosity leads to an increase of the permeability. The rate of increase of permeability - porosity results are different for the constant and falling head permeameters.

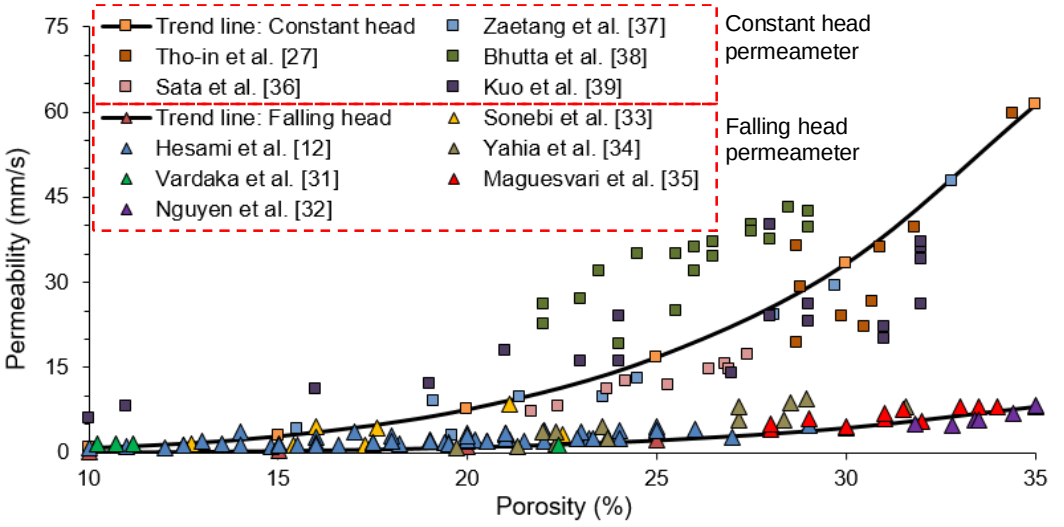

Figure 2.3 – Relation between porosity and permeability from the literature for constant and falling head permeameter.

The difference on the answers of this two tests methods is probably related to the pressure of water applied on the top face of the specimen. The constant head permeameter

method has a constant pressure applied on the top face of the specimen throughout the total duration of the test. On the contrary, the pressure applied on the top face of the specimen in the falling head permeameter method presents a decrease along the duration of the test. The difference of pressures during the test results in a higher permeability obtained with the constant head permeameter method.

Motes and Haselbach [40] proposed the use of the Carman-Kozeny equation [41-42] (Eq. 2.5) to investigate the relationship between porosity and permeability. In this equation, K_{c-k} is the permeability, P is the porosity and α_{c-k} is calculated by Eq. 2.6. In Eq. 2.6, g is the gravitational acceleration, ν_w is the viscosity of the water, S_m is the specific surface of the material and C_0 is an empirical constant.

$$K_{c-k} = \alpha_{c-k} \frac{P^3}{(100 - P)^2} \tag{2.5}$$

$$\alpha_{c-k} = \frac{g \cdot C_0}{\nu_w \cdot S_m} \tag{2.6}$$

Motes and Haselbach [40] estimated a α_{c-k} value of 1.80 for experimental studies performed with a falling head permeameter. Tab. 2.2 presents a relation of α_{c-k} values estimated for the studies [12;27;31-39], indicating the average and standard deviation of falling and constant head permeameter. The high standard deviation is probably related to the different mix designs used in the studies.

Table 2.2 – α_{c-k} estimation for different experimental studies.

Test method	Reference	α_{c-k}	$\bar{x}$	σ
Falling head permeameter	Hesami *et al.* [12]	1.37	0.94	0.41
	Vardaka *et al.* [31]	0.91		
	Nguyen *et al.* [32]	0.72		
	Sonebi *et al.* [33]	0.35		
	Yahia *et al.* [34]	1.56		
	Maguesvari *et al.* [35]	0.71		
Constant head permeameter	Tho-in *et al.* [27]	5.5	6.10	1.99
	Zaetang *et al.* [37]	5.77		
	Sata *et al.* [36]	4.35		
	Bhutta *et al.* [38]	9.95		
	Kuo *et al.* [39]	4.92		

Mechanical Strength

According to ACI 522 [3], the compressive and tensile strengths of pervious concrete are strongly affected by the composition and compaction during placement. ASTM C39/C39M-15a [41] and UNE-EN 12390-3:2009 [42] are used to determine compressive strength of cylindrical and cubic specimens. Fig. 2.4 presents a compilation of porosity–compressive strength relationships from reported studies [12;27;31-39]. The results from these studies suggest that the compressive strength decreases with the increasing of the porosity. The compressive strength range from 2 to 35 MPa. According to Bhutta *et al.* [38], relatively high compressive strengths of pervious concrete mixtures are possible with the proper composition. However, the high strength is achieved only with the reduction of porosity. It results in a reduction in permeability coefficient.

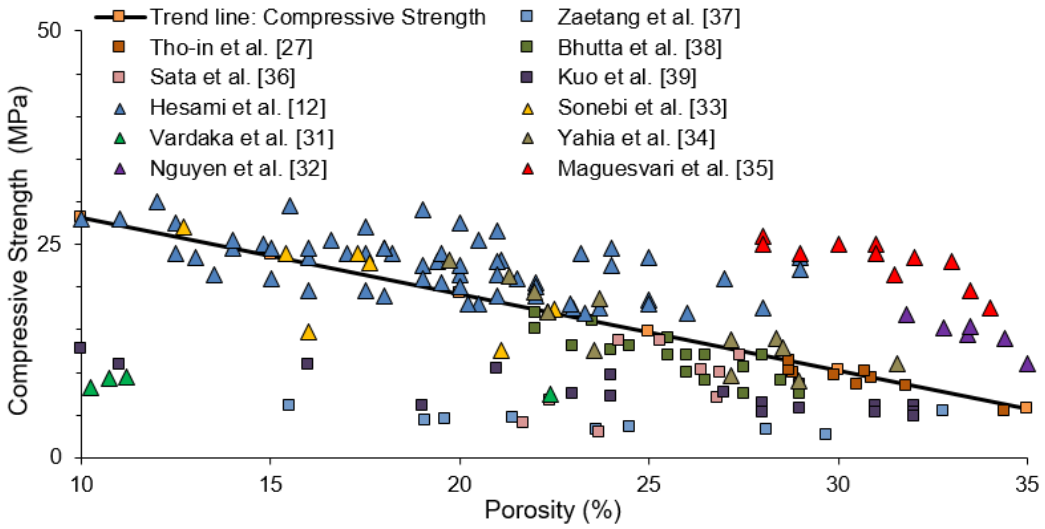

Figure 2.4 – Relation between porosity and compressive strength from the literature.

ASTM C293/C293M-10 [43], ASTM C78/C78M-15a [44] and UNE-EN 12390-5:2009 [45] are used to determine the flexural strength of beam specimens. According to ACI 522 [3], the flexural tensile strength around 3 MPa has been observed for pervious concrete. ASTM C496/C496M-11 [46] and UNE-EN 12390-6:2009 [47] are used to determine the splitting tensile strength of cylindrical and cubic specimens. The splitting tensile strength is generally greater than direct tensile strength and lower than flexural strength.

Fig. 2.5a presents the experimental results of compressive and tensile strenghs obtained by Meininger [48]. The author suggested that the relation between compressive and tensile strength is lower than the expected considering the previous knowledge of conventional concretes. In this sense, Fig. 2.5b shows the evolution of the relation between compressive and tensile strength 'σ_c/σ_t' with the compressive strength. It is

observed that σ_c/σ_t tends to reach a value of 10 in higher values of compressive strength. For pervious concrete with low compressive strength, the σ_c/σ_t are bellow than the expected for conventional concretes.

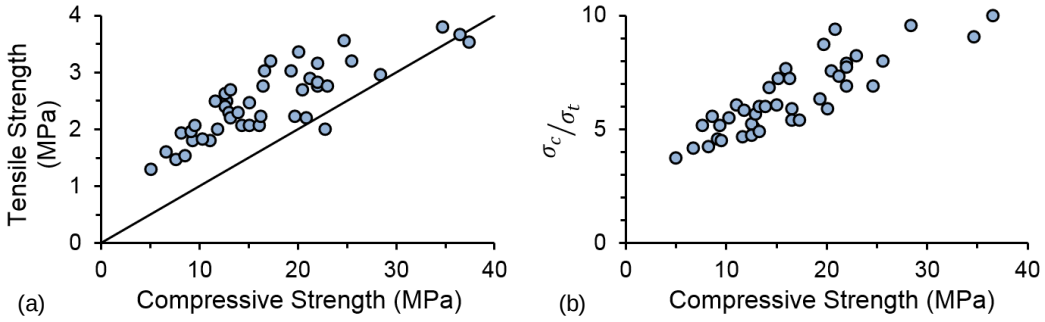

Figure 2.5 – Relationship between tensile strength and compressive strength [48].

2.2.3. Composition

The definition of pervious concrete composition is usually based on trial-and-error procedures. A series of trial batches is developed in the laboratory and then tested in the field to ensure expected performance. In general, the philosophy of mixture proportioning for pervious concrete is to achieve balance between voids, strength, paste content and permeability [3].

According to ACI 522 [3], the composition proportions varies depending on local materials. Currently, an extensive experimental program is required to define the proper composition. Tab. 2.3 presents typical ranges of materials proportions defined by [3] that may be used as a reference.

Table 2.3 – Typical ranges of materials proportions.

Material	Range
Cement (kg/m3)	250 – 400
Aggregate (kg/m3)	1100 – 1500
Water / cement ratio (by mass)	0.25 – 0.35
Cement : Aggregate ratio (by mass)	1 : 4.0 – 1 : 4.5

ACI 522 [3] Method

Chapter 6 of ACI 522 [3] presents a method for initial trial batches for pervious concrete. The trial batches should be than tested to verify the required fresh and hardened properties before applying for the intended use [3]. The method is explained in the sequence:

- Define the desired porosity 'P_d' in percentage, the w/c ratio, the total volume of the specimen 'V_T' and the dry-rodded volume of coarse aggregate in a unit volume of concrete '$\frac{b}{b_0}$' (as defined in ASTM C29 / C29M [49]);
- Calculate the aggregate weight 'W_{ag}' with Eq. 2.7. In this equation ρ_{ag} is the aggregate density;

$$W_{ag} = \rho_{ag} \cdot \frac{b}{b_0} \cdot V_T \tag{2.7}$$

- Correct the W_{ag} to the saturated surface-dry weight 'W_{ssd}' with Eq. 2.8 (in this equation A_w is the absorption);

$$W_{ssd} = W_{ag} \cdot A_w \tag{2.8}$$

- Determine the paste content 'C_p' that is correlated with the porosity by curves proposed by the ACI 522 [3];
- Calculate the paste volume with Eq. 2.9;

$$V_P = V_T \cdot C_p \tag{2.9}$$

- Calculate the cement content 'C' with Eq. 2.10. In this equation SG_c is the specific gravity of the cement;

$$C = \frac{V_P \cdot \rho_w}{0.1 \cdot SG_c + \mathrm{w/c}} \tag{2.10}$$

- Calculate the water content with Eq. 2.11;

$$w = \frac{C}{w/c} \tag{2.11}$$

- Calculate the solid volume of the aggregate, cement and water with Eq. 2.12, Eq. 2.13 and Eq. 2.14, respectively. In these equations the SG_{ag} is the specific gravity of the aggregate and the SG_c is the specific gravity of the cement;

$$V_{ag} = \frac{W_{ssd}}{SG_{ag} \cdot \rho_w} \tag{2.12}$$

$$V_c = \frac{C}{SG_c \cdot \rho_w} \tag{2.13}$$

$$V_w = \frac{w}{\rho_w} \tag{2.14}$$

- Calculate the total solid volume with Eq. 2.15;

$$V_S = V_{ag} + V_c + V_w \tag{2.15}$$

- Calculate the porosity with Eq. 2.16;

$$P = \frac{V_T - V_S}{V_T} \cdot 100 \tag{2.16}$$

- Estimate the properties with the curves proposed by the ACI 522 [3];
- Compare the estimated properties with the experimental results.

2.2.4. Factors that affect the Properties

Aggregates

Ibrahim *et al.* [25] compared the properties of the pervious concrete made with different sizes of uniformly graded crushed limestone aggregates (4.5, 9.5 and 12.5 mm) and 50-to-50 binary blend of this aggregates. According with the study [25], the mixtures with mono size aggregates presented higher compressive strengths and permeability on the concrete mixtures with larger aggregates. The blend mixture with aggregates sizes of 4.5 and 12.5 mm presented the highest compressive strength. However, it also showed the smallest permeability. Ibrahim *et al.* [25] suggested that this difference of behavior is related to the aggregates arrangement that modified the pore structure.

Kim *et al.* [50] compared the difference between pervious concretes using normal and lightweight aggregates. The authors observed that the specimens with lightweight aggregates showed lower compressive strength than their counterparts with normal aggregates. In general, the compressive strength of specimens increased in accordance with a decrease of the total void ratio. In the case of the composition with lightweight aggregates, this relation is less evident and the observed increase in compressive strength is smaller.

On the other hand, Zaetang *et al.* [37] analyzed the properties of pervious concretes made with different types of lightweight aggregates (diatomite aggregate, pumice aggregate and recycled aggregate from autoclaved aerated concrete). The use of lightweight aggregates as coarse aggregates in pervious concrete reduced the density and thermal conductivity compared with the pervious concrete containing natural aggregate (approximate 3 – 4 times). Zaetang *et al.* [37] suggested that these materials might be used for insulate applications, due the low compressive strength presented.

Vardaka *et al.* [31] studied the influence of normal aggregates (limestone), steel slag and a 50-to-50 binary blend of these two aggregates on pervious concrete properties. All previous specimens had sufficient strength and high water permeability coefficient for the range of their intended applications. The incorporation of steel slag leads to an increase of abrasion strength. Also, Vardaka *et al.* [31] studied the influence of a 100 % substitution of the normal aggregate by a 50-to-50 blend of steel slag and construction and demolition recycle aggregates. They observed that blend pervious concrete presented lower compressive strength and permeability than pervious concrete made with normal aggregates.

Bhutta *et al.* [38] suggested that pervious concrete made with recycle aggregates presented lower compressive strength and similar permeability coefficient when compared with pervious concrete made with natural aggregates. Sriravindrarajah *et al.* [51] also compared pervious concrete made with natural and recycle aggregates and observed that for a given porosity recycled concrete aggregate had reduced the compressive strength of pervious concrete. They observed that the influence of aggregate type on compressive strength reduces with the increase in the porosity. In the concern of permeability, the influence of porosity and the use of recycled concrete aggregate had no significant effect [51].

Nguyen *et al.* [32] chosen crushed crepidula seashell (CCS) to substitute part of the normal coarse aggregate, they proposed two different range of sizes of CCS (4 to 6.3 mm and 2 to 4 mm) and 5 different mix proportions (20 and 40 % substitution of normal coarse aggregate). Pervious concrete with CCS had a compressive strength comparable to that of raw normal pervious concrete, while the permeability coefficient was higher when 40 % of normal coarse aggregate were substituted by 4 to 6.3 mm CCS [32].

Aggregate / Cement paste ratio

Torres *et al.* [52] observed that the aggregate / cement paste (A/P) affected the thickness of the cement paste layer around the aggregate. Small values of aggregate / cement paste ratio leads in thicker cement paste layers. Also, Torres *et al.* [52] reported that a relationship exists between the aggregate size and the paste content, such that smaller aggregate with higher paste content exhibits similar porosities to that of the larger aggregate with lower paste content. The porosity and the permeability decrease with a decrease in the aggregate / cement paste ratio. The compressive strength and splitting tensile strength increased with a decrease in the aggregate / cement paste ratio [52].

Water / Cement ratio

The water / cement ratio (w/c) is an important parameter for obtaining desired strength and porosity in pervious concrete [3]. Fig. 2.6 shows the aspect of the pervious concrete with different amount of water. A low w/c will prevent good mixing and tend to cause balling in the mixer, prevent an even distribution of cement paste, and therefore reduce the ultimate strength and durability of the concrete, as observed in the Fig. 2.6a. On the other hand, a high w/c reduces the adhesion of the paste to the aggregate and causes the paste to flow and fill the voids even when lightly compacted (this phenomena is known as segregation), as appreciated in the Fig. 2.6b [3].

Figure 2.6 – Fresh pervious concrete with low w/c (a), high w/c (b) and proper w/c (c) [16].

The proper water content has been described as giving the mixture a sheen, without flowing of the aggregate. A handful of pervious concrete formed into a ball will not crumble or lose its void structure as the paste flows into the spaces between the aggregates, as observed in the Fig. 2.6c [16]. Experience has shown that w/c in the range of 0.26 to 0.45 will provide the best aggregate coating and paste stability. Careful control of aggregate moisture and w/c is important to produce consistent pervious concrete [3].

Compaction

Gafoori *et al.* [53] reported that the compaction energy plays an important role over the final properties of the pervious concrete. They analyzed the permeability, compressive and tensile strengths of four compositions submitted to different levels of compaction energy. Gafoori *et al.* [53] observed a reduction around 75 % in the permeability coefficient in all compositions between the minimum and maximum level of applied compaction energy, as observed in Fig. 2.7a.

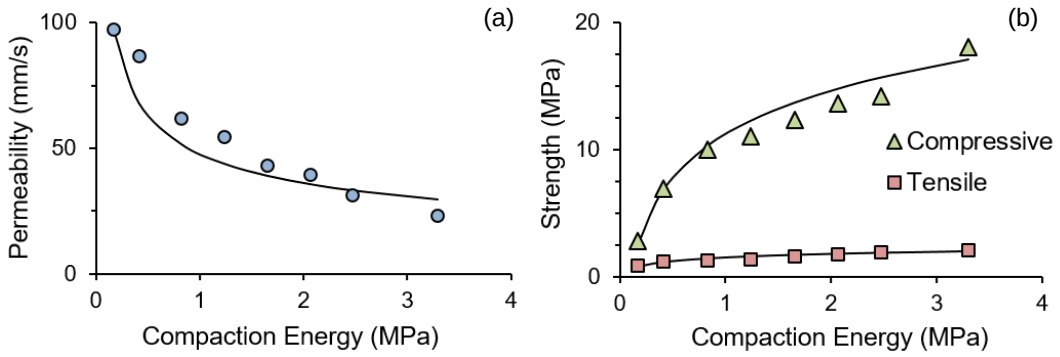

Figure 2.7 – Effect of the compaction energy on the properties of pervious concrete. [53].

The opposite trend was observed, when the mechanical properties were analyzed [53]. The compressive strength and splitting tensile strength increased with an increase of the compaction energy. Fig. 2.7b presents a correlation between the compressive strength (in green triangles) and the tensile strength (in red squares) with the compaction energy.

2.3. SIMULATION OF THE FRESH STATE

This section presents the methods and models used to simulate viscoelastic materials in their fresh state. First, basics rheology models and their constitutive equations are presented. Then, models from the literature to simulate concrete in fresh state and other viscoelastic materials are discussed.

2.3.1. Basics of Rheology Simulation

The rheological behavior of viscoelastic materials may be described by the superposition of three basics elements: linear spring, linear viscous dashpot and linear saint Venant element, as observed in Tab. 2.4. The spring element derivate from the Hooke's law, which states that the stress tensor 'σ' (or force 'F') required to extend or compress a spring by some strain tensor 'ε' (or distance 'u') is proportional to that strain (or distance). The force is calculated by Eq. 2.17 (in this equation, k is the stiffness of the spring). The strain response of spring to an applied stress is instantaneous, without any time dependency. Also, the recovery after released the stress is instantaneous and complete.

The dashpot element is described as a piston displacing a Newtonian fluid in a cylinder. It is physical defined by the Newton's law of viscosity, as expressed by Eq. 2.18. In this equation, η is the viscosity coefficient and $\dot{\varepsilon}$ is the strain rate. The Newton's law of viscosity states that stress tensor 'σ' (or force 'F') intensity is proportional to the strain rate '$\dot{\varepsilon}$' (or velocity 'v'). In this element there is no instantaneous response, the deformation is directly proportional to time and no recovery takes place.

The yield stress phenomenon is represented by the Saint Venant element. The deformation of this element is only possible after the achievement of some critical stress value (yield stress σ_y), as expressed by Eq. 2.19.

Table 2.4 – Basic rheological elements.

Model		Equation	
Spring	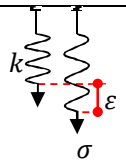	$\sigma = k \cdot \varepsilon(t)$	(2.17)
Dashpot	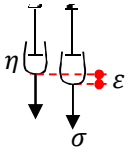	$\sigma = \eta \cdot \dot{\varepsilon}(t)$	(2.18)
Saint Venant	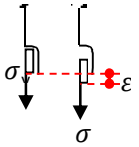	$\begin{cases} \forall\, \sigma < \sigma_y : \varepsilon = 0 \\ \forall\, \sigma > \sigma_y : \varepsilon = \varepsilon(t) \end{cases}$	(2.19)

Tab. 2.5 presents some of the most commons rheological models that were used to simulate viscoelastic binders, such as fresh concrete. The Maxwell model is a viscoelastic model that consist in a spring and a damper connect in series. In this model,

equal stress acts on both elements and the total strain is equal to the sum of the strain of both elements, as expressed in Eq. 2.20. Also, this model allows instantaneous deformation that is related to the spring element.

Table 2.5 – Common rheological models.

	Model		Equation	
Viscous	Maxwell	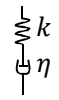	$\sigma + \frac{\eta}{k} \cdot \dot{\sigma} = \eta \cdot \dot{\varepsilon}$	(2.20)
	Kelvin		$\sigma = k \cdot \varepsilon + \eta \cdot \dot{\varepsilon}$	(2.21)
	Burgers	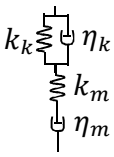	$\sigma + \left(\frac{k_k \cdot \eta_k + k_k \cdot \eta_m + k_m \cdot \eta_k}{k_k \cdot \eta_m}\right) \cdot \dot{\sigma} + \frac{\eta_k \cdot \eta_m}{k_k \cdot k_m} \cdot \ddot{\sigma} = \eta_k \cdot \dot{\varepsilon} + \frac{\eta_k \cdot \eta_m}{k_m} \cdot \ddot{\varepsilon}$	(2.22)
	Standard Solid	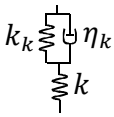	$\sigma + \frac{\eta_k}{k_k} \cdot \dot{\sigma} = k \cdot \varepsilon + \frac{\eta_k \cdot (k_k + k)}{k_k} \cdot \dot{\varepsilon}$	(2.23)
Yield Stress	Prandtl		$\forall\, \sigma < \sigma_y : \sigma = k \cdot \varepsilon$ $\forall\, \sigma \geq \sigma_y : \sigma = \sigma_y$	(2.24)
	Maxwell – Saint Venant	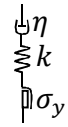	$\begin{cases} \forall\, \sigma < \sigma_y : \sigma + \frac{\eta}{k} \cdot \dot{\sigma} = \eta \cdot \dot{\varepsilon} \\ \forall\, \sigma \geq \sigma_y : \sigma + \frac{\eta}{k} \cdot \dot{\sigma} = \eta \cdot (\dot{\varepsilon} - \dot{\varepsilon}_p) \end{cases}$	(2.25)
	Kelvin – Saint Venant	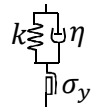	$\begin{cases} \forall\, \sigma < \sigma_y : \sigma = k \cdot \varepsilon + \eta \cdot \dot{\varepsilon} \\ \forall\, \sigma \geq \sigma_y : \sigma = k \cdot (\varepsilon - \varepsilon_p) + \eta \cdot (\dot{\varepsilon} - \dot{\varepsilon}_p) \end{cases}$	(2.26)
	Bingham		$\begin{cases} \forall\, \sigma < \sigma_y : \sigma = 0 \\ \forall\, \sigma \geq \sigma_y : \sigma = \sigma_y + \eta \cdot \dot{\varepsilon} \end{cases}$	(2.27)
	Bingham - Hooke	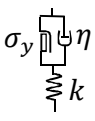	$\begin{cases} \forall\, \sigma < \sigma_y : \sigma = k \cdot \varepsilon \\ \forall\, \sigma \geq \sigma_y \rightarrow \sigma + \frac{\eta}{k} \cdot \dot{\sigma} = \sigma_y + \eta \cdot \dot{\varepsilon} \end{cases}$	(2.28)

The Kelvin model is composed by a spring and a dashpot connect in parallel, as presented by Eq. 2.21. This model does not allows instantaneous deformation, since the stress on the dashpot would be infinite. The deformation in each element remains the same. The Kelvin model also does not describe stress relaxation.

When both models, Maxwell and Kelvin, are combined in series enables a realistic description of the materials with complex behavior. This combined model is known as Burgers model. The Burgers model allows to simulate the creep behavior of the viscous materials. The superposition of Kelvin and Maxwell models is calculated by Eq. 2.22.

The Standard Solid model consist on a Kelvin model with a spring connected in series. This contact model also shows the creep and relaxation behavior, as expressed by Eq. 2.23.

Tab. 2.5 also shows the representation of common viscous models with yield stress, and the response of these models before and after achievement the yield stress value 'σ_y'. The Prandtl model consists of a Saint Venant element and a spring element connected in series. The behavior of this material is characterized by linear elasticity for stress values below the yield strength. When the yield stress is reached, the model exhibits pure plasticity, as presented by Eq. 2.24.

The serial connection of all the basic rheological elements is known as the Maxwell – Saint Venant model. Before achieve the yield stress, the mode behaviors is equal the Maxwell model. For stress values above the yield stress, the behavior of this model is function of $\dot{\varepsilon}_p$, as expressed by Eq. 2.25.

The Kelvin model and Saint Venant element connected in series gives another alternative to represent plastic deformation, as presented by Eq. 2.26. The Kelvin – Saint Venant model exhibits the behavior of the Kelvin model for stress values below the yield stress.

The Bingham model consists of a Saint Venant element and a dashpot connected in parallel. The deformation of this model is not possible before reaching the yield stress. When the yield stress is achieved, the model exhibits visco-plastic deformation, as presented by Eq. 2.27.

The Bingham - Hooke model consists of a Bingham model and a spring connected in series. This model exhibits linear elasticity for stress values lower than the yield stress, analogues as the spring element. For stress values above the yield stress, the behavior of the Bingham – Hook model is similar to the Maxwell model, as expressed by Eq. 2.28.

2.3.2. Concretes

There are no models reported in the literature to simulate the fresh state of the pervious concrete. However, several authors have simulated the fresh state behavior of other types of concrete using DEM [54-59]. Despite the advances observed, it is important to remark that the great majority of the studies with DEM focused on self-compacting concrete with a high fluidity and without accounting for external compaction or vibration.

Nabeta *et al.* [54] introduced the simulations of fresh concretes flow using DEM. Chu *et al.* [55] used DEM to simulate the filling capacity of fresh concrete. The authors considered a homogenous material approach in which all particles share the same properties. Afterwards, other studies [56-58] introduced a heterogeneous approach, using some particles to simulate the aggregates and others to simulate the cement paste or mortar. Nevertheless, with the advances in processing capabilities of modern computers, it becomes possible to use models with elevated complexity. A recent approach to simulate the flow of self-compacting concrete was proposed by Chu *et al.* [58]. In the latter, a bi-phasic particle with an aggregate-like kernel involved by a mortar layer was used to simplify the computation of interactions. In a similar way, Zheng et al. [59] proposed a GPU-based parallel algorithm for particle contact detection in self-compacting fresh concrete simulations.

In order to simulate the fresh state properties of self-compacting concrete, Gram [60] proposed an adaptation of the Bingham contact using a spring connected in parallel with a serial connection of a damper and a Saint-Venant element. Other authors [61-64] have proposed contact models based on stress-strain (σ-ε) curves obtained with laboratory tests in which two spheres surrounded by mortar or cement paste are put in contact. In another study, Remond *et al.* [65] proposed a bi-phasic model with the simulation of a fluid-like interaction between the external layers of the particles.

2.3.3. Similar Materials

DEM was used to simulate the compaction of hot-mix asphalt with the Superpave gyratory compactor [66-68]. In these works, the authors used a Burgers model to simulate the interaction between particles. They also investigated the effects of aggregate grading, gyration number, gyration angle, and parameters of contact model during the compaction.

2.4. SIMULATION OF THE HYDROLOGICAL BEHAVIOR

Porous media, such as rocks, some polymers and concretes, consist of voids (pores) and a solid matrix (the solid matrix may be homo- or heterogeneous). The voids are usually connected, which allows fluid to pass through the porous media. Permeability, as well as other parameters, is strongly influenced by the pore structure and pore-scale physics.

The pore structure of a porous medium and the physical characteristics of the matrix and the fluids that occupy the pore spaces influence the flow process. This process is considered complex in nature due to the intricacy found in the pore structure. The pores tend to have irregular surfaces, which is one of the reasons why fluid flow through them is difficult to simulate. Some of the pores make dead ends and influences the flow behavior significantly [69].

According to Bear [69], the fluid flow properties of a porous medium may be determined if the physical equations on a real pore space are solved. In the sequence, models and methods used in the literature for the fluid flow simulation are discussed.

2.4.1. Pervious Concrete

The scale of interest in pervious concrete varies from a meso- (pore-) to macro-scale. A challenge in mathematical and computational modelling is to handle these scales properly. In general, the modelling approach varies based on the scale at which the porous medium is being described. A schema of macro- and meso-scale is presented in Fig. 2.8a and Fig. 2.8b, respectively. Also, the discretization of the pores at the meso-scale is observed in Fig. 2.8c.

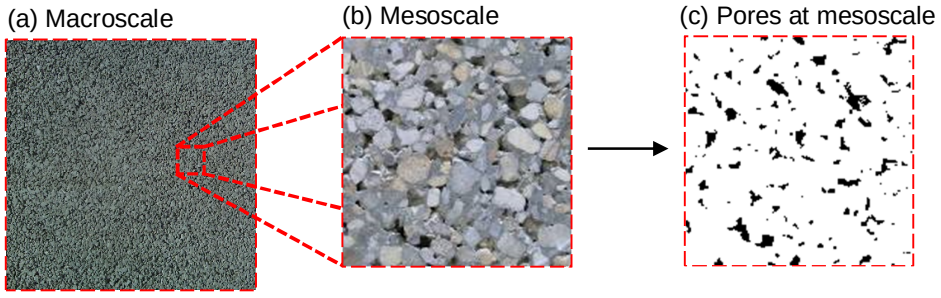

Figure 2.8 - Scales of interest on pervious concrete regarding fluid flow.

A method to predict the permeability using a 3D reconstruction of the pore-structure based on planar imagens of several pervious concrete is presented by [70-72].

The 3D Stokes permeability solver was used. Chung *et al.* [73] investigated the spatial distribution of the voids inside pervious concrete by computed tomography images and reconstructed the models using law-order probability function to reproduce the porosity of the materials. In their study, CFD was used to simulated the permeability of the reconstructed models.

2.4.2. Other types of Concretes

Wang & Ueda [74] simulated the water penetration in a bi-dimensional mesoscale concrete specimen by capillary absorption. They used a Lattice network without the capillary pores discretization, which means that the permeability of the mortar was an input parameter.

Zalzale & McDonald [75] used the Lattice Boltzmann method to calculate the permeability of 3D microstructures determined with a hydration model of the paste. Zhang *et al.* [76] presented a 3D microstructure-based permeability modeling of cementitious materials also using lattice Boltzmann method. Zhang *et al.* [76] observed that the fluid flow is restricted by the solid phase consisting of un-hydrated cement and hydration product, and only passes through the capillary pores.

Abyaneh *et al.* [77] investigated the effect of ITZ and aggregate shape on the diffusivity of mortar and concrete using the Finite Difference method. They applied the Fick's first law of diffusion with mass conservation to simulate the diffusion through the meso-structure. Abyaneh *et al.* [78] presented a 3D simulation of the capillary absorption by treating the concrete as a heterogeneous composite discretized into a cubic lattice.

Chung *et al.* [79] studied the air permeability of cement paste models obtained with X-ray CT images and probabilistic methods. They used Finite Element method to evaluate the air permeability. The comparisons between numerical and experimental results of air permeability were in the same order of magnitude.

2.4.3. Similar Materials

Besides the simulation of the fluid flow through the pervious and other types of concrete matrix, several authors have simulated fluid flow through different kinds of materials using Finite Element [80-83] and Lattice Boltzmann [84-85].

Yazdchi *et al.* [80] simulated the macroscopic permeability of fibrous porous media taking into account the microstructure. They used periodic arrays of parallel cylinders perpendicular to the flow direction to simulate the mesostructure of the material. The effects of shape, orientation, porosity and structure on the macroscopic permeability

of the porous media were simulated and analyzed. Torre *et al.* [81] used micro-computed tomography to generate the open-cell foams models. They analyzed the flow regimes and determined the effects of morphological parameters on the pressure drop. Ranut *et al.* [82] also used micro-computed tomography to generate the aluminum metal foam model. They simulated the flow and heat transfer through three different models. Schafrik & Millar [83] proposed a methodology to simulate the heat transfer in broken rock bodies with the influence of air flow.

Videla *et al.* [84] used X-ray microtomography to generate the model of a limestone aggregates bed. With the simulation of the fluid flow, they determined the direct local flow and micro-permeability for complex porous structures. Wang *et al.* [85] performed a reconstruction model based on several X-ray computed tomography to simulate the permeability of natural rocks.

2.5. SIMULATION OF THE MECHANICAL BEHAVIOR

Considering concrete as a composite, it is meaningful to study the properties of the material on various observation scales the nano- (nm), micro- (μm), meso- (mm – cm), and macro-scale (m), as presented at the Fig. 2.9. At the nano-, micro- and meso-scale of observation concrete is heterogeneous; only at the macro-scale the material may be considered as homogeneous. In this case, the material is idealized considering the properties of the average of an infinitesimal continuum medium.

At the macro-scale (Fig. 2.9a) most of the models proposed in the literature consider phenomenological relations based on macroscopic observations, typically between average strain and average stress on a sufficiently large concrete volume. Despite the oversimplification that this implies, this approach linked to the use of continuum-type constitutive models such as plasticity and/or damage theory plus, in some cases, some principles of fracture mechanics, has led to a relatively satisfactory description of the basic features of the mechanical behavior of concrete.

At the meso-scale (Fig. 2.9b), pervious concrete is assumed to be a composite material formed by mortar matrix, coarse aggregate, interfacial transition zone and pores (voids). In the meso-scale the particles are discretized in a scale of 10^{-5} to 10^{-1} m and is used to simulate the meso compressive and tensile strength (specially to analyze the fracture energy and path.

The micro-scale (Fig. 2.9c) of materials is used to determine its global performance. This fundamental principle of materials science may be adapted to predict the mechanical performance and the permeability of the cement paste. Indeed, the mainly

application of this scale of analysis is about the hydration processes of the cement paste. The nano-scale (Fig. 2.9d) of cementitious materials may be used, for example, to analyze the physical properties and mechanical performance of C-S-H, the principal component in cement-based materials.

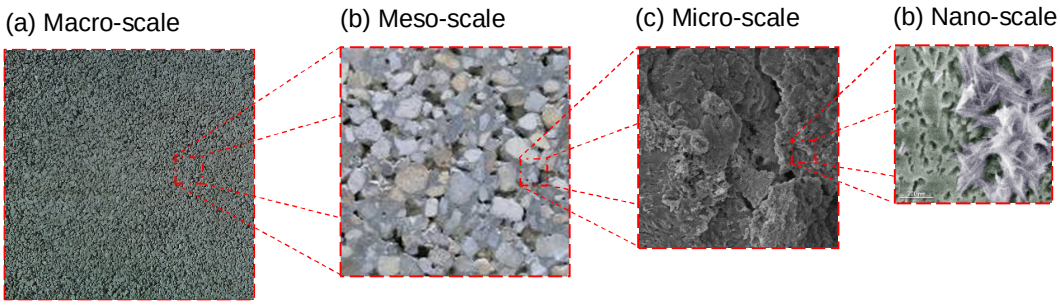

Figure 2.9 - Schematic representation of the scales of analysis: macro (a), meso (b), micro (c) and nano (d).

2.5.1. Pervious Concrete

Deo & Neithalath [86] proposed an analytical model based on stress-strain constitutive relationship and the pore structure features to estimate the compressive strength of pervious concrete. Deo & Neithalath [86] observed that the porosity, pore sizes and pore connectivity were sufficient to model the portion of the stress–strain curve comprehended before the peak stress. However, the portion after the peak stress was found to additionally depend on the mean free spacing between the pores.

Lian *et al.* [87] developed a 2D model based on DEM to simulate the behavior of pervious concrete under compression. The final constitutive model for pervious concrete was designed as a combination of a contact model, a slip model and a parallel bond model and implemented in PFC2D [88]. The set of bond springs were built up spreading over the contact plane between the two particles, which will work together with the single contact springs in the shear and normal directions [87]. According to the authors the numerical model could characterize the behavior, under compression loading using different sets of parameters.

Lian *et al.* [89] obtained numerically the compressive and splitting tensile response of pervious concrete bi-dimensional models. According to the authors the model was improved from [87] and reproduces with low error the final mechanical properties of the material. However, Lian *et al.* [89] observed that when larger aggregate sizes are involved, the influence of the shape and surface texture of the aggregate used in porous concrete is greater and currently the simulation results will not be as satisfactory as for smaller aggregate sizes.

2.5.2. Other types of Concretes

Caballero *et al.* [90] proposed a methodology to create and simulate 3D meso-scale Finite Element models of concrete submitted to uniaxial tension. The stress-strain curves obtained with the simulation showed the initial elastic behavior, the localization of the peak stress and the softening [90]. Snozzi *et al.* [91] simulated the dynamic behavior of 2D meso-scale concrete models submitted to tensile loads using FEM. The models with uniform distribution of the aggregates presented a reduction of the maximum strength, due the alignment of the fracture planes. On the other hand, a random distribution of the aggregates increased the probability to have a weak zones [91]. Li & Li [92] obtained a meso-scale finite element model of concrete specimens using computed tomography method. The authors proposed a methodology to create and simulate the Interfacial Transition Zone (ITZ). It was validated by the simulation of uniaxial tension. Li & Li [92] observed that the numerical results of the post-peak portion of the stress-strain curve agreed with the results obtained in laboratory. Huang *et al.* [93] generated a 3D meso-scale model of a concrete specimen with X-ray Computed Tomography. The model included the discretization of the aggregates, the mortar, the isolated pores and the initial cracks for the Finite Element simulation of uniaxial compression and tension. Huang *et al.* [93] suggested that the intrinsic heterogeneity of the meso-structure may significantly affect the macroscopic responses of concrete.

Schlangen & Garboczi [94] implemented a fracture law in 2D Lattice Model to simulate the rupture behavior of concretes submitted to different types of loads. The authors observed that models with two degrees of freedom per node presented a crack pattern similar to real experiments. Even better results are obtained when three degrees of freedom per node is used [94]. Lilliu & van Mier [95] developed a 3D Lattice Model as a solution of the problem of brittleness in concrete simulation obtained from 2D Lattice Model. The numerical results showed that the model reproduces the fracture processes observed in real experiments. In this sense, Lilliu & van Mier [95] suggested that the 3D lattice version coupled with a realistic representation of the particle distributions might be the solution to the problem of brittleness. Cusatis *et al.* [96-97] proposed and validated the Confinement-shear Lattice Model to simulate the damage evolution in concretes in tension and/or compression. In their approach the model transmit the axial and shear forces, with the shear stiffness exhibiting friction and cohesion. The model simulated all the essential aspects of the tensile, compressive and shear failure of concrete (fracture behavior, post-peak softening and its localization) [97]. Kozicki & Tejchman [98-99] proposed a 2D Lattice Model law to simulate the fracture behavior of the concrete considering the effect of the aggregates sizes and spatial distribution. The simulations of a deterministic size effect showed a decrease of nominal strength with increasing specimen size as well as an increase of fracture energy with size [99].

Šmilauer [100] proposed a constitutive law modeled with local damage, plasticity and viscosity to simulate the concrete as a homogeneous material. This model was implemented on the Yade platform (Šmilauer *et al.* [101]) using Discrete Element method. Tran *et al.* [102] proposed a model based on a three dimensional Discrete Element method to study the behavior of concrete under high-confining pressures. The experimental stress–strain and volumetric curves were well reproduced by the model [102]. Nitka & Tejchman [103-104] simulated the concrete behavior in fracture in 2D. They analyzed the influence of the micro-scale over the crack propagation. Nitka & Tejchman [104] observed that the distribution of internal contact forces in concrete specimens was non-uniform. The number of contact forces continuously decreased in concrete specimens due to the material fracture. Some grain rotations occurred in fractured regions [104]. Skarzynski *et al.* [105] used the open source framework Yade to simulate a three points bending test with the region of interest discretized using X-ray Computed Tomography results of real specimens. The model was capable of reproducing the fracture development including micro- and macro-cracks. Cusatis *et al.* [106-107] proposed and validated the Lattice Discrete Particle Model to simulate the failure behavior in concretes. According to the authors the model seems to simulate the concrete behavior when subjected to different types of loads.

2.6. DISCUSSION

Qualitative and quantitative evaluations of the state of the art dived into the proposed lines of investigation were performed. A significant number of studies were published in the past few years. However, a few studies presented in the literature were centered in the numerical simulation of the pervious concrete. This suggest that the proposed lines of research have importance in the technical and science spheres. However, most of the studies shows that the model are still in an initial phase of development.

Regarding the laboratory investigation of the pervious concrete, a great number of studies concerning new compositions and properties enhancement were conducted at the scientific community. However, there is a lack of studies in the development of methods to define the composition of pervious concrete different from trial and error. This type of method leads to an economic drawback, increasing the costs and delaying the placement of the pervious concrete.

The simulation of the concrete in fresh state is a recent topic of investigation. Hence, some methods were developed to simulate the viscoelastic characteristics of the self-compacting concrete. Nevertheless, none of the current methods include the particularities of the behavior of the pervious concrete in fresh state.

Some isolated publications that treated separately the hydrological and mechanical behavior of pervious concrete in numerical simulations were discussed. Chung *et al.* [73] presented a model that reconstructs the spatial distribution of the voids in pervious concrete to simulate the water percolation. In order to create this model, it is necessary to feed the code with the computed tomography images of the pervious concrete specimen of each mix design. Consequently, a large initial experimental campaign is necessary to validate the models. Lian *et al.* [87;89] proposed a 2D discrete element model to simulate the compressive strength of pervious concrete. Likewise, it is also necessary to perform an experimental program to obtain the meso-structure required for the model. Furthermore, the stress-strain curves obtained in these studies presented a low correlation in the localization portion of the curve and the brittleness problem after the fracture.

In this sense, the need of a method that links the numerical simulations of hydrological and mechanicals properties with the composition of pervious concrete is verified. Additionally, the development of such method would decrease the laboratory costs and lead to projects with optimal compositions created to satisfy the requirement of each application.

3. 2D COMPACTION MODEL

3.1. INTRODUCTION

Granular materials are widely employed in construction, ceramic, metallurgy, seeds and pharmaceutical industries. In some cases, they are composed by grains involved by a binder layer that will harden with time or temperature, providing cohesion to the system. An example of such materials is pervious concrete. This special type of concrete is obtained by eliminating part of the sand to create a system with enough voids to allow water flow.

In the non-hardened state, pervious concrete may be discretized as several independent aggregates particles involved by fresh cement paste [53]. During the production process, the fresh material is subjected to compaction pressure before hardening occurs in order to achieve a predefined density. The energy applied is of great relevance for engineering purposes since it determines the equipment required and the efficiency of the process. An approximated evaluation of this compaction process could contribute to the optimized definition of the equipment required, of the composition of the concrete or of the aggregates grading.

In line with that, an increasing interest on the simulation of the compaction process of granular media is observed in the literature. Generally, two types of computational methods are used to simulate this problem: the discrete-particle approach and the continuum approach. A well-known example of the former is the discrete or distinct element method (DEM) [108-109], where the interactions between particles are usually classified as rigid or soft depending on whether the particle deformation during a collision is explicitly incorporated in the model or not. Even though it has been successfully used for the simulation of granularly media [66;110-114], this approach usually presents a high

computational cost. In addition to that, some simplifications and new implementations have to be assumed for the simulation of biphasic deformable particles in DEM.

In the second approach, a finite element method (FEM) is used to simulate a continuous media whose behavior is described with the elastoplastic theory. This numerical solution was widely used to evaluate the compaction of powder metals and ceramics [115-118]. Although the computational cost is lower than with the DEM and deformations may be directly taken into account, the assessment of parameters such as the porosity or the particles position with the compaction pressure is not possible.

A recent alternative to simulate the compaction process more realistically is to integrate both methods [119-120]. In this case, the discrete element consideration from the DEM is combined with a continuum representation of particles and contacts, which is typical of the FEM. This combined simulation is more accurate than the previous ones and is considered promising since it accounts for aspects such as the deformation of particles and allows the estimation of the porosity. However, the high computational demand still limits its use.

A more simplified analysis may be performed with lattice models. Tab. 3.1 summarizes some of the most relevant studies conducted with this approach to simulate either the compaction process of different materials or the behavior of concrete. Notice that all studies focus on the simulation of materials in the hardened state, that is, no binder in the fresh state is considered in the analysis. Moreover, although several studies on the simulation of the compaction process of granular media or rock with Lattice Models are available in the literature, no simulation of the compaction process of fresh concrete may be found.

In most of the studies regarding the compaction process, the materials simulated present an initial porosity of up to 20 %, meaning that the level of rearrangement of particles is small and the same lattice layout is maintained throughout the analysis. On the contrary, in the case of particles with a binder layer found in pervious concrete, the initial porosity may vary from 20 % to 50 % when it is poured in the molds. Consequently, the level of initial disorder and of rearrangement experienced during the compaction process is much higher than in the case of rock masses. This means that a lattice Model with fixed distribution of bars might not be representative of the material in intermediate compaction stages due to the high level of internal reorganization, which is characterized by a significant increase in the number of contacts.

Table 3.1 – Studies with lattice model to simulate compaction of different materials or the behavior of concrete

Ref.	Material	State	Phases	Type of analysis	Load
[125]	Granular media (1D)	Hardened	Particle / Void	Compaction	Tapping
[126]	Granular media (2D)	Hardened	Particle / Void	Compaction	Tapping
[127]	Granular media (2D)	Hardened	Particle / Void	Compaction	Tapping
[128]	Rock (2D)	Hardened	Continuum	Compaction	Compresion
[129]	Rock (2D)	Hardened	Continuum / Void	Compaction	Compresion
[130]	Concrete (2D)	Hardened	Continuum	Fracture	Tension and Compresion
[94]	Concrete (2D)	Hardened	Aggregate / Mortar / Void	Fracture	Tension and Compresion
[99]	Concrete (2D)	Hardened	Aggregate / Mortar	Fracture	Tension and Compresion
[131]	Concrete (2D)	Hardened	Aggregate / Mortar / Rebar / Fiber	Fracture	Tension and Compresion
[95]	Concrete (2D / 3D)	Hardened	Aggregate / Mortar / ITZ	Fracture	Tension
[97]	Concrete (3D)	Hardened	Aggregate / Mortar	Fracture	Compresion

3.1.1. Objectives

The objective of this Chapter is to propose a simplified approach for the simulation of the compaction of highly deformable granular media such as pervious concrete in the fresh state.

3.1.2. Outline of the Study

The strategy is to use an evolutionary lattice system with local instability to allow the intensive rearrangement expected during compaction, associated with a bar layout and material properties that vary with the load steps. Furthermore, a biphasic particle composed by a rigid inner core involved by a deformable exterior layer is considered. It

allows a simplified representation of complex granular media made of very deformable particles or of a rigid inner core covered with a viscoelastic binder layer.

Initially the model proposed is described and its application is evaluated (from Section 3.2 to 3.5). Then, a numerical comparison using the results by other authors with DEM/FEM simulation is presented in Section 3.5. Finally, an experimental program is conducted to evaluate the compaction process of pervious concrete. The results from the tests are compared with those numerically estimated with the new model in Section 3.7.

3.2. WORK PHILOSOPHY

The model to simulate the compaction of granular media was divided in two complementary stages. The sole purpose of the first stage is to create a particle distribution with the desired initial porosity. The algorithm applied organizes the particles in space, creating a system similar to that obtained in DEM with limitations of no particle movement and with the desired initial porosity (other distribution laws could be implemented depending on the type of material simulated). The distribution generated is the input for the second stage, which is the focus and main contribution of the present study. Based in an adapted lattice method, it simulates the reorganization of the particles after an imposed compaction displacement or vibration. As mentioned before, the algorithm generated is versatile and may be simply adapted to a wide range of applications. The program MATLAB 7.10.0 was chosen for the development since it is of common use in the scientific community and includes a large math library that is capable of solving complex matricial problems. A detailed explanation of both stages is presented in the following sections.

Although the model described here was developed for 2D simulations of circular particles, it could also be generalized to 3D. For that, it would be necessary to modify the original algorithm, including an additional degree of freedom. Furthermore, the verifications performed in the lattice model would have to be adapted for a 3D condition. This would imply additional computation time but would lead to a model more representative of the particle distribution.

3.2.1. Stage 1 –Random Fall

The numerical approach used is based on a simple algorithm designed by Vold [132] for the packing of circular random particles. This approach was modified by several authors [133-135] that implemented new types of contact between particles. Here, the algorithm was further modified to represent the packing of circular particles that might

be involved by a binder with special characteristics, considering several simplifications that would allow reaching an initial porosity typical of pervious concrete. The interaction between particles is based in the linear elastic contact law without friction coefficient. This means that new particles may spin and slide over the existing ones. Such interaction is a simplification of what would occur if a rigid particle without binder or if a particle with a dry binder layer was dropped over another. Notice that the linear elastic contact law is only used in Stage 1 and that other laws could be used instead if necessary.

To find a stable place for each particle, three steps were conducted as illustrated in Fig. 3.1. First, an *x* coordinate is chosen to start the vertical falling process inside the container (see Fig. 3.1a). In the studies about the disposition of granular media, Jullien [133] demonstrated that a segregation phenomenon might occur in case a large number of particles with different sizes are considered and the *x* coordinate of the initial falling point is fixed. Such condition favors a heap accumulation inside the container just under the coordinate *x*. Moreover, the large particles may easily spin over the bed formed by smaller particles, being more likely to accumulate close to the lateral wall of the container and to generate big voids or a non-homogeneous distribution.

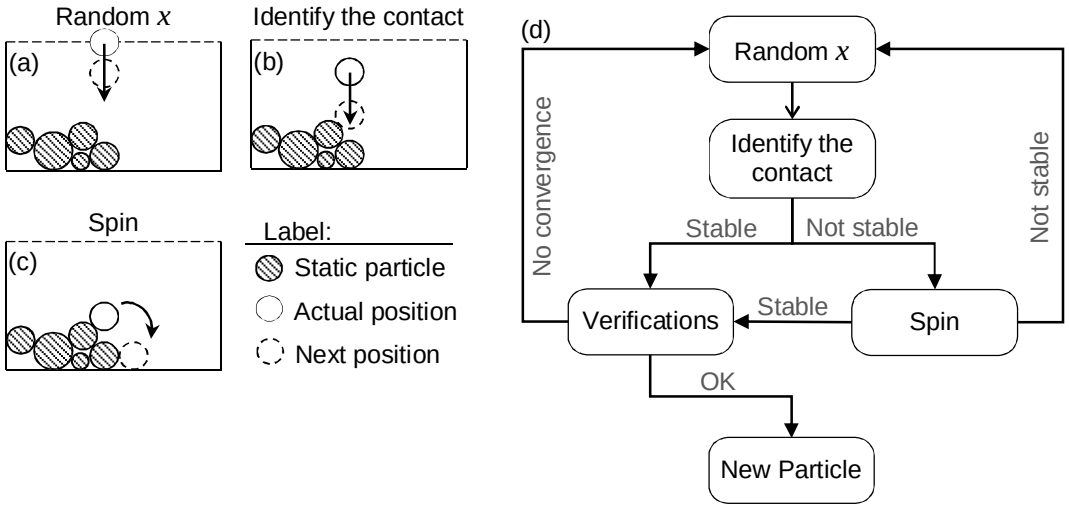

Figure 3.1 – Steps to find a stable position for each particle in Stage 1 (free fall).

To mitigate this problem, two modifications are taken into account in the first step regarding the original algorithm. In this sense, the starting coordinates *x* are randomly chosen according with a probabilistic curve. To diminish even more the heap accumulation, the probabilistic curve is assessed every time a particle falls. It is assumed inversely proportional to the distance in *y*-axis between the dropping point and the height of the granular bed at each position in *x*. Consequently, points with bigger accumulation of particles have a smaller probability of being selected.

Once the *x* coordinate is defined, in the second step the particle falls until the first contact is verified. If the contact occurs with the walls of the container, the particle are automatically fixed. On the contrary, if it occurs with another particle (see Fig. 3.1b), the third step is called. In the latter, the stability of the falling particle is verified considering the support provided by the surrounding ones.

Each contact point is only capable of generating compressive normal forces since, in this stage, the contact between particles is weak. To evaluate the stability, the balance of forces in *x* and in *y* and the balance of moments are used to estimate the contact reactions applied to the contact points of the falling particles, similarly to what is done in statics. If all reactions estimated are positive (indicating compressive forces), the particle is stable. Conversely, if any of the calculated reactions is negative (indicating tensile forces) or if the system of equations may not be solved, the particle is assumed unstable.

In case an unstable condition is observed, the falling particle is allowed to spin around the particle that received the last contact until additional contacts are observed and stability may be verified again, as shown in Fig. 3.1c. During the spin, the center of the particle will always move with the same direction of a vector traced tangent to the last contact, pointing towards the bottom line of the recipient. This procedure is repeated until a stable condition is found or a contact with the walls of the recipient occurs.

After finding a stable condition for the falling particle, a small deformation may exist in the contact region due to the self-weight of the particle (see Fig. 3.2). This deformation is simulated as an overlap.

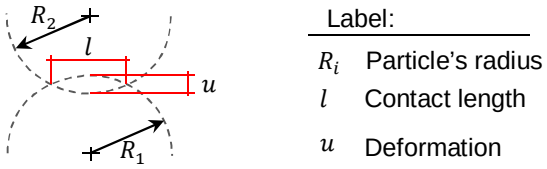

Figure 3.2 – Deformation of the particle represented as an overlap.

The value of the deformation 'u' is calculated through the linear elastic contact law, with is represented by Eq. 3.1. This law depends on the stiffness of the materials in contact 'k_{fpc}' and the force 'F'due to the self-weight of the particle.

$$u = \frac{F}{k_{fpc}} \tag{3.1}$$

With the stable contact established and the initial overlap estimated, the particle becomes fixed and cannot change position or be moved by others. The whole procedure

is repeated with the next falling particle. As a result, the stability of the distribution is always assured. The recipient is filled until the fixed particles cross the line to which the compaction will be applied. All particles located above this line are then removed so a reference initial height of the sample is guaranteed. In this moment, the initial porosity of the system is estimated and compared with the desired one.

The algorithm used for the Stage 1 tends to generate systems of particles with porosities that are below that found in pervious concrete. This occurs because, in reality, particles are not dropped one by one until a stable condition is found. Rather than that, they are poured over the surface all together in big groups. This increases the level of internal disorder, hence the porosity. To correct this and assure the desired initial porosity, some of the particles are removed from the system.

A special procedure is used to select from which points the particles will be removed in order to minimize the modification of the grading curve of the granular medium. First, a diameter is selected according with the proportion of the grading curve used to introduce the particles in the system. Then, all particles with this diameter are listed and one is randomly selected. A verification is performed to evaluate whether the self-weight stability of the system will be maintained after it is removed. If stability is guaranteed, the selected particle is removed and another diameter is selected. If not, another particle with the same diameter is randomly selected and the stability is verified again. This is repeated until a suitable particle is found and removed. In case no particle in the list fulfills the stability criterion, another diameter from the grading curve is selected. In some cases, this will modify slightly the grading curve of the granular media. Anyhow, this procedure is more efficient to achieve the initial porosity than using an algorithm that considers the real interactions between all particles that are poured together.

Another possible situation that will ask for a modification of the initial porosity happens in case non-circular particles are used in reality. In this situation, the porosity generated will be higher than that achieved with Stage 1, which considers only circular particles. In order to correct the porosity of the system, the same procedure described in the previous paragraph for the removal of particles should be applied. For that, the equations that correlate the initial compactness of the sample with the sphericity of the particles presented in the studies of German [137] were used.

It is important to remark that the algorithm used in Stage 1 includes simplifications to decrease the computational effort required to generate a distribution of particles with the desired initial porosity. More realistic alternatives based on DEM may be found in the literature.

3.2.2. Stage 2 – Compaction

This stage is responsible for the simulation of the compaction process. It consists of calculating the geometric position of all particles after a static compaction produced by a small vertical displacement of the top surface of the granular sample. Although this study considers only vertical compressive displacement to compact the granular bed, the same approach is valid for compaction or vibration in all directions.

Fig. 3.3 outlines the algorithm used for each load step in the compaction stage. It initiates with a modified Delaunay Triangulation (DT) method, where nodes and bars are created between adjacent particles. An interactive lattice model analysis with incremental displacement is conducted (the same numerical solution is used to study the hardened concrete fracture by other researchers [138-140]).

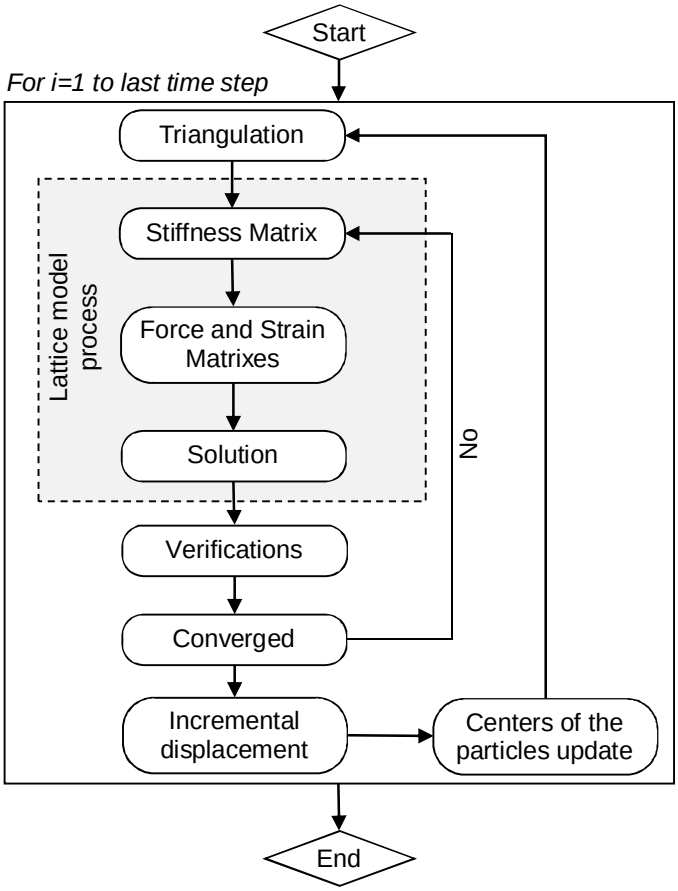

Figure 3.3 – Algorithm of Stage 2 (Compaction).

Then, the balance of forces is verified and an interactive process is performed until reaching convergence. In the present study, the convergence is verified using the Euclidian norm of the out-of-balance forces. The iterations are stopped and the step is

concluded if this norm is smaller than 10^{-4}. Once this occurs, nodal displacement results obtained by the lattice model are used to update the position of the centers of the particles in each time step. This procedure – including the DT to detect new contacts – is repeated at every load step. A detailed description of the different steps from Stage 2 is presented in the following sections.

Triangulation

Initially, the coordinates of the center of the particles and their radius are detected (Fig. 3.4a). After that, a DT (Fig. 4b) is executed using the same algorithm applied by [141]. Then, a geometrical verification (Fig. 3.4c) is conducted to ensure a stable lattice layout. According with this verification, a bar is placed in the lattice model whenever the ratio between the distance of the center of two particles and the sum of their radius is smaller than a detection coefficient (Ω). In this study, it was found that a Ω of 1.5 is usually enough to assure convergence. Notice that by using a Ω bigger than 1, the resulting triangulation includes bars that may represent the real interaction between particles in contact, as well as virtual bars between particles that are not actually in contact.

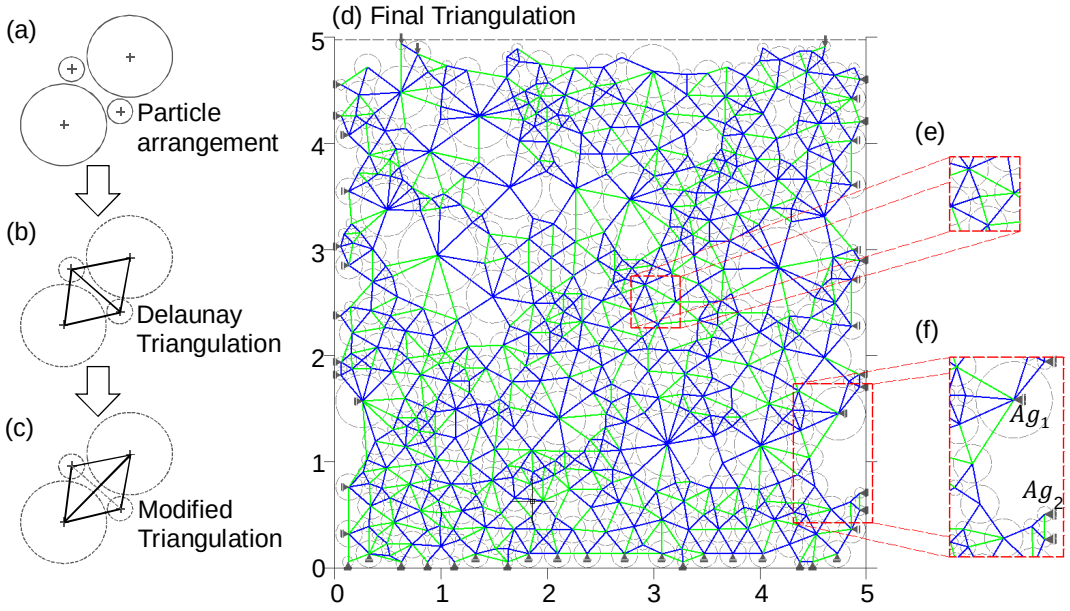

Figure 3.4 – Triangulation process for a certain load step.

The latter does not exist in reality but is necessary to obtain a well-conditioned matricial system. As described in Section 3, special material properties are assigned to each type of contact to reproduce the interactions between particles and to avoid the virtual contact interfering in the compaction results. Fig. 3.4d shows the final

triangulation in a certain time step, highlighting the real and the virtual contacts in blue and in green, respectively.

Even though the arrangement of bars depicted in Fig. 3.4d is globally stable, local instabilities are found if groups of bars are analyzed separately. Consider, for instance, the arrangement highlighted in Fig. 3.4e. It is evident that the relative movement between all nodes present in the local system is restricted. On the other hand, in the arrangement highlighted in Fig. 3.4f, the relative displacement between nodes is possible. This displacement may occur due to the formation of a local mechanism. For instance, aggregate Ag_1 (see Fig. 3.4f) might get closer to aggregate Ag_2 as the lattice connecting them may stretch horizontally during the compaction process. The use of virtual bars with very small stiffness also contributes to this relative movement since big displacements may be achieved even with the smallest forces. This is essential to reproduce the highly porous medium and the rearrangements of particles throughout the time steps.

The resulting lattice layout works as a mesh with bar elements. In each load step, the granular medium is re-meshed since new contacts might arise and old ones might be eliminated. To illustrate it, Fig. 3.5a represents the initial condition without compaction and Fig. 3.5b represents the situation after a compaction of 14.4 %. It is clear that new contacts are detected and the internal instability is reduced throughout the steps. The increase in the number of real contacts is not considered a computational problem since the equations are solved by matricial methods and in this kind of solution the computational cost is more related with the number of nodes, which remains constant throughout the analysis.

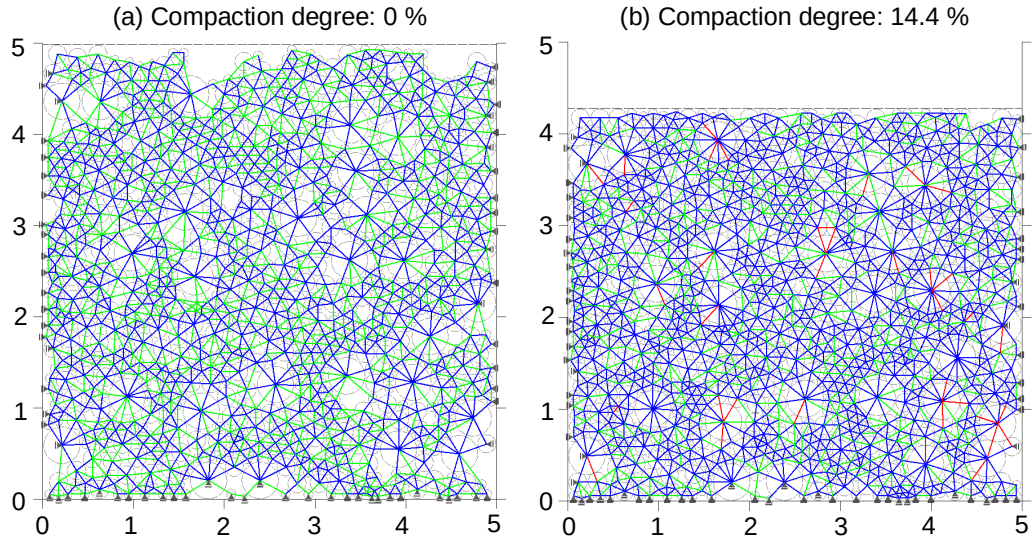

Figure 3.5 – Triangulation at different steps.

Lattice Model Process (LMP)

Once the triangulation for all the particles is finished, the nodes and the bars are passed to the lattice model process (LMP). In this 2D model, all the nodes are articulated and have two degrees of freedom, corresponding to the displacement in two orthogonal directions. Equilibrium conditions regarding the forces in the *x*-direction (Eq. 3.2) and in the *y*-direction (Eq. 3.3) are applied. According to the Principle of Virtual Work (PVW), the total virtual work of the forces acting on the nodes should be zero in each time step. The boundary conditions for this numerical problem are applied only at the nodes of particles in contact with the surfaces of the container, which might have their displacement fixed or might be used for the application of the compaction.

$$\sum F_x = 0 \tag{3.2}$$

$$\sum F_y = 0 \tag{3.3}$$

To understand how the forces and displacements are calculated, consider the simplified example of the bar from Fig. 3.6 that originally extends from node 1 to node 2. If resultant forces are applied in the nodes ($F_1^{(e)}$ and $F_2^{(e)}$, respectively), the bar may deform and move assuming the new position defined by the nodes 1' and 2'. In this situation, the displacements $u_1^{(e)}$ and $u_2^{(e)}$ will be observed.

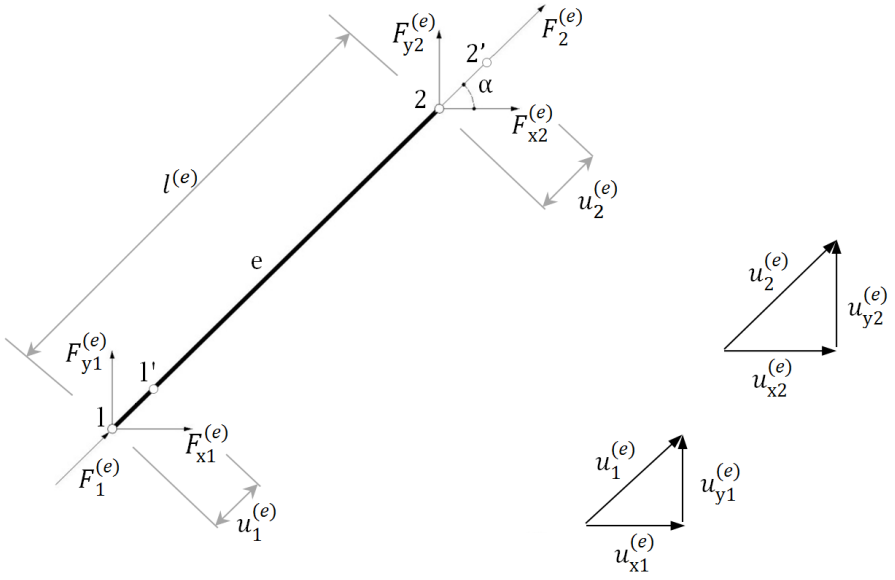

Figure 3.6 – Forces and displacements in the nodes of a bar.

Since equilibrium is maintained in the system, the forces should cancel each other. In this condition, the variation in the position of the nodes may be related with the forces through Eq. 3.4. In this equation, $k^{(e)}$ represents the stiffness of the bar in a certain time step (for a detailed description on the contact laws used to define k see Section 3.4).

$$F_1^{(e)} = -F_2^{(e)} = k^{(e)} \cdot \left(u_1^{(e)} - u_2^{(e)}\right) \tag{3.4}$$

In the matricial form, Eq. 3.4 could be represented through Eq. 3.5. In the latter, the decomposed stiffness $k_{ij}^{(e)}$ should be calculated according to Eq. 3.6, considering the angle α formed between the forces and the coordinate system selected.

$$\begin{bmatrix} k_{11}^{(e)} & k_{12}^{(e)} \\ k_{21}^{(e)} & k_{22}^{(e)} \end{bmatrix} \cdot \begin{bmatrix} u_1^{(e)} \\ u_2^{(e)} \end{bmatrix} = \begin{bmatrix} F_1^{(e)} \\ F_2^{(e)} \end{bmatrix} \tag{3.5}$$

$$k_{ij}^{(e)} = k^{(e)} \cdot \begin{bmatrix} cos^2\alpha & sin\alpha \cdot cos\alpha \\ sin\alpha \cdot cos\alpha & sin^2\alpha \end{bmatrix} \tag{3.6}$$

In a more complex lattice model composed by several bars, Eq. 3.5 may be generalized to Eq. 3.7. Notice that it has the form $k \cdot u = F$, in which k is the stiffness matrix, u is the displacement vector and F is the forces vector.

$$\begin{bmatrix} k_{11}^{(e)} & k_{12}^{(e)} & \cdots & k_{1n}^{(e)} \\ k_{21}^{(e)} & k_{22}^{(e)} & \cdots & k_{2n}^{(e)} \\ \vdots & \vdots & \ddots & \vdots \\ k_{n1}^{(e)} & k_{n2}^{(e)} & \cdots & k_{nn}^{(e)} \end{bmatrix} \cdot \begin{bmatrix} u_{x1}^{(e)} \\ u_{y2}^{(e)} \\ \vdots \\ u_{xn}^{(e)} \\ u_{yn}^{(e)} \end{bmatrix} = \begin{bmatrix} F_{x1}^{(e)} \\ F_{y1}^{(e)} \\ \vdots \\ F_{xn}^{(e)} \\ F_{yn}^{(e)} \end{bmatrix} \tag{3.7}$$

At each step, an updated stiffness matrix (k) for all elements and a vector with the applied forces (F) are assembled. Once the boundary conditions are imposed, the direct stiffness method is applied to determine the displacement vector (u) of the nodes. For that, similarly to what is done in FEM, the system $k \cdot u = F$ must be solved. In the present study, the solution of Eq. 3.7 is iteratively approximated through the Newton-Raphson Method. Convergence criteria based on the displacement and the forces are considered.

All equilibrium equations are applied and the stability of the system is assured in the load steps. This might seem contradictory given that local instabilities might occur

during the compaction process. To simulate such instabilities, the lattice mesh is redefined at each step and virtual bars are included or eliminated.

In the compaction process of a granular material characterized by an inner rigid core and an external deformable layer (such as a binder), the main interactions between particles are deformation of the contact region and rotation of one particle over the others. Although deformations of the contacts may occur by the action of forces in normal and tangential directions, in a uniaxial compaction process the normal forces are the main responsible for the interaction between particles. Indeed, due to the soft nature of the binder, the normal forces generated tend to be several times bigger than the tangential forces. Consequently, the former governs the contact between particles. This allows a simplified consideration of the lattice bars in the present study, which only have axial stiffness.

The rotation of the particles is not explicitly considered in the modified lattice model proposed. This movement is indirectly represented by the possible rotation of the bars around the nodes. Such approximation is only feasible for granular materials in which the rigid connections between particles have not been established, interactions are governed mainly by normal forces and large displacements may occur. This is the typical situation found in the compaction of many granular medium without binder or with binder in the fresh non-hardened state.

Even though it goes beyond the scope of the present study, it is important to remark that the model proposed could produce unreasonable results once rigid connections are established between particles. In this situation, other models are required since the influence of tangential forces associated with the rotation of particles should be taken into account to achieve accurate results.

Verifications

Several verifications are applied to evaluate the correctness of the boundary conditions in each time step. If all verifications are satisfied, the step is concluded and another incremental displacement is applied. If not, the boundary conditions are modified, the force and displacement matrices are changed and the code calls the LMP function to process the step once again. This is repeated until all verifications are satisfied.

Two types of modifications in the boundary conditions are possible, as shown in the Fig. 3.7. The first of them occurs when the calculated reactions of particles in contact with the walls are tensile forces (Fig. 3.7a1) that exceed the tensile strength of this contact. In this case, the change imposed is to exclude the support, as illustrated in Fig. 3.7a2. The second type of modification occurs when a particle passes throw the wall of the container (Fig. 3.7b1). The correction here is to introduce a new support at the node of the particle and to fix its position in contact with the wall, as demonstrated by Fig. 3.7b2.

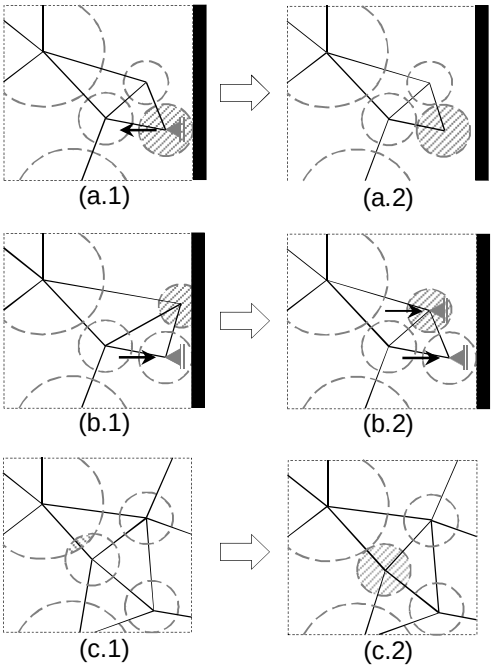

Figure 3.7 – Verification of boundary conditions (a and b) and of overlap condition (c).

Besides the modifications in the boundary conditions, three additional modifications might be necessary at each step. The first of them occurs when an unrealistic overlapping of the inner core of particles occurs after the LMP (Fig. 3.7c1) concludes the analysis. In this case, the code does not send the model back to the LMP to recalculate the step again. Instead, it introduces in the next step a displacement in the overlapping particles equivalent to the overlap distance (Fig. 3.7c2). The second additional modification concerns the change of the material properties of the bar. The distance between the centers of the particles is used to define the type of contact and its properties according with the criterion presented in Section 3.4. The last additional modification only takes place in the initial load steps when the model presents a global instability and the stiffness matrix may not be inverted. If this happens, the triangulation function is called again and the detection coefficient (Ω) is increased to achieve a bigger number of bars in the DT. If the increase in Ω is performed several times in the same step, the analysis is stopped. Based on the experience with the simulations, the number of repetitions observed will depend on the initial porosity of the medium. For the models analyzed here, the initial time steps might require 2 to 3 repetitions. As the analysis proceeds, the number of contact increases and porosity reduces; hence no repetition of the DT is needed within the same step.

Although the successive DT at each time step allows identifying new contacts, it might lead to convergence and stability problems. This is especially evident in the first stages of compaction of systems with high initial porosity due to the significant

movement between particles. To mitigate these problems, it is necessary to apply sufficiently small time steps.

Time steps

The compaction of a granular material is usually a dynamic process given the typical rate of load application and since the value of the forces depends on the physical properties of the interactions between particles, which are affected by the rate of their relative displacement. Instead of using a purely dynamic analysis, some simplifications are assumed in the alternative approach proposed in this study.

Once all bars of the lattice layout are defined, the load is applied as small vertical displacements for each step. This vertical displacement is related to the rate of the compaction process performed in reality. In other words, the displacement is the velocity of the compaction multiplied by the time step. With all the loads and boundary conditions defined, the lattice model is statically solved. The variation in the position of the particles is used to assess the velocity of their relative displacements. For example, considering two particles '*i*' and '*j*' with a distance $\Delta u_{in,i-j}^{t-1}$ at time step t^{-1} and the distance $\Delta u_{in,i-j}^{t}$ at the time step *t*. The modulus of the difference between the difference $\Delta u_{in,i-j}^{t-1}$ and $\Delta u_{in,i-j}^{t}$ divided by the time step 'Δt^{t}' is the velocity of their relative displacement (v_{i-j}^{t}). This velocity is applied in the visco-elastic material model described in Section 3.4.2 to assess the new stiffness of each contact, which is used for the next time step. This procedure is repeated throughout the analysis.

It is evident that the approach proposed combines a static consideration of the balance of forces within every time step but includes the dynamic effects through the redefinition of the stiffness of the interactions between particles and through the adaptive DT. Therefore, it may be considered a quasi-static analysis that intends to simulate a dynamic process. This represents a simplification made with the intent of reducing the time required for the analysis of such dynamic phenomenon. Other models should be used if a more precise representation of the interaction between particles is needed.

3.3. PARTICLE DEFINITION

In pervious concrete, the shape of the particle in reality is governed by the aggregate used. The pervious concrete may be dissociated in several unities with the aspect shown in Fig. 3.8a. Although more complex arrangements are also possible to simulate the real shape, in many cases a simplification can be considered. A bi-phasic spherical particle shown in Fig. 3.8b may be used. The latter has a total radius R_T, being formed by an inner aggregate core with radio R_{ag} surrounded by a paste layer with

thickness t_{eq}. The main advantage of this simplification is the low computational effort required to evaluate the contact, as the overlap of spheres is determined from the spatial distance of their centroids without the need to consider their orientation. Notice that the simplification of an external layer (as cement paste or mortar) surrounding an inner core (as aggregates) corresponds with the reality.

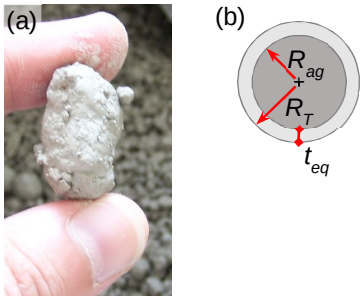

Figure 3.8 – Real particle formed by aggregate involved by cement paste layer in a pervious concrete (a) and simplification considered (b)

To simulate the open grading curve of the aggregates it is also necessary to define the sizes of aggregates that will be used in the discretization. For example, Fig. 3.8a presents the real grading curve of a coarse aggregate that ranges from 2 to 8 mm, showing the volume that passes through the sieves in the vertical axis and the opening of the sieves in millimeters in the horizontal axis. In this example, an approximation with three different sizes of aggregate particles (diameters of 2, 4 and 8 mm) was chosen. Through a balance of masses, the percentage of particles corresponding to each size may be calculated, giving the proportion shown in Fig. 3.9a.

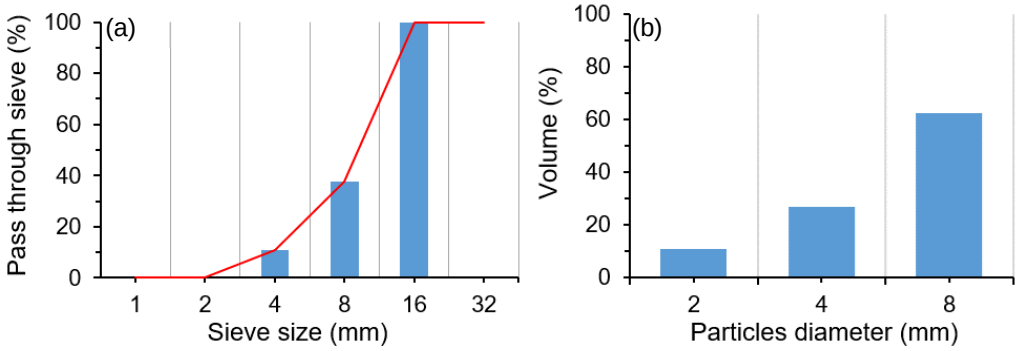

Figure 3.9 – Approximation of a grading curve with three sizes of aggregate particles (a) and percentage of aggregate particles of each diameter (b)

After the definition of the particles sizes, the thickness of the external layer (t_{eq}.) may be calculated. Based on the studies by Klein [142] and Klein et al. [143], it is

considered that t_{eq} is proportional to the radius of the aggregate according with Eq. 3.8. In this equation, α_{eq} is a constant that accounts for the distribution of the cement paste (or mortar) and depends on the composition of the pervious concrete. In order for Eq. 3.8 to hold, α_{eq} should be estimated through Eq. 3.9 with the volume of aggregates (V_{ag}) and the volume cement paste or mortar (V_{ag}) used in the mixture. Since the simulations of the pervious concrete are based on the meso-level criteria, the minimal diameter of aggregate should be bigger than the minimal thickness of the cement paste layer. This is always guaranteed with Eq. 3.8.

$$t_{eq} = R_{ag} \cdot (1 + \alpha_{eq}) - R_{ag} \tag{3.8}$$

$$\alpha_{eq} = 1 - \sqrt[3]{1 - \frac{V_p}{V_{ag}}} \tag{3.9}$$

3.4. MATERIAL PROPERTIES

This section focuses on the material properties for the bars that simulate the real and the virtual contacts between particles. Fig. 3.10a presents a schematic view of the particle and the possible contact types. The total particle radius and the aggregate (or inner core) radius are represented by R_T and $R_{ag,}$ respectively. This leads to three possible contacts defined by the distance between the centers of the particles (d) as illustrated in Fig. 3.10b, 3.10c and 3.10d. Notice that the stiffness is recalculated every load step since contacts might be generated or eliminated. The methodology used to obtain the contact length and the stiffness of each bar is outlined in the following sections.

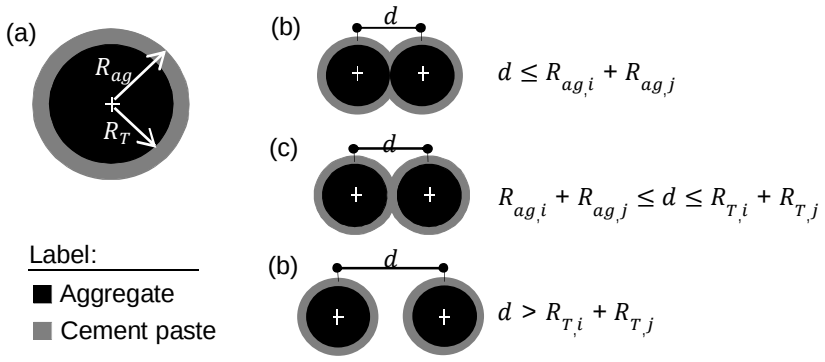

Figure 3.10 – Study particle (a) and situation of inner core contact (b), binder contact (c) and no contact (d).

3.4.1. Aggregate (or Inner Core) Contact Simulation

The first case illustrated in Fig. 3.10b occurs when the two inner cores are in contact, i.e. the distance between the center of the particles is equal or less than the sum of the radius of their cores ($d \leq R_{ag,i} + R_{ag,j}$). To simulate this interaction it is necessary to define the effective interaction area of particles in contact, which is used to calculate the stiffness of the corresponding bar. In the literature, authors like Lu et al. [144] defined that the interaction between two adjacent particles may be represented through Fig. 3.11.

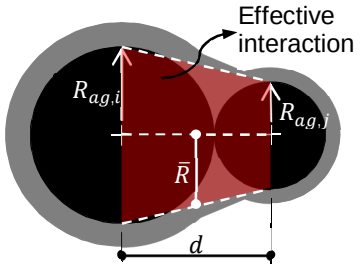

Figure 3.11 – Effective interaction area of particles in contact.

According to this definition, the effective area ($A_{ef,ag}$) may be approximated as a circle with radius ($\bar{R}$) equal the weight average of the diameter of the inner cores, expressed by Eq. 3.10. Usually, the elastic modulus of this contact is very high in comparison with that assumed for the contact of the binders. Therefore, in such applications, the interaction between inner cores may be simulated through a spring with high stiffness. The stiffness of this contact is calculated by multiplying the effective area by a surficial stiffness (k_s) that depends only on the properties of the material from the inner core. This is represented in Eq. 3.11, which takes into account that the sizes of the particles will affect the stiffness of the contact.

$$A_{ef,ag} = \bar{R}^2 \cdot \pi = \frac{{R_{ag,i}}^2 + {R_{ag,j}}^2}{R_{ag,i} + R_{ag,j}} \cdot \pi \tag{3.10}$$

$$k_i = k_s \cdot A_{ef,ag} \tag{3.11}$$

3.4.2. Cement Paste (or Binder) Contact Simulation

Fig. 3.10c represents a case in which the mortar layers of different particles overlap without putting in contact the aggregates (or inner cores). Here the distance of the center of the particles is less than the sum of the radius of the particles and more than

the summed radius from the rigid inner core ($R_{ag,i} + R_{ag,j} < d < R_{T,i} + R_{T,j}$). The binder is assumed as a soft layer susceptible to deformations. When an overlapping occurs, it is necessary to assess the binder deformation and to recalculate the stiffness of the contact.

Binder redistribution due to overlap

The contact between particles with a binder outer layer may produce a redistribution phenomenon. Depending on its rheology, the binder could relocate around the contact point as the overlap increases. This leads to the formation of a lateral increment of the contact length, as depicted in the Fig. 3.12. This increment should be taken into account when the normal forces between particles are estimated.

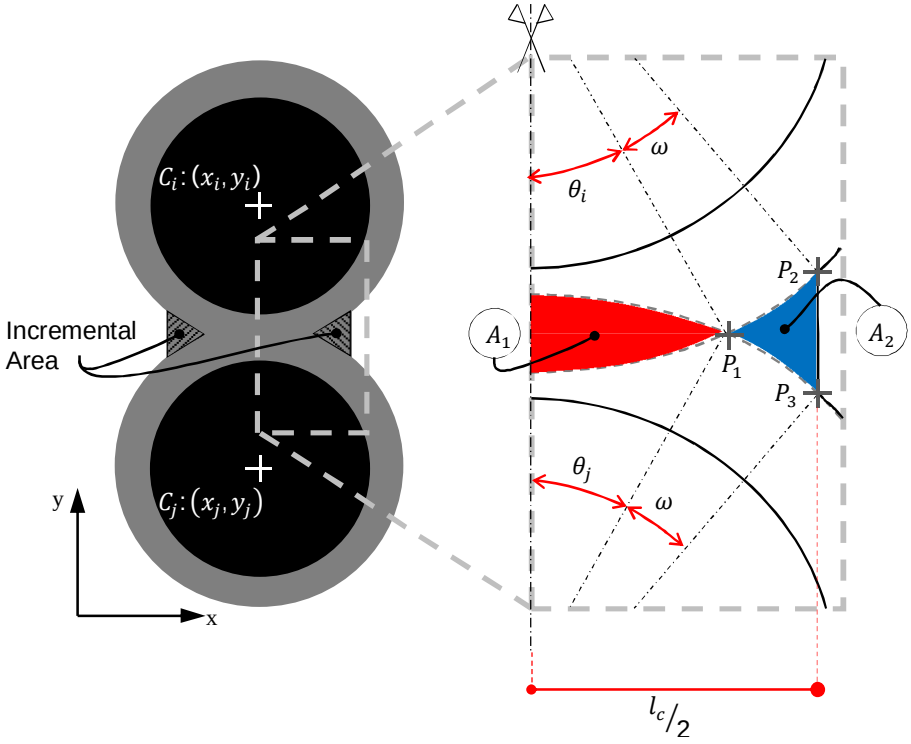

Figure 3.12 – Binder redistribution after overlap.

To assess the final contact area after the overlap, a simple geometric calculation is performed. It is assumed that the area of binder located originally in the overlap region A_1 will equal the area of redistribution in region A_2 of Fig. 3.12. Therefore, once the area of A_1 is estimated for a certain overlap, the area of A_2 is also known. Then, the position of the points P_2 and P_3 may be determined, thus providing the final contact length 'l_c'. To simplify this calculation, it is considered that the angle ω_j that represents the increment

is equal for both particles in contact. This consideration implies a negligible error as long as the thickness of the binder layer is small in comparison with the diameter of the inner core and the sizes of particles do not vary by one order of magnitude. Even though this is the common case with the materials analyzed here, if such conditions are not fulfilled, a more precise calculation should be used to estimate the angle ω_j for each particle.

Stiffness relationship

A numerical simplification is also used to consider the binder-binder stiffness behavior. Fig. 3.13 presents in red this contact, expressed by the relation between the distance 'd' and the equivalent stiffness 'k_b' estimated with the Kelvin-Voigt rheology model ($f(k_n, \eta_n, t)$). This rheology model simulates the viscoelastic behavior of the binder by considering a parallel combination of the linear elastic spring and the linear viscous dashpot. It is important to remark that the Kelvin-Voigt model is extensively used to simulate a visco-elastic interaction between particles of several types of materials [60].

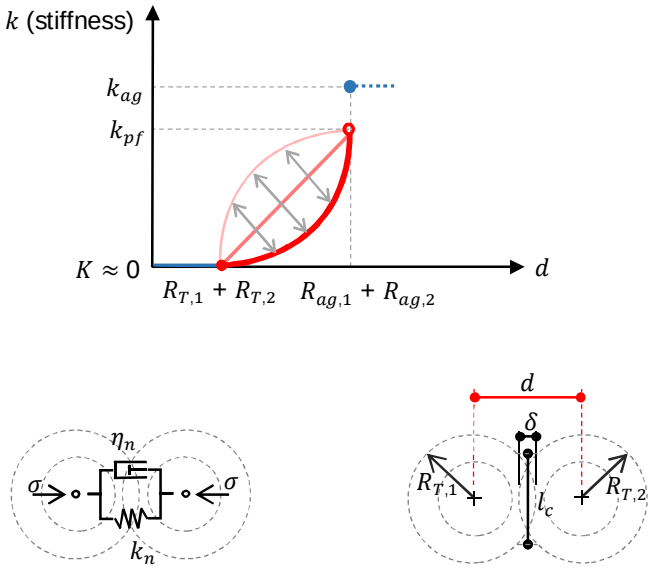

Figure 3.13 – Kelvin-Voigt rheology model for binder interaction.

It is assumed that no bending exists in this type of parallel arrangement. Consequently, the strain experienced by the spring is the same as that experienced by the dashpot. For each step, the strain 'ε' is calculated with Eq. 3.12 that relates the overlap 'δ' and the sum of the radius of the particles ($R_{T,i} + R_{T,j}$). The total stress 'σ' applied in the Kelvin-Voigt model due to the overlap is defined by Eq. 3.13, where k_n represents the elastic modulus of the spring, η_n represents the viscosity of the dashpot, t represents the load time and $\dot{\varepsilon}$ is the relative velocity between the particles in interaction. In this

sense, when a dashpot is used to simulate an interaction, the total stress is an approximation considering a dynamic solution.

$$\varepsilon(t) = \frac{\delta}{\left(R_{T,i} + R_{T,j}\right)} \tag{3.12}$$

$$\sigma = k_n \cdot \varepsilon(t) + \eta_n \cdot \dot{\varepsilon}(t) \tag{3.13}$$

The stiffness in terms of forces and displacement for each bar is calculated through Eq. 3.14, considering the stress 'σ', the strain 'ε', the effective contact area '$A_{ef,b}$' and the distance between the center of the particles 'd'. This rheology model may be adjusted depending on experimental analysis. The same model or a different one could be used to represent the behavior under tensile stress. If a change occurs in the verification function (Section 3.2.2), the modified matrix has to be re-calculated.

$$k_b = \frac{A_{ef,b} \cdot \sigma}{d \cdot \varepsilon(t)} = \frac{\left({}^{l_c}/_{2}\right)^2 \cdot \pi \cdot \sigma}{d \cdot \varepsilon(t)} \tag{3.14}$$

In Eq. 3.14, the contact area '$A_{ef,b}$' is estimated assuming a circle with the diameter equal to the contact length 'l_c'. In other words, the stiffness is related with the square of the contact length. However, in a purely 2D model it would seem more reasonable to use directly the contact length instead.

To understand why this was not assumed in the present study, consider a simplified example in which two spherical particles in a 3D medium are put in contact. Consider also a second set of spherical particles that are also put in contact but have half the diameter of the previous ones. If analogous conditions are assumed, it is evident that the contact area of the first set will be bigger than that of the second set. Since more area means more points to transmit forces, the total force transmitted in the interaction between particles will increase with the area. Consequently, the total force will be related with the square of the contact length, increasing with the square of the diameter of the particle. Now consider the same example in a 2D medium. In this case, the capacity to generate forces will be linearly related with the contact length and, hence, with the diameter of the particle.

This produces a contradiction once a model conceived purely to work in a 2D condition might not be representative of a 3D condition if different sizes of particles are simulated together. Such incongruence might be resolved by modifying the way the stiffness is calculated in 2D. In order to obtain representative results that could be used to

validate the method proposed, the stiffness should be calculated from the area of contact as shown in Eq. 3.14 since this reflects the situation found in practice.

The rheology models used to simulate the contact between particles have a time- and load-dependent behavior. Consequently, the results obtained with the method become highly dependent on the compaction procedure applied. Therefore, to simulate the compaction process properly, it is necessary to define a loading procedure that approaches the expected in practice. Moreover, it is also necessary to define sufficiently small time steps that assure the convergence and the consistency of the steps. The maximum time step possible will depend on the size of the model, the complexity of the interactions between particles and the rheology of the contact.

3.4.3. No Contact (or Virtual Contact) Simulation

The last possible contact (Fig. 3.10d) denotes a no contact situation that happens if the distance between particles *i* and *j* is bigger than or equal to the sum of their radius ($d \geq R_{T,i} + R_{T,j}$). The bars generated in this situation are only virtual and do not represent contact between the inner cores or the binders. In fact, they only contribute to the numerical stability of the model. Without this consideration, many analyses would not converge.

In Fig. 3.4f, bars that represent real contact are indicated in blue. With only these bars, the lattice layout obtained is statically unstable. In fact, it is not possible to solve the equations for the balance of forces in each time step. With the inclusion of the bars that simulate the virtual contact (in green in Fig. 3.4f), the lattice layout become statically stable and may be solved numerically. To minimize the interference in the results and to assure that relative displacements may occur, the virtual bars should have a stiffness several times lower than the bars that represent real contacts.

The low stiffness in the virtual contacts leads to axial forces several times smaller than the others types of contact. As a result, the bars that represent virtual contacts may present high deformation, allowing the big relative displacement observed during compaction and the rotation of one particle over the others.

During the compaction process, tensile stresses may arise between particles. In the present study, it is assumed that the bars that denote contacts subjected to tensile stress present no stiffness, being modeled as a ‘no contact’ material. Other considerations are also possible if necessary.

3.5. RESULTS

In order to evaluate the applicability of the model proposed, several analyses were conducted. All of them consider a rigid inner core involved by a dry binder layer. Results were obtained from the average of 50 simulations with similar characteristics. Such a high number of simulation were required to assure a representative assessment since the randomness of the aggregate grading and distribution produce small variations in the results.

A random law was used to generate the particle with different sizes. According to this, the diameter of particles ranged from 2.5 mm to 10 mm (10 % of 10 mm, 30 % of 7.5 mm, 40 % of 5 mm and 20 % of 2.5 mm). The mix consisted of 54% by volume of inner core and 19.5% by volume of binder, which led to an initial volumetric porosity of 26.5%. The thickness of the binder layer is considered proportional to the diameter of the inner core.

A sample of 60 x 60 mm supported laterally and at the bottom by the walls of a container was subjected to a compaction of 10 mm (compaction degree of 16.67 %) applied at a rate of 100 mm/min to all particles located at the upper boundary. The elastic modulus used for the spring and the viscosity of the dashpot in compression were $2x10^{-4}$ MPa, and $1.74x10^{-3}$ MPa.s, respectively.

Some parameters related to the compaction process should be defined beforehand for a better understanding of the results. The compaction degree (CD) may be represented by the ratio between the initial density and the density after a certain compaction, as shown in Eq. 3.15. In a bi-dimensional model, the density of the material is calculated through the division of its mass (M) and the volume occupied, which depends on the base length of the recipient (b) and the height of the sample (h). During the compaction, the variation of height relative to the initial condition is expressed by Δh.

$$Compaction\ Degree = \frac{\rho_i}{\rho_j} = \frac{\frac{M}{b \cdot h}}{\frac{M}{b \cdot (h - \Delta h)}} = 1 - \frac{\Delta h}{h} \tag{3.15}$$

The density of the sample was calculated through Eq. 3.16. In this equations, the only parameter that changes along the course of the compaction simulation is the total compacted thickness 'Δh'. The area occupied by the inner core 'A_{ag}', the area occupied by the binder 'A_{cp}', the density of the inner core 'ρ_{ag}', the density of the binder 'ρ_b', the sample initial length 'b' and the sample initial height 'h' remain constant.

$$Density = \frac{1}{b \cdot (h - \Delta h)} \cdot \left(A_{ag} \cdot \rho_{ag} + A_{cp} \cdot \rho_{cp}\right) \tag{3.16}$$

3.5.1 Types of Contact

An assessment of the different types of contact observed throughout the compaction process is performed. According with Pöschel and Schwager [145], the increase of the compaction degree should lead to an increase in the contact between particles. Consequently, an increase of the contact between inner cores and in the contact between the binders as well as a decrease of 'no contact' should happen.

Fig. 3.14a presents an area chart with the average proportion of the different types of contact depending on the compaction degree. As expected, in the initial step (compaction degree equal 0 %) almost 30 % of the bars were simulating contact between binders and the remaining 70 % comprised bars with 'no contact'.

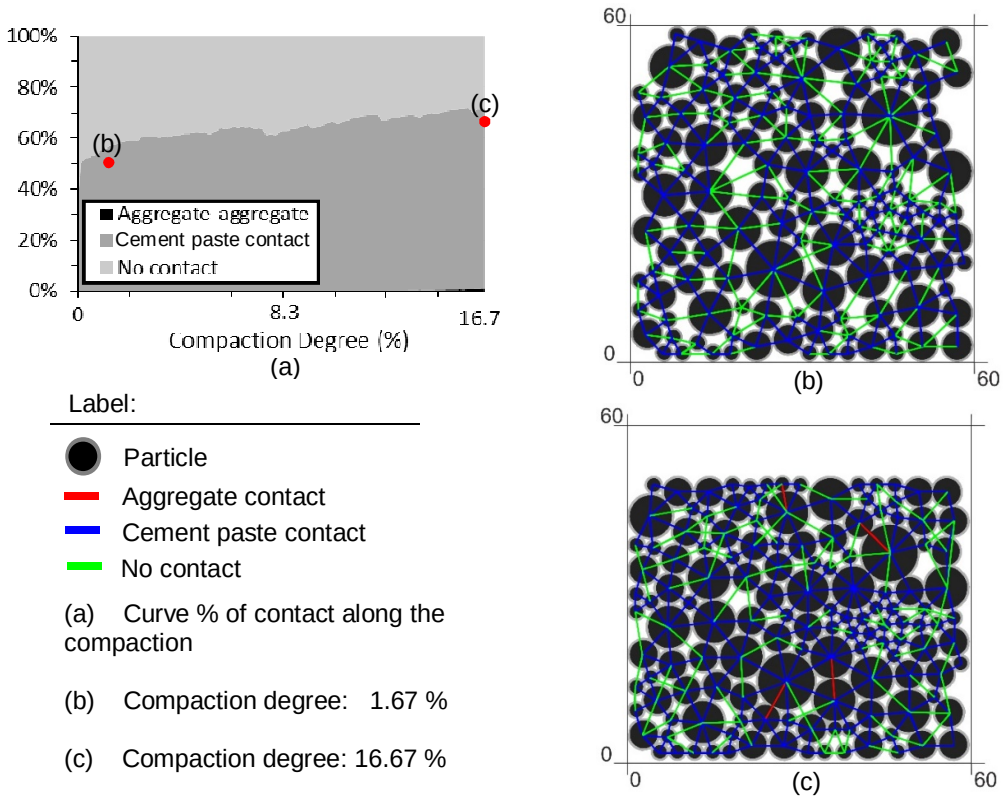

Figure 3.14 – Types of contact depending on the compaction degree.

However, in the final step (compaction degree equal 16.7 %) of this simulation, the 'no contact' decreased to 25 %, whereas the contact between binders increased to

72 %. The remaining 3 % represent inner core contact. Fig. 3.14b and 3.14c show the types of contact between particles for the compaction degrees of 1.67% and 16.67%, respectively. Again, it is evident that the increase in the compaction leads to the reduction on the number of green bars that represent a 'no contact'. On the contrary, the increase in the number bars that represent the real contact is observed.

3.5.2. Support Reactions

Another result to be considered is the support reaction on the walls and base of the container. When a pressure is applied on the top of a granular material, the reaction on the walls depends on the height and compactness of the sample. In fact, the reaction in the base (vertical) increases with the compaction pressures, whereas the wall reaction (horizontal) should increase with less intensity.

Fig. 3.15 presents two figures that illustrate this situation. The first of them (Fig. 3.15a) shows the ratio between the horizontal and the vertical reactions for different compaction degrees of all simulations. It is observed that the adjusted curve presents a negative slope, indicating that the average ratio goes from 0.69 to 0.57, approximately. This means that the sum of horizontal reaction is between 35% and 50% smaller than the sum of vertical reaction. It is worth mentioning that the ratio calculated between the horizontal and the vertical reactions is analogous to the coefficient of lateral pressure at rest (K_0) of a soil. Even though the material compacted may present special characteristics, the values obtained here are close to the typical K_0 considered for loose granular soil.

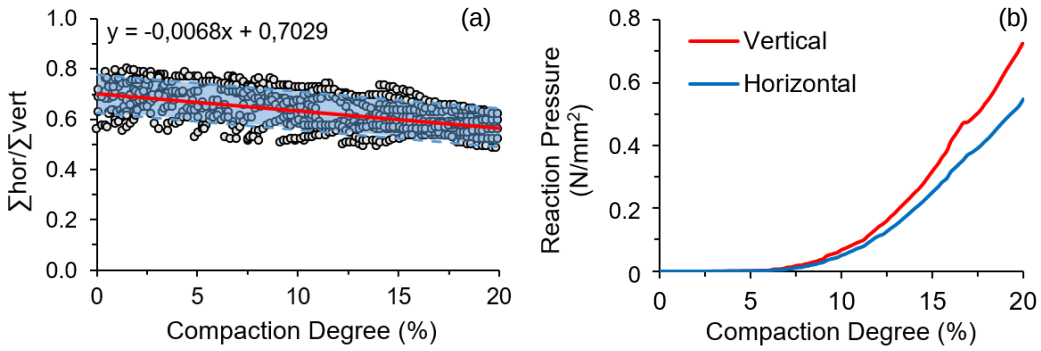

Figure 3.15 – Relation between the horizontal and vertical pressure with the compaction.

Fig. 3.15b correlates the vertical and horizontal reaction pressures with the compaction degree for one of the simulations performed. This figure helps to understand the behavior observed in Fig. 3.15a. It shows that both pressures increase with the

compaction degree. However, the rate of increase is bigger in the vertical direction due to a better connection between particles that favors the transmission of vertical loads.

3.6. NUMERICAL COMPARISON

Considering the lack of studies on the simulation of the compaction of pervious concrete, the results from Frenning [124] are used to validate the model proposed here. Even though binder is not present, the simulations performed by the author using a coupled Finite/Discrete Element Model assume the contact of deformable 3D particles. In theory, this deformation could be represented by the binder behavior considered in the model proposed here.

To calibrate the properties of the interaction, first a simulation of the contact of two particles is performed just like the described by Frenning [124] (see Fig. 3.16a). The two particles are spheres with diameters equal to 1 mm, density of 1.5 g/cm^3, Young's modulus of 250 kPa and zero Poisson's ratio. They were enclosed in a rectangular container that restrained the lateral motion while a relative displacement of 0.01 mm/ms is applied, which is the same as applied in the simulations by Frenning [124]. Time steps of 10^{-5} s were used to assure the convergence of the iterations. Fig. 3.16b shows the force applied and the total relative displacement. It is important to remark that all simulations with the model developed here were performed in equivalent 2D configuration.

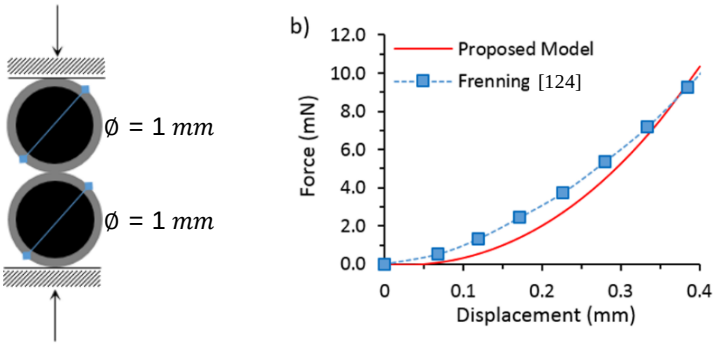

Figure 3.16 – Representation (a) and behavior (b) of the contact between two particles.

The results from the simplified model fit well the obtained from the literature, showing a correlation coefficient (R^2) of 0.974 with the latter. For that, the damper without coefficient and elastic modulus of 0.08 MPa were used as input parameters for the Kelvin-Voigt model. Once the contact parameters were calibrated, the analysis of a granular media was performed. Such analysis was originally conducted by Frenning [124] for a granular media composed by spherical particles randomly disposed in a cubic

container of 17.3 mm of side. The grading of the particles considered by the author is summarized in Tab. 3.2.

Table 3.2 – Grading and properties of the particles simulated by Frenning [124].

Diameter (mm)	Amount (%)
1.8	28.6
1.9	42.8
2.0	28.6

Fig. 3.17 presents the results of the compaction simulation for the granular media. A very good fit is obtained between the simplified model and the model by Frenning [124]. The comparison of the results for equivalent displacements shows a correlation coefficient (R^2) of 0.99. Notice that the results of Frenning [124] were validated with the obtained by Hassanpour [146]. The latter used a DEM with the contact law based on the model of Herzt for initial contact. When the force exceeds the yield value, the contact law was changed to the model of Thornton and Ning [147]. Therefore, the new approach developed here seems to reproduce satisfactorily the results from other more complex models.

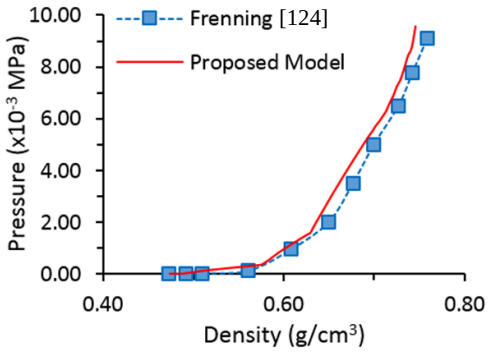

Figure 3.17 – Relation between density and compressive pressure.

3.7. EXPERIMENTAL COMPARISON

The experimental comparison is performed with pervious concrete, which is obtained by eliminating the finer fraction of sand from the composition and by reducing the water-to-cement ratio until a very dry paste is achieved. As a result, the aggregates become involved by the cement paste that has a sufficiently high viscosity not to flow. The material obtained after compaction is porous with interconnected macro voids (see Fig. 3.18a).

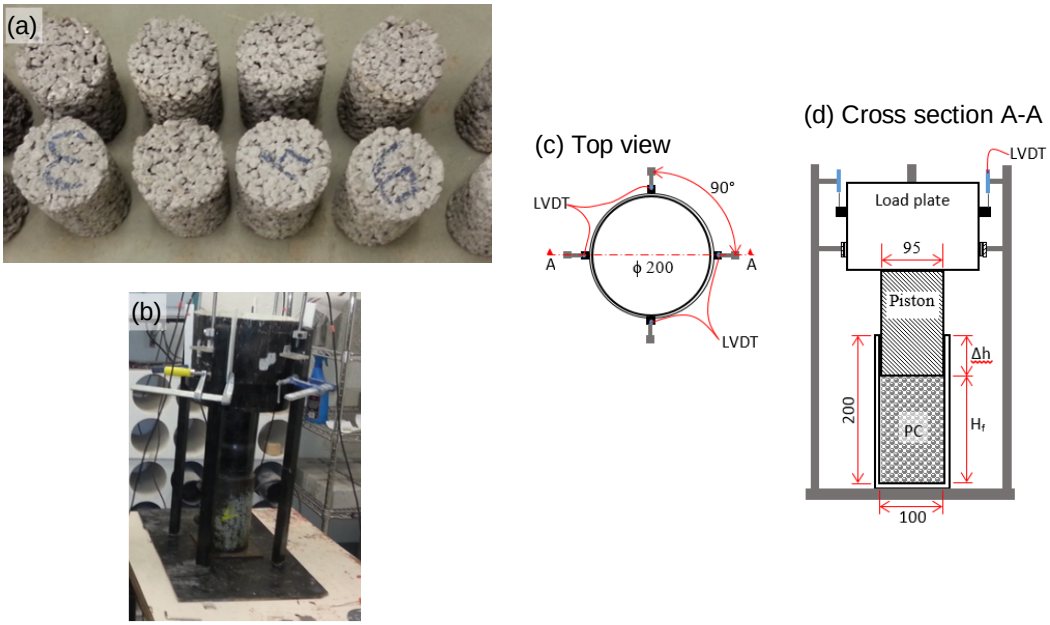

Figure 3.18 – Pervious concrete specimens in hardened state (a) and test setup for compaction in the fresh non-hardened state (b, c and d).

To evaluate the compaction process of pervious concrete, the testing equipment shown in Fig. 3.18b, 3.18c and 3.18d was used. It is composed by an external support frame that holds a piston that moves vertically. A recipient is placed just below the piston with the material to be tested. The piston is positioned over the sample and the load is manually increase by placing known weights at a plate located on the opposite side of the piston. After a weight is placed, enough time is waited for the displacement to stabilize before additional load is applied. This is necessary given that the cement past surrounding the aggregates has a viscoelastic behavior that induces a time dependent response. During the whole procedure, 4 displacement sensors measure the movement of the piston, which is used to assess the porosity and the compactness of the sample throughout the test.

Total loads of up to 80 kg were reached, leading to compactions of 6.5%. Higher load values were not applied for safety reasons and due to difficulties to keep the piston aligned with the supports. In the experimental program, two typical compositions of pervious concrete were tested with different cement contents and the same water-to-cement ratio (w/c) of 0.35. This way, the rheology of the cement paste is maintained while the thickness of the layer surrounding the aggregate is modified. Consequently, if the model proposed is working properly, the same input parameter should allow the simulation of the compaction curve of both compositions.

The composition PC-300 included 1400 kg of limestone aggregate (with specific density of 2.6 g/cm³) and 300 kg of cement (with specific density of 3.1 g/cm³), whereas

the PC-350 had 1400 kg of the same limestone aggregate and 350 kg of cement. The equivalent thickness of the cement paste layer in the compositions PC-300 and PC-350 are approximately 0.1189 times and 0.1363 times the radius of the aggregate, respectively. For each composition, a minimum of 8 samples were tested.

The recipient used in the test was always filled to the same initial height and the weight of the sample was measured before starting the test. With those measurements, the density and the proportion of the components, it is possible to estimate the initial density, the initial porosity and the variation of the compaction degree during the procedure.

Fig. 3.19a presents a typical curve that relates the displacement and the time for one of the tests. In this curve, two phases are observed. When the weight is applied, a fast displacement occurs (see Fig. 3.19b). After that, additional displacement is observed at much smaller rates, which decreases with time due to the viscous behavior of the contact between the cement paste layers. Fig. 3.19c and 3.19d show the final compaction curves obtained with the experimental tests related to the compositions PC-300 and PC-350, respectively. The average compaction reached in PC-300 is approximately 2.5%, whereas in PC-350 it was approximately 4.0% considering the compaction pressure equals 0.05 MPa. This difference is attributed to the bigger cement paste content in PC-350, which induces a thicker binder layer and higher deformability.

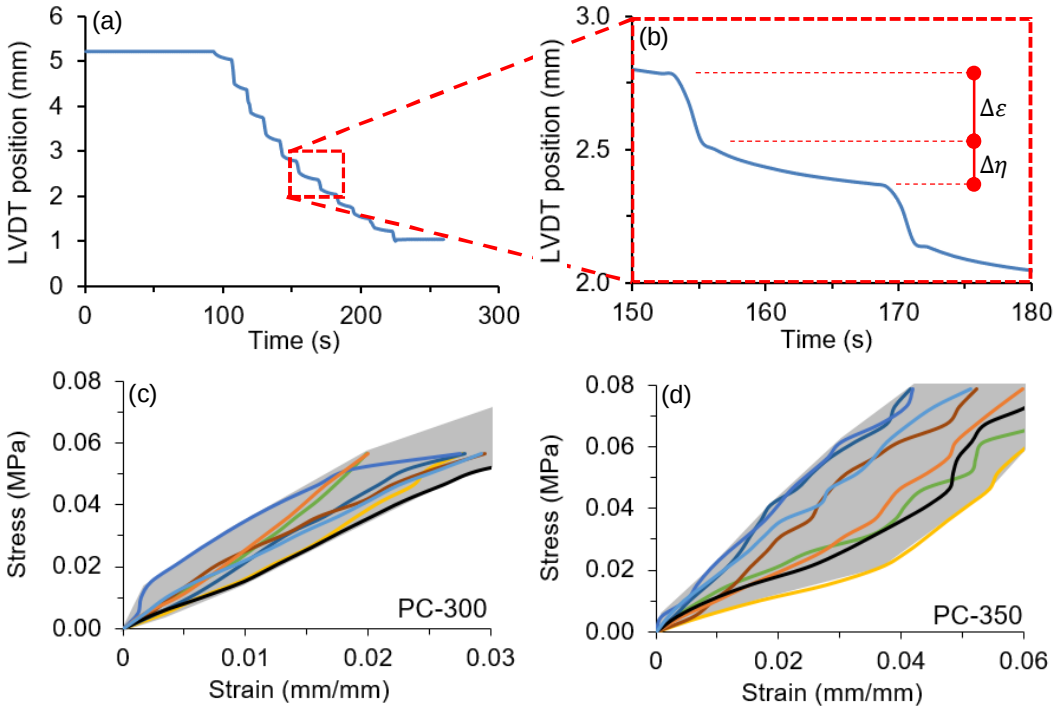

Figure 3.19 – Typical displacement-time curve (a and b), experimental curves for pervious concrete PC-300 (c) and PC-350 (d).

The average experimental result was used to validate the model developed here. The grading curve measured in the laboratory for the aggregate was used to define the proportion and the sizes of the particles introduced in the model. Based on that, the total volume of aggregate was divided in 18 % of particles with radius equals 4.66 mm, 35 % of particles with radius equals 6.3 mm and 47 % of the particles with radius equals 8.0 mm. The initial porosity assessed in the laboratory is taken as a reference for the definition of the initial particle distribution in the Stage 1, according with Section 3.2.1.

The elastic modulus (k_n) and the viscosity (η_n) of the cement paste were assumed 200 MPa and 200 MPa·s, respectively. The superficial stiffness (k_s) of the aggregate was set to 65 MPa/mm. The stiffness of the bars that represent the situation of no contact or virtual contact according with Section 3.4 was set to approximately $1x10^{-3}$ N/mm. The same parameters are used for the simulation of both pervious concrete tested, despite their differences in terms of the thickness of the cement past layer. The rate of displacement applied during the test was approximately the same as during the test. Time steps of 10^{-5} s were used in all analyses.

Fig. 3.20a and Fig. 3.20b show the comparison between the experimental results (in gray shade) of the composition PC-300 and PC-350, respectively, and the obtained by the numerical models N-300 and N-350, respectively. Despite considering the same input parameters, a good agreement is obtained for the whole extent of the experimental curves. This confirms that the model is capable of reproducing the compaction curves and the repercussions of changes in the composition of the pervious concrete.

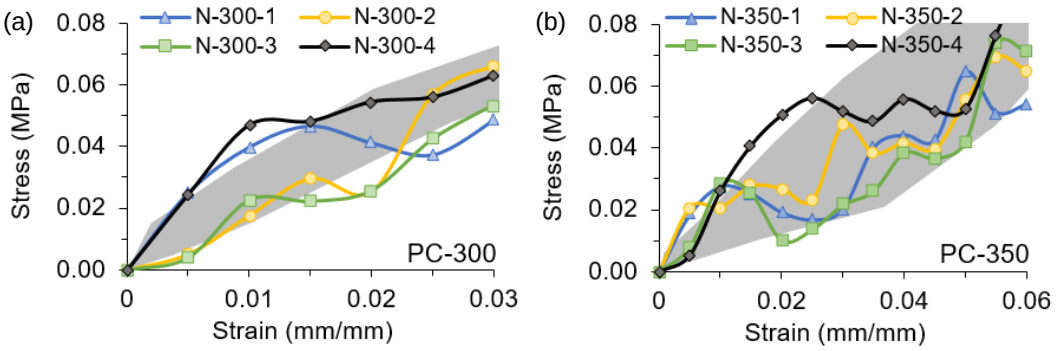

Figure 3.20 – Numerical curves for pervious concrete models N-300 (a) and N-350 (b).

3.8. CONCLUDING REMARKS

In this Chapter, a method for predicting the geometrical disposal of a granular media submitted to compaction was proposed, using an evolutionary lattice model. The method yields reasonable results and is suitable for a wide range of applications,

potentially requiring less computation effort than some of the existing methods from the literature. The following conclusions are derivate from the results.

- The change of the element type of the bars and the modification of the boundary conditions along the course of the steps represent well the movements of the particles. Furthermore, the proposal of an evolutionary lattice system that is redefined in each time step and admits internal instability has proven to allow the intensive rearrangement of particles expected in a poorly compacted medium. Finally, this method presents a possibility to correlate the compaction pressure with the porosity, density and the compacted thickness.
- The results from the simulation of a deformable granular medium show a good agreement with those obtained in the literature with more complex models (DEM or in combined FEM/DEM). Likewise, the numerical results estimated with the model developed here agree with those assessed during the experimental compaction process of two compositions of pervious concrete. Once again, this suggests that this method is capable of reproducing the behavior of a deformable granular medium subjected to compaction. In fact, it provides an alternative approach and a useful tool to the prediction of aspects such as the optimum compositions of the materials or the possible repercussions of modifications in the compaction process.

Despite the good results, more studies are required to assess the input parameters related with the contact between two particles by means of specific tests. This way it would be possible to estimate the stiffness of the spring and the viscosity of the dashpot more accurately.

4. 3D COMPACTION MODEL

4.1. INTRODUCTION

The traditional philosophy used to achieve a pervious concrete is to reduce the amount of fines provided by the sand and to use cement paste contents just enough to create a connection between coarse aggregates. The fresh state mixture obtained may be dissociated in several unities. Each unity is composed by an aggregate involved by a thin layer of very dry cement paste obtained by using low water-to-cement ratios or special thickening admixtures. The low fluidity achieved is a key point that helps to reduce the risk of segregation of the mixture.

The bulk material obtained after mixing usually has a porosity around 50 % by volume. On the other hand, values ranging from 15 % to 30 % are commonly found in the final application after the compaction process. It is evident that the compaction process plays a fundamental role on the performance of the material [53;148-149] since bigger porosities increase the drainage capacity but compromise the mechanical strength.

In general, the evaluation of the compaction process and of the final porosity of pervious cocnrete is performed experimentally through a trial and error approach. The assessment of the fresh state behavior of the material and the compaction process using numerical simulations is still a relatively unexplored field.

The discrete element method (DEM) is a powerful tool capable of simulating the movement and the interaction of a large number of particles found in granular materials. Particles are assumed as spherical bodies that may have contact with each other. Traditionally, a linear elastic contact approximation is used to simulate interactions, considering that an overlap is possible between two particles at the points of contact. This overlap generates forces of interaction governed by a constitutive law.

Several authors have simulated the fresh state behavior of concrete using DEM [54-59]. Despite the advances observed, it is important to remark that the great majority of the studies with DEM focuses on self-compacting concrete with a high fluidity and without accounting for external compaction or vibration. On the contrary, scarce information about the evaluation of the fresh state properties of pervious concrete may be found, especially regarding the simulation of the compaction process.

4.1.1. Objectives

In view of the exposed, the objectives of the study described in this chapter are the following:

- evaluate the influence of the aggregate to cement paste ratio and the grading of the aggregates over the compaction process of pervious concrete in fresh state;
- propose and validate a constitutive law (DEM based) to simulate the interaction of two particles (or aggregates) surrounded by a thin layer of cement paste in fresh state.

4.1.2. Outline of the Study

The experimental program related to the compaction process of the pervious concrete in fresh state is presented in Section 4.2. In this experimental program, 2 different types of aggregates and 4 aggregate-to-cement paste ratio. The results obtained with this experimental program were analyzed in Section 4.3.

A biphasic particle and a new constitutive law for the interactions between particles more representative with pervious are proposed and implemented in the open source framework YADE, as described in Section 4.4. The solution process is discussed in Section 4.5. In Section 4.6, the fit of the contact law with the experimental results from by Shyshko *et al* [61] is evaluated. In Section 4.7 the model is validated with the results from an experimental program. The compaction process described in this chapter provides the basis to the studies developed in Chapter 5 and Chapter 6 regarding the simulation of hydrological and mechanical behavior, respectively.

4.2. EXPERIMENTAL PROGRAM

This experimental program was performed to understand the influence of the aggregate-to-cement paste ratio and grading of the aggregates in the compaction process of fresh pervious concrete mixtures. For a better understand of the experimental program, it was divided into two phases. Phase I presents the studies regarding the effect of the aggregate / cement paste ratio. Phase II is centered on the effect of the grading of the aggregates. Tests were performed in the Laboratory of Technology of Structures Luis Agulló from the Univeristat Politècnica de Catalunya (UPC).

4.2.1. MATERIALS PROPERTIES

In Phase I, spherical glasses aggregates (see Fig. 4.1a) with diameter equal 18 ± 0.5 mm were used. In Phase II, crushed limestone was selected as aggregate. The crushed limestone aggregates were sieved to ensure that all the particles sizes were between 5 to 12 mm (see Fig. 4.1b) and 9 to 20 mm (see Fig. 4.1c). In order to maximize the porosity achieved, after the sieving process, the aggregates were washed to eliminate remaining limestone dust. The grading curves of the aggregates used in both phases are presented in Fig. 4.1d. The properties of the aggregates used in Phase I and II of the experimental program are presented in the Tab. 4.1. The cement used in both phases was CEM II/A-L 42.5 R.

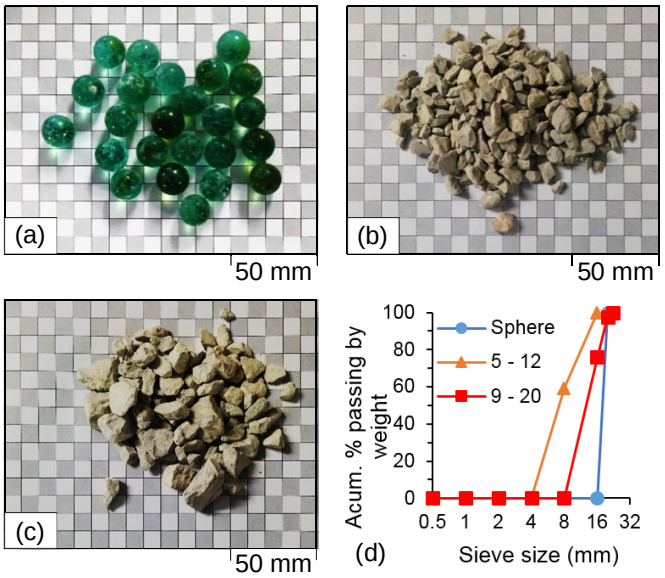

Figure 4.1 – Surficial aspect of spherical glasses (a), limestone with different grading (b-c) and the grading curves (d)

Table 4.1 – Properties of the aggregates.

Phase	Coarse Aggregate	Size (mm)	Density (kg/m^3)	Water absorption (%)	Shape
I	Glass	18	2570	-	Spherical
II	Limestone	5 to 12 9 to 20	2640	0.83	Polyhedral

4.2.2. Compositions

Phase I

The compositions used in this phase are summarized in the Tab. 4.2. For all compositions the content of spherical aggregates selected was fixed in 2300 kg/m^3. The main variable of the study related with the composition of the pervious concrete with spherical aggregates is the aggregate-to-cement paste ratio (A/P) by weight, which ranged from 3.63 and 4.17. These A/P are equivalent to the contents of cement ranging from 350 to 500 kg/m^3. According to the content of cement, the mixture compositions were divided in 4 families: G350, G400, G450 and G500. The water-to-cement ratio (w/c) employed was the same for all compositions in order to guarantee that the cement pastes obtained after mixing have similar rheology. Moreover, 1 % of retardant by cement weight was added in order to diminish variations in the fresh state properties of the concrete during the compaction of the several specimens that had to be produced for each mix.

Table 4.2 – Compositions.

Phase	Family	A/P	Aggregate (kg/m^3)	Cement (kg/m^3)	w/c	Retardant (kg/m^3)
I	G350	5.17	2300	350	0.27	3.5
	G400	4.53	2300	400	0.27	4.0
	G450	4.03	2300	450	0.27	4.5
	G500	3.63	2300	500	0.27	5.0
II	L400a	2.73	1400	400	0.27	4.0
	L400b	2.73	1400	400	0.27	4.0

Phase II

The compositions used in this phase are summarized in the two final lines of Tab. 4.2. The main variable is the grading of the crushed limestone aggregates. According to the grading of the aggregates, the mixture compositions were divided in 2 families: L400a and L400b. The former corresponds to the mixture composition where the grading curve 5 to 12 mm was used. The latter is related to the mixture composition where the grading

curve 9 to 20 was employed. For both mixture compositions, the content of aggregate, the content of cement and w/c ratio were fixed in 1400 kg/m³, 400 kg/m³ and 0.27, respectively. The amount of water to correct the absorption of the crushed limestone aggregate was added to the w/c. Also, 1 % of retardant by cement weight was added.

4.2.3. Mixing Process

The pervious concrete was prepared in a planetary mortar mixer type 65/2 K-3, using 65 liters container. Paddle rotation and planetary speed were 150 and 40 rpm, respectively. First, cement and aggregates were mixed during 60 s. Then, 70 % of the total water was added and mixed during additional 30 s. Finally, the rest of the water and the retardant was added and mixed during additional 60 s.

Once the fresh pervious concrete was mixed, it was immediately placed into a cylindrical mold (with height equals to 200 mm and diameter equal to 100 mm) in three layers. After the mold were filled, the excess of material surpassing the top of the mold was removed to ensure that the initial height of all specimens were 200 mm. This removal was performed with care, so to avoid introducing compaction forces. The weight of each sample was measured to achieve comparable levels of fresh density.

4.2.4. Test Method

The press used in this study to access the compaction pressure curve was the "Ibertest Autotest-200/10" with a load cell of maximum 10 kN and 1 % of accuracy, operating in displacement controlled mode with a velocity equal to 3.33×10^{-4} m/s (20 mm/min). A compaction cylinder with dimensions 65 x Ø95 mm was fixed to the load cell at the top of the press, as depicted in Fig. 4.2. At the bottom of the press there is a piston that moves with constant velocity (20 mm/min) in the axial direction in order to compact the specimen. The specimen (mold filled with the pervious concrete in fresh state) was positioned between the piston and the compaction cylinder. A laser distance sensor was equipped on the mold wall, in order to measure the distance between the top of the mold and the bottom of the compaction cylinder. The data of the displacement and the load cell were transmitted to a data acquisition system ever 0.2 s. The test is stopped when the maximum load of 10 kN or the maximum displacement of 40 mm is reached.

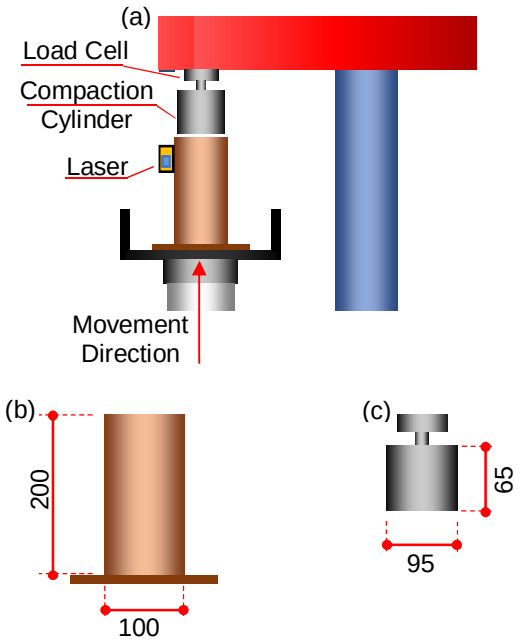

Figure 4.2 – Experimental setup (a), mold (b) and compaction cylinder (c) dimensions.

4.3. EXPERIMENTAL RESULTS AND DISCUSSION

4.3.1. Phase I

The initial mass and density of each specimen prior to the test are summarized in Tab. 4.3. The same table shows how long after mixing the test was performed and the number of spheres presented. Considering all the samples, the average mass was 2.01916 kg with a standard deviation of 0.0713.

During the compaction process, the specimen undergoes a sudden internal rearrangement due to the high sphericity, low roughness and mono size of the aggregates. The press identifies this phenomena as a rupture and stops the increment of the load as presented in Fig 4.3a. In order to avoid this problem, the results of the compaction obtained in this phase of the experimental program should pass through a first treatment process before the analysis. In this sense, only the points with an increment of stress were selected, as depicted in Fig 4.3b.

Table 4.3 – Mixture compositions.

Specimen	Age (min)	Mass (kg)	Density (kg/m^3)	Approx. # of spheres
G350-1	7	1.9150	1219.13	165
G350-2	10	2.0005	1273.56	172
G350-3	13	1.9880	1265.60	171
G350-4	16	1.9980	1271.97	172
G400-1	7	1.9860	1264.33	162
G400-2	10	1.9690	1253.50	161
G400-3	13	1.9380	1233.77	158
G400-4	16	1.9205	1222.63	157
G450-1	7	2.1375	1360.77	166
G450-2	10	2.1285	1355.05	165
G450-3	13	2.0250	1289.16	157
G450-4	16	2.0995	1336.58	162
G500-1	7	2.0505	1305.39	151
G500-2	10	2.0605	1311.76	152
G500-3	13	2.1235	1351.86	156
G500-4	16	1.9665	1251.91	145

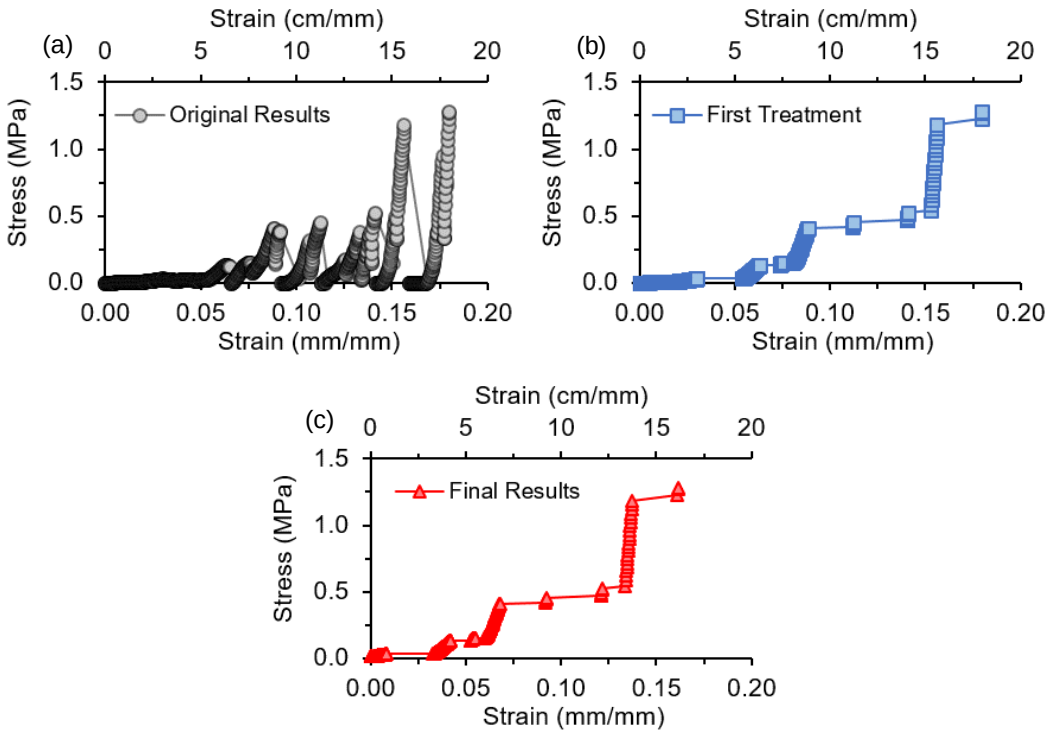

Figure 4.2 – Treatment process of the compaction experimental results.

The test starts with a low load and in order to homogenize the results, a minimum load was set. This minimum load characterizes the total contact between the surface of the compaction cylinder and the specimen, avoiding a localized contact. This was done by defining a minimum preload equal to 0.0127 MPa (1 % of the maximum load of the press), which coincides with the sensitivity of the press. Defined this, the point corresponding to the preload was moved to the coordinate axis, as depicted in Fig. 4.3c.

Despised the careful production of the specimen, the results of the compaction process show high scatter for specimen of the same family. The main cause of this scatter is related to the sudden internal rearrangement of the material, as explained. According to the results presented in the Fig. 4.4a, 4.4b, 4.4c and 4.4d (compaction curves of the specimens of the families G350, G400, G450 and G500, respectively), the scatter seams to reduce as the A/P reduces.

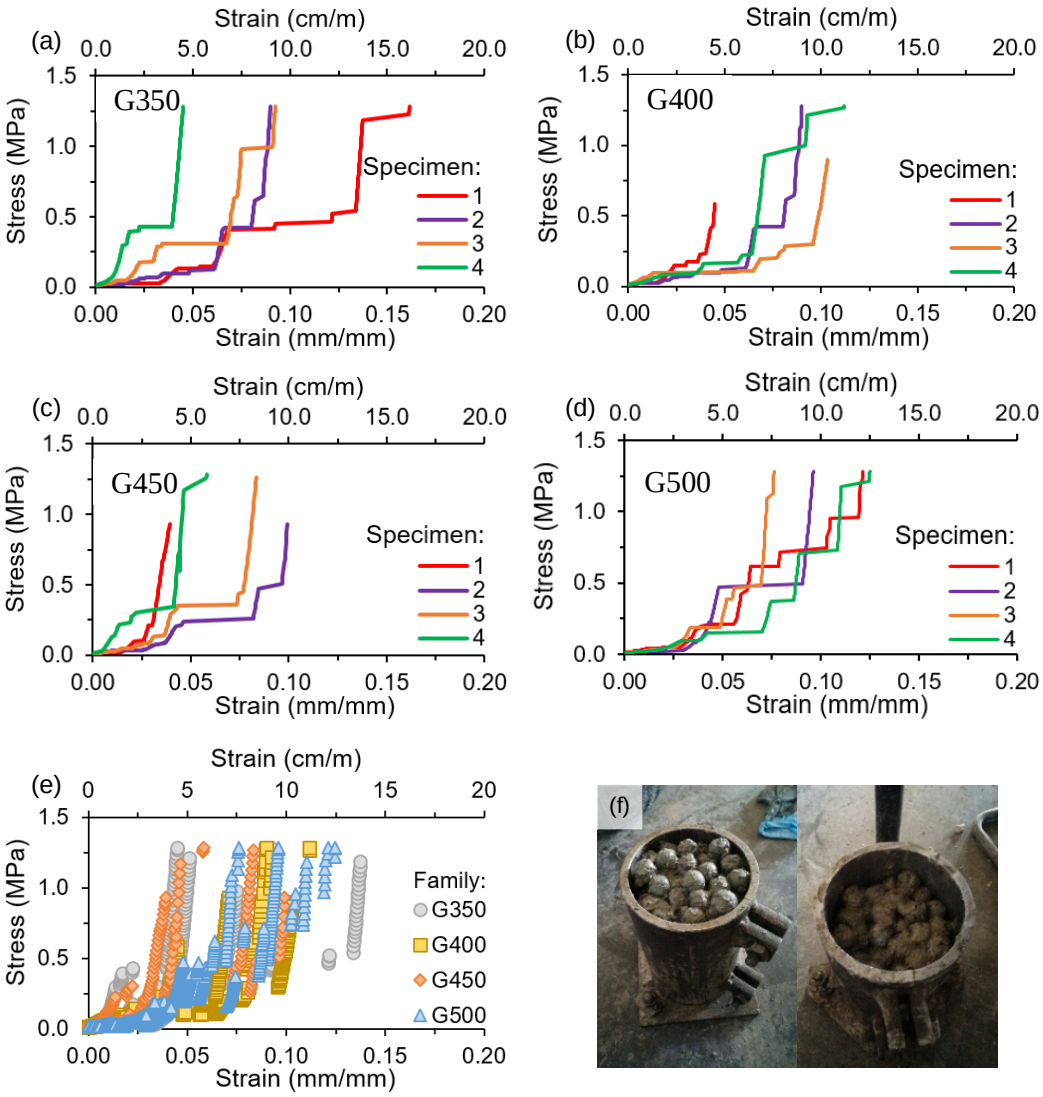

Figure 4.4 – Measured stress-strain curves (a to e) and test before and after photo (f).

This reduction is related to the increase of the distance between the aggregates and reduction of the number of contacts when the A/P is reduced. The dispersion of the results complicates the analysis of the relation between the A/P and the pressure necessary to increase the compaction of the material, as illustrate in Fig. 4.4e. Fig. 4.4f shows a picture of a specimen before and after the compaction procedure. For the A/P interval analyzed no clear difference between the compaction process of the different specimens was observed.

4.3.2. Phase II

In the case of limestone aggregate, the same abrupt changes which was observed in Phase I was not observed. This is possibly due to the irregular shape and surface roughness of these aggregates that are bigger than those of the spherical glasses. So it was not necessary to perform any correction in the curves, which are more continuous. However, the homogenization of the initial compaction pressure with a preload is still required. Fig. 4.5a and 4.5b present the final results of the families L400a and L400b, respectively. The figures show smaller scatter in comparison with those from Phase I (see Fig. 4.4).

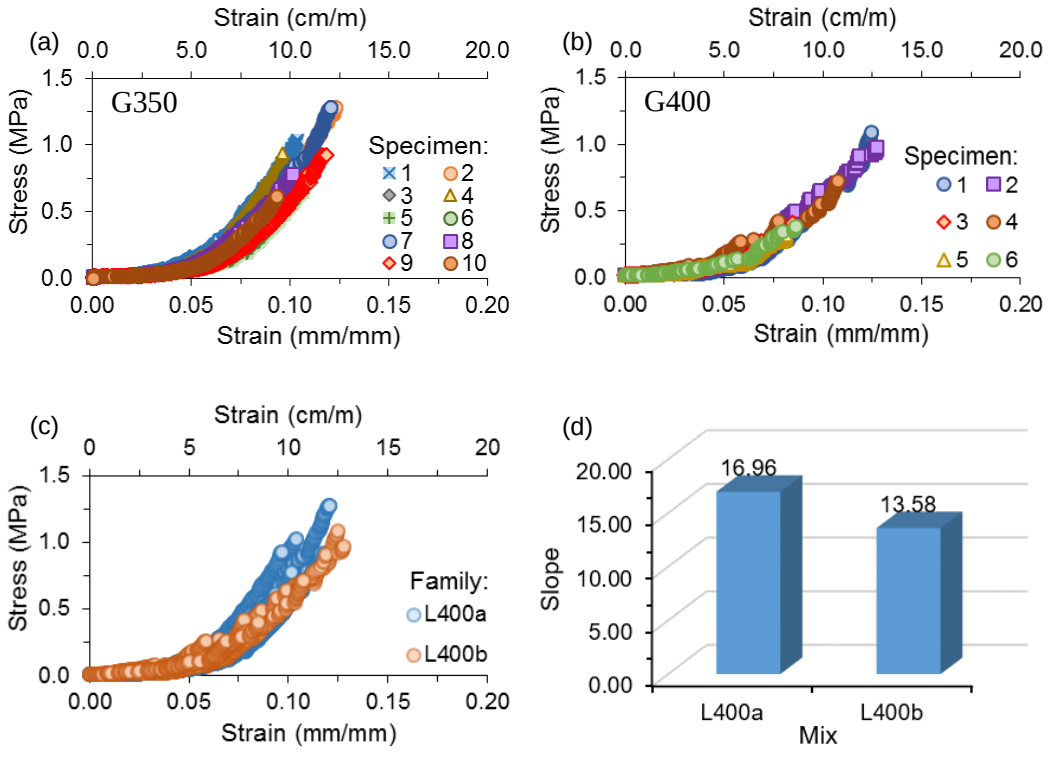

Figure 4.5 – Measured stress-strain curves of mixtures L400a and L400b.

Fig. 4.5c shows the stress – strain curves of all specimens tested from families L400a and L400b. The pressure necessary to compact the specimens from L400b is lower than the ones from L400a. This effect is related to the number of contacts between particles. Since the total volume of the mold is the same. When a smaller aggregate is used, more aggregates are necessary to fill the space. This generates a greater number of contacts between aggregates. By contrast, when an aggregate of bigger dimension is used, the number of aggregates necessary to fill this space decreases, also reducing the contact number. In other words, more contacts are observed when smaller particles are used. This increase of contacts difficults the internal rearrangement of the particles and more pressure is necessary to increase the compaction. Fig. 4.5d presents the difference between the slope of the final part of the curves L400a and L400b, which shed lights on the repercussion of the size of the particles on the evolution of the stress in compaction tests. A difference equals 20 % is observed, confirming the relationship between the aggregate size and the compaction energy.

4.4. PROPOSAL OF A CONSTITUTIVE MODEL

4.4.1. Characteristics of the Contact

In the DEM, the particles may interact with each other or with predefined surfaces such as the walls of the molds or of the formwork. The former is known as sphere-sphere (s-s) contact and the latter is known as sphere-wall (s-w) contact, both of which are governed by force-displacement laws.

Considering the definition of the particle discussed in Section 3.3, the first contact occurs with the viscous mortar or paste external layer surrounding the aggregate. As the overlap increases, the aggregates push the surrounding layer away from the point of contact, causing a lateral volume increase and the formation of a contact bridge (CB). A meniscus-like arrangement depicted in Fig. 4.6a appears and the mortar or paste thickness separating the aggregate cores or the aggregate core and the wall reduces. Once the initial thickness is consumed, a direct contact is established between aggregates or with the walls.

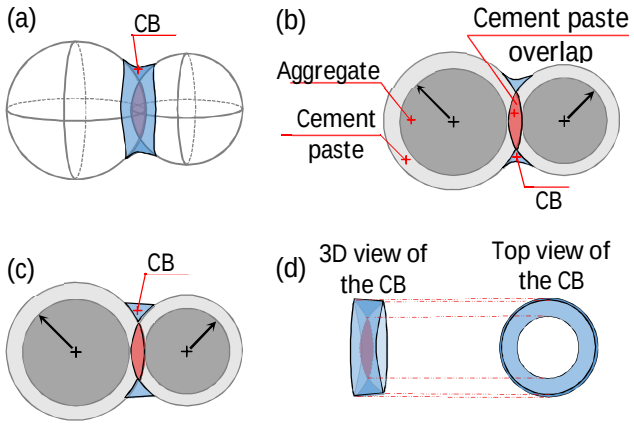

Figure 4.6 – Formation (a-b) and approximation (c-d) of the CB.

Although the exact simulation of the paste or mortar rearrangement around the aggregate may be performed, it comes with a high computational cost. To mitigate this drawback, the geometrical consideration illustrated in Fig. 4.6c and 4.6d was assumed. In line with the results obtained by Klein et al. [143], it is assumed the surface tension of very dry cement paste or mortar is close to 0, which leads to the formation of an almost straight meniscus. In this context, a straight linear average surface is considered a fair approximation of the real situation.

An important geometrical parameter of the contact is the overlapped volume. This is related with the force to produce an approximation of the particles. It is expected that the rearrangement of a bigger volume of paste would require the application of bigger forces. The overlapped volume of the S-S and S-W interactions may be obtained through Eq. 4.1 and 4.2, respectively. Notice that if the inner core of one sphere overlaps with external mortar layer of the other, the volume of the overlapped inner core must be discounted of the $V_{u,s-s}$ and $V_{u,s-w}$ obtained.

$$V_{u,s-s} = \frac{\pi \cdot u_i^t}{6} \cdot \left\{3 \cdot \left\{2 \cdot R_i \cdot \sin\left[\operatorname{acos}\left(\frac{R_i - u_i^t}{R_i}\right)\right]\right\}^2 + {u_i^t}^2\right\} + \frac{\pi \cdot u_j^t}{6} \cdot \left\{3 \cdot \left\{2 \cdot R_j \cdot \sin\left[\operatorname{acos}\left(\frac{R_j - u_j^t}{R_j}\right)\right]\right\}^2 + {u_j^t}^2\right\} \quad (4.1)$$

$$V_{u,s-w} = \frac{\pi \cdot u^t}{6} \cdot \left\{3 \cdot \left\{2 \cdot R \cdot \sin\left[\operatorname{acos}\left(\frac{R - u^t}{R}\right)\right]\right\}^2 + {u^t}^2\right\} \quad (4.2)$$

4.4.2. Material Model

In the DEM, the relative movement between particles or between particle and the wall might occur in the normal and in the tangential directions. Therefore, it is necessary to establish a rheological constitutive models that represents the behavior of the contact in both directions for the bi-phasic particle proposed.

Normal Direction

Studies from other authors [60-64] showed that the motion of the fresh pervious concrete in the normal direction has elastic and viscous components working simultaneously. The Kelvin-Voigt rheological model is generally used to represent this condition. This model is composed by an ideal spring arranged in parallel to a dashpot. The spring accounts for the elastic behavior of the mortar whereas the dashpot accounts for the effect of its viscosity.

Despite the widespread use, the Kelvin-Voigt rheological model induces some inconsistencies when applied to pervious concrete. Consider, for instance, two particles in contact at one point of their surrounding paste layer. When external forces are applied to approximate both particles, a rearrangement of the paste takes place around the contact point. If after a certain displacement the external forces are eliminated, the elastic part of the overlap is recovered whereas the inelastic part is maintained. The latter is the result of the viscous behavior of the dry paste that is not capable of assuming the original position once the forces are eliminated, leaving a permanent overlap.

Conversely, the Kelvin-Voigt rheological model does not allow permanent overlaps if subjected to the same loading procedure. Even though it may provide reasonable trends for the approximation stage, the same is not observed when the external loads are eliminated. The existing overlap generates an internal force induced by the spring. This force acts over the dumper connected in parallel, producing the gradual recovery of the overlap. Although this displacement reduces the overlap and the internal force of the spring, the remaining force leads to further displacement of the dumper. This process should continue until the force of the springs becomes 0, which will only occur when the whole overlap is recovered.

The behavior described in the previous paragraph highlights another underlying inconsistency of the Kelvin-Voigt rheological model when applied to pervious concrete. Notice that the recovery of the elastic part of the overlap is influenced by the dumper, which regulates the release of the spring. In other words, the recovery of the elastic overlap would not be instantaneous as expected in the case of a dry cement paste.

In order to solve these conceptual inconsistencies and reproduce with more accuracy the interaction between particles found in pervious concrete, the new contact model depicted in Fig. 4.7a is proposed. It is composed by a Kelvin-Voigt rheological model placed in line with a spring and a dumper, better known as Burger's model. In this case, the Kelvin-Voigt rheological model accounts for the unbalanced forces that might exist in the interaction once the applied force varies over time. On the other hand, the additional spring is responsible for the instantaneous elastic recovery and the additional dumper is responsible for the inelastic part of the overlap. A contact element is also included in the representation from Fig. 4.7a to account for the fact that, due to the dry nature of the cement paste, breakage of contact might occur when particles are separate by a certain distance.

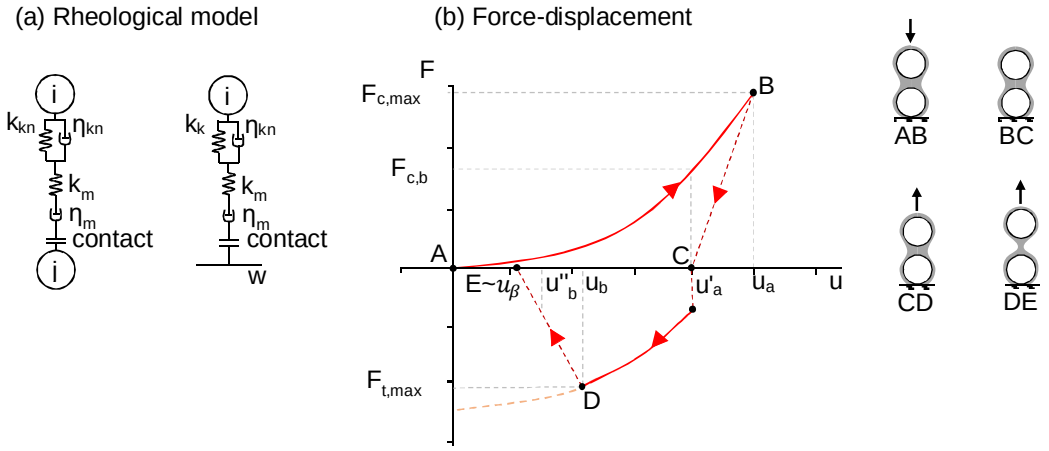

Figure 4.7 – Force-displacement constitutive law for an external layer contact in normal direction.

Suppose now that two particles are put in contact and an external normal force produces an overlap u with a velocity of penetration over time of $\dot{u}$. It is easy to demonstrate that, according with the rheological model of Fig. 4.7a, the internal normal force (F^t) generated in this contact may be calculated with Eq. 4.3. In this equation, Δu is the difference between the total overlap deformation (u^t) at time t and the total overlap deformation from the previous time step (u^{t-1}), u_K^{t-1} is the overlap corresponding to Kelvin-Voigt part of the model (defined by Eq. 4.4) and F^{t-1} is the force in the previous time step. The parameters A, B, C and D are defined in Eq. 4.5 to 4.8. k_{kn} and η_{kn} are the binder elastic coefficient and viscous coefficient for the Kelvin-Voigt part, respectively. k_{mn} is the binder elastic coefficient of the additional spring, whereas η_{mn} is the binder viscous coefficient for the additional dumber.

$$F^t = \frac{1}{A} \cdot \left[\Delta u + u_K^{t-1} \left(1 - \frac{B}{C} \right) - D \cdot F^{t-1} \right] \tag{4.3}$$

$$u_K^t = \frac{1}{C} \cdot \left[A \cdot u_K^{t-1} + \frac{\Delta t}{2 \cdot \eta_{kn}} \cdot (F^{t-1} + F^t) \right] \tag{4.4}$$

$$A = \frac{\Delta t}{2 \cdot \eta_{kn} \cdot B} + \frac{1}{k_{mn}} + \frac{\Delta t}{2 \cdot \eta_{mn}} \tag{4.5}$$

$$B = 1 - \frac{k_{kn} \cdot \Delta t}{2 \cdot \eta_{kn}} \tag{4.6}$$

$$C = 1 + \frac{k_{kn} \cdot \Delta t}{2 \cdot \eta_{kn}} \tag{4.7}$$

$$D = \frac{\Delta t}{2 \cdot \eta_{kn} \cdot B} - \frac{1}{k_{mn}} + \frac{\Delta t}{2 \cdot \eta_{mn}} \tag{4.8}$$

The stiffness of the springs and the viscosity of the dumpers should be closely related with the total volume of displaced paste at a certain time step ($V_{u,s-s}$ or $V_{u,s-w}$). It is reasonable to suppose that bigger overlapped volumes would imply higher values for these parameters given that any increment on the overlap would involve the displacement of a bigger paste volume. To simplify this consideration, it is assumed that the stiffness and the viscosity parameters may be obtained by multiplying the total overlapped volume and a base coefficient that depends solely on the rheological properties of the surrounding paste. This is represented mathematically in Eq. 4.9 to 4.12. The force-displacement curve obtained when compressive forces are applied in Eq. 4.3 is depicted as the curve AB in Fig. 4.7b.

$$k_{kn} = \begin{cases} \forall\ s-s\ : V_{u,s-s} \cdot B_{k,kn} \\ \forall\ s-w\ : V_{u,s-w} \cdot B_{k,kn} \end{cases} \tag{4.9}$$

$$\eta_{kn} = \begin{cases} \forall\ s-s\ : V_{u,s-s} \cdot B_{\eta,kn} \\ \forall\ s-w\ : V_{u,s-w} \cdot B_{\eta,kn} \end{cases} \tag{4.10}$$

$$k_{mn} = \begin{cases} \forall\ s-s : V_{u,s-s} \cdot B_{k,mn} \\ \forall\ s-w : V_{u,s-w} \cdot B_{k,mn} \end{cases} \tag{4.11}$$

$$\eta_{mn} = \begin{cases} \forall\ s-s : V_{u,s-s} \cdot B_{\eta,mn} \\ \forall\ s-w : V_{u,s-w} \cdot B_{\eta,mn} \end{cases} \quad (4.12)$$

The constitutive model proposed considers that the unloading path after an initial compression may be approximated through a straight line extending from the last point of the curve and a point in the x-axis defined by the product of the maximum displacement reached and a parameter α (curve BC in Fig. 4.7b). This parameter determines the level of inelastic deformation experienced by the contact, which will depend on the characteristics of the binder. An α equal to 0 indicates that all deformation is inelastic, not being recovered. On the contrary, for higher values of α, part of the deformation is recovered.

If tensile forces are applied after the unloading stage is finished, the paste layer should deform so that the particles would start to separate from each other, as depicted by curve CD in Fig. 4.7b. This separation takes place according with Eq. 4.3 until a yielding tensile force ($F_{t,max}$) is reached. Once this occurs, the paste starts to flow around the aggregates and a striction of the meniscus take place, causing an increase in the separation of the particles with a reduction of the tensile force applied (line DE in Fig. 4.7b).

The value of $F_{t,max}$ depends on the level of overlap and the load applied in the compressive stage ($F_{c,max}$). Higher absolute values of $F_{c,max}$ will lead to a bigger overlap and, consequently, bigger $F_{t,max}$. For that reason, Eq. 4.13 is proposed to estimate $F_{t,max}$. This equation considers that $F_{t,max}$ is obtained by multiplying $F_{c,max}$ by the proportionality constant ψ.

$$F_{t,max} = -\psi \cdot F_{c,max} \quad (4.13)$$

For the striction part of the diagram (CD), the stress-displacement relation is described as a straight line. This line starts at the point of $F_{t,max}$ occurs and extends over a distance that is proportional to the reduction of overlap ($u_b - u'_a$) experienced due to the tensile forces. The theoretical point u_β in which the striction curve crosses the x-axis is obtained by the Eq. 4.14.

$$u_\beta[0-1] = \frac{(0.8-\beta)\cdot u_b}{0.8} \quad (4.14)$$

Fig. 4.8a shows an example of the constitutive law obtained with α equal to 0, ψ equal to 0.5 and β equal to 0.8. Fig. 4.8b shows the evolution of forces over time. Fig. 4.8c presents the evolution of elastics (k_{kn} and k_{mn}) and viscous (η_{kn} and η_{mn}) coefficients over time.

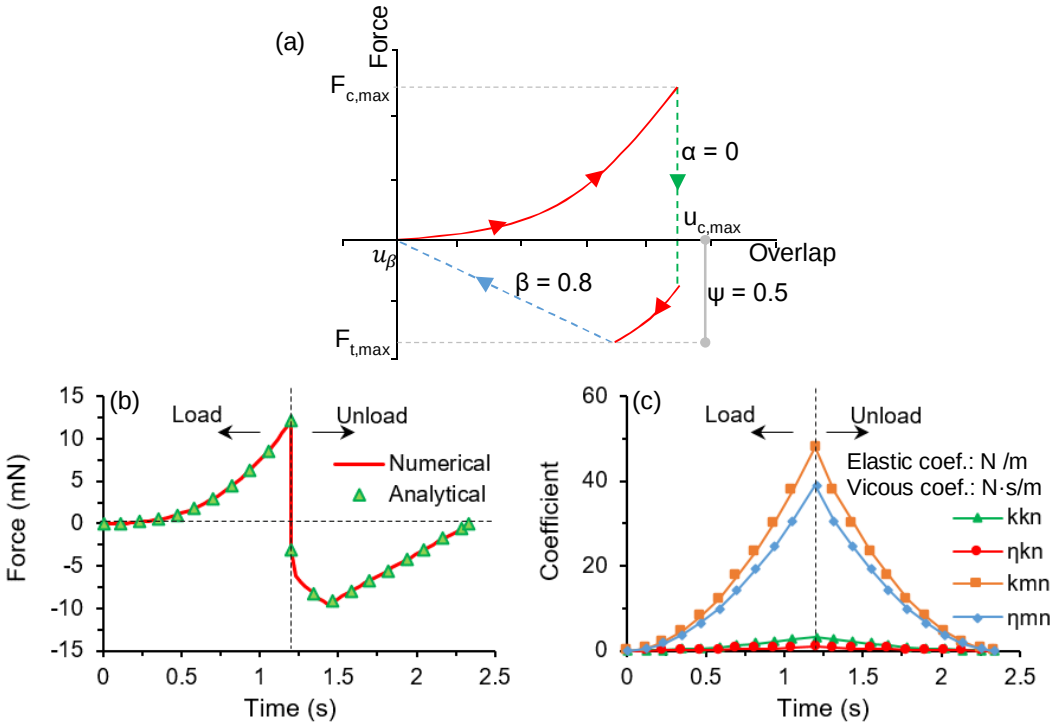

Figure 4.8 – Example of a force-displacement relation (a), variation of force (b) and coefficients (c) over time.

Another type of interaction occurs when the inner cores of the particles get in contact, this will happen whenever the overlap is bigger than the sum thickness of the external layer around the two particles. An analogues situation may also be found in the contact between a particle and then wall. With the overlap is bigger than the thickness of the external layer, a direct contact is establish between the two contacts. The rheological model used to represent both interactions is a spring in parallel with a contact element, as depicted in the Fig. 4.9a.

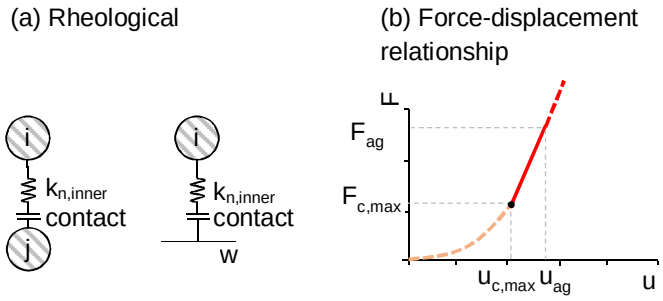

Figure 4.9 – Force-displacement relationship for a direct contact between the inner cores *in normal direction.*

The stiffness coefficient of the interaction in this case should be considerably bigger than that of the contact between the external layers. Fig. 4.9b shows an example of the complete force-overlap curve for two particles put in contact. It is assumed that the maximum overlap of the external layers (before the contact of the inner cores is establish) is equal to '$u_{c,max}$'. For overlaps bigger than this value, the direct contact between the inner cores take place. Eq. 4.15 represents this relationship for overlaps bigger than $u_{c,max}$.

$$F^t = F_{c,max} + k_{n,inner} \cdot \left(u^t - u_{c,max}\right) \tag{4.15}$$

Tangential Direction

The constitutive models presented so far depend only on the overlap in the normal direction. In fact, to determine the normal forces it is only necessary how the overlaps vary over time. In the case of the behavior in the tangential directions, a combined effect between the normal movement and tangential movement occurs. This is assumed because the tangential forces are affected by the normal forces acting in the contact.

The material model in the tangential direction selected is the Bingham-Hooke model, depicted in Fig 4.10a. The contact element, which is responsible to identify the contact between particles or particle and wall, in series with a Bingham-Hooke model is placed. The characteristic of the tangential motion is shear displacement in the corresponding time step, in contrast to the distance between entities in the case of normal direction. Fig. 4.10b shows schematically the force–displacement relationship for the interaction in the tangential direction.

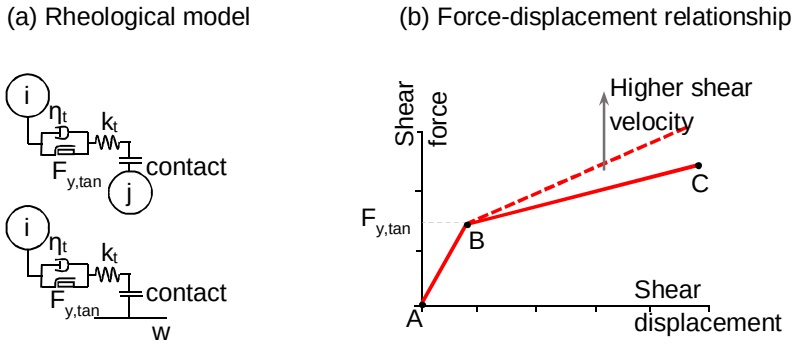

Figure 4.10 – Force-displacement relationship in tangential direction.

The resulting force of the tangential motion 'F_{tan}' consists of two components: elastic and viscous. The elastic component 'k_t' of the contact force is velocity-

independent and depends on the tangential displacement 'u_{tan}'. The viscous component 'η_t' of the contact force is velocity-dependent and proportional to the velocity '$\dot{u}_{tan}$' of tangential motion. The force-displacement relation contact may be divided into two parts according to the noticeable change in its inclination. The first part (represented in the Fig. 4.10b as the straight line AB) is elastic with small deformation, which represents the yield stress behavior. It is assumed that the deformation is small with a shear force that increases quickly, as expressed in the Eq. 4.16a. The tangential yield force '$F_{y,tan}$' is characterized as a 'slip-condition' (or 'shear cohesion'), that means the particles will move in the tangential direction more easily. The movement between particles in the tangential direction corresponds to the second part of the force–displacement relation (represented in the Fig. 4.10b as the straight line BC) and start after achieve tangential yield force value. The increase of the tangential force, presented in the second part of the force-displacement curve in Fig. 4.10b, is velocity dependent, as presented in the Eq. 4.16b.

$$\begin{cases} \forall\ F_{tan} < F_{y,tan} :\ F_{tan} = k_t \cdot u & \text{(4.16a)} \\ \forall\ F_{tan} \geq F_y \rightarrow\ F_{tan} = F_{y,tan} + \eta_t \cdot \dot{u}_{tan} - \dfrac{\eta_t}{k_t} \cdot \dot{u}_{tan} & \text{(4.16a)} \end{cases}$$

For simplification procedures, the k_t and η_t are related to harmonic averange of the elastics and viscous coeficients defined for the normal direction by the Eq. 4.17 and Eq. 4.18, respectively. Notice that it is very complicated to obtained the tangential force response from experimental results.

$$k_t = \frac{k_{kn} \cdot k_{mn}}{(k_{kn} + k_{mn}) \cdot (1 + \upsilon)} \tag{4.17}$$

$$\eta_t = \frac{\eta_{kn} \cdot \eta_{mn}}{(\eta_{kn} + \eta_{mn}) \cdot (1 + \upsilon)} \tag{4.18}$$

The force–displacement relation for tangential direction, also, includes two different types, one for the direct inner cores contact and another for the contact between the external layers. The difference between these two types consists in their different coefficients of friction, the friction between cores by direct contact and the internal friction in the cement paste layer.

4.5. SOLUTION PROCESS

The first step is modelling the geometry of the equipment and the molds. For instance, the following equipment and accessories should be modelled: the mold (Fig. 4.11a), the funnel (Fig. 4.11b) and the compaction plate (Fig. 4.11c). These elements should be modelled before the generation of particles of fresh pervious concrete. All parts of the equipment may be modelled using facet elements in YADE. The behavior of the facets in YADE depends on the following parameters: normal stiffness, shear stiffness, and coefficient of friction. The facet elements does not interact with each other; they interact only with particles.

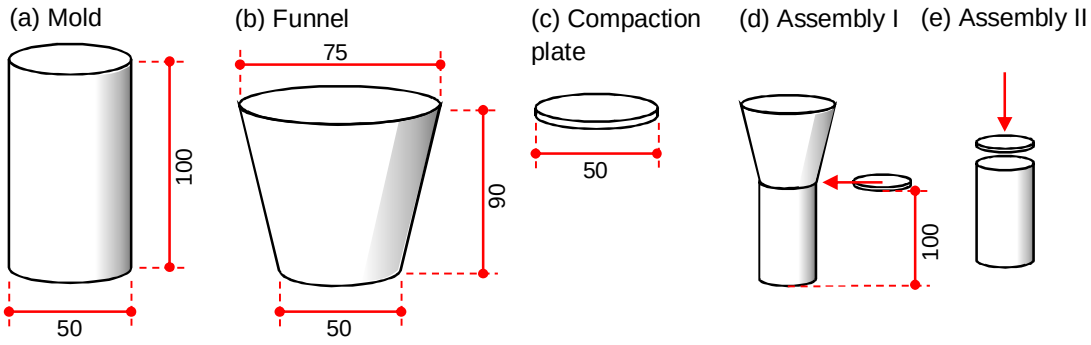

Figure 4.11 – Equipment.

At the first stage of the simulation, the mold and the funnel are assembled in each other. The mold is responsible to store the particles that represent the aggregates involved by cement paste. The funnel guarantees the correct position of all particles inside the mold during the falling process, as presented in Fig. 12a. This process simulates the gravitational deposition of the particles inside the mold. Once all particles are in a stable position inside the mold and the funnel, the compaction plate is generated and positioned according to the Fig. 11d. The compaction plate moves horizontally and is responsible to assure the separation between all particles above and below the height of the mold (see Fig. 12b).

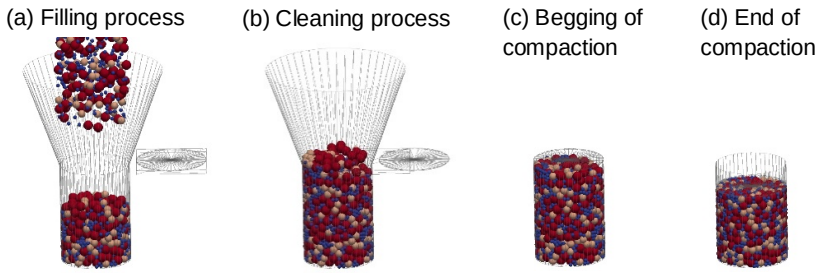

Figure 4.12 – Simulation process.

Then, the funnel and the particles above the compaction plate are erased, which guarantee that all models present the same height (100 mm). Just the particles inside the mold, the mold and the compaction plate are used in the next stage of the simulation, as presented in Fig. 11e and Fig.12c.. The compaction plate starts descend and compacting the particles. This last process will increase the number of interaction. Fig. 4.12c presents the sample with no compaction and Fig. 4.12d presents the sample at the end of the simulation.

Fig. 4.13 presents the flowchart step by step of the solution process. The procedures of calculation of the forces and displacements for each interaction is described in this figure. At the begging of each time step, the code detects all the entities with real interactions (both s-s and s-w interaction). The force and displacement is calculated for each interaction (by a pair of entities) separately. The centers and radius of the particles in contact are accessed. With the geometrical parameters of the entities, the zone of interaction is verified. This verification is performed to define if the interaction occurs in the external layer zone or in the inner core zone. Depending on the zone of contact, the material model (see Section 4.4.2) used to calculate the forces in the interaction is selected.

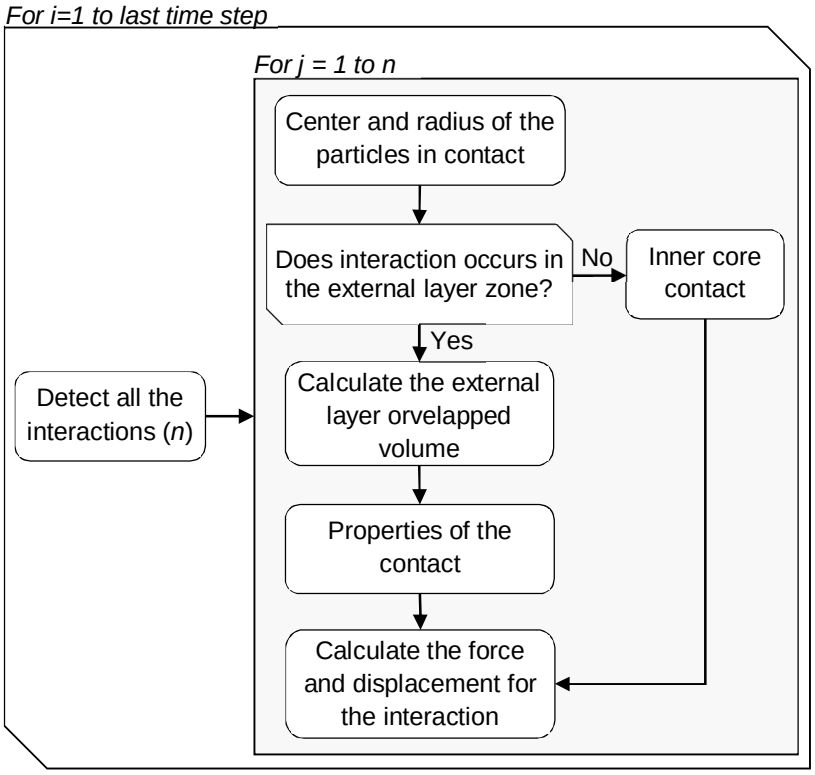

Figure 4.13 – Flowchart of the solution process.

In the case of the contact occurs in the external layer zone, the overlapped volume is calculated and the properties of the contact are assessed. Then, the forces and displacement of the entities is calculated. If the contact occurs in the inner core zone, the model represents the elastic contact and does not need the value of the overlapped volume. Thus, the properties of the contact are assessed immediately and the forces and displacement of the entities are calculated.

4.6. CALIBRATION WITH SHYSHKO *et al.* [61] RESULTS

The parameters (discussed in Section 4.4) related to the elastics and viscous components of the normal force need calibration. This calibration was performed with the experimental results presented by Shyshko *et al.* [61]. In this study [61], the normal interaction forces between two spheres (diameter equals 10 mm), with a viscoelastic material in the middle, was measured. The cement paste presents different rheological parameters over time (known as time-dependence). This complicates the tests, generating no comparable results. To mitigate this problem, the authors [61] used an aqueous solution made of Carbopol polymer. This solution was chosen because it presents a behavior according to the Bingham model and is not time-dependent. The Carbopol solution (concentration of 0.3 % by mass of water) had a viscosity of 4.9 Pa·s and a Yield stress of 42 Pa according to the Bingham model. In the case of "sphere - viscoelastic material - sphere" contact, the initial position of the spheres were in directed contact. The top of the bottom sphere was covered with the Carbopol solution. The test began with an increase of the distance between spheres from the initial position, until the complete rupture of the meniscus of Carbopol polymer was observed (tensile mode). Then, the authors decreased the distance between the spheres (compression mode), until the direct contact of the spheres was observed. Such experiments resulted in five force-displacement curves. The difference between the curves is related to the velocity of the approximation of the spheres.

In this Doctoral Thesis the simulations were compared with the experimental results using Carbopol solution (concentration of 0.3 % by mass) presented by Shyshko *et al.* [61]. The values of the parameters of the constitutive law obtained with the calibration are presented in Tab. 4.4.

Fig. 4.14 presents the comparison between the experimental results of Shyshko et al. [61] and the results obtained numerically with the proposed constitutive law. A good fit is obtained between the model and the experiments. The comparison of the results for equivalent displacements showed correlation coefficients (R2) of 0.975, 0.97, 0.936, 0.947 and 0.935 for the velocities 200, 100, 50, 20 and 10 mm/min, respectively. This confirms that the constitutive law proposed in this Doctoral Thesis is capable of

reproducing the interaction between two particles involved by a material that simulates the cement paste.

Table 4.4 – Values of the parameters of the constitutive law obtained with the pervious calibration.

Symbol	Value
α [-]	0
β [-]	1.333
ψ [-]	0.775
$B_{k,kn}$ [N/(m·m^3)]	5.50x10^6
$B_{\eta,kn}$ [N·s/(m·m^3)]	1.50x10^6
$B_{k,mn}$ [N/(m·m^3)]	8.00x10^7
$B_{\eta,mn}$ [N·s/(m·m^3)]	6.50x10^7

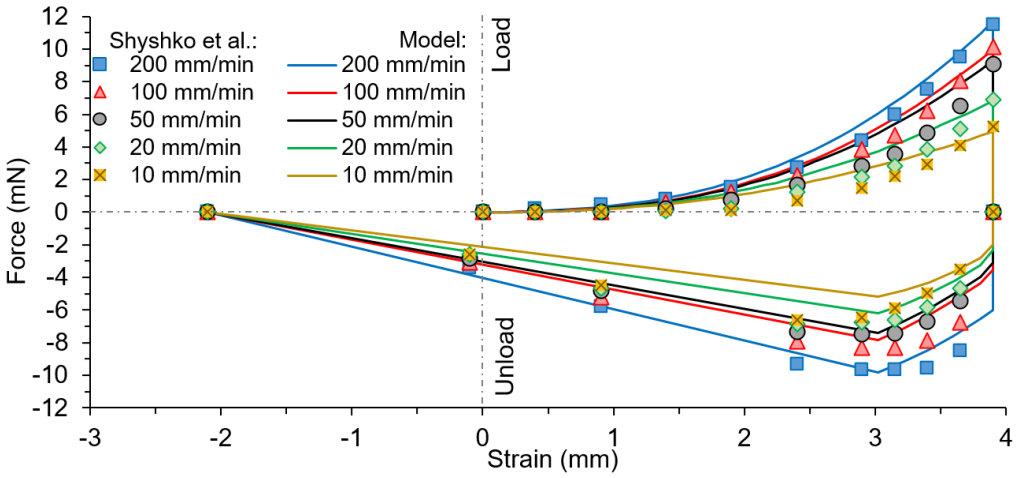

Figure 4.14 – Comparison of experimental results from [61] with the results obtained from the proposed model.

4.7. NUMERICAL SIMULATION

4.7.1. Phase I

The experiments presented in the Section 4.2 were simulated in order to assess the proposed constitutive law capability to simulate the behavior of pervious concrete in fresh state subjected to uniaxial compaction. It was assumed that base coefficients (elastics and viscous) with different rheology are proportional. In this sense, the input parameters defined in the Tab. 4.4 were multiplied by a proportional factor 'X' in order to simulate the cement paste used in the experimental program described in Section 4.2. The calibration of the parameters factor X, $\alpha_{fric,e}$, Yield, $k_{n,inner}$ and $\alpha_{fric,i}$ were performed with the experimental data obtained from the compaction of family G500. The values obtained in this calibration are summarized in Tab. 4.5. The values for the distribution of the cement paste (α_{eq}) were calculated analytically according to the procedure described in Section 3.3 The α_{eq} values used in the simulations for the models related to the families G350, G400, G450 and G500 are presented in Tab. 4.5. The parameters obtained with the calibration using G500 family were used to validate the results from families G350, G400 and G450.

Table 4.5 – Parameters used in the simulation.

Parameter		Value
External layer	X	1000
	$\alpha_{fric,e}$	0.6
	Yield	1.0×10^6
Inner core	$k_{n,inner}$	5.5×10^{10}
	$\alpha_{fric,i}$	0.25
G350	$\alpha_{eq,G350}$	0.0755
G400	$\alpha_{eq,G400}$	0.0854
G450	$\alpha_{eq,G450}$	0.0952
G500	$\alpha_{eq,G500}$	0.1048

Fig. 4.15a shows the comparison between experimental (in gray area) and numerical (in straight lines) macroscopic stress-strain curves. Overall, the proposed constitutive law predicts correctly the increase of the stress. The shape of the stress-strain curve obtained with the numerical results shows a first portion with a low rate of increase of stress, and the second part presents an abrupt increase in stress. The second part on some results is characterized by an oscillation in stress level. Despite the numerical results that simulate the different families presented a relatively different points of abrupt increase of stress (see Fig. 4.15b), the shapes of the curves are similar. The comparison

between experimental and numerical results showed good agreement. In particular, the model was capable of estimating the stress–strain behavior.

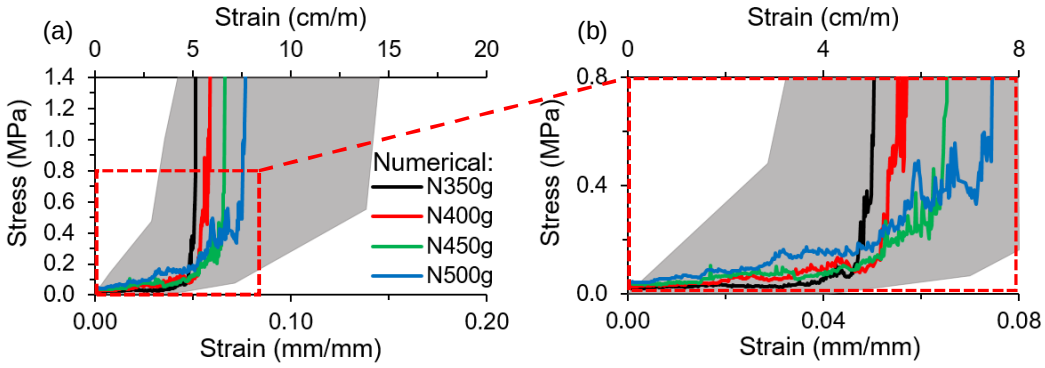

Figure 4.15 – Fresh pervious concrete with spherical aggregates under uniaxial compaction behavior, numerical and experimental comparison.

4.7.2. Phase II

This section presents the validation of the proposed model with the experimental results related to the specimens of the families L400a and L400b, and the study of how the grading of the aggregates affect the stress-strain behavior. The parameters used in these simulations were the same parameters used for the simulations presented in Phase I, with the exception of the friction between aggregates ($\alpha_{fric,i}$) that was changed to 0.75. The value calculated for α_{eq} was 0.1372. The grading curves measured in the laboratory for the aggregates were used to define the proportion and the sizes of the particles introduced in the models acordding to the procedure discussed in Section 3.3.

The shape of the stress-strain curve obtained with the numerical results for the tests L400a starts with a low stress increase rate, as presented in Fig. 4.16a. The second part of the curve shows a faster increase in stress, but no abrupt change was observed. Fig. 4.16a shows the comparison between experimental results of L400a (area in grey) and obtained by the numerical models N400a1, N400a2 and N400a3 (in straight lines). The numerical results for the L400b tests showed an oscillation in stress level. However, the variability in results between these stress-strain models were lower, as observed in Fig. 4.16b. Fig. 4.16b shows the strain-stress curve comparison between experimental L400b (area in grey) and the numerical models (N400b1, N400b2 and N400b3) results.

The difference observed on the results probably derive from the spherical shape of the particles considered as simplification in the numerical model. Notice that the parameters used in this simulations were calibrated with the experimental results with spherical glass as aggregates (G500). In this sense, the parameters does not consider the

corrections for irregular polyhedral shapes. Even without this consideration, the proposed constitutive law predicts well the increase of stress.

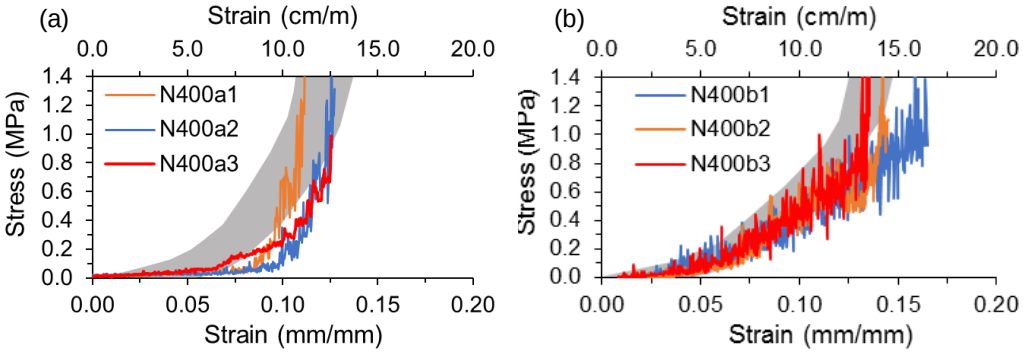

Figure 4.16 – Fresh pervious concrete with crushed limestone aggregates under uniaxial compaction behavior, numerical and experimental comparison.

4.8. COMPARISON WITH 2D MODEL PROPOSED IN CHAPTER 3

This section presets a comparison between the numerical and experimental results obtained in this chapter with the results obtained with the 2D Evolutionary Lattice model proposed in Chapter 3. The calibration of the parameters necessary to simulate the compaction with the model proposed in Chapter 3 were performed with the experimental and numerical results obtained from the compaction of family L400a. The elastic modulus (k_n) and the viscosity (η_n) of the cement paste were assumed 250 MPa and 200 MPa·s, respectively. The surficial stiffness (k_s) of the aggregate was set to 65 MPa/mm. The stiffness of the bars that represent the situation of no contact or virtual contact according with Section 3.3 was set to approximately $1x10^{-3}$ N/mm. The same parameters founded with this calibration were used to validate the results from family L400b. The value for α_{eq} used in both simulations was the same used in Section 4.7.2.The rate of displacement applied during the test was the same as during the test. Time steps of 10^{-5} s were used in all analyses.

Fig. 4.17a presents the numerical results (C3-400a) obtained with the model proposed in Chapter 3 that simulated the family L400a. The shape of the C3-400a curve is similar with the ones obtained with DEM (N400a1, N400a2 and N400a3). Fig. 4.17b shows the numerical results (C3-400b) obtained with the model proposed in Chapter 3, which simulated the family L400b. The C3-400b results presented less oscillation in the stress level than the ones obtained with DEM (N400b1, N400b2 and N400b3). The comparison between the results obtained in this chapter and the numerical results obtained with the 2D Evolutionary Lattice model (proposed in Chapter 3) presented agreement.

This confirms that 2D Evolutionary Lattice model is an alternative approach and useful tool to the estimation of aspects such as the optimum compositions of the materials. However, if more realistic estimations are necessary, the combinaiton of the proposed constitutive law (presented in Section 4.4) and DEM is a better option.

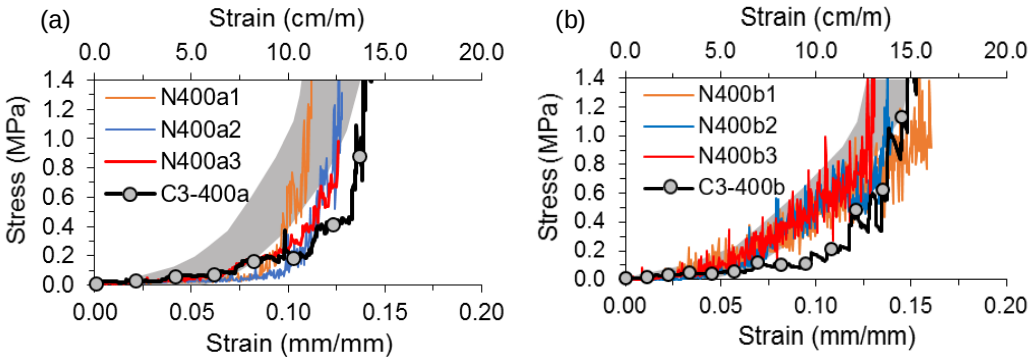

Figure 4.17 – Numerical comparison between the DEM model and the Evolutionary Lattice model.

4.9. CONCLUDING REMARKS

Chapter 4 presented the results of an experimental program and numerical simulations involving the compaction of pervious concrete in fresh state. The following conclusions are derived from the results.

- The experimental results of the compaction of pervious concrete produced with spherical aggregates showed that the studied range of A/P does not affect the compressive pressure necessary to increase the compaction.
- The experimental study of the compaction of pervious concrete in fresh state produced with crushed limestone in two different grading (5 to 12 mm and 9 to 20 mm) showed that lower pressure was necessary to compact the specimens with bigger size of particles. This phenomena is related to the number of contacts between aggregates, which is inversely proportional to the size of particles. In other words, there are more contacts when small particles are used. This increase of contacts difficult the internal rearrangement of the particles.
- The Kelvin-Voigt rheological model is generally used to represent the interaction between aggregates surrounded by cement paste in fresh state. However, the same induces some inconsistencies when applied to pervious concrete. This inconsistencies were mitigated with the proposed constitutive law.

- The proposed constitutive law reproduced the normal behavior of the contact between two identical spheres with a visco-elastic material in the middle (experiments conducted by Shyshko *et al.* [61]) with accuracy. The comparison of the numerical and experimental results for equivalent displacements showed a correlation coefficient (R^2) of 0.975, 0.97, 0.936, 0.947 and 0.935 for the velocities of approximation of 200, 100, 50, 20 and 10 mm/min, respectively.
- The simulations of the compaction process of pervious concrete in fresh state showed that the proposed constitutive law is capable of reproducing the behaviors observed when different grading curves were experimentally tested.
- The simplifications made in the constitutive law regarding the simulation of the cement paste as a thin layer around the aggregate and the simulation of the aggregates as spherical particles showed small differences when compared to the experimental results.

5. PERMEABILITY SIMULATION

5.1. INTRODUCTION

The Chapter 4 of this thesis showed that the numerical model in DEM with the proposed constitutive law reproduces well the behavior of the pervious concrete in fresh state. Nevertheless, the spatial disposal of the aggregates inside the meso-structural pervious concrete model was not properly validated. It is known that the pervious concrete contains a large number of internal voids, which are induced by the type and grading curve of the aggregate, aggregate / cement paste ratio, applied compaction, among others factors (see Section 2.2.4).

It is reasonable to assume that if the internal voids are represented correctly by the numerical model, then the spatial disposal of the aggregates is also predicted. Consequently, it is possible to indirectly validate the spatial disposal of the aggregates by the comparison of the permeability obtained by experimental tests and numerical simulations.

Therefore, further experimental test to measure the permeability of pervious concrete with controlled compaction is required. Moreover, simulations to predict the permeability of the meso-structural models obtained from the method proposed in Chapter 4 should be conducted.

5.1.1. Objectives

The main goal pursued in this chapter is to simulate numerically the hydrological behavior of pervious concrete. For that, the following specific objectives are defined:

- determine the factors that influence the permeability coefficient of the pervious concrete;
- propose an analytical model to evaluate the permeability coefficient of the pervious concrete, considering its mix design;
- propose a numerical procedure to predict the permeability of pervious concrete;
- validate the geometrical model generation (proposed in Chapter 4) with the comparison between experimental and numerical permeability results.

5.1.2. Outline of the Study

Initially, in Section 5.2, an experimental program is proposed to study the hydrological response of pervious concrete specimens with different compositions and degrees of compaction. In this section, the main properties of the material as well as the tests performed are described. In Section 5.3, the results obtained from tests are analyzed in terms of porosity, density and permeability.

In Section 5.4, the generation of the numerical models is discussed. In Section 5.5, the results provided by the model are compared with the experimental data in terms of porosity and permeability. Finally, in Section 5.6, the concluding remarks of this study are highlighted.

5.2. EXPERIMENTAL PROGRAM

This experimental program was performed to understand the influence of the content of cement paste and the degree of compaction in the water permeability coefficient. The production and the permeability characterization of the pervious concrete were performed at the Laboratory of Technology of Structures Luis Agulló (UPC). First, four pervious concrete compositions were defined and produced. The proportions used were selected in order to reproduce typical composition of pervious concrete. After the production, different degrees of compaction were applied by uniaxial compression. Finally, the porosity, density and permeability tests were conducted.

5.2.1. Materials and Methods

The compositions used in this study are summarized in the Tab. 5.1. Crushed limestone was selected as aggregate. The aggregates were sieved to ensure that all the particle size were between 5 to 12 mm. In order to maximize the porosity achieved, after the sieving process, the aggregates were washed to eliminate remaining limestone dust. Fig. 5.1a shows the surface aspect of the crushed limestone aggregates after the sieving and washing process. Fig. 5.1b shows the grading curve of the aggregate used. The density and the water absorption of the crushed limestone after the washing process were 2640 kg/m^3 and 0.83 %, respectively. For all mixtures compositions the content of aggregates selected was fixed in 1400 kg/m^3.

Table 5.1 – Compositions.

Family	Aggregate (kg/m^3)	Cement (kg/m^3)	w/c	Retardant (kg/m^3)	A/P	Degree of compaction (%)	Group
L300	1400	300	0.27	3.0	3.70	10	L300-10
L300	1400	300	0.27	3.0	3.70	15	L300-15
L300	1400	300	0.27	3.0	3.70	20	L300-20
L350	1400	350	0.27	3.5	3.12	10	L350-10
L350	1400	350	0.27	3.5	3.12	15	L350-15
L350	1400	350	0.27	3.5	3.12	20	L350-20
L400	1400	400	0.27	4.0	2.73	10	L400-10
L400	1400	400	0.27	4.0	2.73	15	L400-15
L400	1400	400	0.27	4.0	2.73	20	L400-20
L450	1400	450	0.27	4.5	2.42	10	L450-10
L450	1400	450	0.27	4.5	2.42	15	L450-15
L450	1400	450	0.27	4.5	2.42	20	L450-20

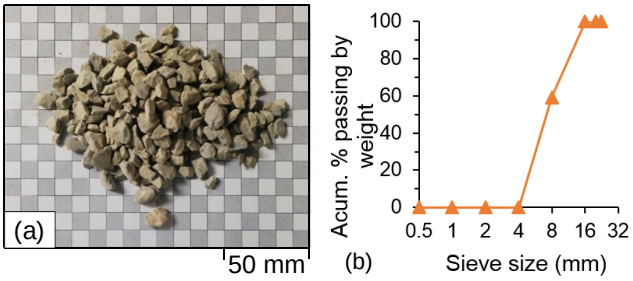

Figure 5.1 – Surface aspect (a) and the grading curve (b) of crushed of limestone.

The cement used was CEM II/A-L 42.5 R. The content of cement change in the range from 300 to 450 kg/m^3, increasing in intervals of 50 kg/m^3. According to the content of cement, the mixture compositions were divided in 4 families: L300, L350, L400 and L450. The water-to-cement ratio (w/c) used was the same for all compositions in order to guarantee that the cement pastes obtained after mixing have similar rheology. The amount of water to correct the absorption of the crushed limestone was added to the w/c. Moreover, 1 % of retardant by cement weight was added in order to diminish variations in the fresh state properties of the concrete during the compaction of the several specimens that had to be produced for each composition.

The main variable of the study related with the composition of the pervious concrete is the aggregate-to-cement paste ratio (A/P) by weight, which ranged from 2.42 and 3.70. This parameter affects the compaction process and may also have repercussion in the final permeability. In theory, for the same degree of compaction, a composition with bigger A/P should present smaller permeability.

The mixing process was the same for all mixes produced. First, aggregates and cement were mixed for 60 s. Then, 70 % of the content of water was added and mixed for 30 s more. Finally, the remaining water and the retardant were added and mixed during 60 s more.

The fresh pervious concrete obtained was immediately placed into a cylindrical mold (with height equal to 200 mm and diameter equal to 100 mm) in three layers. The excess of material surpassing the top of the mold was removed to ensure that the initial height of all specimens was 200 mm. This removal was performed with care, so to avoid introducing compaction forces. The weight of each sample was measured to achieve comparable levels of initial porosity in mixtures with the same A/P.

The second variable of the experimental program that holds close relation with the permeability is the compaction degree applied. In order to guarantee the homogeneity of the compaction in all specimens, the compaction was applied in a hydraulic press with 10 kN of nominal load capacity and with closed loop capability. Uniaxial compaction with displacement control was employed to achieve 3 degrees of compaction: 10, 15 and 20 % (see Tab. 5.1). For each family and degree of compaction, 10 specimens were produced. Notice that the mixing, casting and compaction process were performed according to the same procedure undertaken in the experimental program described in Section 4.2.3 and 4.2.4.

After the compaction process, specimens were wrapped in a plastic bag during the first 24 hours to ensure good curing conditions. Then, they were demolded and submerged in water until the age of testing.

5.2.2. Test Methods

In this section, the test methods included in the experimental program are described. The tests performed for pervious concrete were porosity and density (ASTM C1754 [19]) and permeability. Notice that the test of permeability does not follow any standard due to the lack of widely accepted testing procedures available in the scientific community.

Porosity and density

Before the test to determine porosity and density, specimens were extracted from the submerged curing and left to dry under laboratory conditions for 72 hours [25;34;150-151]. Then, the diameter, the height and the dry weight of the specimens were measured.

Subsequently, the specimens were submerged in water for 48 hours, until they were completely saturated. Finally, the hydrostatic weight of the specimens was measured using a hydrostatic balance. The porosity 'P' of each specimen was estimated using Eq. 5.1. The density D of each specimen was estimated using Eq. 5.2. In these equations, W_1 represents the dry weight, W_2 is the hydrostatic weight, $\emptyset_s$ is the diameter of the specimen, L_s represents the height of the specimen and ρ_w is the density of the water at 25ºC.

$$P = \left[1 - \frac{4 \cdot (W_1 - W_2)}{\rho_w \cdot \pi \cdot \emptyset_s^2 \cdot L_s}\right] \cdot 100 \tag{5.1}$$

$$D = \frac{4 \cdot W_1}{\pi \cdot \emptyset_s^2 \cdot L_s} \tag{5.2}$$

Permeability

The permeability is a property that describes how easily water can pass through the interconnected porosity of the pervious concrete. Two types of equipments are commonly used to measure the permeability of pervious concrete: falling head permeameter and constant head permeameter. Section 2.2.2 presents an explanation of both methods.

The constant head pemeameter was adopted here. This choice is better explained in Section 5.5. The principle of this method is to measure the amount of water that passes

through the specimen in a certain time interval. Based on the study by other authors other authors [27;36-39], the apparatus depicted in Fig. 5.2a was designed to perform this test.

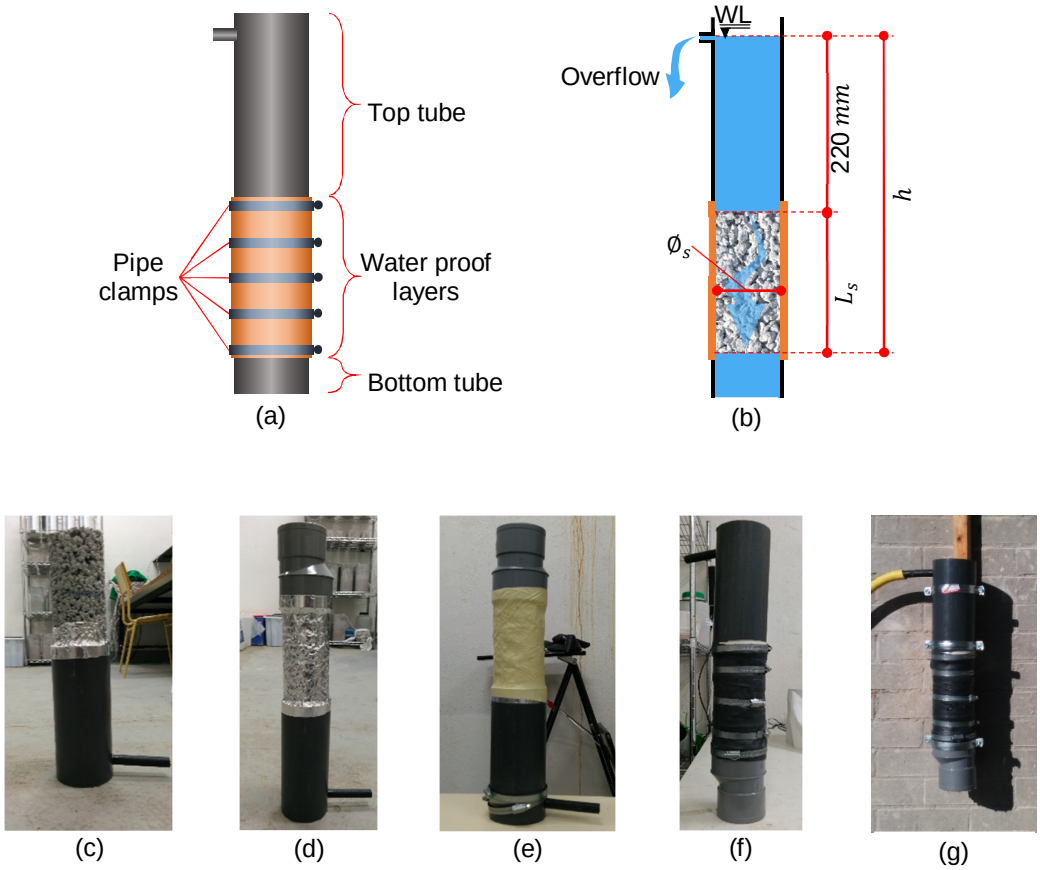

Figure 5.2 – Constant head permeameter scheme (a), cross section scheme (b) and assembly process (c-g).

For better understanding, Fig 5.2b shows a cross section scheme of the apparatus. It is composed by 3 parts: top tube, water proof layers and bottom tube. The top tube is placed above the specimen. It guarantees that the water level is maintained at 220 mm above its top face, this water level was defined in order to avoid the turbulent flow. The water proof layers are placed around the specimen to reduce the water flow along the side of the specimen during the test. Finally, the bottom tube is positioned bellow the specimen with an outlet to control the water flow.

The procedure used to assembly the test of the same for all specimens. First, the specimen was fixed in the middle of the two tubes using waterproof adhesive aluminum tape (Fig. 5.2c). The same waterproof adhesive aluminum tape was used to involve the specimen (Fig. 5.2d). Next, the specimen was wrapped with two layers of crepe-adhesive tape to protect the adhesive aluminum tape (Fig. 5.2e). A rubber sheet was used to involve

the specimen. It was fixed with at least five adjustable pipe clamps (Fig. 5.2f). Finally, the equipment was fixed on the wall to ensure the verticality and the test was ready to start (Fig. 5.2g).

Once the assembly procedure was completed, the end of the bottom tube was closed. Next, the volume of water necessary to fill the bottom tube and the pore spaces of the specimen was measured (q_1). Then, the apparatus was completely filled with water and the bottom tube was opened. Finally, the volume of water that passed through the specimen in 60 s was measured (q_2).

The permeability '*K*' was estimated using Darcy's law (Eq. 5.3). In this equation q is the difference between both measured volumes of water ($q_2 - q_1$), h is the distance between the bottom of the specimen and the water level (WL) and t is time interval (60 s).

$$K = \frac{4 \cdot q \cdot L_s}{\pi \cdot \emptyset_s^2 \cdot h \cdot t} \tag{5.3}$$

5.3. EXPERIMENTAL RESULTS

The results from the experimental program described in Section 5.2 are presented separately. Therefore, first the results of the porosity and density are analyzed. Finally, the results of the permeability are analyzed.

5.3.1. Porosity and Density

Fig. 5.3 gathers the relation between the experimental results of porosity in % and of density in kg/m^3 obtained for all specimens. In this figure, the results were plotted according to the correspondent Families: L300 (Fig. 5.3a), L350 (Fig. 5.3b), L400 (Fig. 5.3c) and L450 (Fig. 5.3d). The porosity ranges from 25 to 45 %, whereas the density ranges from 1400 to 1800 kg/m^3. These differences are attributed to the A/P and the degree of compaction applied. On one hand, the porosity decreases with lower values of A/P and with higher values of degree of compaction. On the other hand, the density decreases with higher values of A/P and with lower values of degree of compaction.

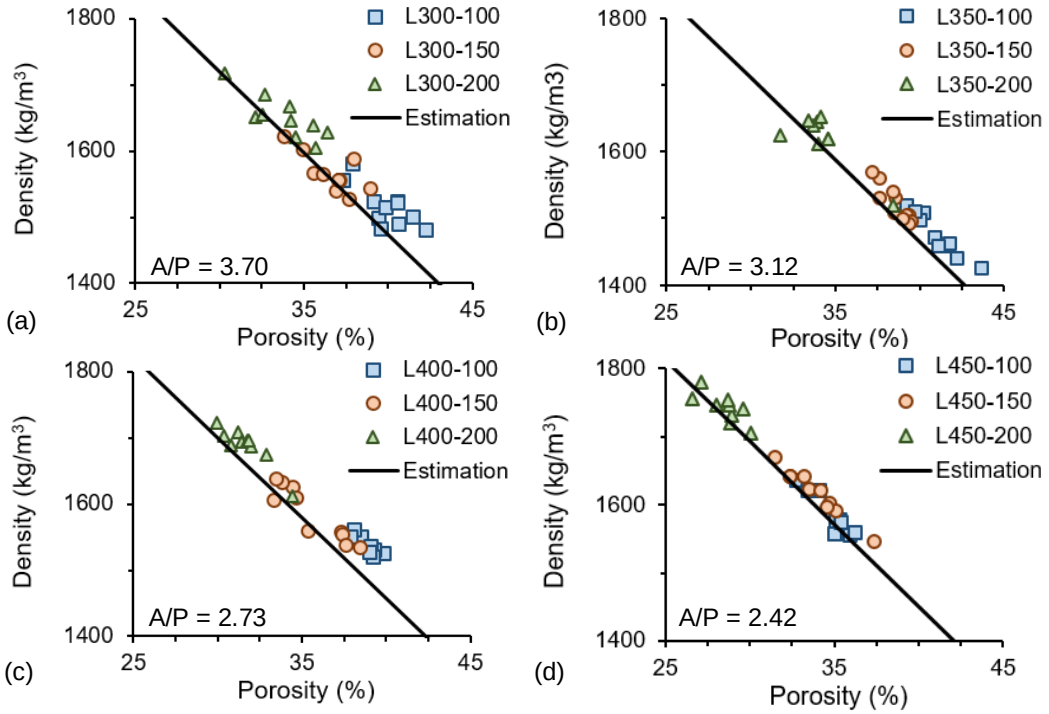

Figure 5.3 – Relationship between porosity and density for the mixes families L300 (a), L350 (b), L400 (c) and L450 (d).

An analytical model was developed to correlate the density with the porosity. Several simplifications were made to derive this model. The aggregate grading curve considered in the deduction of the analytical formulation was composed by spherical particles with the same size, as explained in Section 3.3. The cement paste involves perfectly the spherical aggregate with a layer of constant thickness. The estimated density ρ_{est} was obtained using Eq. 5.4. In this equation, R_{eq} is the equivalent radius of the aggregate grading curve, α_{eq} is a constant that consider the distribution of the cement paste and the A/P (based on studies by Klein [142] and Klein et al. [143] and explained in Section 3.3), ρ_{ag} is the density of the aggregate, ρ_{cp} is the density of the cement paste and P is the porosity of the pervious concrete (expressed in %). Fig. 5.3 presents the estimation density results obtained with the analytical model (Eq. 5.4) for all compositions. The comparison of the results for equivalent porosity shows an average correlation coefficient (R^2) of 0.966.

$$\rho_{est} = \frac{R_{eq}^3 \cdot \rho_{ag} + \left\{\left[R_{eq} \cdot \left(1 + \alpha_{eq}\right)\right]^3 - R_{eq}^3\right\} \cdot \rho_{cp}}{\left[R_{eq} \cdot \left(1 + \alpha_{eq}\right)\right]^3} \cdot \left(1 - \frac{P}{100}\right) \qquad (5.4)$$

Fig. 5.4 shows the evolution of the porosity related to the A/P and the degree of compaction. Fig. 5.4a was composed with the average porosity obtained with the experimental results. In this figure, the influence of the composition over the porosity is better illustrated.

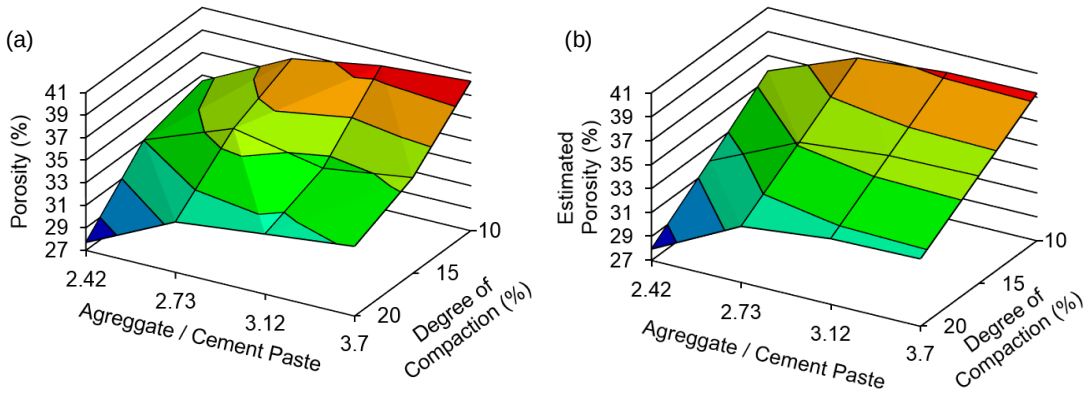

Figure 5.4 – Relationship between A/P, degree of compaction and porosity: experimental results (a) and estimated results (b).

With the porosities of all the experimental results, a regression to obtain the estimated porosity using 2 independent variables (A/P and degree of compaction) was performed. In this sense, the estimated porosity P_{est} is calculated by Eq. 5.5. In this equation, DoC is the degree of compaction.

$$P_{est} = 46.1 \cdot DoC^{\left(-5353.5 \cdot A/P^{-13.5}\right)} - 0.67 \cdot DoC \quad (5.5)$$

Fig. 5.4b was composed using the estimated porosity values obtained with Eq. 5.5. A good fit is obtained between the estimation and the experiments. The comparison of the results for equivalent A/P and degree of compaction shows a correlation coefficient (R^2) of 0.907.

5.3.2. Permeability

The relation between porosity and permeability for all specimens are presented in Fig. 5.5a. The permeability varies from 5 to 30 mm/s, increasing exponentially with the porosity, as discussed in the Section 2.2.2. However, there is not a notable variability related to the effect of the A/P.

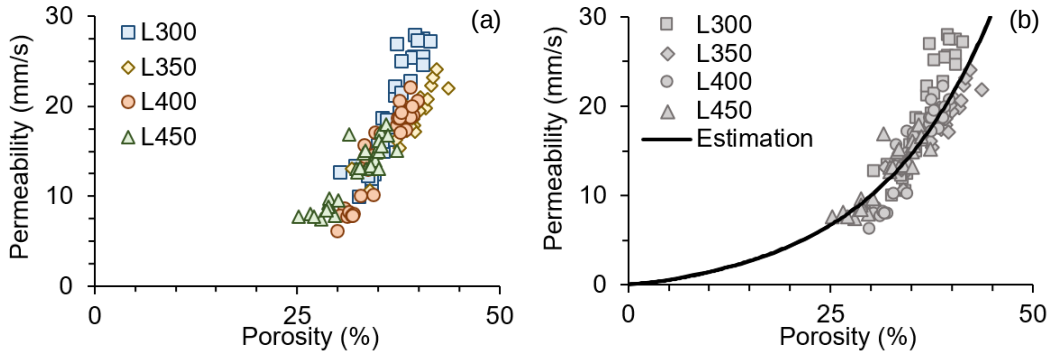

Figure 5.5 – Relationship between porosity and permeability.

Moreover, it is assumed that the porosity influences directly the permeability and studied parameters (A/P and degree of compaction) have an indirectly influence. In this sense, the nonlinear regression was performed using the porosity as independent variable to obtain the permeability. The final equation to find the estimated permeability K_{est} is presented in Eq. 5.6.

$$K_{est} = 1.50 \cdot (e^{0.068 \cdot P} - 1) \quad (5.6)$$

Fig. 5.5b presents the estimated permeability values obtained with Eq. 5.6. A good fit is obtained between the estimation and the experiments. The comparison of the results for equivalent porosity shows a correlation coefficient (R^2) of 0.873.

Although the proposed relationship between porosity and permeability of the specimens of different families presents a good fit, the adjustment is improved when the porosity (that depends of the composition) is calculated with Eq. 5.5. In this sense, Fig. 5.6 presents the experimental results of permeability related with A/P and degree of compaction compared with the estimations given by Eq. 5.5 and Eq. 5.6. A good fit is obtained between the estimation and the experiments. The comparison of the results for equivalent A/P and degree of compaction shows a correlation coefficient (R^2) of 0.941. The error of prediction increases for higher values of A/P and lower values of degree of compaction.

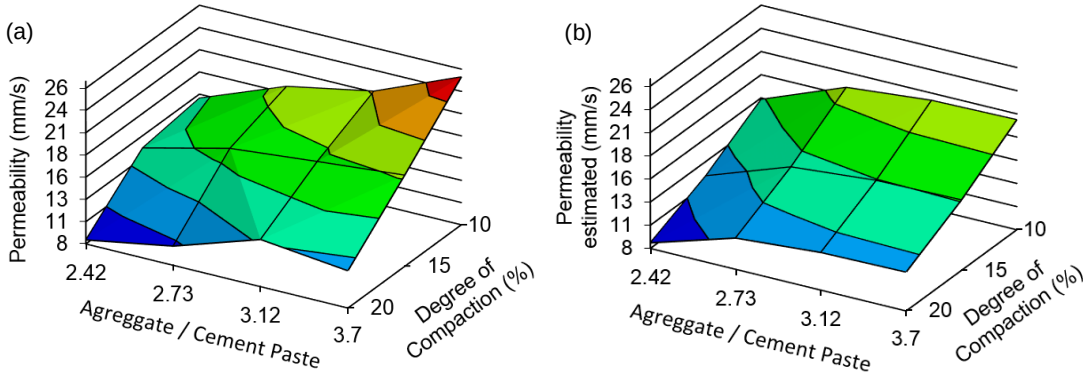

Figure 5.6 – Relationship between A/P, degree of compaction and permeability, experimental results (a) and estimated results (b).

Notice that this nonlinear expressions relating porosity with A/P and degree of compaction (Eq. 5.5) and permeability with porosity (Eq. 5.6) are only valid for the specimens and the range of values covered in this research. However, they may be used as a reference for the design of other compositions.

5.4. Model Generation

In this section, the process used to generate the numerical model to assess the permeability is presented. The procedures used to generate the geometrical model is discussed. Then, the mesh generation process using "SolidWorks Flow Simulation Mesh Generator" is showed. Finally, the boundary conditions and the input parameters are presented.

5.4.1. GEOMETRICAL MODEL

Compacted model

The method proposed in Chapter 4 was used to generate the 3D compacted models of pervious concrete. This method takes into account parameters related to the composition of the pervious concrete, like the aggregate grading curve, the A/P ratio and the rheology of the cement paste. The simulations were performed using Discrete Element Method (DEM). The YADE was selected as open-source framework for these simulations.

Some simplifications were introduced to reduce the computational cost of the simulation. Most of them are related to the aggregates. A bi-phasic spherical particle shown in Fig. 5.7a is used. It is formed by an inner core with radio R_{ag} surrounded by an external layer with thickness t_{eq}. The former represents the aggregate and the later represents the cement paste, these points were further discussed in Section 3.3. The grading curve from the aggregates (see Fig. 5.1) was divided in 3 zones. For each zone, an equivalent diameter and the number of particles was assessed using a weighted calculation of masses. The equivalent diameters of 4.66 mm, 5.81 mm and 6.48 mm were obtained. The volume of aggregate corresponding to each equivalent diameter was 17.94 %, 35.16 % and 46.89 %, respectively.

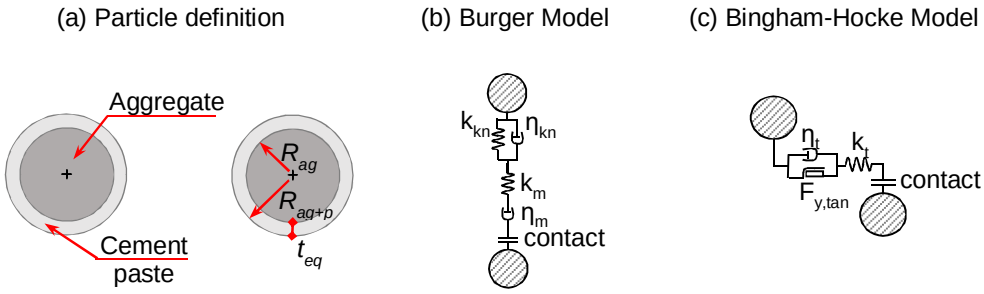

Figure 5.7 – Particle definition (a) and contact models (b and c).

In order to consider the A/P ratio, an equivalent thickness α_{eq} is calculated through the procedure proposed by [142-143] (see Eq. 3.9 in Section 3.3). In this sense, Tab. 5.2 presents the four model families with the calculated α_{eq}. After the definition of the aggregates sizes and the α_{eq}, the t_{eq} is calculated for each aggregate size (see Eq. 3.8 in Section 3.3).

Table 5.2 – α_{eq} used in the simulation.

Model family	α_{eq}	Associated with the mixture family	A/P	Number of generated models
N300	0.08272	L300	3.70	10
N350	0.09512	L350	3.12	10
N400	0.10715	L400	2.73	10
N450	0.11887	L450	2.42	10

In the DEM, the particles may interact with each other. The interactions are governed by force-displacement laws. A modified Burger Model (Fig. 5.7b) is used to simulate the normal interaction between the external layers of the particles. A purely elastic interaction law is used to simulate the contact between the inner cores. A modified

Bingham-Hocke law (Fig. 5.7c) is used to model the tangential contact. An in depth discussion was presented in Section 4.4.2.

The compaction simulation emulates the experimental procedure. It starts with the gravity deposition of the particles inside a cylindrical mold. Particles located above the upper limit of the mold are removed by means of a plane that passes horizontally above the specimen. Then, a cylindrical plate descends, compacting the particles. The model is compacted until the desired degree of compaction is achieved. In order to describe the position of the particles in a 3D Cartesian coordinate system, two parameters are required: the center coordinates (*x*, *y*, *z*) and the radius of the particles. A deeper discussion of the process was presented in Section 4.5.

The input parameters used in this work to simulated the compaction process of the pervious concrete and generate the 3D compacted models are presented in Tab. 5.3. The elastics and viscous parameters of the adapted Burger Model were defined in Section 4.7.2. 10 compacted models with different degrees of compaction were generated for each family, totalizing 40 models.

Table 5.3 – Parameters used in the simulation.

Parameter		Value
External layer	$B_{k,kn}$	5.50×10^{10} N/(m·m^3)
	$B_{\eta,kn}$	1.50×10^{10} N·s/(m·m^3)
	$B_{k,mn}$	8.00×10^{11} N/(m·m^3)
	$B_{\eta,mn}$	6.50×10^{11} N·s/(m·m^3)
	$\alpha_{fric,e}$	0.6
	Yield	1.0×10^6
	α_{eq}	Values in Tab. 5.2
Inner core	$k_{n,inner}$	5.5×10^{10} N/m
	$\alpha_{fric,i}$	0.75

Meso-structure

The 3d meso-structure of the achieved after the compaction is formed by the solid phase (aggregates and cement paste) and the pore phase (voids represented by the hollows between particles). However, the model obtained with the DEM simulation does not generate the geometries of cement paste redistribution due to the overlap. The proper consideration of the cement paste redistribution is necessary since it affects the total volume of voids, which is related with the porosity and permeability. Indeed significant difference may arise between models that do and do not contemplate the cement paste redistribution.

In this sense, some adjustment on the solid phase of the compacted model are needed for a better geometrical representation of a pervious concrete. In the compaction process, initially the contacts between particles occurs with the external layer (that represents the cement paste) by overlaps. As the distance between particles decreases, the inner cores (aggregates) push the surrounding layer away from the point of contact, causing a lateral volume increase (cement paste redistribution) and the formation of a contact bridge (CB).

Fig. 5.8 presents an image of a pervious concrete specimen. In this figure, 3 types of CBs are depicted in blue. The first one, represented in Fig. 5.8b, is formed by the interaction where one particle overlaps with the wall of the mold. The second one appears when two particles overlap with each other, observed in Fig. 5.8c. The last one appears when three or more entities (particles and/or wall) overlap simultaneously, as depicted in Fig. 5.8d. In the last case, the CBs are studied separately in pairs of entities.

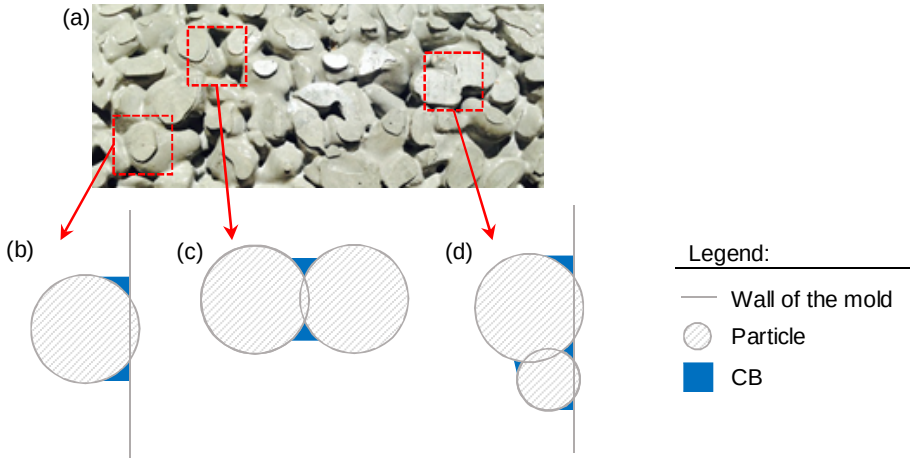

Figure 5.8 – Types of CBs.

The algorithm developed in this work to represent the 3D formation of CB analyzes the interaction between two entities (particle-particle or particle-wall) at a time. For nomenclature purposes the interaction between two aggregates (particle-particle) is called sphere-sphere (S-S) and the interaction between aggregate and wall (particle-wall) is named sphere-wall (S-W).

To assess the CB a simple geometric calculation is performed. It is assumed that the volume of cement paste located originally in the overlap region equals the volume that should be redistributed. Fig. 5.9a illustrates this consideration for an S-S interaction. In this figure the overlap volume is hatched in red and the CB volume is hatched in blue.

Fig. 5.9b presents the cross section of the interaction S-S. Once the volume of overlap is estimated for a certain interaction, the volume of the CB is also known. Then,

the position of the points P2 and P3 are determined. The volume of the object formed by the revolution of the triangle P1-P2-P3 (CB region hachured in blue in Fig. 5.9a) around the y-axis is then calculated. To simplify this calculation, it is considered that the angle ω that represents the increment is equal for both particles in contact. This consideration implies a negligible error as long as the thickness of the cement paste layer is small in comparison with the diameter of the aggregate and the sizes of particles do not vary by one order of magnitude. Even though this is the common case with the materials analyzed here, if such conditions are not fulfilled, a more precise calculation should be used to estimate the angle ω for each particle. Fig. 5.9c depicts the interaction S-W. Notice that the volume of redistributed paste may be calculated in an analogous way.

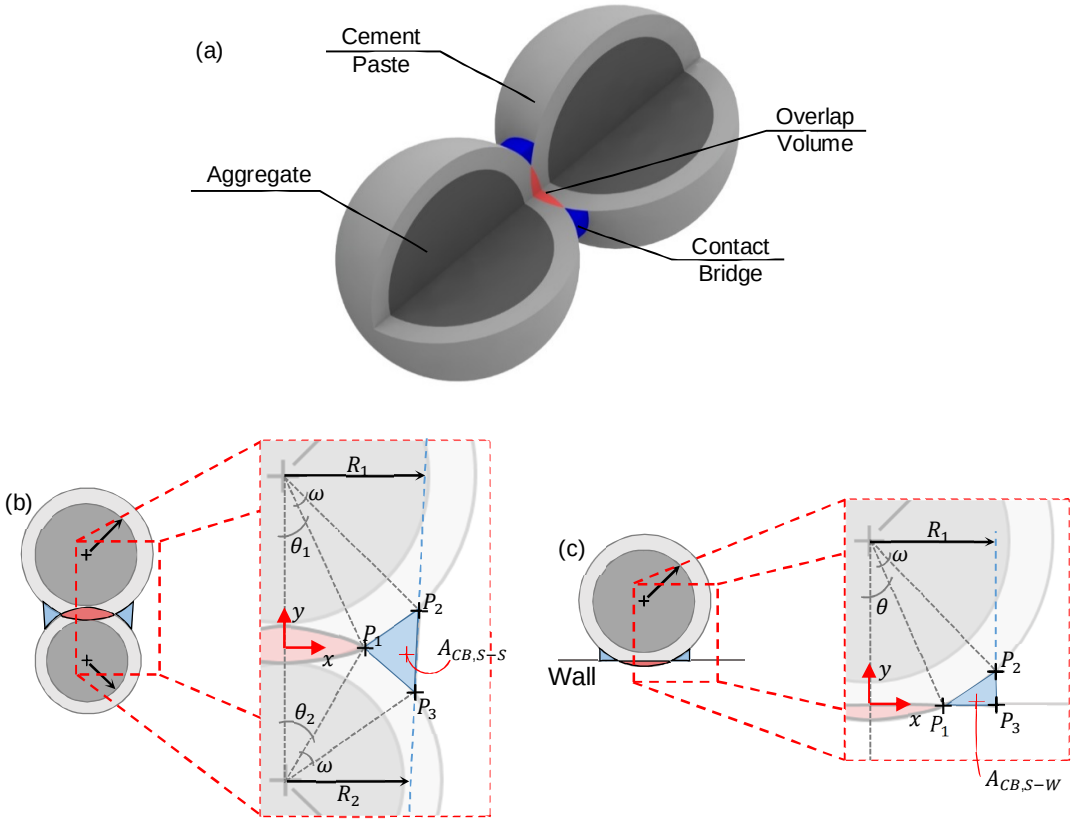

Figure 5.9 – CB formation for the interaction S-S (a and b) and S-W (c).

Geometrical model

With the geometrical properties of the particles and the CB for each interaction, a VBA code (integrated in SolidWorks) generates the solid geometry. This model consists of a unified volume of all particles and the CBs, as presented in Fig. 5.10.

Figure 5.10 – Geometrical model of a pervious concrete specimen.

5.4.2. CFD Mesh Generation

The porous phase (voids) and the surface of the solids are meshed for the CFD analysis. This is necessary since the water flow is governed by porous phase. This means that the negative representation of the model in Fig. 5.10 is obtained before meshing. The mesh was generated using SolidWorks Flow Simulation, a 3D CFD solver that uses a Cartesian Mesh (CM) with octree refinement. Dassault Systèmes [152] showed that the CM requires less elements for same accuracy as other CFD mesh generation approaches. This reflects in a reduction of the computational effort.

The mesh generation is initiated with a division of the fluid domain into a series of coarse cuboids formed by intersection of planes parallel to the axis of coordinate system. Next, this coarse mesh is refined. The refinement process consist of dividing a specific cuboid into eight or more geometrically similar cuboids. The criteria used in the software to define the cuboids that should be divided follows the proposed by Dassault Systèmes [152] and Sabachkin and Dumnov [153]. Details of the validation process of meshing and refinement used in Flow Simulation were discussed by Sabachkin and Dumnov [153].

In the context of the work reported here, a numerical study that aimed to investigate the influence of the mesh refinement over the permeability results was performed. Fig. 5.11a presents the relation between the number of elements of a mesh and the permeability result. In order to achieve different levels of refinement, the minimal size of the element was changed. To extrapolate the minimal size of the element to other models, which may present a totally different geometry, the analysis was related with the number of elements (N_{Elem}) that fit inside the in the diameter of smallest aggregate particle ($\emptyset_{min}$) of the system. Fig. 5.11b and Fig. 5.11c present meshes with 4 $N_{Elem}/\emptyset_{min}$. and 16 $N_{Elem}/\emptyset_{min}$, respectively. An increase in the number of elements allows a finer reproduction of the porous surface. According to Fig. 5.11a, similar results

are obtained for meshes with $N_{Elem}/\emptyset_{min}$ bigger than 12. The mesh discretization used here for all simulations was 16 $N_{Elem}/\emptyset_{min}$.

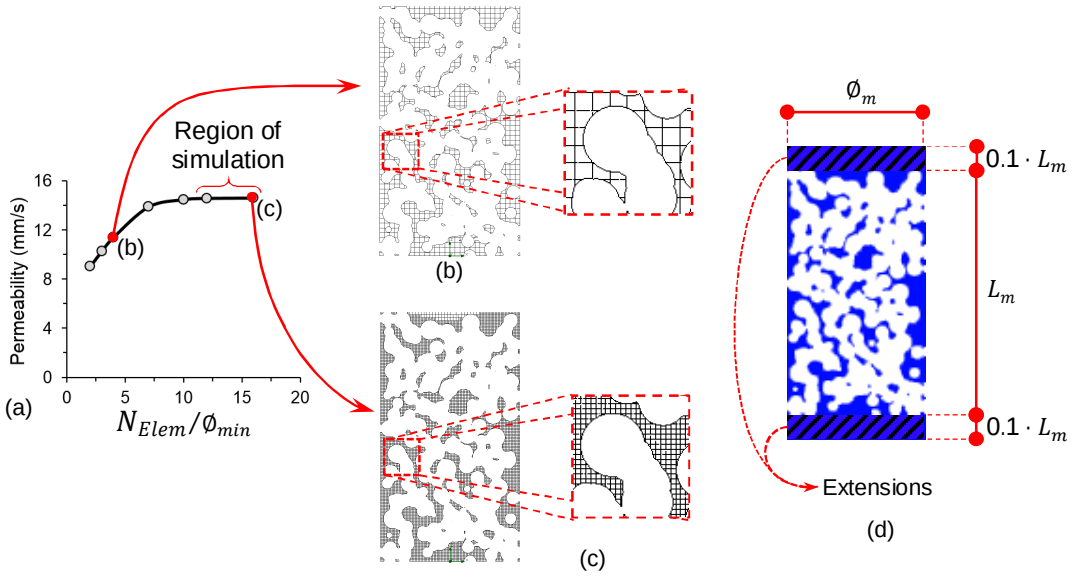

Figure 5.11 – Influence of the mesh discretization over the results (a to c) and dimensions of the section of the model (d).

The dimensions of the cross section used in the models are presented schematically in Fig. 5.11d. The top and the bottom of the model were extended, these extensions were defined in order to avoid the turbulent flow and to guarantee the direction of the flow. Moreover, these extensions were also defined as pore phase.

5.4.3. Input Parameters and Boundary Conditions

In this study, water at 25 ºC was used as the fluid, gravity was assumed as 9.81 m/s^2 in the Z direction and the roughness applied on the walls of the model was 5.0 µm [154]. The boundary conditions imposed were the pressures at inlet and outlet prescribed at the top and bottom planes normal to the Z direction, as depicted in Fig. 5.12. The boundary conditions correspond to the static pressure imposed in each location regarding the water level applied in the experimental program.

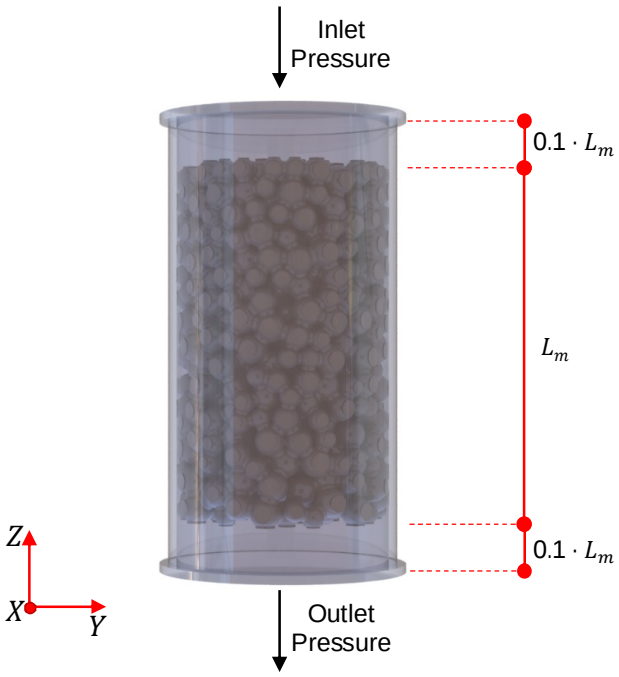

Figure 5.12 – Boundary condition.

5.5. NUMERICAL SIMULATION

In this section, the results from the numerical simulation are discussed. Therefore, first a comparison between the numerical and experimental results of the permeability is shown. Then, a study regarding the relation between the geometrical properties of the models and the fluid flow velocity is presented. Finally, the numerical results of the fluid flow tortuosity are analyzed.

5.5.1. Comparison of Experimental Results and CFD Simulation

In this work, SolidWorks Flow Simulation was used as solver. This software, solves the Navier-Stokes equation to predict the flow for, both, turbulent and laminar regimes. The formulation of the model is described in detail in [155].

The solution reach the steady-state flow condition when the difference of the average velocity between two consecutive interactions is less than 1.0×10^{-6}. After, the volume flow is obtained. Then, the permeability 'k_m' (in m^2) may be calculated according to Darcy's Law, presented in Eq. 5.7. In this equation, Q is the volume flow rate in m^3/s,

μ is the dynamic viscosity of the water expressed in Pa·s, L_m is the height of the model expressed in m, $A_m$is the cross section area of the model expressed in m^2 and Δp is the pressure gradient expressed in Pa.

$$k_m = \frac{Q \cdot \mu \cdot L_m}{A_m \cdot \Delta p} \tag{5.7}$$

The permeability of the model 'K_m' (or hydraulic conductivity expressed in mm/s) is obtained according to Eq. 5.8. In this equation, ρ_w is the density of the water in kg/m^3 and g is the acceleration of gravity expressed in m/s^2.

$$K_m = k_m \cdot \frac{\rho_w \cdot g}{\mu} \cdot 1000 \tag{5.8}$$

The relation between numerical results of porosity and permeability for all models are presented in Fig. 5.13a. The permeability of the models range between 8 and 33 mm/s, increasing exponentially with the porosity.

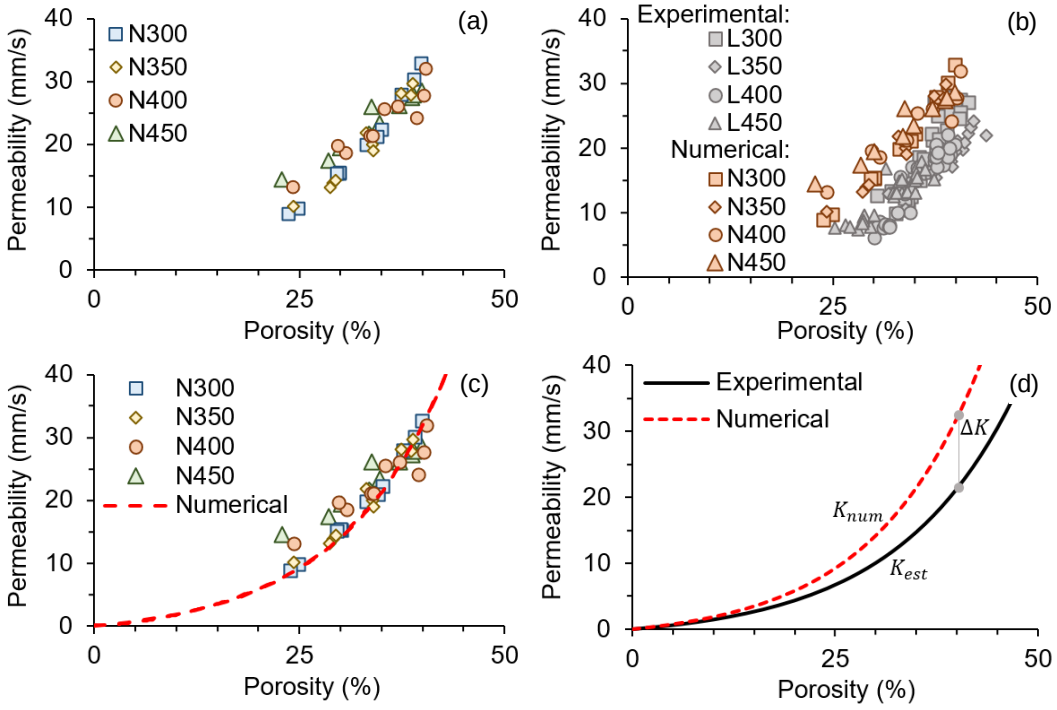

Figure 5.13 – Numerical and experimental permeability depending on the porosity.

A comparison between the numerical and experimental results of permeability depending on the porosity is given in Fig. 5.13b. The experimental results showed higher

scatter than the numerical results. This is reasonable since variabilities induced by the testing method are not present in the numerical simulations. However, the numerical results showed a similar trend of the one obtained with the experimental results. This highlights the capability of the model to simulate the permeability of the pervious concrete.

Fig. 5.13c presents the plot of a nonlinear regression in dashed red line. This regression was performed using the porosity as independent variable to obtain the numerical permeability. The final equation to find the numerical estimation of the permeability K_{num} is presented in Eq. 5.9. A good fit is obtained between the numerical estimation and the numerical results. The comparison of the results for equivalent porosity shows a correlation coefficient (R^2) of 0.942.

$$K_{num} = 1.66 \cdot (e^{0.075 \cdot P} - 1) \tag{5.9}$$

A comparison between the numerical and experimental nonlinear regressions of permeability depending on the porosity is given in Fig. 5.13d. The small difference ΔK observed in the numerical and experimental comparison might be attributed to several factors. On one hand, it is difficult to represent the complex structure of the pervious concrete. The simplifications made regarding the shape of aggregates, considering they as perfect spheres, create a pore structure with more continuity than the observed in reality for irregular shaped aggregates. This is increased by the fact that the particle size distribution of the aggregates were discontinuous in the simulation (just 3 different diameters were considered). Also, the simplifications to consider the A/P ratio in the simulation might lead to some errors regarding the correct redistribution of the cement paste.

In order to correct this small difference, a linear regression was performed using the permeability calculated with Eq. 5.9 and the permeability obtained with the simulation as independent variable to obtain the adjusted permeability '$K_{n,adj}$'. The final equation to find the $K_{n,adj}$ is presented in Eq. 5.10. In this equation, K_m is the permeability obtained with the simulation.

$$K_{n,adj} = 0.64 \cdot K_m \tag{5.10}$$

Fig. 5.14 presents the comparison between the experimental results of the permeability and the adjusted permeability (calculated by Eq. 5.10 using the results from the numerical model) depending on the porosity. The adjusted permeability $K_{n,adj}$ was calculated with Eq. 5.10 using the numerical results (Fig. 5.13a). Using this equation, it is possible to predict the permeability with the simulation with more accuracy.

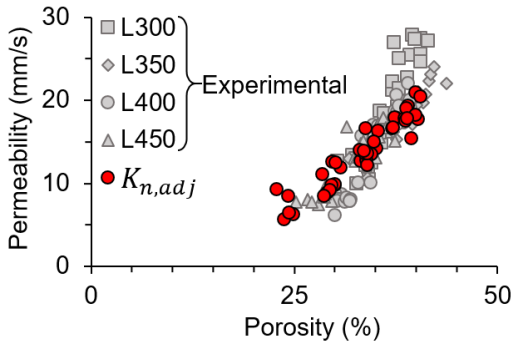

Figure 5.14 – Adjusted and experimental permeability depending on the porosity.

5.5.2. Geometric Properties

The study of the porosity profile compared to the profile of the average velocity in the direction of the flow simulation (Z direction) is important to understand how the compaction process affects the simulation of the permeability. In order to establish a relation between the evolution of the porosity with the different degrees of compaction, the models were dived into slices in the Z direction. For each slice, the sectional porosity was determined. Fig. 5.15 presents the porosity profile of the numerical models of the family N300 with 3 different degrees of compaction. This figure also presents the profile of the average velocity numerically obtained in the same direction.

The smallest values of porosity are observed in slices closer to the surface of the model that received the compaction loads. A more intensive reorganization of the particles close to the face that receives the forces was observed. The particle-to-particle stress transmission dissipates the energy that is not fully transmitted to the adjacent slices. This becomes less evident as the average degree of compaction increases. In fact, for high degrees of compaction, the structure of the top layers practically does not change, which forces a rearrangement of the bottom layers.

The velocity profile follow the inverse trend, being higher for the top sections and smaller for the bottom ones. Such outcome may be explained by the continuity principle. In steady state, the same volume of water passes through each layer per time interval. Given that the top layers are less porous, they present less space to accommodate the flow of water. Consequently, high velocities have to be achieved to keep the total volume of water constant. In the layers with higher porosity, more space is left, hence smaller velocities are needed to keep the flow constant.

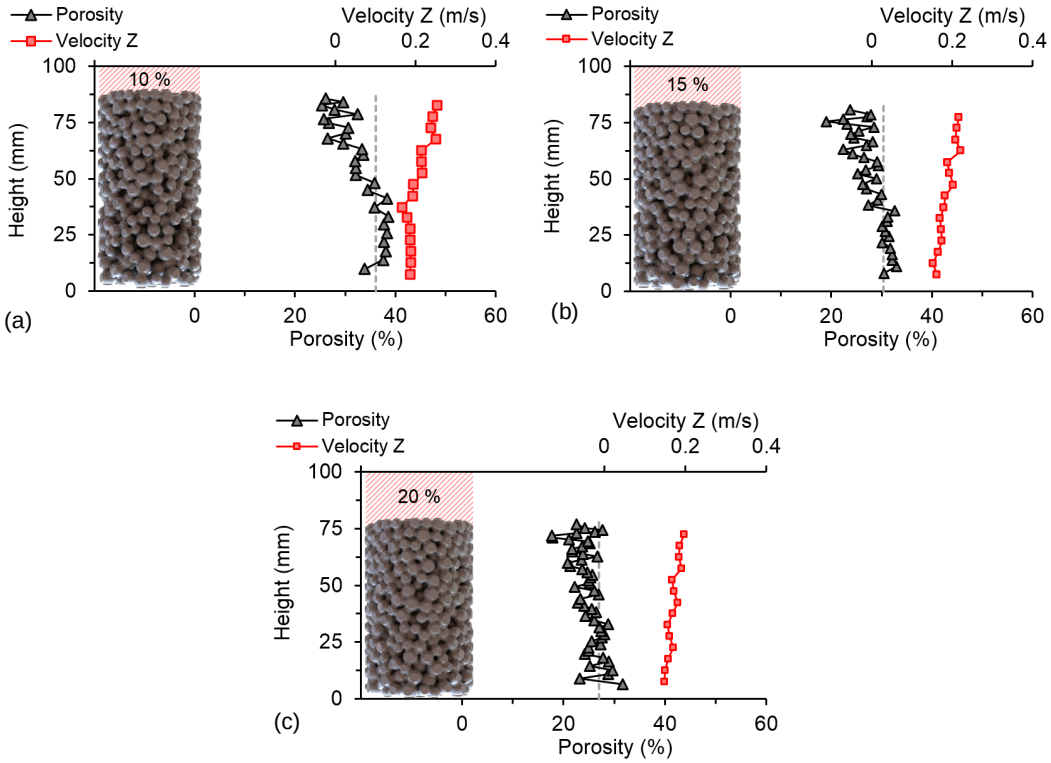

Figure 5.15 – Porosity and velocity profile in the direction of the flow simulation.

In this study the porosity profile was not defined experimentally. Even though the results presented in this section are obtained from numerical models, they are in line with experimental results by [20;23]. These authors also showed that a difference in the level of compaction of different slices might occur depending on the compaction degree and the proximity with the application of the compaction load. This fact may be used to justify the need of first simulating the compaction to obtain the meso-structure and, then, simulating the permeability.

5.5.3. Fluid Flow Streamline and Tortuosity

Certain particularities of the fluid flow inside the specimen are hard to assess experimentally. This is the case of the fluid flow streamline and its relation with the tortuosity, which are easier to analyze with numerical models. Fig. 5.16 presents horizontal and vertical cross-sections of the model N300 with a degree of compaction of 15 % in which the velocity in Z direction is plotted. In order to understand better how the fluid flow is influenced by the solid phase, a region of the Fig. 5.16b is outlined. In this region, arrows indicate the flow direction. An abrupt change in the direction of the flow

occurred when the fluid impacted against the solid phase. This results in a dissipation of the velocity of the fluid flow.

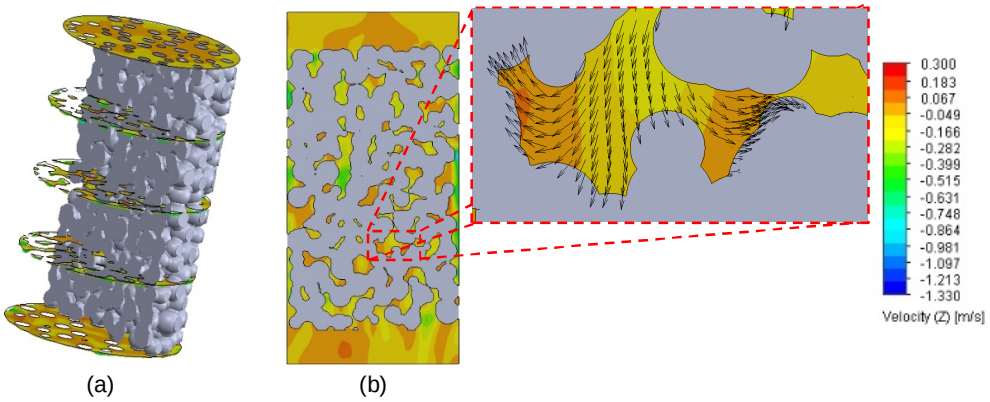

Figure 5.16 – Plot of the velocity in the fluid flow main direction (direction Z).

Fig 5.17a shows the fluid flow streamline at the steady-state along the main direction of the flow. The velocity is strongly dependent on the size and the connectivity of the voids (pores). Voids with smaller cross-sections present an increase in the velocity of the fluid flow. The variation of the velocity magnitude with the size of the connected voids is better observed in Fig. 5.17b.

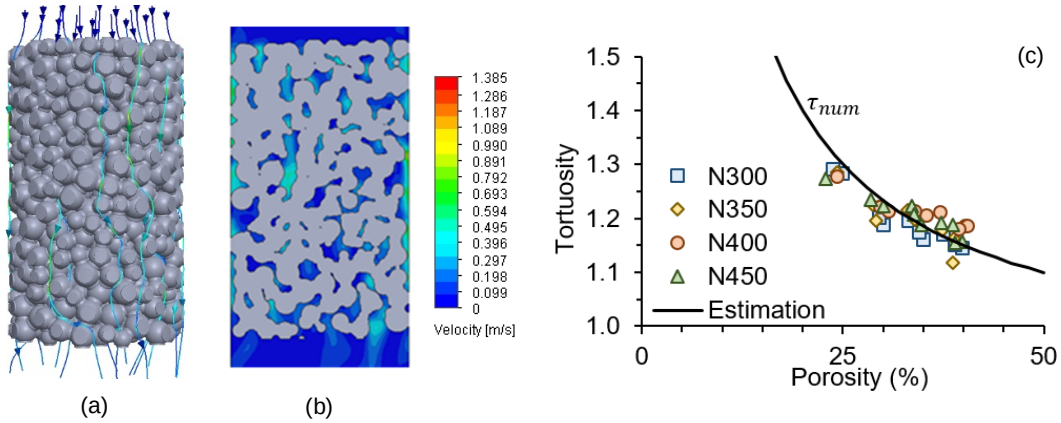

Figure 5.17 – Plot of the fluid flow streamline (a), magnitude velocity (b) and the tortuosity as depending on the porosity (c).

It is assumed that all effects arising from pore orientation, connectivity and size variation can be lumped together as a single tortuosity factor. This tortuosity may be determinate by dividing the height of the model by the length of the average path taken by the fluid. A large number of possible paths exist inside a specimen. In order to establish a number of paths needed to achieve a representative tortuosity factor of a model, a

sensibility analysis was conducted. It was found that 900 paths randomly selected were needed to obtain stable tortuosity factor. The relation between the porosity and the tortuosity for the models is depicted in Fig. 5.17c. It is observed that the effect of the A/P ratio over the tortuosity for the analyzed models is negligible. Moreover, it is assumed that the porosity influence directly the tortuosity. In this sense, a nonlinear regression was performed using the porosity as independent variable to obtain the tortuosity. The final equation to find the numerical tortuosity 'τ_{num}' is presented in Eq. 5.11. A good fit is obtained between the estimation and the simulations. The comparison of the results for equivalent porosity shows a correlation coefficient (R^2) of 0.883.

$$\tau_{num} = 1 - \left(0.1 - \frac{10}{P}\right) \tag{5.11}$$

5.6. CONCLUDING REMARKS

This study shows that it is possible to predict numerically the permeability of compositions with different A/P ratios and compaction degrees. This opens up the possibility of performing a numerical design of compositions before conduction experimental verifications, which might reduce the number of tests needed to achieve the composition that better suits the permeability of each application. From the findings of the present study, the following conclusions may be derived.

- The experimental permeability results showed that the main factor that influences the permeability is the porosity. Since, the studied range of A/P ratio (2.42, 2.73, 3.12 and 3.70) does not affect the order of magnitude of the permeability when a similar porosity is analyzed. This is caused by the similarity of the channels that are created by the interconnected pores, since the aggregates used are the same. Notice that with lower A/P ratio, less energy of compaction is required to achieve a specific level of permeability.
- The numerical and experimental permeability results are of the same order of magnitude for the same levels of porosities. Simplifications regarding the aggregate grading curve and shape in the numerical model usually lead to permeability that are higher than the permeability assessed experimentally.
- The CFD analysis provides interesting insight about the velocity distribution related to the porosity profile. Like the permeability, no clear relation between the tortuosity and the A/P ratio was found. This is probably due to the similarity of the channels that are created by the interconnected pores. A clear

relation between porosity and tortuosity was observed. In general, the porosity decreases as the tortuosity increases.

6. MECHANICAL SIMULATION

6.1. INTRODUCTION

In pervious concrete the loads are transmitted by the network of contacting particles, through the matrix of cement paste bridges. The volume and the contact surface of the cement paste bridge between two the particles have a certain influence over the mechanical strengths. Other phenomena such as debonding of interfaces make experimental and theoretical prediction of the mechanical behavior of pervious concrete difficult. In this sense, the mechanisms governing the mechanical behavior of granular materials cemented, such as pervious concrete, are complex.

Independent of the work philosophy proposed, it is necessary to simulate the pervious concrete as a lumped of discrete particles in order to obtain real mechanical interactions between particles. In this sense, a DEM approach is necessary to study the mechanical properties of pervious concrete depending on the volume fraction of binder matrix at the interface between two aggregates. This three-dimensional model material should be subjected to compressive and tensile loading in order to investigate the effective strength, the transmission of stresses and failure mechanisms related to the pervious concrete in general.

There are different ways to perform the simulation of contacts, which invariably involve some simplification of the problem find in practice. Consequently, the mechanical response obtained may be different from the experimental results. In this context, it is important to define and adapt to DEM a constitutive law considered more appropriate for the fracture analysis of interactions between aggregates bonded by hardened cemented paste. Then, the proposed constitutive law should be applied in this approach to characterize the behavior and failure of the models in compression and tension.

6.1.1. Objectives

The objectives of the study described in this chapter are the following:

- determine the main factors that influence the mechanical properties of the pervious concrete;
- propose an analytical model to evaluate the mechanical behavior of the pervious concrete, considering its composition;
- propose and validate a constitutive law (DEM based) to simulate the interaction between two aggregates bonded by hardened cement paste;
- compare the fracture behavior observed in the numerical models with the ones obtained experimentally.

6.1.2. Outline of the Study

The first part of the study shows the philosophy of the experimental program, as described in Section 6.2. Then, the experimental results are presented in the Section 6.3. In the latter section, an analytical model that allows to estimate the mechanical properties of pervious concrete is developed.

Then, the Section 6.4 describes the proposed constitutive law based on Discrete Element Method (DEM). In the Section 6.5 is discussed the generation of the numerical models. Finally, in the Section 6.6, the results obtained with the numerical models are compared with the ones obtained experimentally. The numerical mechanical response is validated with the experimental results.

6.2. EXPERIMENTAL PROGRAM

The same specimens used for the evaluation of the permeability were characterized for the experimental program included in this chapter. Just for recapitulation and an easy comprehension of this experimental program, 4 different compositions of pervious cocnrete were produced and for each one 3 different degree of compaction were obtained. In total, 12 combinations (see Tab. 5.1) were analyzed and a total of 120 specimens were casted. The specimens received the denomination that designate first the type of aggregate used (in this case only limestone was studied), than the content of cement in kg/m^3, than the level of applied compaction in mm/m, and finally the number of the specimen. For example the designation ‘L450-200-1’ indicates a

specimen with limestone as aggregate, 450 kg/m^3 of cement, with degree of compaction equals 20 % and this is the specimen number 1 of this group.

6.2.1. Mechanical Tests

The focus of the experimental program is to evaluate the compressive and tensile strength of pervious concrete with different amount of cement paste in different degrees of compaction. The press used in this research to access the compressive and tensile strengths was an "Instron 8803" with a load cell of maximum 200 kN and 1 % of accuracy, operating in displacement controlled mode with a velocity equals 1.67x10^{-6} m/s (0.1 mm/min). The tests were performed with displacement control in order to facilitate the simulations, and also to obtain the complete stress-strain curves.

In this sense, the plate-to-plate displacements were recorded to determine the strains. Notice, the top of the specimens were not totally flat and parallel to the bottom, so a thin layer of mortar (with high content of cement) was needed to regularize this area. Fig. 6.1a presents the compressive test assembly with a specimen, where the bottom plate is static and the top plate is articulated. The maximum compressive stress (or peak stress) σ'_c in MPa may be calculated by the maximum applied force $F_{c,max}$ in the normal direction divided by the surface in mm^2 where the load is applied ($\pi \cdot R_s^2$, where R_s is the radius of the specimen).

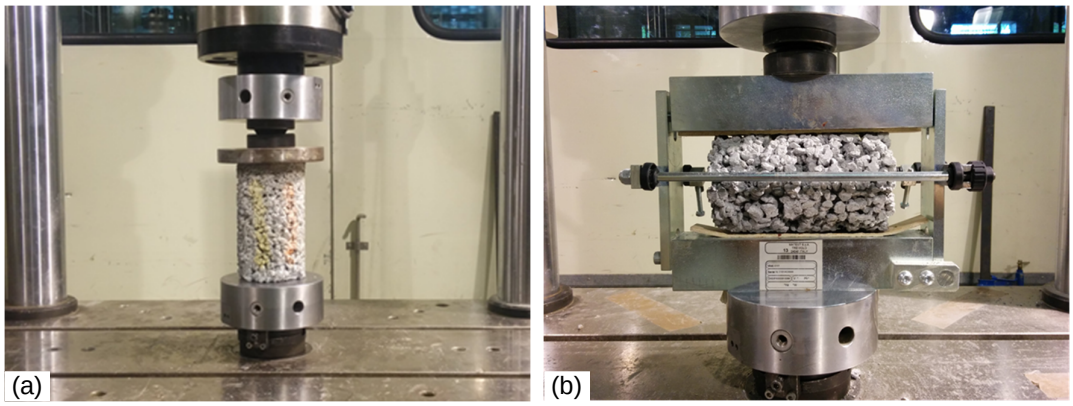

Figure 6.1 – Compressive test assembly (a) and Brazilian test assembly (b).

The tensile strength was determined with the Brazilian test, as depicted in Fig. 6.1b. The Brazilian test induces a traction stresses in the center of a lying specimen when the same has two compressed parallel side.

Notice that the compressive and Brazilian tests of the experimental trails that belong to the group L400-200 were performed on "Ibertest Autotest-3000" with a load

cell of maximum 3000 kN and 1 % of accuracy. The tests were operating in displacement controlled mode with a velocity equals $1.67x10^{-6}$ m/s (0.1 mm/min). After the testes were performed, some problems were detected in the results obtained with Ibertest. In order to mitigate this problems, the rest of the test were performed with Instron.

6.3. EXPERIMENTAL RESULTS

The results from the experimental program described in Section 6.2 are presented separately. Therefore, first the results of the compressive behavior are shown and analyzed. Finally, the results of the tensile behavior are analyzed.

6.3.1. Compressive Behavior

The relation between porosity and compressive strength for all specimens are presented in Fig. 6.2a. The compressive strength varies from 2.5 to 8 MPa, decreasing exponentially with the porosity, in accordance with the results from the literature (see Section 2.2.2). It was observed that the A/P and the degree of compaction also influenced directly the compressive strength. The opposite effect of observed in the experimental results of permeability (discussed in Section 5.3.2), where the results were directly influenced only by the porosity. This difference is probably related to the amount and distribution of cement paste that bonds two aggregates that changes with the A/P and the degree of compaction, as observed by [156].

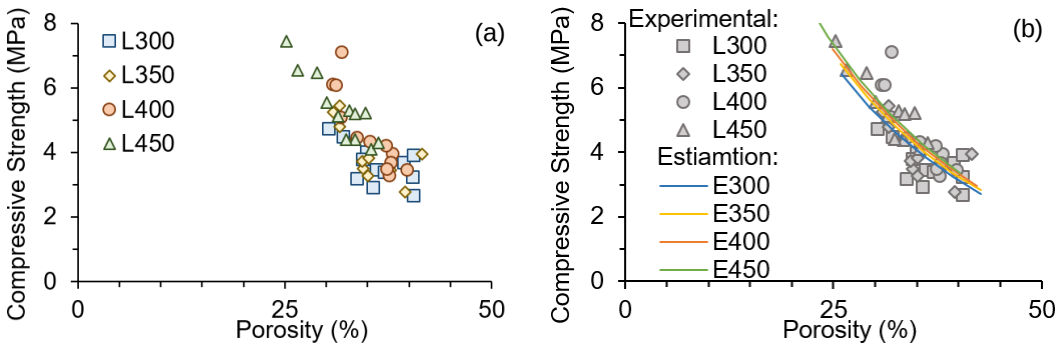

Figure 6.2 – Relationship between porosity and compressive strength.

It is assumed that the studied parameters influence indirectly the compressive strength. In this sense, the nonlinear regression was performed using the porosity as independent variable to obtain the compressive strength. The final equation to find the estimated maximum compressive strength '$\sigma'_{c,est}$' is presented in Eq. 6.1. This equation

may give the erroneous idea that the higher the degree of compaction, the lower is the resistance. This is false, because the porosity (presented in the Term B of the equation) is affected by the increasing degree of compaction. Consider, for instance, an increase from 10 to 20 % in the degree of compaction of a composition with the A / P equals 3.70. This results in a decrease smaller than 1 % in the Term A, while the Term B increases by about 40 %. In this example, the compressive strength also increases about 40%.

$$\sigma'_{c,est} = \underbrace{(-5.0x10^{-5} \cdot DoC - 1.07x10^{-2} \cdot A/P + 0.20)}_{\text{Term A}} \cdot \underbrace{\left[e^{0.05\cdot(100-P)} - 1\right]}_{\text{Term B}} \quad (6.1)$$

Fig. 6.2b presents the estimated compressive strength values obtained with Eq. 6.1. A good fit is obtained between the estimation and the experiments. The comparison of the results for equivalent porosity shows a correlation coefficient (R^2) of 0.863.

The adjustment of the Eq. 6.1 was obtained from the experimental results of porosity and compressive strength. However, the porosity may also be predicted with the Eq. 5.5 from the A/P and the degree of compaction. This equation was used within Eq. 6.1 to predict the compressive strength, and a correlation coefficient of 0.929 was obtained. Fig. 6.3 presents the experimental results of compressive strength related with A/P and degree of compaction compared with the estimations given by Eq. 5.5 and Eq. 6.1. The values of the Fig. 6.3a were obtained with the average of the experimental results of each combination.

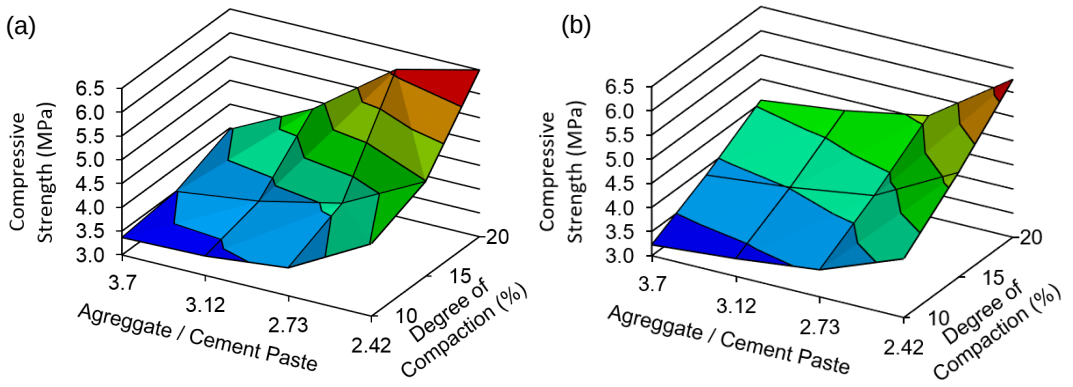

Figure 6.3 – Relationship between A/P, degree of compaction and compressive strength: experimental results (a) and estimated results (b).

Notice that this nonlinear expressions relating porosity with A/P and degree of compaction (Eq. 5.5) and compressive strength with porosity (Eq. 6.1) are only valid for the specimens and the range of values covered in this research. However, they may be used as a reference for the design of other mixes.

6.3.1.1. Strain at peak stress

As observed by [157-158], the strain at compressive strength (or peak stress) depends on the mix composition, shape/size and type of the aggregates, curing conditions, shape and size of specimen, loading rate, age of loading, and test techniques used. However, the strain at peak stress is commonly correlated with the correspondent compressive strength. The relationship between the compressive strength and the strain at peak stress for all specimens tested in the experimental campaign is shown in Fig. 6.4a. In spite of considerable scatter, a correlation between the compressive strength and the strain at peak stress seems to exist.

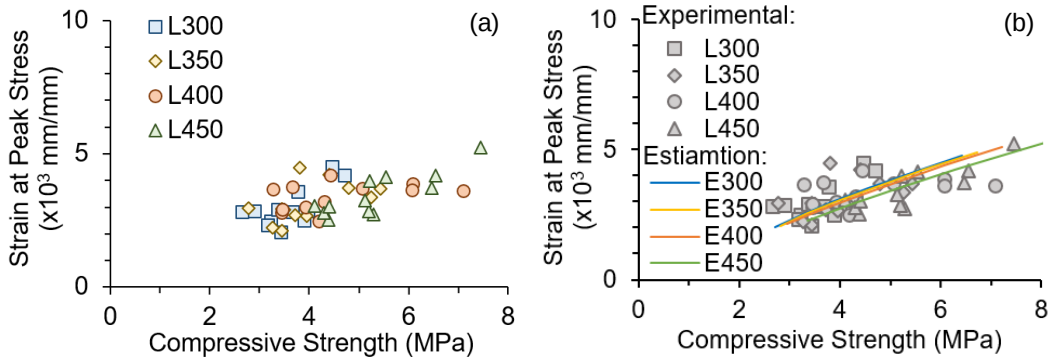

Figure 6.4 – Relationship between compressive strength and strain at peak stress.

A linear regression was performed using the compressive strength as independent variable to obtain the strain at peak stress. The final equation to find the estimated strain at peak stress '$\varepsilon_{0,est}$' is presented in Eq. 6.2. In this equation, σ'_c represents the compressive strength.

$$\varepsilon_{0,est} = 4.0x10^{-4} \cdot \sigma'_c + 5.0x10^{-5} \cdot DoC + 7.0x10^{-4} \quad (6.2)$$

Fig. 6.4b presents the estimated strain at peak stress values obtained with Eq. 6.2. A reasonably good fit is obtained between the estimation and the experiments. The comparison of the results for equivalent compressive strength shows a correlation coefficient (R^2) of 0.675 for a range of compressive strength from 2.5 to 8 MPa.

In order to correlate the estimated strain at peak stress with the composition, the compressive strength σ'_c used in the Eq. 6.2 is defined by Eq. 6.1. In this sense, Fig. 6.5 presents the experimental results of strain at peak stress related with A/P and degree of compaction compared with the estimations given by Eq. 6.2 and Eq. 6.1. The values of the Fig. 6.5a were obtained with the average of the experimental results of each combination. A good fit is obtained between the estimation and the experiments. The

comparison of the results for equivalent A/P and degree of compaction shows a correlation coefficient (R^2) of 0.956.

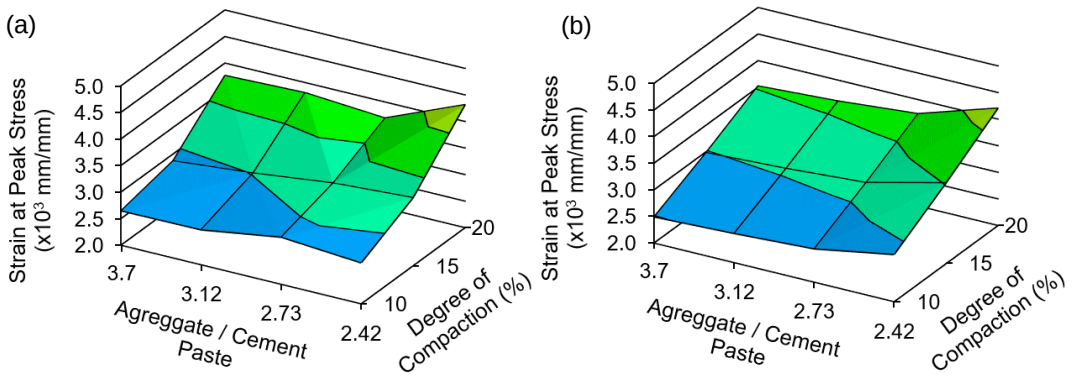

Figure 6.5 – Relationship between A/P, degree of compaction and strain at peak stress, experimental results (a) and estimated results (b).

6.3.1.2. Stress-strain curve

Fig. 6.6 shows the stress-strain responses of all pervious concrete specimens tested. The stress-strain curves are depicted separately according to the group of specimens. The analysis of the experimental results was divided in pre-peak and post-peak responses. The pre-peak response is depicted in Fig. 6.7a and comprehends the initial phase of the load (defined by the point A) until the maximum stress is reached which define by point C (ε_0 , σ'_c). This part of the stress-strain curve is divided into the linear phase ($\overline{AB}$) and the nonlinear phase ($\overline{BC}$). The average and standard deviation of the initial slope (considering the pre-peak portion of the curves) were equal 1520 and 201, respectively. Moreover, the peak stresses are found to increase with increasing degree of compaction and decreasing A/P ratio, this was also observed in Section 6.3.1.1. The gray areas presented in Fig. 6.6 represent the envelope of the experimental results.

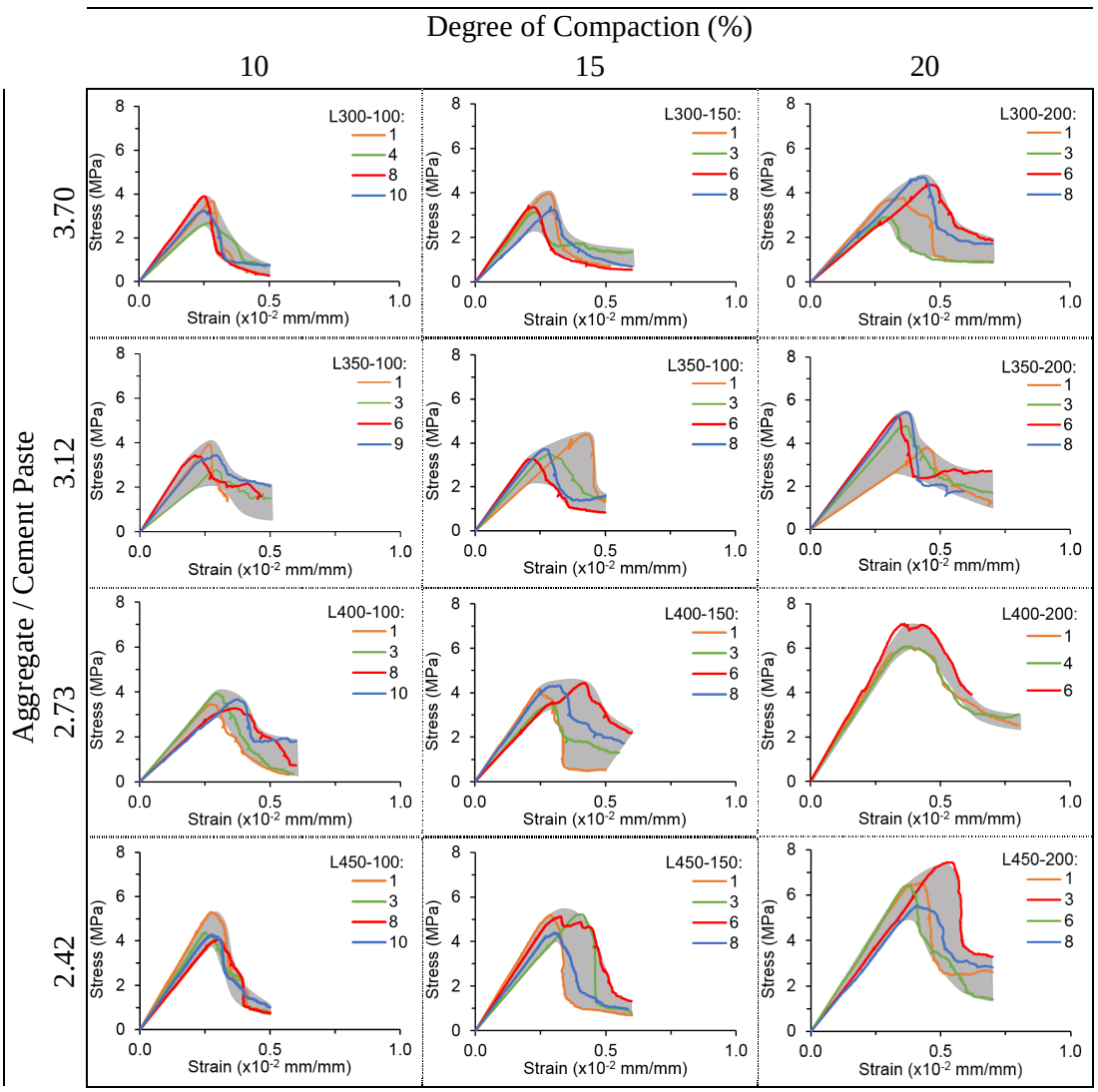

Figure 6.6 – Compressive stress-strain response for the different mix designs and degree of compaction.

The post-peak response is depicted in Fig. 6.7a and comprehends the maximum stress defined by the point C until the specimen reaches complete failure (or the test was stopped) defined by the point D (ε_f , σ_f). This part of the stress-strain curve ($\overline{CD}$) is nonlinear. The post-peak response in the stress-strain curves suggests that the pervious concrete specimens become brittle as the degree of compaction increases. The low A/P ration in this kind of concrete produces a limited volume of cement paste connecting the aggregates. This insufficient connection reduces the possible length for the cracks to grow and propagate, which is related to the brittle behavior observed. The porosity (pore size, distribution and connectively) is random for pervious concretes and influences in the dissipation of energy in the post-peak region. This randomness contributes to the different stress-strain curves obtained experimentally.

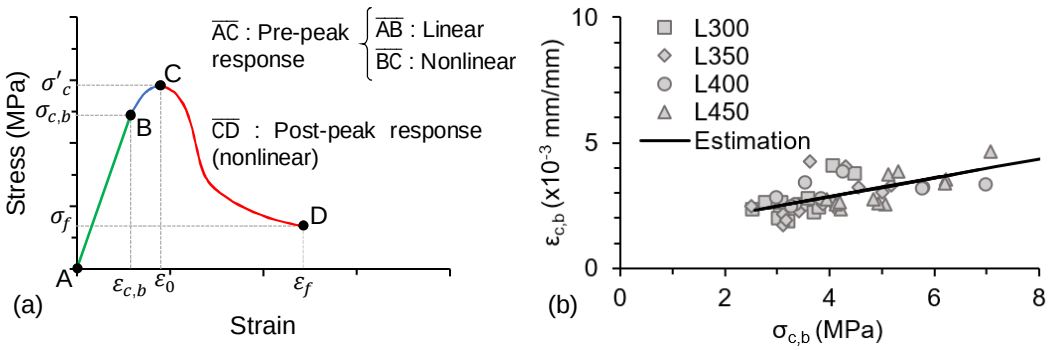

Figure 6.7 – Typical compressive stress-strain response (a) and relation between the coordinates of point B (b).

An analysis to define the coordinates of the point B (in Fig. 6.7a) of all the experimental data was performed, the results are presented in Fig. 6.7b. A linear regression was performed using $\sigma_{c,b}$ as independent variable to estimate $\varepsilon_{c,b}$. The final equation to find estimate $\varepsilon_{c,b}$ ($\varepsilon_{c,b,est}$) is presented in Eq. 6.3. Moreover, the correlation between the $\sigma_{c,b}$ and the compressive strength is expressed in Eq. 6.4.

$$\varepsilon_{c,b,est} = 3.76x10^{-4} \cdot \sigma_{c,b} + 1.35x10^{-3} \tag{6.3}$$

$$\sigma_{c,b} = 0.95 \cdot \sigma'_c \tag{6.4}$$

In order to estimate the complete stress-strain curves the model reported by Lubliner *et al.* [159] was employed with some considerations. Although, the primary use of this model is to simulate the nonlinear behavior of concrete in finite element analysis, its concepts are suitable for this work. For the prediction of the compressive behavior, the model was divided in two portions: linear and nonlinear. The linear portion of the curve is defined when the strain 'ε' is lower than or equal to $\varepsilon_{c,b}$. On the other hand, the nonlinear portion of the curve present strains higher to $\varepsilon_{c,b}$, passing by the peak stress until reaches the complete failure. The final equation to estimate the stress evolution '$\sigma_c(\varepsilon)$' is presented in Eq. 6.5. In this equation, ω_k represents a damage variable which is interpreted as the formation and growth of cracks. Notice that the maximum value possible for the variable ω_k is 1 when a fully damaged condition is reached. More experimental studies are necessary to define the value of the variable ω_k that determines the situation of total failure of the material. However, in this work this situation was assumed when ω_k is 1.

$$\sigma_c(\varepsilon) = \begin{cases} \varepsilon \cdot \dfrac{\sigma_{c,b}}{\varepsilon_{c,b}} & for\ \varepsilon \le \varepsilon_{c,b} \\ \sigma_{c,b}\left(1.63 \cdot \sqrt{1 + 5.64 \cdot \omega_k} - 3.58 \cdot \omega_k - 0.635\right) & for\ \varepsilon > \varepsilon_{c,b} \end{cases} \quad (6.5)$$

$$\omega_k = 1 - 1.45 \cdot e^{\left(-1000 \cdot \frac{\varepsilon}{\varepsilon_{c,b}}\right)} + 0.44 \cdot e^{[-2000 \cdot (\varepsilon - \varepsilon_{c,b})]} \quad (6.6)$$

Fig. 6.8 presents the estimated responses of the stress-strain curves using Eq. 6.5 and Eq. 6.6. The porosity used in this estimation was obtained from Eq. 5.5, where the A/P and the degree of compaction were considered.

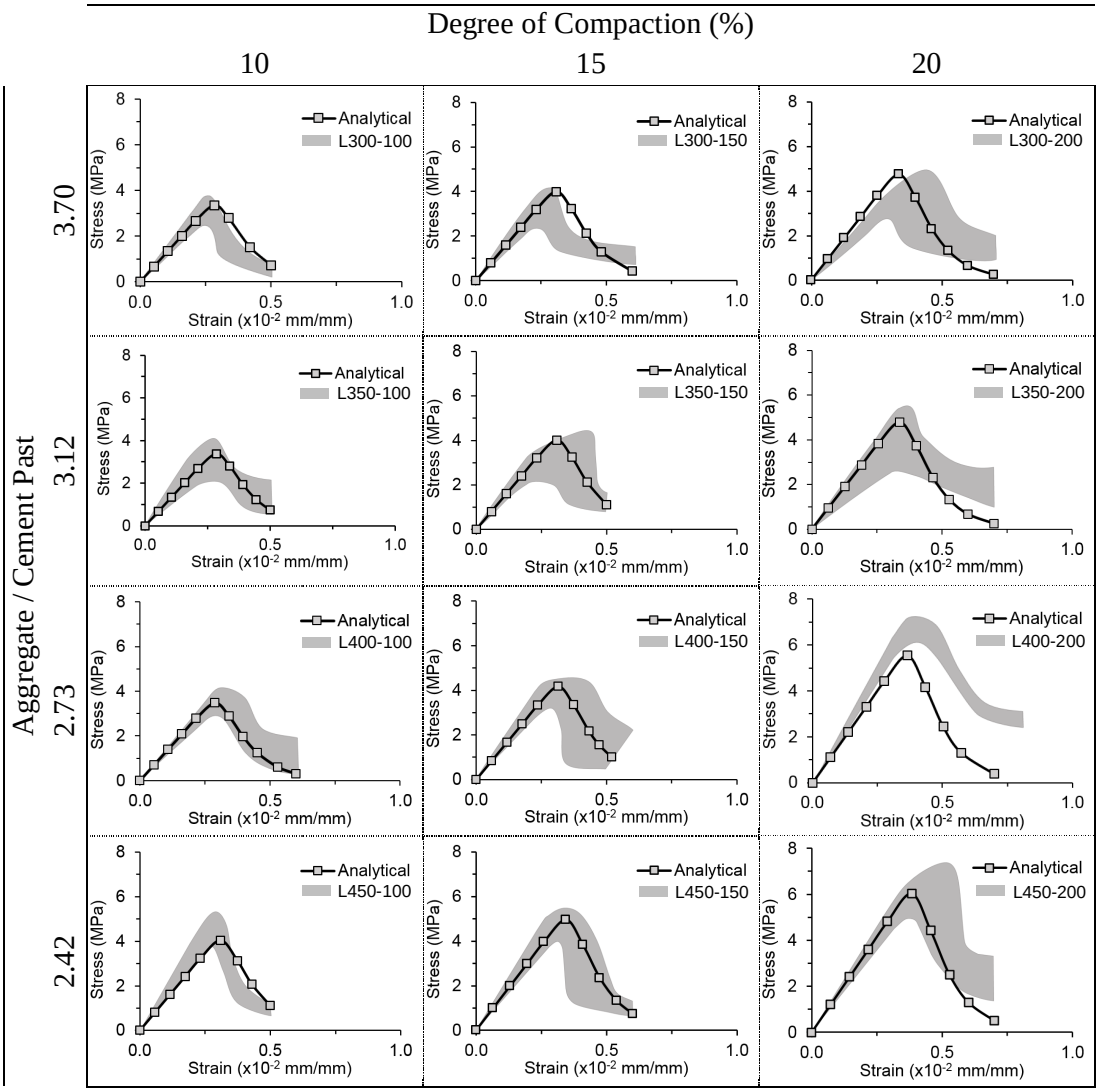

Figure 6.8 – Experimental data and analytical model fits for compressive stress-strain response.

The coordinates of the point B (defined in Fig. 6.7a) were estimated using Eq. 6.5 ($\varepsilon_{c,b}$) and Eq. 6.4 ($\sigma_{c,b}$). In the same way, the coordinates of the point C (defined in Fig. 6.7a) were estimated using Eq. 6.2 (ε_0) and Eq. 6.1 (σ'_c). Moreover, Fig. 6.8 presents the experimental results for all previous concrete specimens in gray shade.

The prediction of the pre-peak response for all compositions and degree compaction are well represented by the model. The prediction with the analytical model agree with the numerical results. A discrepancy between the experimental and analytical results for the group L400-200 was observed. This discrepancy of the results is explained due the group L400-200 was tested with a different press (see Section 6.2.1).

6.3.1.3. Absorbed energy

The total energy absorbed in the test is related with the fracture mechanism observed in pervious concrete. In this sense, the increase of the area under the load-displacement curve increases the absorbed energy.

In this study, two portions of the area under the load-displacement curve were calculated and analyzed. The energy absorbed until the peak load 'W_p' is the area quantified under the load-displacement curve up to the peak load 'P'_c' (correspondent to the peak stress), as depicted in Fig. 6.9a. The area under the load-displacement curve up to one third of the peak load [160] was used to compute the total compressive energy absorption 'W_f', as presented in Fig. 6.9b.

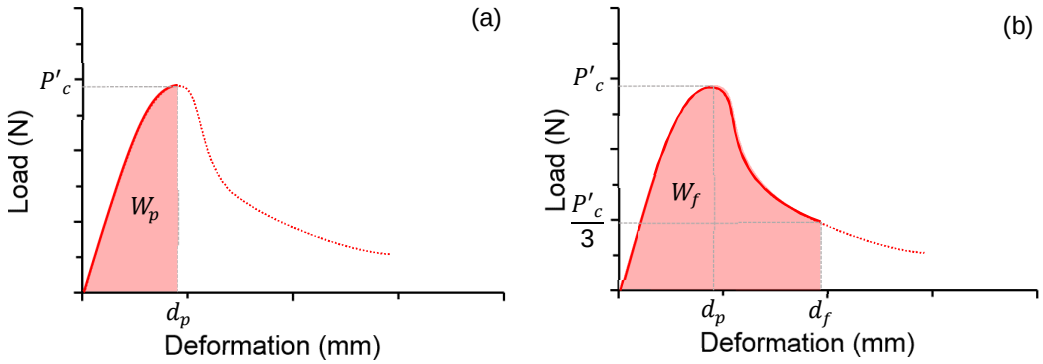

Figure 6.9 – Absorbed energy until peak (a) and total absorbed energy (b).

W_p and W_f were calculated using the experimental results, and also using the analytical curves obtained with Eq. 6.5. The results of both calculations are depicted in Fig. 6.10. This figure presents the results of W_p related with A/P and degree of compaction. It is observed that the W_p increases with higher values of degree of compaction and lower values of A/P. The comparison of the results for equivalent A/P and degree of compaction showed a correlation coefficient (R^2) of 0.893.

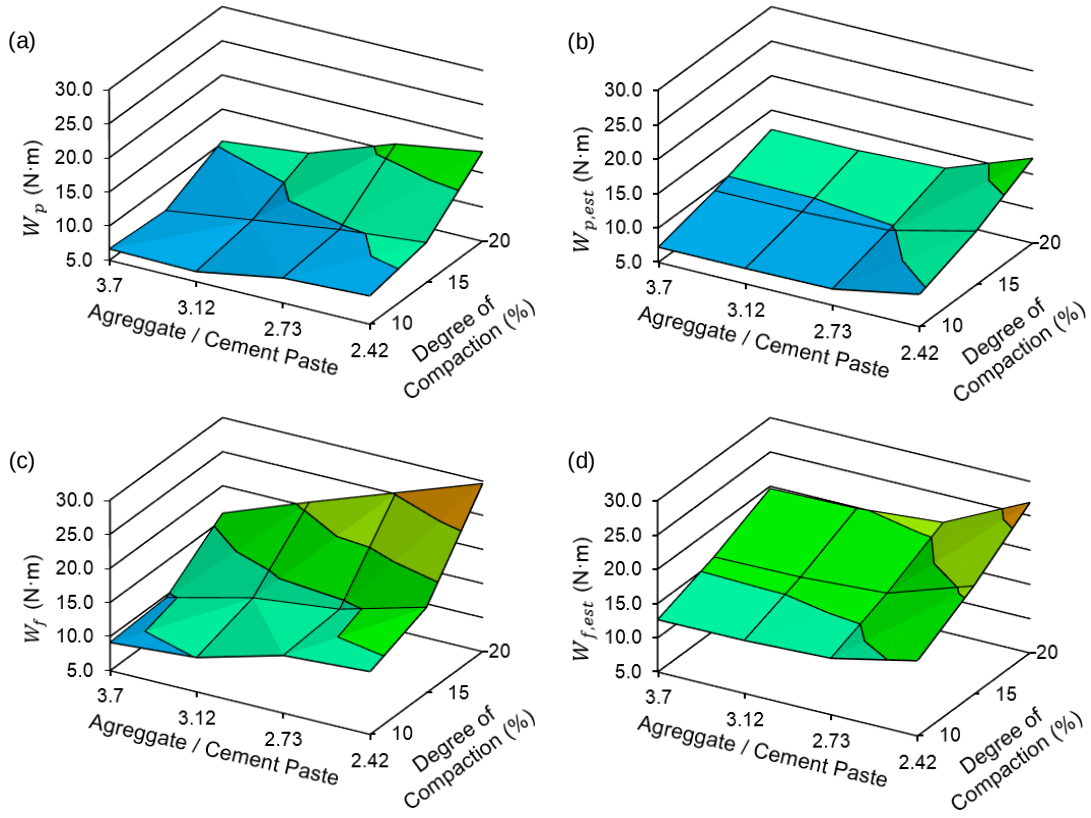

Figure 6.10 – Relationship between A/P, degree of compaction and strain at peak stress, experimental results (a) and estimated results (b).

Fig. 6.10c and 6.10d presents the experimental and estimated results, respectively, of W_f related with A/P and degree of compaction. As well as W_p, the W_f increases with the increasing of the degree of compaction and decreasing of the A/P. The comparison of the results for equivalent A/P and degree of compaction shows a correlation coefficient (R^2) of 0.914. Although the W_p and W_f were estimated by calculating the areas under load-displacement curve presented in Section 6.3.1.2, they may be directly estimated by the porosity using Eq. 6.7 and 6.8, respectively.

$$W_{p,est} = 6.33x10^{-2} \cdot \left[e^{7.80x10^{-2} \cdot (100-P)} - 1\right] \quad (6.7)$$

$$W_{f,est} = 2.20x10^{-1} \cdot \left[e^{6.67x10^{-2} \cdot (100-P)} - 1\right] \quad (6.8)$$

Fig. 6.11a presents the experimental and the estimated (obtained from Eq. 6.7) W_p values. A good fit is observed between the estimation and the experiments. The comparison of the results for equivalent porosity shows a correlation coefficient (R^2) of

0.936. In the same way, Fig. 6.11b presents the experimental and the estimated (obtained from Eq. 6.8) W_f values. The comparison of the results for equivalent porosity shows a correlation coefficient (R^2) of 0.927.

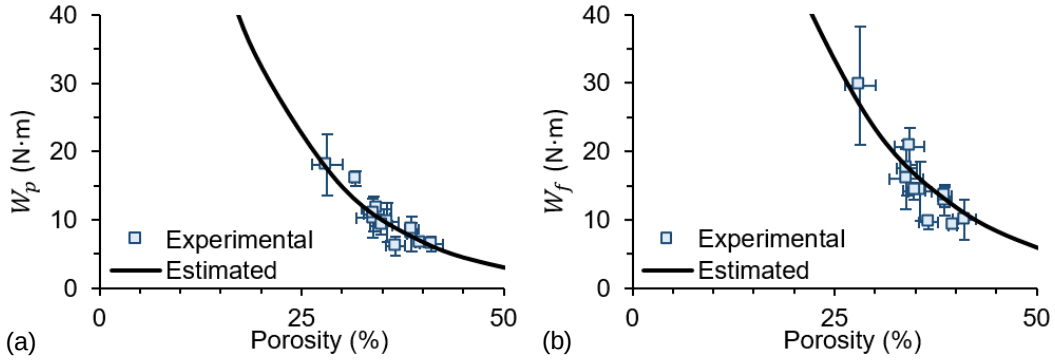

Figure 6.11 – Relationship between porosity and W_p (a) and W_f (b).

6.3.2. Tensile Behavior

The relation between porosity and tensile strength for all specimens are presented in Fig. 6.12a. The tensile strength varies from 0.8 to 1.4 MPa, decreasing exponentially with the porosity. In accordance with the results from literature (see Section 2.2.2).

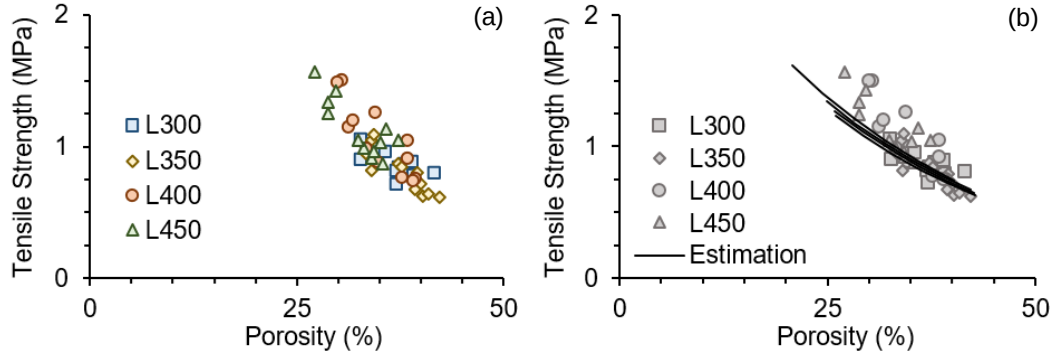

Figure 6.12 – Relationship between porosity and tensile strength.

It is assumed that the studied parameters influence indirectly the tensile strength, in a similar way as discussed for the compressive strength (see Section 6.3.1). In this sense, the nonlinear regression was performed using the porosity as independent variable to obtain the tensile strength. The final equation to find the estimated tensile strength $\sigma'_{t,est}$ is presented in Eq. 6.9.

$$\sigma'_{t,est} = (-1.5x10^{-4} \cdot DoC - 2.95x10^{-3} \cdot A/P + 0.083) \cdot \left[e^{0.04 \cdot (100-P)} - 1\right] \quad (6.9)$$

Fig. 6.12b presents the estimated tensile strength values obtained with Eq. 6.9. A good fit is obtained between the estimation and the experiments. The comparison of the results for equivalent porosity shows a correlation coefficient (R^2) of 0.720.

The adjustment of the Eq. 6.9 was obtained from the experimental results of porosity and tensile strength. However, the porosity may also be predicted with the Eq. 5.5 from the A/P and the degree of compaction. This equation was used within Eq. 6.9 to predict the tensile strength, and a correlation coefficient of 0.876 was obtained. Fig. 6.13 presents the experimental results of tensile strength related with A/P and degree of compaction compared with the estimations given by Eq. 5.5 and Eq. 6.9. The values of the Fig. 6.13a were obtained with the average of the experimental results of each combination.

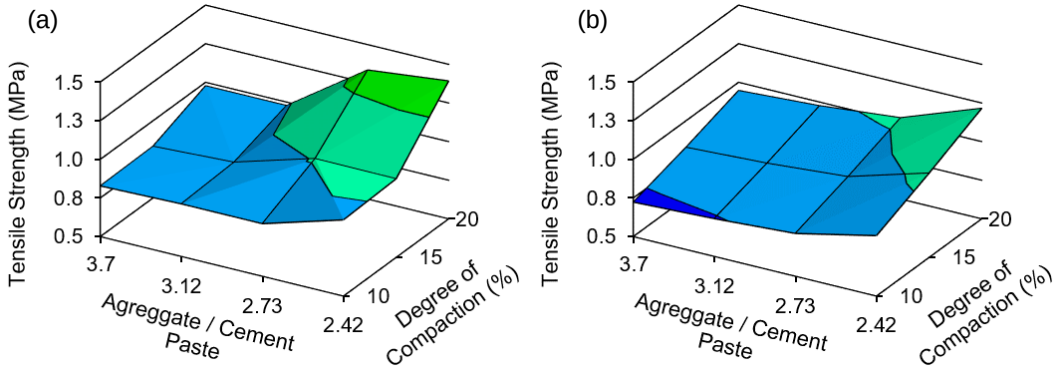

Figure 6.13 – Relationship between A/P, degree of compaction and tensile strength: experimental results (a) and estimated results (b).

6.4. CONSTITUTIVE LAW OF THE CONTACT

6.4.1. Characteristics of the Contact

One of the most important numerical features proposed and incorporated in DEM for the simulation of the pervious concrete properties is the paste redistribution due to the overlap of two particles in contact. The use of this numerical feature was previously discussed in Section 4.4.1 and 5.4.1 for the simulation of the fresh state and the permeability properties, respectively.

The redistribution of the cement paste also presented an important role for the simulation of the mechanical properties of the pervious concrete. In this sense, the contact bridge (CB) formed by the redistribution of the cement paste is calculated for all the interactions. The process of calculation is the same as presented in Section 5.4.1. Fig. 6.14a illustrate the CB consideration for a sphere-sphere (S-S) interaction. The particles are formed by the inner cores (aggregate), the external layers (cement paste) and CB, which depends on the overlap. Fig. 6.14b presents a reduced version of the interaction between two spheres, where the cement paste and the CB are no more represented. In this figure, a line (d_{ref}) that connects the centers of the spheres is represented in green, and an area (A_{s-s}) that crosses perpendicular the line d_{ref} at the contact point $\bar{C}$ is represented in blue. The A_{s-s} is the area responsible to transmit the stress of the interaction between a pair of spheres. Fig 6.14c illustrated a simplified set of the interaction, where only the important geometrical (d_{ref} and A_{s-s}) properties were depicted.

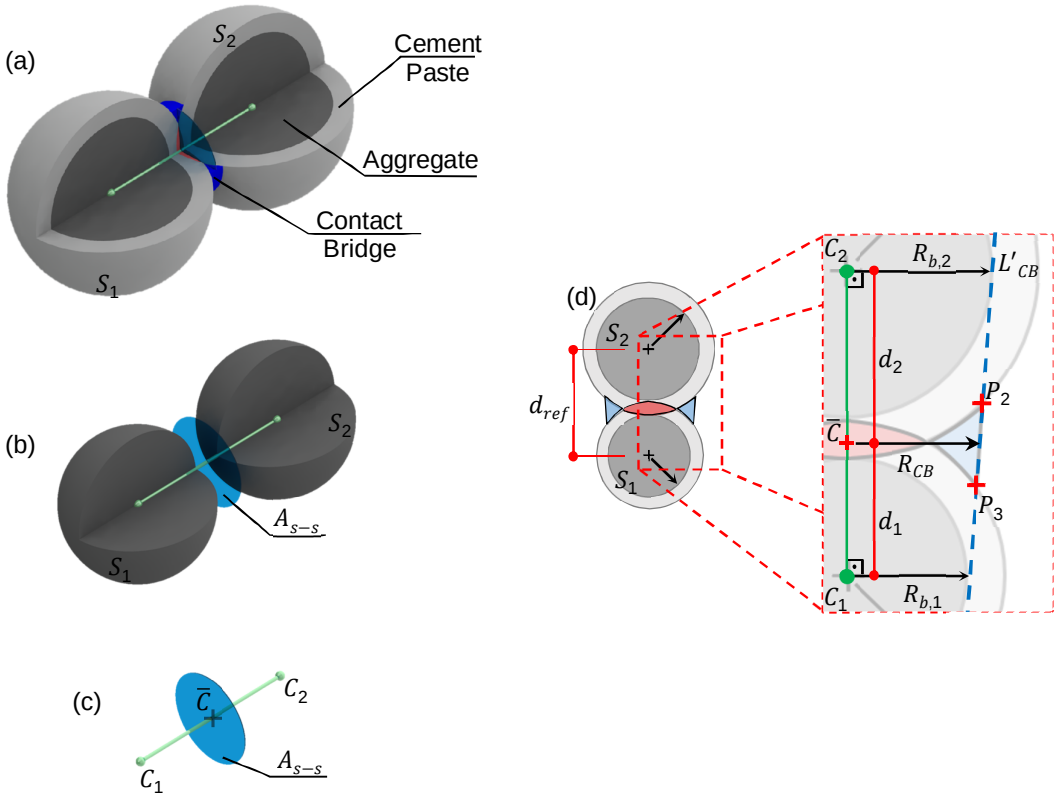

Figure 6.14 – Interaction between two spheres (a-c) and geometrical definitions of the interaction (d).

Fig. 6.14d presents the cross section of the interaction S-S. Once the geometrical porperties of the CB are estimated for a certain interaction, the radius of the cross section of the CB 'R_{CB}' may be calculated with Eq. 6.10. In this equation, d_1 and d_2 are distance

between the center (C_1 and C_2) of the first and second spheres to the contact point $\bar{C}$, $R_{b,1}$ and $R_{b,2}$ are the distances between the center (C_1 and C_2) of the first and second spheres to the line L'_{CB}. Finally, the area A_{s-s} can be easlly calculated by Eq. 6.11.

$$R_{CB} = \frac{R_{b,1} \cdot d_1 + R_{b,2} \cdot d_2}{d_1 + d_2} \tag{6.10}$$

$$A_{s-s} = \pi \cdot R_{CB}^2 \tag{6.11}$$

6.4.2. Material Model

In this section, the material model, which provides the relationship between force 'F' and displacement 'u', is proposed. The material model is divided in two types of interaction, cohesive and non-cohesive. Fig. 6.15 presents a simplified algorithm of the material model with the definitions of the cohesive and non-cohesive interactions along the simulation steps.

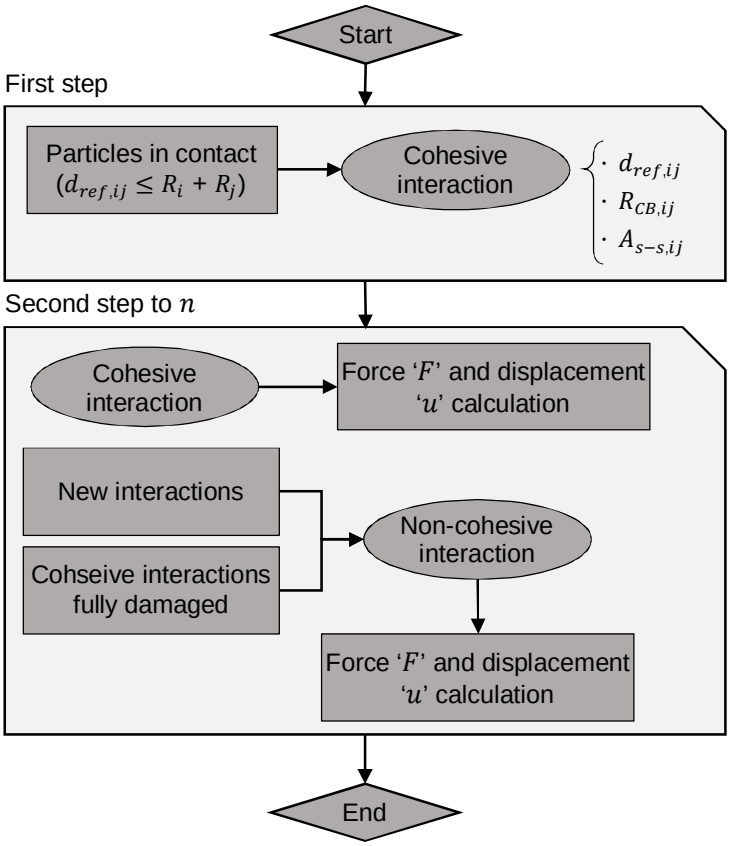

Figure 6.15 – Simplified material model algorithm.

The cohesive interactions are defined at the first step of the simulation and characterize the aggregates bonded by cement paste. In a numerical language the cohesive interactions are defined when the distance between the centers of the spheres '$d_{ref,ij}$' is lower than the sum of the radius of the particles in contact 'R_i' and 'R_j'. On the other hand, the non-cohesive interactions are defined when there is a total damage of the contact, or when a new contact between particles that originally were not in contact is identified.

6.4.2.1. Cohesive constitutive law

The constitutive law proposed by Lubliner *et al.* [159] was selected and adapted to simulate the interaction between two particles bonded by cement paste. This constitutive law was chosen due its extended use in commercial software like ABAQUS [161]. In the DEM, the relative movement between particles might occur in the normal and in the tangential directions. Therefore, it is necessary to establish a constitutive model that represents the behavior of the contact in both directions.

Normal Direction

The contact in the normal direction between two particles bonded by hardened cement paste may transmit tensile (when the distance between the centers of the particles are increasing) and compressive forces (when the distance between the centers of the particles are decreasing). Both forces of particles are represented by similar laws. In this sense, the elastic behavior exists in tension and compression since the beginning of the movement of the particles until a level of strain (or stress) equal ε_b is reached. The elastic behavior is formulated by assuming that the normal stress '$\sigma_N(\varepsilon)$' is proportional to the corresponding strain, as expressed in Eq. 6.12. In this equation, ε represents the strain, ε_b represents the strain where the linear behavior ends and E_0 represents the modulus of elasticity of the contact. The ε_b is different in tension and compression, as defined by Eq. 6.13.

$$\forall\ \varepsilon \leq \varepsilon_b\ : \sigma_N(\varepsilon) = \varepsilon \cdot E_0 \tag{6.12}$$

$$\begin{cases} \forall\ tensile\ : \varepsilon_b \approx \varepsilon_{t,b} = \dfrac{\sigma_{t,b}}{E_0} \\ \forall\ compression\ : \varepsilon_b \approx \varepsilon_{c,b} = \dfrac{10 \cdot \sigma_{t,b}}{E_0} \end{cases} \tag{6.13}$$

After the ε_b is reached, the non-linear behavior takes place. The model consider that for tensile stress the interaction also presents plastic behavior, while for compression stress the interaction is elastic. The formulation proposed by Lubliner *et al.* [159] for the non-linear behavior of the contact is expressed by Eq. 6.14. In this equation, σ_b represents the stress when the non-linear behavior starts, a represents the relation between σ_b and σ', and ω_k represents the damaged variable. The constant a is calculated with Eq. 6.15.

$$\forall\ \varepsilon > \varepsilon_b :\ \sigma_N(\varepsilon) = \frac{\sigma_b}{a}\left[(1+a)\sqrt{1+a(2+a)\omega_k} - (1+a(2+a)\omega_k)\right] \tag{6.14}$$

$$a = \frac{2\sigma'}{\sigma_b} - 1 + 2\sqrt{\left(\frac{\sigma'}{\sigma_b}\right)^2 - \frac{\sigma'}{\sigma_b}} \tag{6.16}$$

The damage variable ω_k may be calculated by Eq. 6.16. This formulation was proposed by Lubliner *et al.* [159] and may serve as either tension or compression with different considerations depending on the case. In this equation, b is a constant that may be correlated to the fracture energy 'g' through Eq. 6.17.

$$\omega_k = 1 - \frac{1}{2+a}\cdot\left\{2(1+a)e^{\left(-b\cdot\frac{\varepsilon}{\varepsilon_b}\right)} - a\cdot e^{[-2b\cdot(\varepsilon-\varepsilon_b)]}\right\} \tag{6.16}$$

$$b = \frac{\sigma_b}{g}\left(1+\frac{a}{2}\right) \tag{6.17}$$

For tension the stress that corresponds to the beginning of the non-linearity '$\sigma_{t,b}$' and the maximum tensile stress 'σ'_t' are considered to be equal. In this sense, the constant a calculated with Eq. 6.15 results in 1, as defined in Eq. 6.18. Considering $a = 1$, Eq. 6,15 may be reduced to Eq. 6.19, and Eq. 6.16 may be reduced to Eq. 6.20.

$$\sigma'_t = \sigma_{t,b} \ \therefore\ a = 1 \tag{6.18}$$

$$\forall\ \varepsilon > \varepsilon_b\ AND\ tensile :\ \sigma_N(\varepsilon) = \sigma_{t,b}\left[2\sqrt{1+3\omega_k} - (1+3\omega_k)\right] \tag{6.19}$$

$$\forall\ tensile :\ \omega_k = 1 - \frac{1}{3}\cdot\left\{3\cdot e^{\left(-b\cdot\frac{\varepsilon}{\varepsilon_{t,b}}\right)} - e^{[-2b\cdot(\varepsilon-\varepsilon_{t,b})]}\right\} \tag{6.20}$$

In the case of compression, an adaptation is made when the maximum compression stress is reached. In this specific case, the resistant capacity is maintained. This adaptation is expressed by Eq. 6.21.

$$\forall\ \sigma_N(\varepsilon) > \sigma'_c\ :\ \sigma_N(\varepsilon) = \sigma'_c \tag{6.21}$$

Fig. 6.16a presents a typical relation between stress and strain in tensile in a load-unload model. The load process starts elastic (solving the Eq. 6.12), represented by the curve $\overline{AB}$. The maximum tensile stress '$\sigma_{t,b} \approx \sigma'_t$' is reached at the point B. If the load process continues, the behavior of the interactions becomes non-linear (solving the Eq. 6.19 and 6.20). Suppose now that the load process continues until the point C is reached, than the unload takes place. During the load from B to C, a plastic damage 'w_k' was inflicted to the contact. This damage produces a reduction in the modulus of elasticity, since the contact is damaged. The damaged modulus of elasticity may be estimated through Eq. 6.22. In this sense, the unload process produces a plastic and elastic strain, ε_t^{pl} and ε_t^{el} respectively.

$$E_d = (1 - w_k)E_0 \tag{6.22}$$

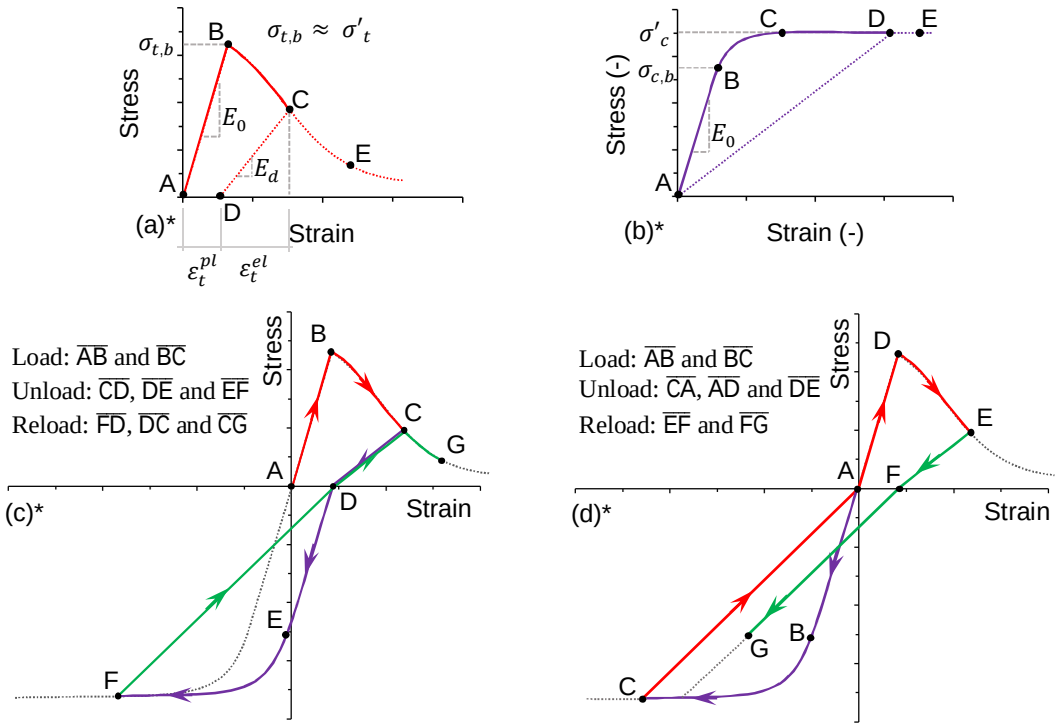

* The curves are not in scale

Figure 6.16 – Typical relation between normal stress and normal strain in tensile (a) and in compression (b), load-unload-reload model (c).

Fig. 6.16b presents a typical relation between stress and strain in compression in a load-unload model. Similar to the tensile behavior, the load process starts elastic (solving the Eq. 6.12), represented by the curve $\overline{AB}$. The compression stress '$\sigma_{c,b}$' is reached at the point B. If the load increases, the behavior of the contact becomes non-linear (solving the Eq. 6.14 and 6.16). The point C is related to the maximum compression stress 'σ'_c'. From this point on, the stress is maintained regardless of the strain. At the point D, the unload process takes place. Differently to the tensile behavior, the strains (or deformations) are totally recovered.

Fig. 6.16c presents a typical relation between stress and strain in a load-unload-reload model beginning in tension, and then alternating between compression and tensile. Fig. 6.16d presents a typical relation between stress and strain in a load-unload-reload model beginning in compression than passing through tensile-compression.

As disscused previously, the formulations soves the motion equations in DEM using force and displacement. In this sense, the normal stress calculated by the proposed model should be transformed in normal force 'F_N' using Eq. 6.23.

$$F_N = \sigma_N \cdot A_{s-s} \tag{6.23}$$

Tangential Direction

The contact in the tangential direction between two particles bonded by hardened cement paste transmits shear forces. In a first moment, the behavior of the contact is elastic. The elastic behavior is formulated by assuming that the shear stress 'σ_T' is proportional to the corresponding tangential strain 'ε_T', as expressed in Eq. 6.24. In this equation, G_0 represents the shear modulus of the contact.

$$\sigma_T(\varepsilon_T) = \varepsilon_T \cdot G_0 \tag{6.24}$$

The Mohr-Coulomb failure criteria is used to determine the fracture surface. This criteria is represented by the relation between the shear and normal stress, expressed in Eq. 6.25. In this equation, $\sigma_{T,y}$ represents the yield shear stress, C_d represents the cohesion (or the point where the failure envelope intercepts the shear stress axis), σ_N represents the applied normal stress and φ_d represents the angle of internal friction (or the slope of the failure envelope).

$$\sigma_{T,y} = C_d - \sigma_N \cdot tan\,\varphi_d \tag{6.25}$$

The cohesion and the internal friction depends on the damage variable 'w_k'. The cohesion is estimated by Eq. 6.26. In this equation, C_0 represents the cohesion with no damage (or the virgin cohesion). In case the contact is fully damaged, the cohesion is null. The internal friction is estimated by Eq. 6.27. In this equation, φ_0 represents the internal friction with no damage (or the virgin internal friction) and φ_r represents the fully damage internal friction. In Eq. 6.26 and 6.27, β_C and β_φ are parameters that control the shape of the damage curves. The parameters β_C and β_φ may represent a line or a curve of damage evolution between the parameters C_0 and φ_0, as depicted in Fig. 6.17.

$$C_d = \left[1 - \frac{w_k \cdot e^{\beta C}}{1 + w_k \cdot (e^{\beta C} - 1)}\right] C_0 \tag{6.26}$$

$$\varphi_d = (\varphi_0 - \varphi_r) \cdot \left[1 - \frac{w_k \cdot e^{\beta \varphi}}{1 + w_k \cdot \left(e^{\beta \varphi} - 1\right)}\right] C_0 + \varphi_r \tag{6.27}$$

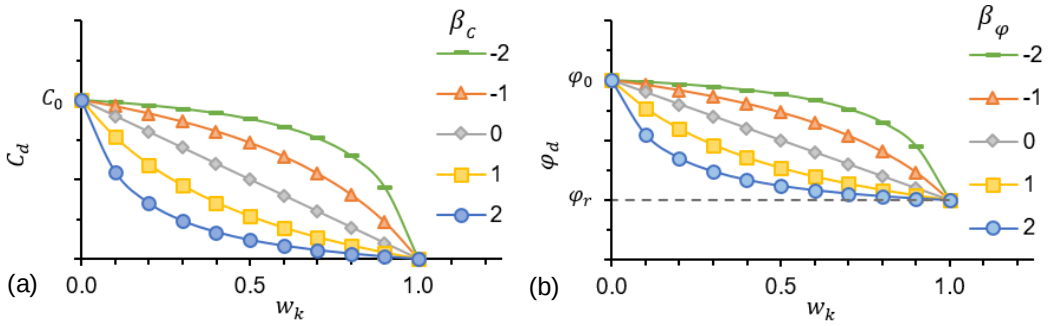

Figure 6.17 – Relation between the damage variable with the cohesion (a) and with the internal friction (b) according to different values of β.

Fig. 6.18 presents the evolution of the failure surface (or the failure envelop) of the virgin and the fully damaged material. It is observed that the interception point of the failure envelop with the shear stress axis and the slope of the failure envelop decrease with the evolution of the damage in the contact. The evolution of the damage affects the cohesion due to decrease of the contact surface, and the internal friction due also to decrease of the contact surface and the beginning of displacement.

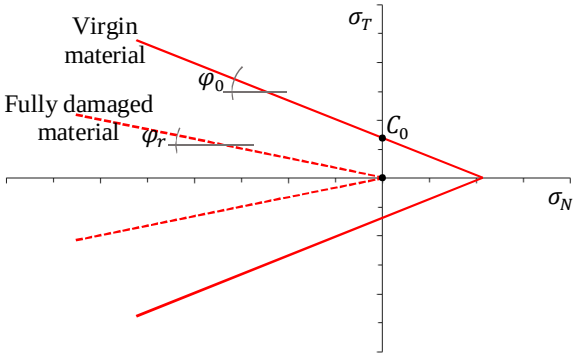

Figure 6.18 – Evolution of the failure surface.

In order to apply the Mohr-Coulomb failure criteria, the shear stress '$\sigma_T(\varepsilon_T)$' calculated with Eq. 6.24 migth be compared to the failure shear stress '$\sigma_{T,y}(\sigma_N)$' calculated with Eq. 6.25. If the shear stress is lower than the failure shear stress there is no plastic slip between the particles. However, if the shear stress is higher than the failure shear stress there is rupture in the contact and the shear stress is update to the same value as the failure shear stress, as expressed in Eq. 6.28.

$$\begin{cases} \forall\ \sigma_T(\varepsilon_T) \leq \sigma_{T,y}(\sigma_N) : \ \sigma_T(\varepsilon_T) = \sigma_T(\varepsilon_T) \\ \forall\ \sigma_T(\varepsilon_T) > \sigma_{T,y}(\sigma_N) : \ \sigma_T(\varepsilon_T) = \sigma_{T,y}(\sigma_N) \end{cases} \tag{6.28}$$

The same as normal stress, the sehar stress calculated by the proposed model should be transformed in shear force 'F_T' using the Eq. 6.29.

$$F_T = \sigma_T \cdot A_{s-s} \tag{6.29}$$

6.4.2.2. Non-cohesive constitutive law

The non-cohesive interaction in the normal direction transmits only compression forces. The forces in compression 'F_N' are governed by a linear elastic law, as expressed in Eq. 6.30. In this equation, the normal stiffness 'k_N' is estimated with Eq. 6.31 and 'u_N' represents the normal overlap of the particles.

$$F_N(u_N) = \begin{cases} \forall\ tension\ : \ 0 \\ \forall\ compression\ : \ k_N \cdot u_N \end{cases} \tag{6.30}$$

$$k_N = \frac{2 \cdot E_1 \cdot R_1 \cdot E_2 \cdot R_2}{E_1 \cdot R_1 + E_2 \cdot R_2} \tag{6.31}$$

The interaction in the tangential direction between two particles is governed by the Mohr-Coulomb plasticity surface without cohesion. The shear force 'F_T' is calculated by Eq. 6.32. In this equation, the tangential stiffness 'k_T' is estimated with Eq. 6.33 and 'u_T' represents the tangential overlap of the particles.

$$F_T(u_T) = k_T \cdot u_T \tag{6.32}$$

$$k_T = \frac{2 \cdot G_1 \cdot R_1 \cdot G_2 \cdot R_2}{G_1 \cdot R_1 + G_2 \cdot R_2} \tag{6.33}$$

The maximum value of the shear force '$F_{T,y}$' is defined by the plasticity condition, through Eq. 6.34. In this equation 'φ' is the friction angle.

$$F_{T,y}(F_N) = F_N \cdot tan\,\varphi \tag{6.34}$$

In order to apply the Mohr-Coulomb plasticity criteria, the shear force '$F_T(u_T)$' calculated with Eq. 6.32 migth be compared to the maximum shear force '$F_{T,y}(F_N)$' calculated with Eq. 6.34. If the shear force is lower than the maximum shear force there is no plastic slip between the particles. However, if the shear force is higher than the maximum shear force there is plastic slip between particles and the shear force is updated to the same value of the maximum shear force, as expressed in Eq. 6.35.

$$\begin{cases} \forall\, F_T(u_T) \leq F_{T,y}(F_N) : \; F_T(u_T) = F_T(u_T) \\ \forall\, F_T(u_T) > F_{T,y}(F_N) : \; F_T(u_T) = F_{T,y}(F_N) \end{cases} \tag{6.35}$$

6.5. MODEL GENERATION

The geometrical models used for the simulation of the mechanical properties of the pervious concrete in this chapter were the same described in Section 5.4. However, modifications regarding the simulation of the bottom and top plates of the press were necessary. Fig. 6.19a and 6.19b present a rendered geometrical model of the pervious concrete specimen assembled for the compressive and Brazilian test, respectively. The

constitutive law between particles (that represented the pervious concrete) and the plates of the press were defined as pure elastic. The velocity of the top plate displacement was equals $1.67x10^{-6}$ m/s (0.1 mm/min) for both simulations (the same velocity used in the experimental program).

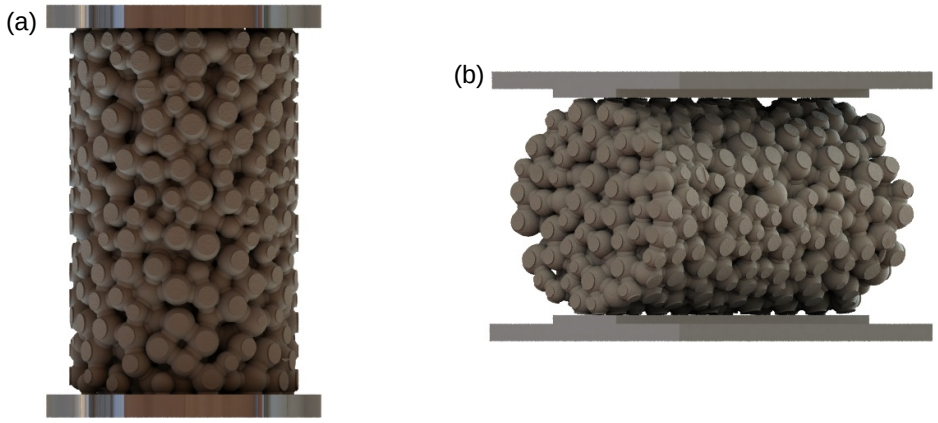

Figure 6.19 – Geometrical model of a pervious concrete specimen for compression (a) and Brazilian test (b).

6.6. NUMERICAL SIMULATION

In this section, the procedure used to calibrate and validate the constitutive law (proposed in Section 6.4) is presented and discussed. The constitutive law depends on a set of parameters that needs to be calibrated. These parameters are described in Tab. 6.1. Moreover, α_{eq} is used in the constitutive law to represent the relation between aggregate and cement paste (A/P), as discussed in Section 6.4.1. In order to simulation the different A/P ratios, the values of α_{eq} used were 0.08272, 0.09512, 0.10715 and 0.11887 for the A/P ratios of 3.7, 3.12, 2.73 and 2.42, respectively (the same presented in Tab. 5.2). The A/P ratios were obtained from the experimental program.

Table 6.1 – Parameters of the constitutive law.

Symbol		Description	Values
E_0 (Pa)	→	Modulus of elasticity of the contact	9.38×10^9
ν	→	Coefficient of Poisson	0.2
σ'_t (Pa)	→	Tensile strength	4.35×10^6
a_t	→	Relation between $\sigma_{b,t}$ and σ'_t	1
g_t (Pa)	→	Tensile energy of fracture	7.06×10^4
a_c	→	Relation between $\sigma_{b,c}$ and σ'_c	3.42
g_c (Pa)	→	Compressive energy of fracture	8.93×10^5
G_0 (Pa)	→	Shear modulus of the contact	$G_0 = \frac{E_0}{2(1+\nu)}$
C_0 (Pa)	→	Initial cohesion	7×10^6
φ_0 (rad)	→	Initial angle of fracture	0.5
φ_r (rad)	→	Fully damaged angle of fracture	0.4
β_C	→	Parameter that controls the shape of the cohesion evolution	1
β_φ	→	Parameter that controls the shape of the angle of fracture evolution	1
α_{eq}	→	Parameter that estimates the A/P ratio	--

The calibration of the parameters of the constitutive law was obtained through the best fitting of the complete stress-strain curve and the tensile strength relevant to the experimental results of the group L450-200. In this sense, the best fitting of the complete stress-strain curve was reached through a heuristic technique based on a visual assessment of the agreement between the average response of the 4 experimental results of the group L450-200 and the numerical result obtained by averaging the numerical response of the 4 models with different meso-structure distribution (generated aleatory). The values of the parameters of the constitutive law are reported in Tab. 6.1.

Finally, the validation of the model was performed by simulating the experimental test (reported in Section 6.3) that were not used in the calibration. It is important to remark that in the validation no additional adjustment of the parameters was permitted.

In the sequence, the results from the numerical simulation are discussed. First a comparison between the numerical and experimental results of the compressive behavior including compressive strength, complete stress-strain curve, absorbed energy and

fracture behavior. Then, the comparison between the numerical and experimental results of the tensile behavior, regarding the tensile strength and the fracture behavior.

Notice that in this section the nomenclature top and bottom of the specimen (or model) were used to indicate the face and opposite face that received the compaction loads, respectively.

6.6.1. Compressive Behavior

The relation between numerical results of porosity and compressive strength for all models are presented in Fig. 6.20a. The compressive strength of the models range between 1.5 and 7.0 MPa, decreasing exponentially with the porosity. A comparison between the numerical and experimental results of compressive strength depending on the porosity is given in Fig. 6.20b. It is observed that the scatter of the numerical and experimental results are similar. This highlights the capability of the model to simulate the variability of the pervious concrete regarding the difference in the mesostrucural dispersion of the aggregates. With higher porosities the numerical model shows lower values of compressive strength than the expected.

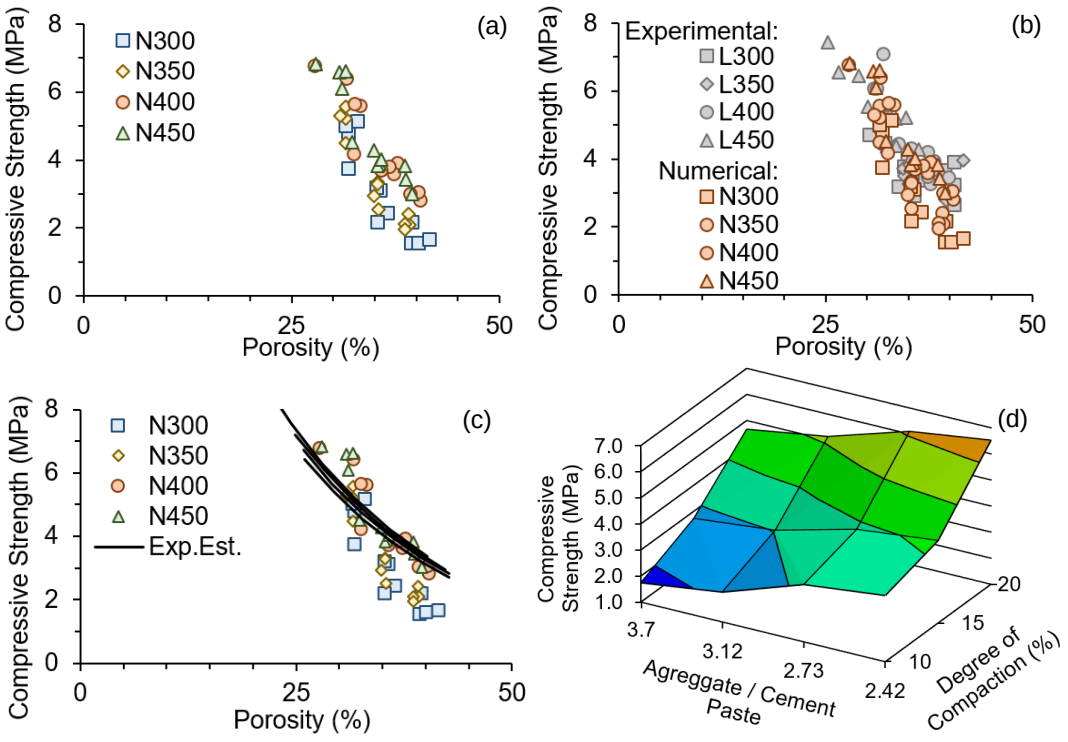

Figure 6.20 – Numerical and experimental compressive strength depending on the porosity.

A comparison between the numerical results and the estimation of the experimental results (calculated with Eq. 6.1) is presented in Fig. 6.20c. Overall, the model predicts well the compressive strength for the pervious with different A/P ratio and porosities. The model predicts correctly the increase of concrete strength due to the increase of the degree of compaction, as depicted in Fig. 6.20d. The response of the models with A/P ratios of 3.7 and 3.12 with 10 % of applied degree of compaction are somewhat less accurate, but still satisfactory. This is due to the fact that in these cases the low paste content combined with low degree of compaction and the spherical particles conducted to a contact area 'A_{s-s}' between two particles that seems to be lower than the contact area in real specimens. Consequently, the model is not capable of fully reproducing the fine features of the specimen.

6.6.1.1. Stress-strain curve

Fig. 6.21 shows the comparison between experimental and numerical stress-strain curves for all models. The gray areas are the experimental results and the colored solid curves are the results of the numerical simulations. It is observed that the model predicted well the pre-peak and post-peak response for the models with all A/P ratios and degree of compaction of 15 and 20 %. For the models with lower degree of compaction, the imperfections regarding the contact area (as discussed in Section 6.6.1) affected the post-peak, and as the A/P ratio increases the accuracy of the model prediction of the pre-peak decreases.

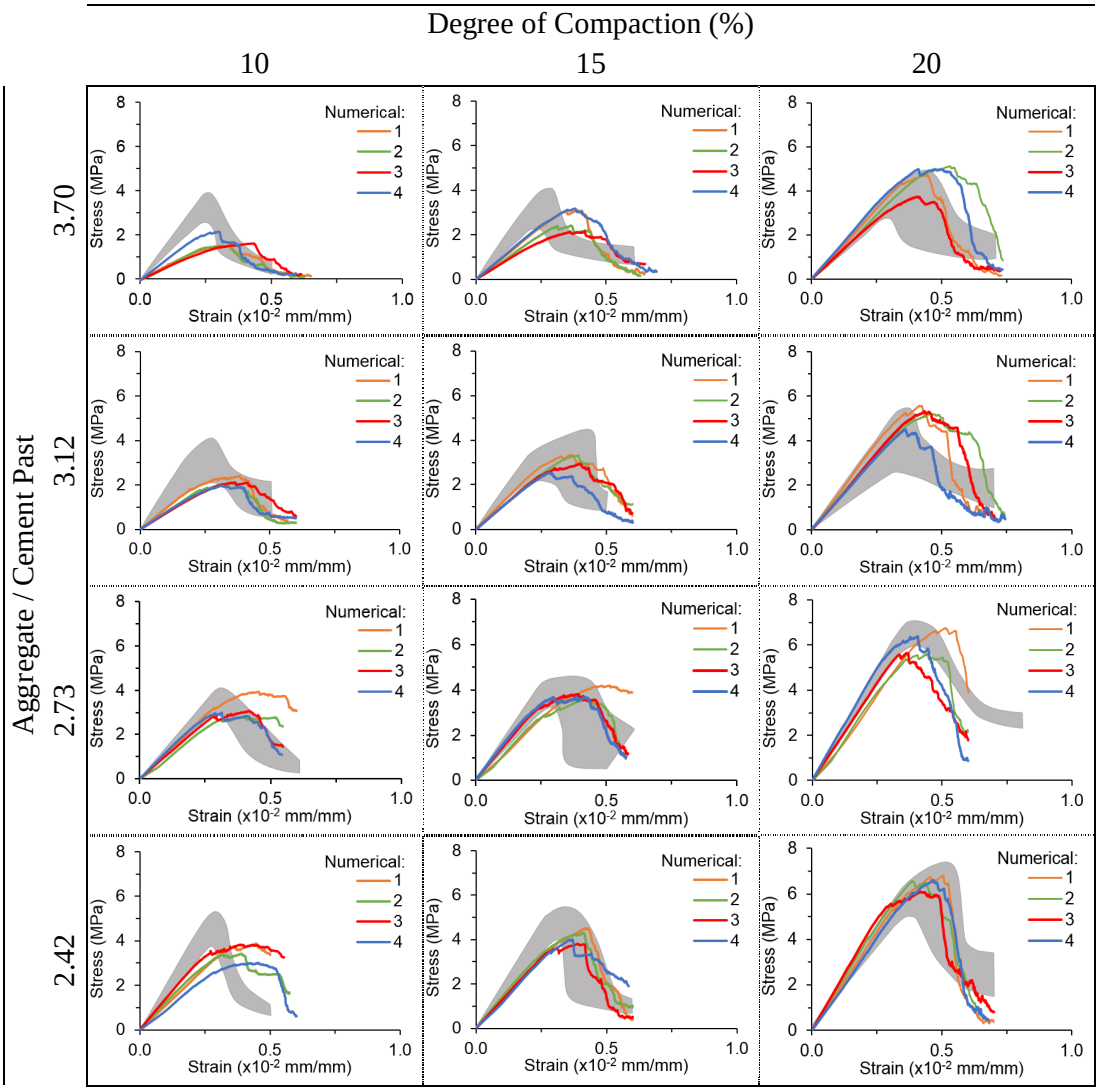

Figure 6.21 – Numerical and experimental data for compressive stress-strain response.

6.6.1.2. Fracture behaviour

Fig. 6.22 presents a comparison between photos of the experimental specimens after cracking and the respective models with contours of meso-scale damage. Fig. 6.22a shows a photo with the typical plane of fracture observed in the specimens of pervious concrete with 10 % of degree of compaction. The type of compaction and the low energy applied conducted to a specimen with more porosity in the bottom than in the top (as discussed in Section 5.5.2). Because of that the failure occurred frequently in the bottom of the specimen. Indeed, the models predicted satisfactory the fracture of pervious concrete with 10 % of degree of compaction with failure characterized by localized damage in the bottom of the model, as observed in Fig. 6.22b.

For the degrees of compaction of 15 and 20 % two typical typologies of planes of fracture were observed. On one hand, the cracks propagates through one side to the other of the specimen with a failure characterized by shear bands with an inclination of about 45º, as observed in Fig. 6.22c. The models with more than 15 % of degree of compaction predicted this type of rupture satisfactory. Fig. 6.22d presents the numerical result of a model with 15 % of degree of compaction. An isolated damage is observed in the model due to the small contact area between some aggregates. This leaded to fragile failure. An isolated cracks were also observed in the experimental tests.

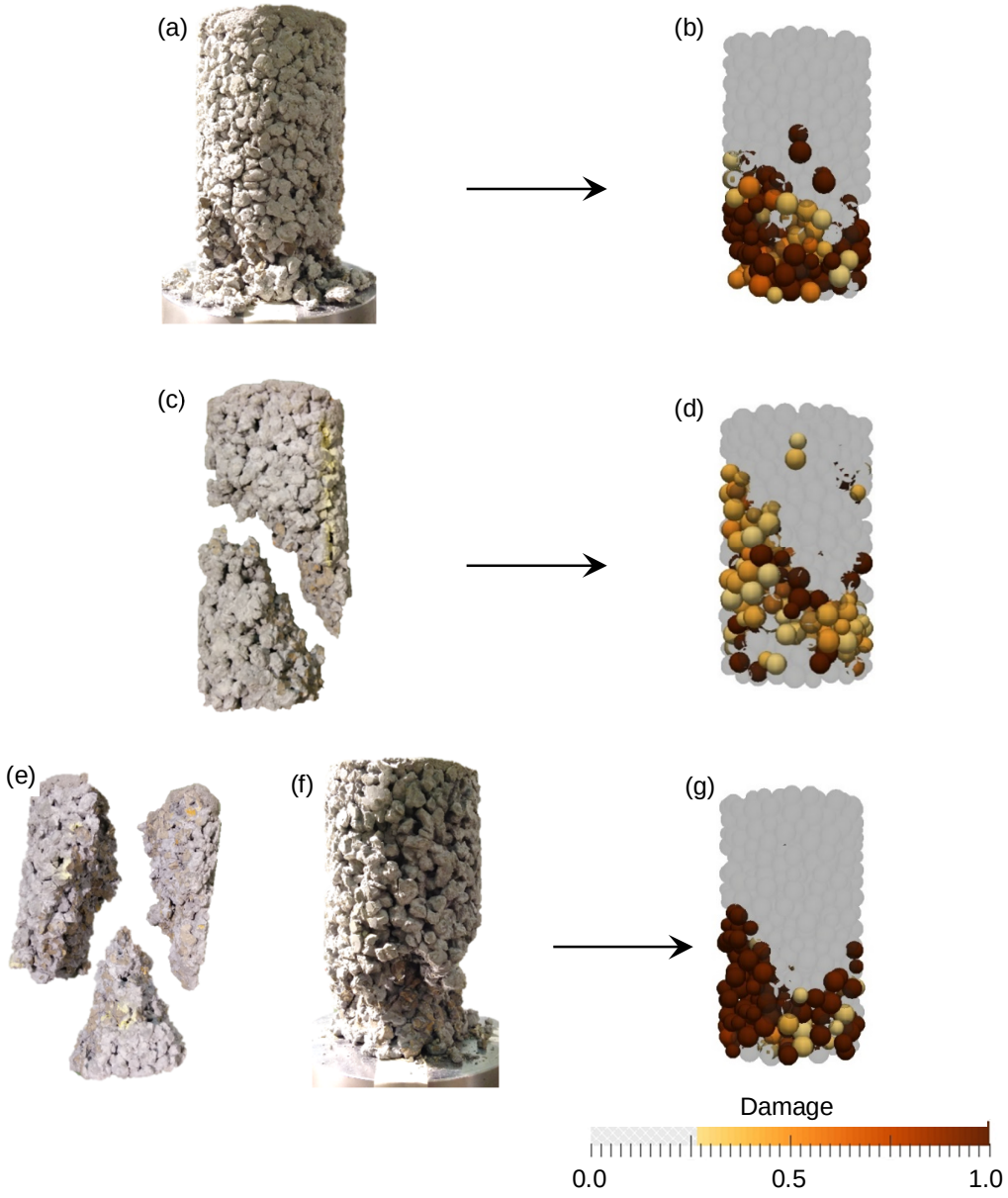

Figure 6.22 – Experimental fracture behavior (a-c-e-f) and numerical contours of meso-scale damage (b-d-g) at compressive loads.

The other type of failure observed in the specimens with more than 15 % of degree of compaction was the formation of vertical crack that extend to the height of the specimen, as observed in Fig. 6.22e. Fig. 6.22f shows the same specimen slightly before the total failure, where part of the cone on the bottom of the specimen is visible. This pattern of fracture was also observed in some models, as presented in Fig. 6.22g. The discussed failures observed in the numerical models are an evidence of the good predictions provided by the constitutive law.

6.6.2. Tensile Behavior

The relation between numerical results of porosity and tensile strength for all models are presented in Fig. 6.23a. The tensile strength of the models range between 0.5 and 1.5 MPa, decreasing exponentially with the porosity. A comparison between the numerical and experimental results of tensile strength depending on the porosity is given in Fig. 6.23b. It is observed that the scatter of the numerical results are similar. This scatter, also observed in the results of compressive models, shows that meso-structures obtained with the compaction model (Chapter 4) reproduces satisfactory the variability observed in pervious concrete.

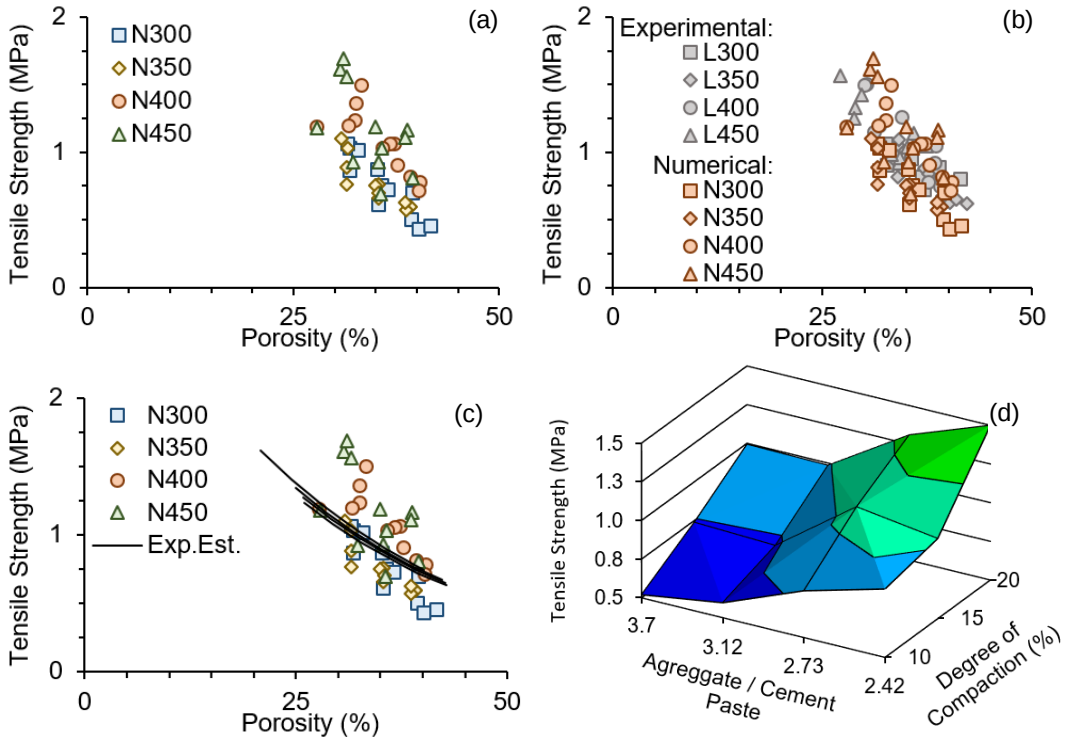

Figure 6.23 – Numerical and experimental tensile strength depending on the porosity

Fig. 6.23c presents a comparison between the numerical and the analytical (calculated with Eq. 6.9) of the tensile strength. Generally, the model predicts well the tensile strength for the pervious with different A/P ratio and porosities obtained with the Brazilian Test. Specially, the model predicts correctly the increase of tensile strength due to the increase of the degree of compaction, as depicted in Fig. 6.23d. The same problems observed in the compressive simulations was also observed here, the numerical results that simulated the models with A/P ratios of 3.7 and 3.12 with 10 % of degree of compaction ware lower than the expected. As discussed in Section 6.6.1, this is related to the simplification of the particles as spheres combined with low paste content and low degree of compaction.

6.6.2.1. Fracture behaviour

Fig 6.24 presents a visual comparison between photos of the experimental specimens after the failure and the corresponding models with contours of meso-scale damage. Fig. 6.24a shows a photo with the typical failure observed on the top of the specimens of pervious concrete with more than 15 % of degree of compaction. In comparison, Fig. 6.24b presents a typical distribution of the meso-scale damage on the top face of the models with more than 15 % of degree of compaction after the failure in the simulation of Brazilian Test.

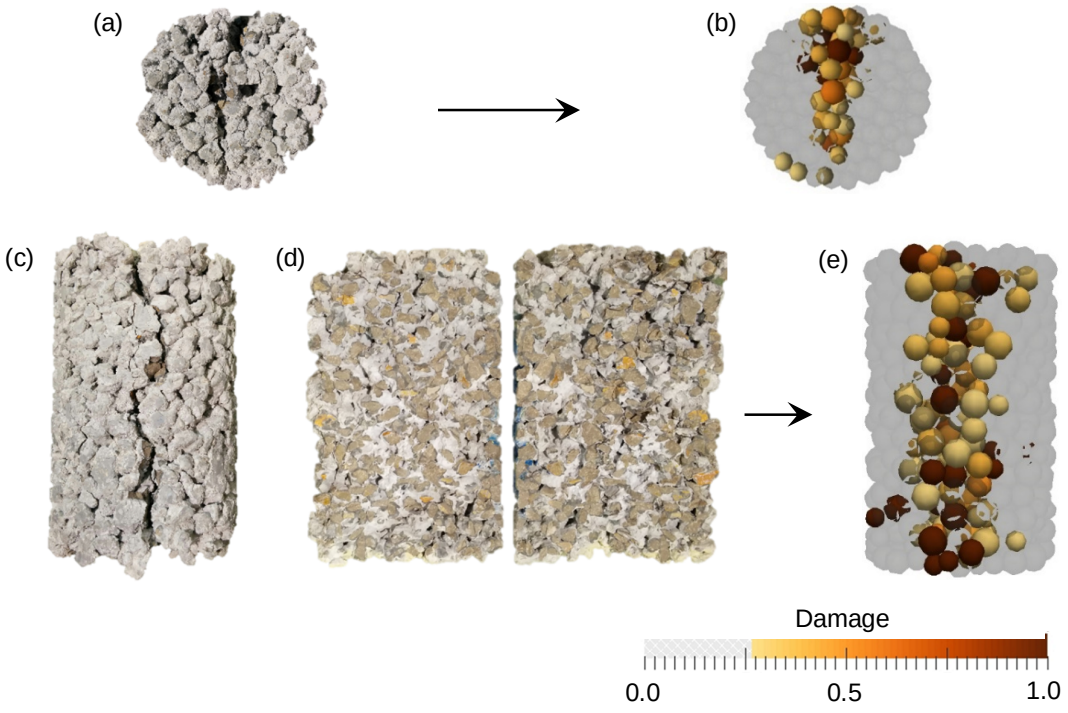

Figure 6.24 – Experimental and numerical typical fracture plane in specimens with more than 15 % of degree of compaction.

The crack initiated, in the case of experiments, on the face that was in contact with the application area of loads (see Fig. 6.24c), and the same was reproduced in the numerical model (see Fig. 6.24e). Fig. 6.24d shows the specimen after the total failure. The division of the specimen at the middle was observed in the specimens with more than 15 % of degree of compaction.

Fig. 6.25a shows the failure in the top of the specimen with 10 % of degree of compaction. In comparison, Fig. 6.25b presents a typical distribution of the meso-scale damage on the top face of the models with same characteristics as the specimen of the Fig. 6.25a.

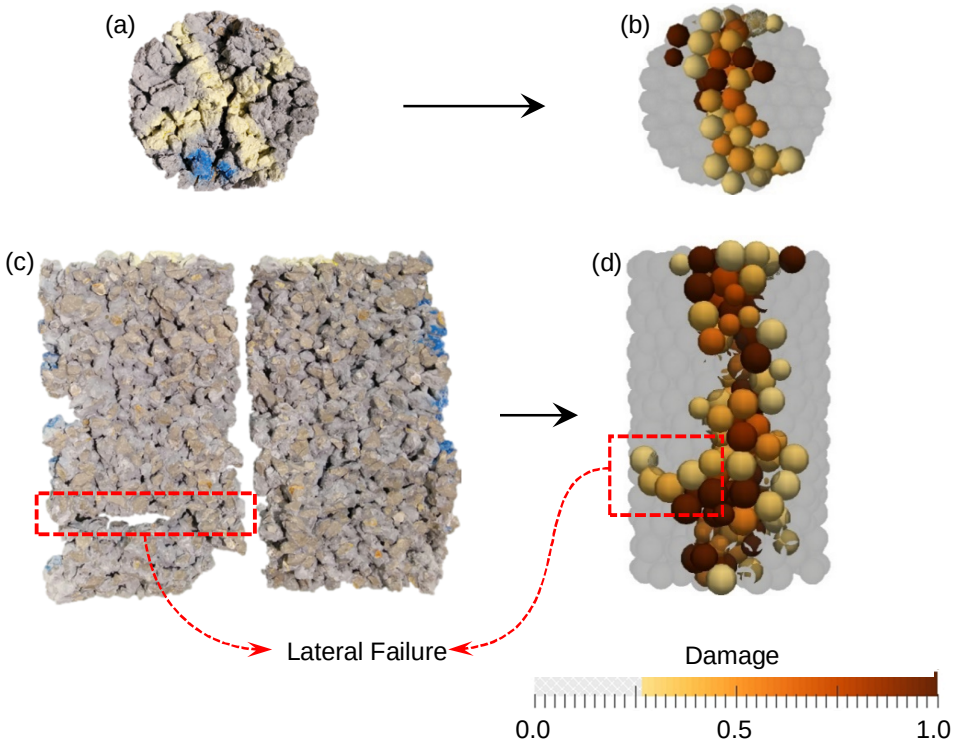

Figure 6.25 – Experimental and numerical typical fracture plane in specimens with 10 % of degree of compaction.

As discussed in Section 6.6.1.2, the failure that was commonly observed in the specimens with low compaction (10 % of degree of compaction) after the rupture in the Brazilian Test is different than the failure observed in the specimens with more compaction. This difference is better observed after the total failure of the specimen, as presented in Fig. 6.25c. The lateral failure in one side of the bottom of the specimen was generally observed in this cases. This characteristic failure was also observed in the simulations. The meso-scale damage on the side of the model where the load was applied is observed in Fig. 6.25d. The damage was observed with more intensity in the bottom of

the model in agreement with the experimental results. The concentration of failure in the bottom of the model and specimen is related to the type of compaction and low compaction energy applied. These leaded to a model and a specimen with more porosity in the bottom than in the top.

6.6.3. Relation between Tensile and Compressive Strength

Fig. 6.26 shows the relationship between the evolution of the compressive and the compressive/flexural strengths ratio 'σ'_c / σ'_t' of pervious concrete obtained by the Meninger [48], the experimental results (Section 6.3) and the numerical results predicted by the proposed constitutive law. The experimental and numerical results obtained in this chapter were multiplied by the factor 1.476, in order to adapt the tensile strength obtained from Brazilian Test to flexural strength (this factor was obtained with the results presented by Joshaghani *et al* [162]). This indicates that the results obtained with the numerical model fits with the trend presented by Meninger [48].

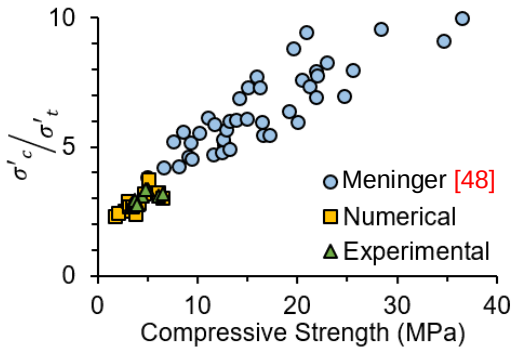

Figure 6.26 – Relationship between tensile and compressive strength for pervious concrete.

6.7. CONCLUDING REMARKS

Part of this study focused on relating the composition (A/P ratio, degree of compaction and porosity) with mechanical properties of the pervious concrete. The following are the major concluding remarks from this study:

- The mechanical properties (compressive and tensile strengths) are mainly influenced by the porosity of the sample. The geometrical properties of the cement paste that bonds the aggregates also influenced the mechanical

properties. The influence of the cement paste bond over the mechanical properties may be estimated by the A/P ratio and the degree of compaction.

- An analytical (based on empirical considerations) model was developed to predict the behavior of a pervious concrete specimen under compressive loads. The analytical model depends on parameters defined by the composition of a pervious concrete (A/P ratio and compaction degree). The comparison between the experimental and analytical results showed good agreement.

In this study a constitutive law to simulate the mechanical properties of pervious concrete was formulated. An extensively calibration and validation process were performed with real experiments. The results showed that it is possible to predict the compressive and tensile strengths numerically of compositions for different A/P ratios and compaction degrees. This opens up the possibility of performing a numerical design of composition before conduction experimental verifications, which might reduce the number of tests needed to achieve the composition that better suits the mechanical requirements of each application. From the findings of the present study, the following concluding remarks may be exposed:

- The proposed constitutive law simulates accurately the behavior of the pervious concrete under compression and tension. It succeeds in the goal of predicting the stress-strain curve in compression without any compressive softening behavior in the constitutive equations. This suggest that the response of pervious concrete under compression is governed mainly by tensile fracture and cohesive-frictional behavior. The proposed constitutive law reproduces with accuracy the effect of compaction degree and different A/P ratio. The pre- and post-peak numerical results obtained with the model were in agreement with experimental results. Also, the models predicted with accuracy the failure which depended mainly on the degree of compaction.
- The variability in compressive and tensile strengths presented by the numerical results obtained with the random disposal of the particles are in agreement with the results obtained experimentally. This shows that the model is capable of reproducing the variability inherent of the pervious concrete.
- The ratio estimated with numerical models between the compression strength and tensile strength fits the trend registered in the literature. This indicates that the model fits the reality.

7. CONCLUSION

7.1. GENERAL CONCLUSIONS

In the past 20 years, great advances in pervious concrete technology were observed. However, several aspects still require further research. Therefore, a generalist numerical and experimental work was conducted in order to provide clear and practical answers to the general objective: propose a design process of pervious concrete based on numerical simulations. In this sense, the doctoral thesis was focused on three important research lines: characterization of the fresh state behavior, characterization of the hydrological behavior (permeability) and characterization of the mechanical behavior. This section presents the general conclusions obtained for each one of them in response to the general objectives defined in Section 1.2.1.

As it is known that is difficult to determine the real spatial disposal of the aggregates inside a pervious concrete specimen, due the shape and size of the aggregates, the grading curve, the amount of cement, the amount of water, the type and the energy of the applied compaction, among other factors. However, the study of the first subject shows that the prediction of the spatial disposal of the aggregates is possible if the aggregates are considered as discrete particles. In this sense, the simulation of the interactions between aggregates involved by a thin layer of cement was performed using DEM. The comparison between experimental data and numerical results obtained by means of the proposed constitutive law showed good agreement. In particular, the model was capable of estimating the stress – strain compaction behavior, when different compositions of pervious concrete were considered.

The outcomes of the second subject represent an advance regarding the prediction of the permeability coefficient of pervious concrete with different compositions and

porosities using CFD. In this context, the study carried out not only identified the main properties that influence the hydrological behavior of the material but also showed that is possible to simulate the water flow inside the channels formed by the interconnected pores of the pervious concrete. The experimental results validated the numerical simulations of permeability. The geometrical models used in the permeability simulations were generated from the meso-structure obtained with the compaction model. In this sense, the comparison between experimental and numerical results also validated the meso-struture (spatial disposal of the aggregates) generated with the compaction model.

The outcome of the last subject also represents an advance considering the current models used to simulate the mechanical behavior of pervious concrete. A constitutive law in DEM for three-dimensional analysis of the mechanical interaction between two aggregates bonded by cement paste was proposed. This constitutive law predicted the compressive and tensile strength of pervious concrete considering different compositions and degree of compaction.

Based on all the studies carried out throughout the present doctoral thesis, a framework using several numerical methods to simulation the behavior of the pervious concrete considering different variables was developed. The new philosophy of design showed suitable to simulate the whole process that involves the pervious concrete. This approach reduces the experimental work prior to the definition of the final composition.

7.2. SPECIFIC CONCLUSIONS

Section 1.2.2 outlines several specific objectives for each one of the three subject studied in this thesis. The results and improvements were detailed in previous chapters. In order to give a general idea of the accomplishments obtained, the most relevant specific conclusions are presented in the following sections.

7.2.1. Fresh State Behavior

In Chapter 3 and 4 the fresh state behavior of the pervious concrete was studied experimentally and numerically. The main conclusions were:

- A high variability of the compaction pressure necessary to increase the density of the fresh specimens of pervious concrete was observed. This behavior is justified by the random spatial disposal of the aggregates, which interferes with the number of contacts between aggregates linked by fresh cement paste.

- An internal rearrangement of the aggregates during the compaction procedure was observed, when mono-sized aggregates were used in the composition. This internal rearrangement is necessary to displace surrounding aggregates in order to increase the compaction.
- The influences of two aggregate grading curves (5 to 12 mm and 9 to 20 mm) in the compaction process were experimentally analyzed. This study revealed that the compositions with smaller size of aggregates needed higher pressures to increase the compaction level. In order to achieve a degree of compaction equals 10 %, pressures average of 0.73 MPa and 0.48 MPa were obtained for the specimens with aggregate grading curves between 5 to 12 mm and 9 to 20 mm, respectively.
- The aggregate / cement paste ratio (comprehended in the interval of 3.63 to 5.17) showed little influence on the compaction process. However, with less aggregate / cement paste ratio, less compaction is required to achieved lower levels of porosities.
- The comparison between the experimental and numerical (obtained with the proposed 2D Evolutionary Lattice model) results showed an average correlation coefficient equals 0.948 for degree of compaction lower than 5 %. In addition, the proposed 2D Evolutionary Lattice model is an alternative approach and useful tool to the estimation of aspects such as the optimum compositions of the materials.
- The Kelvin-Voigt rheological model is commonly used to represent the interaction between aggregates surrounded by cement paste in fresh state. However, the same does not allow permanent deformations. In contrast, the dry paste (presented in pervious concrete in fresh state) is not capable of assuming the original position once the forces are eliminated, leaving a permanent deformation. This difference was mitigates with the proposed constitutive law (based on the Burgers model) using DEM.
- The comparison between the results of the compaction obtained numerically (in DEM) and experimentally showed that the constitutive law proposed is suitable to simulate such material as the pervious concrete. The average correlation coefficient obtained with the numerical and experimental results was equals 0.897. The simplifications made in the model regarding the simulation of the cement paste as a thin layer around the aggregate and the simulation of the aggregates as spherical particles had small effect in the simulations.

7.2.2. Hydrological Behavior

Concerning the experimental work and numerical simulations to determine the hydrological behavior of the pervious concrete presented in Chapter 5, the main conclusions were:

- The experimental permeability results showed that the studied range of aggregate / cement paste (2.42 to 3.70) does not affect the order of magnitude of the permeability when a similar porosity was analyzed. It was caused by the similarity of the channels that were created by the interconnected pores, since the aggregates used were the same. Also, the experimental results showed that the main factor that influences the permeability was the porosity.
- The parameters that influences the porosity were experimental analyzed. This study revealed that lower aggregate / cement paste ratio and higher degree of compaction conducted to a specimen with lower porosity.
- A new analytical model based on the experimental results was proposed. This analytical model predicted (with a correlation coefficient of 0.907) the porosity considering the aggregate / cement paste ratio (range from 2.42 to 3.70) and the degree of compaction (range from 10 to 20%). Moreover, it was estimated (with a correlation coefficient of 0.941) the permeability considering the porosity.
- A meso-structure geometry of the pore phase of pervious concrete was generated from the compaction model. In order to obtain the permeability, this geometry was used to simulate the water flow inside the pores channels. The comparison between experimental and numerical results showed good agreement, with a correlation coefficient equals 0.968.
- The good agreement between the experimental and numerical permeability is a strong indicative that the method presented in Chapter 3 is suitable for the analysis of the spatial disposal of the aggregates simulate. Such conclusion amplify the possibility of carrying out studies like the ones shown here.

7.2.3. Mechanical Behavior

Regarding the experimental work and numerical simulations to determine the mechanical behavior of the pervious concrete presented in Chapter 6, the main conclusions were:

- The main factor that influenced the compressive and tensile strength was the porosity (notice that no studding about the influence of the aggregate shape factor was performed). However, the experimental results showed

that the aggregate / cement paste ratio and the degree of compaction have smaller impact on the mechanical behavior of the pervious concrete. This influence is related to the amount and distribution of cement paste that bonds two aggregates, with gives strength to the contact.

- The stress-strain curves obtained from the compression tests showed a brittle behavior. Moreover, the ends of the linear portion of the stress-strain curve to the peak stress is far below the expected (considering normal concretes). This is caused by the poor connection between aggregates. In such connections, there is insignificant space for the micro cracks to grow before the total failure of the connection.
- An analytical model based on experimental results was developed to predict the behavior of a pervious concrete specimen under compressive loads. The analytical model depends on the composition of a pervious concrete (aggregate / cement paste ratio and degree of compaction) and the porosity. The coefficient of correlations calculated between the analytical and experimental results was equals 0.929. Also, the results showed that this analytical model predicted the stress-strain curve obtained experimentally.
- An analytical model was proposed to estimate the tensile strength based on the Brazilian test results. The analytical model depends on the aggregate / cement paste ratio, degree of compaction and the porosity. The comparison between analytical and experimental results showed good agreement, with a correlation coefficient equals 0.876.
- The proposed constitutive law simulated accurately the mechanical behavior of the pervious concrete under compression loads. It succeeds in the goal of predicting the stress-strain curve without any compressive softening behavior in the constitutive equations. This suggest that the response of pervious concrete under compression is governed mainly by tensile fracture and cohesive-frictional behavior. The proposed constitutive law predicted (correlation coefficient of 0.991) with accuracy the compressive strength considering the effect of compaction degree and different content of cement paste. The pre- and post-peak numerical results obtained with the model were in agreement with experimental results. The model predicted with accuracy the planes of failure observed in the specimens of the experimental tests. It also showed how the compaction degree affects these planes of failures.
- The numerical model predicted (correlation coefficient of 0.992) the macroscopic tensile strength of pervious concrete as experimentally obtained through Brazilian Tests (tensile splitting). It also predicted the planes of failure observed experimentally.
- The dispersion in compressive and tensile strengths presented by the numerical results obtained with the random spatial disposal of the particles

(generated with the compaction model) were in concordance with the results obtained experimentally. This showed that the model is capable to reproduces the variability inherent of the pervious concrete.

7.3. FUTURE PERSPECTIVES

In spite of the advances described in the previous section, during the development of this Doctoral Thesis others possible associate issues and aspects that required further research emerged. This section presents some suggestions for future research.

- Regarding the behavior of the cement paste in fresh state, the rheological characterization of cement paste with different compositions (also considering additives and admixtures) using viscometers should be performed. In this sense, it is important to correlate the rheological parameters with the constitutive law used in DEM to improve the simulations of the interactions between two aggregates linked by fresh cement paste.
- The compaction simulation in DEM should be compared to the experimental results using different types of compaction (roller, proctor, vibration table and others).
- It is important to extend the experimental characterization of pervious concrete in fresh and hardened state, for instance, focusing on the influence of the shape factor of the coarse aggregate.
- Regarding the numerical simulation, it is necessary to simulate the particles with the shape of real aggregates. The X-ray computed tomography technology may be used to characterize the geometrical property of aggregates. With the combination of X-ray computed tomography technology and clump technique (the use of more than two spherical particles fixed with each other to simulate different shapes) and/or polyhedral particles, the shape of aggregates may be better simulated and DEM simulation of pervious concrete in fresh state compaction could come closer to compaction behavior observed on the experimental results.
- The characterization of the spatial disposal of the aggregates and the pores should be studied in depth. In this sense, several techniques (image analysis performed in cross-sectional cuts or X-ray computed tomography) might be used to perform such characterization. Additional comparison between the experimental and numerical results are still required.

- It is necessary to couple DEM with other methods (such as Lattice Boltzmann or Lagrange) to improve the simulation of the cement paste behavior in fresh state. This coupled methods should be capable to capture the segregation of the cement paste. In this sense, it may be possible to assess numerically the probability of the segregation considering different compositions.
- It is necessary to create a stochastic method to generate the spatial disposal of the aggregates based on a large number of compacted models and experimental results, considering different factors such as types of compaction, degrees of compaction, aggregates with different shapes and sizes, aggregate / cement paste ratio, among others. This stochastic method should decrease the computational time spent to generate a geometrical model of pervious concretes.
- The numerical simulations to estimate the permeability and mechanical strengths should be performed considering the shape factor of the aggregates. This improvement may decrease the different between the numerical estimation and the experimental results.
- The introduction of the aggregate failure on the numerical models are necessary for the simulation of pervious concrete with higher strength.
- Numerical simulations coupling DEM and FEM should be performed to evaluate and understand the stress distribution during a mechanical simulation (under compressive or tensile loads).

REFERENCES

[1] Vorosmarty, C.J., McIntyre, P.B., Gessner, M.O., Dudgeon, D., Prusevich, A. Green, P., Glidden, S., Bunn, S.E., Sullivan, C.A., Reidy Liermann, C., Davies P.M., **Global threats to human water security and river biodiversity.** *Nature*, 2010 ; 467 ; 555-561.

[2] Brakenridge, GR., **Dartmouth Flood Observatory**, CSDMS, INSTAAR, University of Colorado.

[3] ACI Committee 522, **Report on Pervious Concrete**, 2010.

[4] Lay, M. G., **Ways of the World: A History of the World's Roads and of the Vehicles that used them.** *Rutger Univeristy Press*, New Brunswick, New Jersey, 1999, Pages 401.

[5] Chen, Y., Wang, K., Wang, X., Zhou, W., **Strength, fracture and fatigue of pervious concrete.** *Construction and Building Materials*, 2013 ; 42 ; 97-104.

[6] Yang, J., Jiang, G., **Experimental study on properties of pervious concrete pavement materials.** *Cement and Concrete Research*, 2003 ; 33(3) ; 381-386.

[7] Zhong, R., Wille, K., **Material design and characterization of high performance pervious concrete.** *Construction and Building Materials*, 2015 ; 98 ; 51-60.

[8] Lian, C., Zhuge, Y., **Optimum mix design of enhanced permeable concrete – An experimental investigation**. *Construction and Building Materials*, 2010 ; 24 (12) ; 2664-2671.

[9] Vázquez-Rivera, N. I., Soto-Pérez, L., St John, J. N., Molina-Bas, O. I., Hwang, S. S., **Optimization of pervious concrete containing fly ash and iron oxide nanoparticles and its application for phosphorus removal.** *Construction and Building Materials*, 2015 ; 93 (15) ; 22-28.

[10] Vancura, M., MacDonald, K., Khazanovich, L., **Microscopic analysis of paste and aggregate distresses in pervious concrete in a wet, hard freeze climate.** *Cement and Concrete Composites*, 2011 ; 33(10) ; 1080-1085.

[11] Luck, J. D., Workman, S. R., Coyne, M. S., Higgins, S. F., **Consequences of manure filtration through pervious concrete during simulated rainfall events**. *Biosystems Engineering*, 2009 ; 102(4) ; 417-423.

[12] Hesami, S., Ahmadi, S., Nematzadeh, M., **Effects of rice husk ash and fiber on mechanical properties of pervious concrete pavement.** *Construction and Building Materials*, 2014 ; 53 ; 680-691.

[13] Huang, B., Wu, H., Shu, X., Burdette, E. G., **Laboratory evaluation of permeability and strength of polymer-modified pervious concrete.** *Construction and Building Materials*, 2010 ; 24(5) ; 818-823.

[14] Shu, X., Huang, B., Wu, H., Dong, Q., Burdette, E. G., **Performance comparison of laboratory and field produced pervious concrete mixtures.** *Construction and Building Materials*, 2011 ; 25(8), 3187-3192.

[15] Gesoğlu, M., Güneyisi, E., Khoshnaw, G., İpek, S., **Investigating properties of pervious concretes containing waste tire rubbers.** *Construction and Building Materials*, 2014 ; 63 ; 206-213.

[16] Tennis, P. D., Leming, M. L., Akers, D. J., **Pervious Concrete Pavements.** *Portland Cement Association*, Skokie, Illinois, 2004.

[17] ACI Committee 301, **Specifications for Structural Concrete.** 2010.

[18] ASTM C1688 / C1688M-14a, **Standard Test Method for Density and Void Content of Freshly Mixed Pervious Concrete**, *ASTM International*, West Conshohocken, PA, 2014.

[19] ASTM C1754 / C1754M-12, **Standard Test Method for Density and Void Content of Hardened Pervious Concrete**, *ASTM International*, West Conshohocken, PA, 2012.

[20] Martin, W. D., Putman, B. J., Kaye, N. B., **Using image analysis to measure the porosity distribution of a porous pavement.** *Construction and Building Materials*, 2013 ; 48 ; 210–217.

[21] Sumanasooriya, M. S., Bentz, D. P., Neithalath, N., **Predicting the Permeability of Pervious Concretes from Planar Images.** in: *NRMCA Concrete Technology Forum*, 2009 ; 11.

[22] Sumanasooriya, M. S., Neithalath, N., **Stereology- and Morphology-Based Pore Structure Descriptors of Enhanced Porosity (Pervious) Concretes.** *Materials Journal*, 2009 ; 106(5) ; 429-438.

[23] Martin, W. D., Kaye, N. B., Putman, B. J., **Impact of vertical porosity distribution on the permeability of pervious concrete.** *Construction and Building Materials*, 2014 ; 59 ; 78–84.

[24] ASTM D7063 / D7063M-11, **Standard Test Method for Effective Porosity and Effective Air Voids of Compacted Bituminous Paving Mixture Samples**, *ASTM International*, West Conshohocken, PA

[25] Ibrahim, A., Mahmoud, E., Yamin, M., Patibandla, V. C., **Experimental study on Portland cement pervious concrete mechanical and hydrological properties.** *Construction and Building Materials*, 2014 ; 50 ; 524–529.

[26] Gaedicke, C., Marines, A., Miankodila, F., **A method for comparing cores and cast cylinders in virgin and recycled aggregate pervious concrete.** *Construction and Building Materials*, 2014 ; 52 ; 494–503.

[27] Tho-in, T., Sata, V., Chindaprasirt, P., Jaturapitakkul, C., **Pervious high-calcium fly ash geopolymer concrete.** *Construction and Building Materials*, 2012 ; 30 ; 366–371.

[28] Neithalath, N., Sumanasooriya, M. S., Deo, O., **Characterizing pore volume, sizes, and connectivity in pervious concretes for permeability prediction**, *Materials Characterization*, 2010 ; 61(8) ; 802–813.

[29] Coleri, E., Kayhanian, M., Harvey, J.T., Yang, K., Boone, J.M., **Clogging evaluation of open graded friction course pavements tested under rainfall and heavy vehicle simulators.** *Journal of Environmental Management*, 2013 ; 129 ; 164–72.

[30] Agar Ozbek, A.S., Weerheijm, J., Schlangen, E., van Breugel, K., **Dynamic behavior of porous concretes under drop weight impact testing.** *Cement and Concrete Composites*, 2013 ; 39 ; 1– 11.

[31] Vardaka, G., Thomaidis, K., Leptokaridis, C., Tsimas, S., **Use of Steel Slag as Coarse Aggregate for the Production of Pervious Concrete.** Journal of Sustainable Development of Energy, Water and Environment Systems, 2014 ; 2(1) ; 30–40.

[32] Nguyen, D.H., Boutouil, M., Sebaibi, N., Leleyter, L., Baraud, F., **Valorization of seashell byproducts in pervious concrete pavers.** *Construction and Building Materials*, 2013 ; 49 ; 151–160.

[33] Sonebi, M., Bassuoni, M. T., **Investigating the effect of mixture design parameters on pervious concrete by statistical modelling.** *Construction and Building Materials*, 2013 ; 38 ; 147–154.

[34] Yahia, A., Kabagire, K. D., **New approach to proportion pervious concrete.** *Construction and Building Materials*, 2014 ; 62 ; 38–46

[35] Maguesvari, M. U., Narasimha, V. L., **Studies on Characterization of Pervious Concrete for Pavement Applications.** *Procedia - Social and Behavior Sciences*, 2013 ; 104 ; 198–207.

[36] Sata, V., Wongsa, A., Chindaprasirt, P., **Properties of pervious geopolymer concrete using recycled aggregates.** *Construction and Building Materials*, 2013 ; 42 ; 33–39.

[37] Zaetang, Y., Wongsa, A., Sata, V., Chindaprasirt, P., **Use of lightweight aggregates in pervious concrete.** *Construction and Building Materials*, 2013 ; 48 ; 585–591.

[38] Bhutta, M. A. R., Hasanah, N., Farhayu, N., Hussin, M. W., Tahir, M. B. M., Mirza, J., **Properties of porous concrete from waste crushed concrete (recycled aggregate).** *Construction and Building Materials*, 2013 ; 47 ; 1243–1248.

[39] Kuo, W.-T., Liu, C.-C., Su, D.-S., **Use of washed municipal solid waste incinerator bottom ash in pervious concrete.** *Cement and Concrete Composites*, 2013 ; 37 ; 328–335.

[40] Montes F., Haselbach L. M., **Measuring hydraulic conductivity in pervious concrete.** *Environmental Engineering Science*, 2006 ; 23(6) ; 960-970.

[41] ASTM C39/C39M-15a, **Standard Test Method for Compressive Strength of Cylindrical Concrete Specimens**, *ASTM International*, West Conshohocken, PA, 2015.

[42] AENOR, UNE-EN 12390-3:2009 - **Ensayos de hormigón endurecido. Parte 3: Determinación de la resistencia a compresión de probetas**, (2009).

[43] ASTM C293/C293M-10, **Standard Test Method for Flexural Strength of Concrete (Using Simple Beam With Center-Point Loading)**, *ASTM International*, West Conshohocken, PA, 2010.

[44] ASTM C78/C78M-15a, **Standard Test Method for Flexural Strength of Concrete (Using Simple Beam with Third-Point Loading)**, *ASTM International*, West Conshohocken, PA, 2015.

[45] AENOR, UNE-EN 12390-5:2009 - **Ensayos de hormigón endurecido. Parte 5: Resistencia a flexion de probetas**, (2009).

[46] ASTM C496 / C496M-11, **Standard Test Method for Splitting Tensile Strength of Cylindrical Concrete Specimens**, *ASTM International*, West Conshohocken, PA, 2004.

[47] AENOR, UNE-EN 12390-6:2009 - **Ensayos de hormigón endurecido. Parte 6: Resistencia a tracción indirecta de probetas**, (2009).

[48] Meininger, R. C., **No-Fines Pervious Concrete for Paving.** *Concrete International*, 1988 ; 10 ; 20-27.

[49] ASTM C29 / C29M, **Standard Test Method for Bulk Density (Unit Weight) and Voids in Aggregate**, *ASTM International*, West Conshohocken, PA, 2009.

[50] Kim, H. K., Lee, H. K., **Influence of cement flow and aggregate type on the mechanical and acoustic characteristics of porous concrete.** *Applied Acoustics*, 2010 ; 71(7) ; 607–615.

[51] Sriravindrarajah, R., Wang, N. D. H., Ervin, L. J. W., **Mix Design for Pervious Recycled Aggregate Concrete.** *International Journal of Concrete Structures and Materials*, 2012 ; 6(4) ; 239–246.

[52] Torres, A., Hu, J., Ramos, A., **The effect of the cementitious paste thickness on the performance of pervious concrete.** Construction and Building Materials, 2015 ; 95 ; 850-859.

[53] Gafoori, N., Dutta, S., **Laboratory Investigation of Compacted No-Fines Concrete for Paving Materials.** *Journal of Materials in Civil Engineering*, 1995 ; 7(3) ; 183–191.

[54] Nabeta, K., **Flow simulation of fresh concrete by distinct element method.** *Proceedings of the Japan Concrete Institute*, 1994 ;16 ; 479-484.

[55] Chu, H., Machida, H., Suzuki, N., **Experimental investigation and DEM simulation of filling capacity of fresh concrete.** *Transactions of the Japan Concrete Institute*, 1996 ; 16 ; 9–14.

[56] Noor, U. A., Uomoto, T., **Three-dimensional discrete element method of rheology tests of self-compacting concrete.** In: *Proceeding of the First International RILEM Symposium on Self-Compacting Concrete*, Stockholm, Sweden, 1999.

[57] Puri, U., Uomoto, T., **Numerical modeling – a new tool for understanding shotcrete.** *Materials and Structures*, 1999 ; 32 ; 266-272.

[58] Chu, H., Machida, A., **Experimental evaluation and theorical simulation of self-compacting concrete by modified distinct element method (MDEM)**. In: *Recent Advances in Concrete Technology*, Fourth CANMET/ACI/JCI International Conference, Tokushima, Japan. 1998 ; 691-714.

[59] Gram, A., **Numerical Modelling of Self-Compacting Concrete Flow - Discrete and Continuous Approach.** *Doctoral Thesis, Royal Institute of Technology*, 2009, Pages 66.

[60] Zheng, J., An, X. and Huang, M., **GPU-based parallel algorithm for particle contact detection and its application in self-compacting concrete flow simulations.** *Computers & Structures*, 2012 ; 112–113 ; 193-204.

[61] Shyshko, S. Mechtcherine, V., **Developing a Discrete Element Model for simulating fresh concrete: Experimental investigation and modelling of**

interactions between discrete aggregate particles with fine mortar between them. *Construction and Building Materials*, 2013 ; 47 ; 601-615.

[62] Mechtcherine, V., Gram, A., Krenzer, K., Schwabe, J. H., Shyshko, S., Roussel, N., **Simulation of fresh concrete flow using discrete element method (DEM): theory and applications.** *Materials and Structures*, 2014 ; 47 ; 615–630.

[63] Hoornahad, H., Koenders, E. A. B., **Simulation of macroscopic behavior of a self-compacting mixture based on DEM.** *SCC 5th North American Conference on the Design and Use of Self-Consolidating Concrete*, Chicago (USA), 2013.

[64] Mechtcherine, V., Shyshko, S., **Simulating the behaviour of fresh concrete with the Distinct Element Method – Deriving model parameters related to the yield stress.** *Cement and Concrete Composites*, 2015 ; 55 ; 81-90.

[65] Remond, S., Pizette, P., **A DEM hard-core soft-shell model for the simulation of concrete flow.** *Cement and Concrete Research*, 2014 ; 58 ; 169-178.

[66] Chen, J., **Discrete Element Method (DEM) Analyses for Hot-Mix Asphalt (HMA) Mixture Compaction.** *Doctoral Thesis, University of Tennessee*, 2011, Pages 161.

[67] Chen, J., Huang, B., Shu, X., **Air-Void Distribution Analysis of Asphalt Mixture Using Discrete Element Method.** *Journal of Materials in Civil Engineering*, 2013 ; 25(10) ; 1375-1385.

[68] Chen, J., Huang, B., Chen, F., Shu, X,. **Application of discrete element method to Superpave gyratory compaction.** *Road Materials and Pavement Design*, 2012 ; 13(3) ; 480-500.

[69] Bear, J., **Dynamics of Fluids in Porous Media.** *Dover Publications Inc.*, 1989, Pages 784.

[70] Neithalath, N., Bentz, D. P., Sumanasooriya, M. S., **Predicting the Permeability of Pervious Concrete.** *Concrete International*, 2010 ; 32(5) ; 35-40.

[71] Neithalath, N., Sumanasooriya, M.S., Deo, O., **Characterizing pore volume, sizes, and connectivity in pervious concretes towards permeability prediction.** *Materials Characterization*, 2010 ; 61(8) ; 802-813.

[72] Sumanasooriya, M. S., Bentz, D. P., Neithalath, N., **Planar image based reconstruction of pervious concrete pore structure and permeability prediction.** *ACI Materials Journal*, 2010 ; 107(4) ; 413-421.

[73] Chung, S. -Y., Han, T. -S., Kim, S. -Y., Lee, T. –H., **Investigation of the permeability of porous concrete reconstructed using probabilistic**

description methods. *Construction and Building Material*, 2014 ; 66(15) ; 760-70.

[74] Wang, L., Ueda, T., **Mesoscale modeling of water penetration into concrete by capillary absorption.** *Ocean Engineering*, 2011 ; 38(4) ; 519-528.

[75] Zalzale, M., McDonald, P. J., **Lattice Boltzmann simulations of the permeability and capillary adsorption of cement model microstructures.** *Cement and Concrete Research*, 2012 ; 42(12) ; 1601-1610.

[76] Zhang, M., Ye, G., van Breugel, K., **Microstructure-based modeling of permeability of cementitious materials using multiple-relaxation-time lattice Boltzmann method.** *Computational Materials Science*, 2013 ; 68 ; 142-151.

[77] Abyaneh, S. D., Wong, H. S., Buenfeld, N. R., **Modelling the diffusivity of mortar and concrete using a three-dimensional mesostructure with several aggregate shapes.** *Computational Materials Science*, 2013 ; 78 ; 63-73.

[78] Abyaneh, S. D., Wong, H. S., Buenfeld, N. R., **Computational investigation of capillary absorption in concrete using a three-dimensional mesoscale approach.** *Computational Materials Science*, 2014 ; 87 ; 54-64.

[79] Chung, S. –Y., Han, T. –S., Kim, S. -Y., **Reconstruction and evaluation of the air permeability of a cement paste specimen with a void distribution gradient using CT images and numerical methods.** *Construction and Building Materials*, 2015 ; 87 ; 45-53.

[80] Yazdchi, K., Srivastava, S., Luding, S., **Microstructural effects on the permeability of periodic fibrous porous media.** *International Journal of Multiphase Flow*, 2011 ; 37 ; 956-966.

[81] Torre, A. D., Montenegro, G., Tabor, G. R., Wears, M. L., **CFD characterization of flow regimes inside open cell foam substrates.** *International Journal of Heat and Fluid Flow*, 2014 ; 50 ; 72–82.

[82] Ranut, P., Nobile, E., Macini, L., **High resolution microtomography-based CFD simulation of flow and heat transfer in aluminum metal foams.** *Applied Thermal Engineering*, 2014 ; 69 ; 230-240.

[83] Schafrik, S., Millar, D. L., **Verification of a CFD code use for air flow simulations of fractured and broken rock.** *Applied Thermal Engineering*, 2015 ; 90 ; 1131-1143.

[84] Videla, A. R., Lin, C. L., Miller, J. D., **Simulation of saturated fluid flow in packed particle beds - The lattice-Boltzmann method for the calculation of permeability from XMT images.** Journal of the Chinese Institute of Chemical Engineers, 2008 ; 39(2) ; 117-28.

[85] Wang, J., Ju, Y., Huang, Y., Zheng, J., Zheng, Z., **Study of the influence of porous structure on the permeability of rock using Lattice Boltzmann method.** *Procedia Engineering*, 2015 ; 102 ; 1835-1841.

[86] Deo, O., Neithalath, N., **Compressive behavior of pervious concretes and a quantification of the influence of random pore structure features.** *Materials Science and Engineering A*, 2010 ; 528 ; 402-412.

[87] Lian, C., Zhuge, Y., Beecham, S., **Modelling Pervious Concrete under Compression Loading – A Discrete Element Approach.** *Advanced Materials Research*, 2011 ; 168-170 ; 1590-1600.

[88] ITASCA. **PFC2D particle flow code in two dimensions**, *Itasca Consulting Group*, Inc. (1995).

[89] Lian, C., Zhuge, Y., Beecham, S., **Numerical simulation of the mechanical behaviour of porous concrete.** *Engineering Computations*, 2011 ; 28(8) ; 984-1002.

[90] Caballero, A., López, C. M., Carol, I., **3D meso-structural analysis of concrete specimens under uniaxial tension.** *Computer methods in applied mechanics and engineering*, 2006 ; 195 ; 7182-7195.

[91] Snozzi, L., Caballero, A., Molinari, J. F., **Influence of the meso-structure in dynamic fracture simulation of concrete under tensile loading.** *Cement and Concrete Research*, 2011 ; 41 ; 1130-1142.

[92] Li, S., Li, Q., **Method of meshing ITZ structure in 3D meso-level finite element analysis for concrete.** *Finite Elements in Analysis and Design*, 2015 ; 93 ; 96-106.

[93] Huang, Y., Yang, Z., Ren, W., Liu, G., Zhang, C., **3D meso-scale fracture modelling and validation of concrete based on in-situ X-ray Computed Tomography images using damage plasticity model.** *International Journal of Solids and Structures*, 2015 ; 67-68 ; 340-352.

[94] Schlangen, E., Garboczi, E. J., **Fracture simulations of concrete using Lattice Models: Computational Aspects.** *Engineering Fracture Mechanics*, 1997 ; 57(2/3) ; 319-332.

[95] Lilliu, G., van Mier, J. G. M., **3D lattice type fracture model for concrete.** *Engineering Fracture Mechanics*, 2003 ; 70(7-8) ; 927-941.

[96] Cusatis, G., Bazant, Z. P., Cedolin, L., **Confinement-Shear Lattice Model for Concrete Damage in Tension and Compression: I. Theory.** *Journal of Engineering Mechanics*, 2003 ; 129(12) ; 1439-1448.

[97] Cusatis, G., Bazant, Z. P., Cedolin, L., **Confinement-Shear Lattice Model for Concrete Damage in Tension and Compression: II. Computation and Validation.** *Journal of Engineering Mechanics*, 2003 ; 129(12) ; 1449-1458.

[98] Kozicki, J., Tejchman, J., **2D Lattice Model for Fracture in Brittle Materials.** *Archives of Hydro-Engineering and Environmental Mechanics*, 2006 ; 53(2) ; 137-154.

[99] Kozicki, J., Tejchman, J., **Effect of aggregate structure on fracture process in concrete using 2D Lattice Model.** *Archives of Mechanics*, 2007 ; 59(4-5) ; 365-384.

[100] Šmilauer, V., **Cohesive Particle Model using the Discrete Element Method on the Yade Platform.** *Doctoral Thesis, Czech Technical University*, 2010, Pages 149.

[101] Šmilauer, V., Catalano, E., Chareyre, B., Dorofeenko, S., Duriez, J., Gladky, A., Kozicki, J., Modenese, C., Scholtès, L., Sibille, L., Stránský, J., Thoeni, K., **Yade Documentation 2nd ed. The Yade Project.** <http://yade-dem.org/doc/>.

[102] Tran, V. T., Donzé, F. –V., Marin, P., **A discrete element model of concrete under high triaxial loading.** *Cement & Concrete Composites*, 2011 ; 33 ; 936-948.

[103] Nitka, M., Tejchman, J., **Discrete modeling of micro-structure evolution during concrete fracture using DEM.** *Computational Modelling of Concrete Structures*, 2014 ; 1 ; 345-354.

[104] Nitka, M., Tejchman, J., **Modelling of concrete behavior in uniaxial compression and tension with DEM.** *Granular Matter*, 2015 ; 17 ; 145–164.

[105] Skarzynski, L., Nitka, M., Tejchman, J., **Modeling of concrete fracture at aggregate level using FEM and DEM based on X-ray μCT images of internal structure.** *Engineering Fracture Mechanics*, 2015 ; 147 ; 13-35.

[106] Cusatis, G., Pelessone, D., Mencarelli, A., **Lattice Discrete Particle Model (LDPM) for failure behavior of concrete. I: Theory.** *Cement & Concrete Composites*, 2011 ; 33 ; 881-890.

[107] Cusatis, G., Pelessone, D., Mencarelli, A., **Lattice Discrete Particle Model (LDPM) for failure behavior of concrete. II: Calibration and validation.** *Cement & Concrete Composites*, 2011 ; 33 ; 891-905.

[108] Cundall, P. A., Strack, O. D. L., **BALL – A program to model granular medium using the distinct element method.** *Technical Note: Advanced Technology Group*, London, 1978.

[109] Cundall, P. A., Strack, O. D. L., **A discrete numerical model for granular assemblies.** *Geotechnique*, 1979 ; 29 ; 47–65.

[110] Martin, C. L., Bouvard, D., Shima, S., **Study of particle rearrangement during powder compaction by the discrete element method.** *Journal of the Mechanics and Physics of Solids*, 2003 ; 51(4) ; 667–693.

[111] He, H., Guo, Z., Stroeven, P., Stroeven, M., Sluys, L. J., **Characterization of the packing of aggregate in concrete by a discrete element approach.** *Materials Characterization*, 2009 ; 60 ; 1082-1087.

[112] Markauskas, D., Kacianauskas, R., **Compacting of particles for biaxial compression test by the discrete element method.** *Journal of Civil Engineering and Management*, 2006 ; 12(2) ; 153-61.

[113] Jerier, J. –F., Richefeu, V., Imbault, D., Donzé, F. -V., **Packing spherical discrete elements for large scale simulations.** *Computer Methods in Applied Mechanical Engineering*, 2010 ; 199(25-28) ; 1668–1676.

[114] Toomey, A., Bean, C. J., **Numerical simulation of seismic waves using a discrete particle scheme.** *Geophysical Journal International*, 2000 ; 141 ; 595-604.

[115] Wu, C. –Y., Ruddy, O. M., Bentham, A. C., Hancock, B. C., Best, S. M., Elliott, J. A., **Modelling the mechanical behavior of pharmaceutical powders during compaction.** *Powder Technology*, 2005 ; 152 ; 107-117.

[116] Sinha, T., Bharadwaj, R., Curtis, J. S., Hancock, B. C., Wassgrena, C., **Finite element analysis of pharmaceutical tablet compaction using a density dependent material plasticity model.** *Powder Technology*, 2010 ; 202 ; 46-54.

[117] Rahman, M. M., Ariffin, A. K., Nor, S. S. M., **Development of a finite element model of metal powder compaction process at elevated temperature.** *Applied Mathematical Modeling*, 2009 ; 33 ; 4031-4048.

[118] Aydin, I., Briscoe, B. J., Sanlitürk, K. Y., **The internal form of compacted ceramic components: A comparison of a finite element modelling with experiment.** *Powder Technology*, 1996 ; 89 ; 239–254.

[119] Zhang ,J., **A study of compaction of composite particles by multi-particle finite element method.** *Composites Science and Technology*, 2009 ; 69(13) ; 2048-53.

[120] Harthong, B., Jérier, J. –F., Dorémus, P., Imbault, D., Donzé, F. -V., **Modeling of high-density compaction of granular materials by discrete element method.** *International Journal of Solids and Structures*, 2009 ; 46(18-19) ; 3357–3364.

[121] Gethin, D. T., Yang, X. –S., Lewis, R. W., **A two dimensional combined discrete and finite element scheme for simulating the flow and compaction of systems comprising irregular particles.** *Computer Methods in Applied Mechanical Engineering*, 2006 ; 195 ; 5552-5565.

[122] Ransing, R. S., Gethin, D. T., Khoei, A. R., Mosbah, P., Lewis, R. W., **Powder compaction modeling via the discrete and finite element method.** *Materials & Design*, 2000; 21(4) ; 263-269.

[123] Gethin, D. T., Ransing, R. S., Lewis, R. W., Dutko, M., Crook, A. J. L., **Numerical comparison of a deformable discrete element model and an equivalent continuum analysis for the compaction of ductile porous material.** *Computer and Structures*, 2001 ; 79 ; 1287-94.

[124] Frenning, G., **An efficient finite/discrete element procedure for simulating compression of 3D particle assemblies.** *Computer Methods in Applied Mechanical Engineering*, 2008 ; 197 ; 4266–4272.

[125] Brey, J. J., Prados, A., Sánchez-Rey, B., **Simple model with facilitated dynamics for granular compaction.** *Physical Review E*, 1999 ; 60(29) ; 5685-92.

[126] Fusco, C., Fasolino, A., Gallo, P., Petri, A., Rovere, M., **Microscopic two-dimensional lattice model of dimer granular compaction with friction.** *Physical Review E*, 2002 ; 66(3) ; 031301-9.

[127] Ludewig, F., Vandewalle, N., Dorbolo, S., **Compaction of granular mixtures.** *Granular Matter*, 2006 ; 8 ; 87–91.

[128] Katsman, R., Aharonov, E., Scher, H.. **Numerical simulation of compaction bands in high-porosity sedimentary rock.** *Mechanics of Materials*, 2005 ; 37(1) ; 143-162.

[129] Katsman, R., Aharonov, E., **Study of compaction bands originating from cracks, notches, and compacted defects.** *Journal of Structural Geololy*, 2006 ; 28(3) ; 508-518.

[130] Kozicki, J., Tejchman, J., **2d lattice model for fracture in brittle materials.** *Archives of Hydro-Engineering and Environmental Mechanics*, 2006 ; 53(2) ; 71–88.

[131] Liu, J. X., Zhao, Z. Y., Deng, S. C., Liang, N. G., **Modified generalized beam lattice model associated with fracture of reinforced fiber/particle composites.** *Theoretical and Applied Fracture Mechanics*, 2008 ; 50(2) ; 132–141.

[132] Vold, M. J., **A numerical approach to the problem of sediment volume.** *Journal of Colloid Science*, 1959 ; 14(2) ; 1681-74.

[133] Jullien, R., Meakin, P., Pavlovtich, A., **Recent advances in computer modelling of granular systems.** *Journal de Physique IV*, 1993 ; 3 ; 1981-1986.

[134] Goia, G., Cuitiño, A. M., Uribe, T., Zheng, S., **Two-phase densification of cohesive granular aggregates.** *Physical Review Letters*, 2002 ; 88 ; 1-4.

[135] Schwager, T., Pöschel, T., **Efficient numerical simulation of granular matter using the bottom-to-top reconstruction method.** *Behaviour of Granular medium*, 2006 ; 151-159.

[136] Wills, H. H., **On the theory of Hertzian fracture.** *Proceedings of the Royal Society of London A*, 1967 ; 299 ; 291-306.

[137] German, R. M., **The role of particle packing density in powder injection molding.** *Reviews on Powder Metallurgy and Physical Ceramics*, 1992 ; 5 ; 81-110.

[138] Cusatis, G., Bazant, Z. P., Cedolin, L., **Confinement-shear lattice CSL model for fracture propagation in concrete.** *Computational Methods in Applied Mechanical Engineering*, 2006 ; 159 ; 7154–7171.

[139] Ince, R., Arslan, A., Karihaloo, B. L., **Lattice modelling of size effect in concrete strength.** *Engineering Fracture Mechanics*, 2003 ; 70 ; 2307–2320.

[140] Liu, J. X., Liang, N. G., **Algorithm for simulating fracture processes in concrete by lattice modeling.** *Theoretical and Applied Fractures Mechanics*, 2009 ; 52 ; 26-39.

[141] Montero-Chacón, F., Medina, F., **A lattice-particle approach to determine the RVE size for quasi brittle materials.** *Engineering with Computers*, 2013 ; 30(2) ; 246-62.

[142] Klein, N. S., **El rol físico del Agua en mezclas de cemento Portland.** *Doctoral Thesis, Universitat Politècnica de Catalunya*, 2012, Pages 247

[143] Klein, N. S., Bachmann, J., Aguado, A., Toralles-Carbonari, B., **Evaluation of the wettability of mortar component granular materials through contact angle measurements.** *Cement and Concrete Research*, 2012 ; 4 (12) ; 1611-1620.

[144] Lu, G., Wanga, K., Rudolphi, T. J., **Modeling rheological behavior of highly flowable mortar using concepts of particle and fluid mechanic.** *Cement and Concrete Research*, 2008 ; 30(1) ; 1-12.

[145] Pöschel, T., Schwager, T., **Computational granular dynamics: Models and algorithms.** *Springer*, Germany, Berlin, 2005, Pages 322.

[146] Hassanpour, A., Ghadiri, M., **Distinct element analysis and experimental evaluation of the Heckel analysis of bulk powder compression.** *Powder Technology*, 2004 ; 141 ; 251-261.

[147] Thornton, C., Ning, Z., **A theoretical model for the stick/bounce behaviour of adhesive, elastic–plastic spheres.** *Powder Technology*, 1998 ; 99 ; 154–162.

[148] Suleiman, M. T., Kevern, J. T., Schaefer, V. R., Wang, K., **Effect of Compaction Energy on Pervious Concrete Properties.** *Proceedings of the 2006 NRMCA Concrete Technology Forum – Focus on Pervious Concrete*, Nashville, TN, 2006.

[149] Kevern, J. T., Schaefer, V. R., Wang, K., **Evaluation of Pervious Concrete Workability Using Gyratory Compaction.** *ASCE Journal of Materials in Civil Engineering*, 2009 ; 21(12) ; 764:770.

[150] Gaedicke, C., Marines, A., Miankodila, F., **Assessing the abrasion resistance of cores in virgin and recycled aggregate pervious concrete.** Construction Building Materials, 2014 ; 68 ; 701-708.

[151] Yeih, W., Fu, T. C., Chang, J. J., Huang, R., **Properties of pervious concrete made with air-cooling electric arc furnace slag as aggregates.** *Construction Building Materials*, 2015 ; 93 ; 7337-745.

[152] Dassault Systèmes, **Advanced boundary Cartesian meshing technology in SolidWorks Flow Simulation.** *Dessault Systèmes technical paper*, 2013, Pages 31.

[153] Sabachkin, A., Dumnov, G., **Numerical Basis of CAD-Embbed CFD.** *National Agency for Finite Element Methods and Standards (NAFEMS)*, World Congress, Salzburg, Austria, 2013, Pages 20.

[154] Apedo, K. L., Munzer, C., He, H., Montgomery, P., Serres, N., Fond, C., Feugeas, F., **Cement paste surface roughness analysis using coherence scanning interferometry and confocal microscopy.** *Materials Characterization*, 2015 ; 100 ; 108-119.

[155] Dassault Systèmes. **Technical Reference SolidWorks Flow Simulation.** 2014. 2014, Pages 68.

[156] Torres, A., Hu, J., Ramos, A., **The effect of the cementitious paste thickness on the performance of pervious concrete.** *Construction and Building Materials*, 2015 ; 95(1) ; 850-859.

[157] Deo, O., Neithalath, N., **Compressive response of pervious concretes proportioned for desired porosities.** *Construction and Building Materials*, 2011 ; 25 ; 4181-9.

[158] Tasdemir, M. A., Tasdemir, C., Akyuz, S., Jefferson, A. D., Lydon, F. D., Barr B. I. G., **Evaluation of Strains at Peak Stress in Concrete: A Three-Phase Composite Model Approach.** *Cement and Concrete Composites*, 1998 ; 20 ; 301-18.

[159] Lubliner, J., Oliver, J., Oller, S., Oñate, E., **A Plastic-Damage Model for Concrete.** *International Journal of Solids and Structures*, 1989 ; 25(3) ; 299-326.

[160] Rokugo, K., Koyanagi, W., **Role of Concrete Fracture Energy of Concrete on the Failure Behavior of Reinforced Concrete Beams, in Applications of Fracture Mechanics to Reinforced Concrete.** *A. Carpinteri (ed.), Elsevier Applied Science* 1992 : 437-64.

[161] Dassault Systèmes. **ABAQUS Documentation**, Providence, RI, USA 2014.

[162] Joshaghani, A., Ramezanianpour, A. A., Jaberizadeh, M., **Mechanical Characteristic of Pervious Concrete Considering the Gradation and Size of Coarse Aggregates.** *Research Journal of Environmental and Earth Sciences*, 2014 ; 6(9) ; 437-442.